Application of Polymeric Materials in the Fabrication of Flexible Biosensors

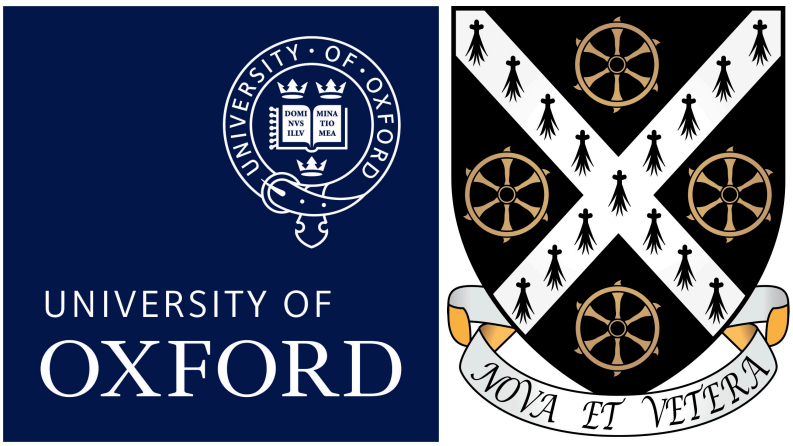

Harry Potter

St Catherine's College

Department of Materials, University of Oxford

A Thesis submitted for the degree of

Doctor of Philosophy

Michaelmas Term 2024

DECLARATION

Word Count: 39,778

This thesis is an account of work carried out by the author in the Department of Materials, University of Oxford under the supervision of Professor Hazel E. Assender. I declare that this thesis has not been submitted to any other institution for the purpose of examination and was solely undertaken during this DPhil project. Any work of others that has been utilised, directly or indirectly, has been appropriately cited. Parts of this thesis have been published in the following scientific journals or conference presentations:

H Potter, G Francis, B W. Stuart and H E. Assender, in *65th Annual Technical Conference Proceedings*, Society of Vacuum Coaters, Albuquerque, May 2022, pp. 239-245.

H Potter, R Schofield, K Zhang, H E. Assender, Poster presented in part at the *7th International Symposium Frontiers in Polymer Science*, Gothenburg, May 2023.

ACKNOWLEDGMENTS

Firstly, I would like to sincerely thank my supervisor, Professor Hazel Assender, for her continuing support over the duration of this project. Despite immensely challenging circumstances, her guidance and encouragement has allowed me to undertake this work in a positive and enjoyable environment. A special thank you to Richard Turner, Greg Cook and Professor Andrew Watt for their technical support and discussions at Begbroke. I would like to extend thanks to the technical staff and scientists at the Oxford Materials Characterisation Service as well as those in the departments of chemistry, physics, and materials for the training and assistance on the many pieces of equipment used throughout this research.

Many thanks are given to my friends and colleagues, especially those in the Assender, Grobert and Grant research groups, as you have made our offices a truly special and productive place to work. Particular thanks are extended to Ryan Schofield for the countless discussions and support on the polythiophene synthesis, Holly Yeo for conducting the GPC analysis and Maya Landis for helping me with NMR. I also thank my former teammates at the Oxford University Handball Club, for giving me a place to escape and for making my time in Oxford so memorable.

Finally, a heartfelt appreciation goes out to my parents and my partner, Emma, for their constant and unconditional support throughout the long journey.

ABSTRACT

Flexible and organic electronics, such as wearable biosensor devices, have gained increasing success over recent decades. A key objective at the intersection of industry and academia remains the development of processes and materials that enable the commercial-scale fabrication of these devices. By utilising high-throughput printing techniques, such as flexography, it is possible to produce large-area and wearable sensors at low cost, with a reduced environmental impact. To support the realisation of high-throughput device manufacturing, this thesis investigates the development of flexible, printable biosensor devices using conductive polymers. Central to this research is the covalent immobilisation of enzyme bioreceptors for glucose-sensing electrodes, alongside the exploration of a selective metallisation process with focus on the reuse of printing plates through the regeneration of the patterning surface to improve process sustainability and enable the rapid prototyping of devices.

A chemical oxidative polymerisation method, employing chloroform and acetonitrile as reaction solvents, was used to produce a series of novel copolymers based on 3-hexylthiophene and a functional, carboxylic acid-derived comonomer. These polymers were prepared for the purpose of covalently immobilising bioreceptors for the fabrication of flexible biosensor devices via solution deposition methods. Analytical techniques, including ATR-FTIR, NMR, UV-Vis, and GPC-SEC, were utilised to confirm the structures and properties of the polymers. The synthesised copolymers exhibited varying molecular weights and solubility, as such further optimisation of the synthetic process is required to improve device characteristics and processability.

An investigation into the use of UV/Ozone-oxidised polydimethylsiloxane stamps in a selective metallisation process has advanced the theoretical understanding of this novel technique. This includes deeper insight into the recovery of Krytox1506 contact angle and the determination of underlying chemical changes resulting from thermally and chemically enhanced surface regeneration processes. The application of both the synthesised, soluble copolymers and UV/Ozone-polydimethylsiloxane selective metallisation in the fabrication

of flexible glucose biosensor electrodes is described. Covalent immobilisation of glucose oxidase on the electrode surfaces was confirmed via o-dianisidine binding assays and mediatorless electrochemical testing. The biosensors demonstrated sensitive and selective glucose detection over an extended period, highlighting the stable immobilisation that arises from use of both the carboxylic acid and N-succinimidyl ester functionalised copolymers. Chronoamperometry and cyclic voltammetry were employed to assess sensor performance, revealing specific glucose recognition and resistance to interference from urea. All sensors exhibited full or partial linearity across physiological glucose concentrations.

The findings indicate that 3-hexylthiophene based copolymers are promising for use in the mass production of flexible biosensors and in the application as a generalised, conductive binding agent. The use of UV/Ozone-PDMS in metal electrode deposition has been shown to produce functional electronic devices comparable to those fabricated with the traditional methods.

Contents

List of Figures

List of Tables

List of Acronyms

3HT 3-hexylthiophene

3MT 3-methylthiophene

AJP Aerosol jet printing

ALD Atomic layer deposition

ATP Adenosine-5'-triphosphate

ATR-FTIR Attenuated total reflectance - fourier transform infrared spectroscopy

CA Chronoamperometry

CNT Carbon nanotube

CPs Conductive polymers

CTP Catalyst transfer polycondensation

CV Cyclic voltammetry

DAO Diamine oxidase

DCA Diiodomethane contact angle

DCC Dicyclohexyl-carbodiimide

DET Direct electron transfer

EDC 1-ethyl-3-(3-dimethylaminopropyl) carbodiimide

EDOT 3,4-ethylenedioxythiophene

F8BT Poly(9,9-di-n-octylfluorene-alt-benzothiadiazole)

FAD Flavinadenine dinucleotide

FPT Freeze-pump-thaw

GOx Glucose oxidase

GPC Gel permeation chromatography

GRIM Grignard metathesis polymerisation

HOMO Highest occupied molecular orbital

HPLC High-performance liquid chromatography

HRP Horseradish peroxidase

IJP Inkjet printing

IoT Internet of Things

ITO Indium-Tin-Oxide

IUPAC The International Union of Pure and Applied Chemistry

KCA Krytox1506 contact angle

KCTP Kumada catalyst transfer polymerisation

LMW Low molecular weight

LoD Limit of detection

LUMO Lowest unoccupied molecular orbital

M3T3YA Methyl 3-(thiophen-3-yl)acrylate

M3TA Methyl 3-thiophene acetate

M3TC Methyl 3-thiophene carboxylate

MAO Monoamine oxidase

MIPs Molecularly imprinted polymers

MOSFETs Metal-oxide-semiconductor field effect transistors

NFC Near-field communication

NHS N-hydroxysuccinimide

NMR Nuclear magnetic resonance

NP Nanoparticles

OEs Flexible, printed and organic electronics

OLED Organic light-emitting diode

OPV Organic photovolatic

OTFT Organic thin-film transistors

OTFT-TIA Organic thin-film transistor transimpedance amplifier

OWRK The Owens, Wendt, Rabel and Kaelble model

P3AT Poly(3-alkylthiophenes)

PA Polyacetylene

PAM Polyacrylamide

PBS Phosphate-buffered saline

PDI Polydispersity index

PDMS Polydimethylsiloxane

PEDOT Poly(3,4-ethylenedioxythiophene)

PEDOT:PSS Poly(3,4-ethylenedioxythiophene):poly(styrene sulfonate)

PEN Polyethylene napthalate

PET Polyethylene terephthalate

PFPE Perfluoropolyether

P-PDMS Pristine polydimethylsiloxane

P3HT Poly(3-hexylthiophene)

PPV Poly(*p*-phenylene vinylene

PSI Phase shifting interferometry

PSS Polystyrene sulfonate

PTFE Polytetrafluoroethylene

PTh Poly(thiophene)

PVD Physical vapour deposition

QCM Quartz crystal microbalance

R2R Roll-to-roll

RR Regioregularity

RSD Relative standard deviation

S3T3YA N-succinimidyl 3-(thiophen-3-yl)acrylate

S3TA N-succinimidyl 3-thiophene acetate

Sa Arithmetic mean surface height

SEM Scanning electron microscopy

SFE Surface free energy (mJ m^{-2})

SMU Source measure unit

SPR Surface plasmon resonance

T3AA Thiophene-3-acetic acid

T3CA Thiophene-3-carboxylic acid

T3T3YAA Trans-3-thiophen-3-yl-acrylic acid

THF Tetrahydrofuran

TMS Tetramethylsilane

Ure Urease

UV-Vis Ultraviolet-visible

UVO240-PDMS UV/Ozone-oxidised polydimethylsiloxane (240 min duration)

VTE Vacuum thermal evaporation

WCA Water contact angle

WLI White light interferometry

XOD Xanthine oxidase

XPS X-ray photoelectron spectroscopy

List of Polymers

(1) Poly(3-hexylthiophene) - P3HT

(2) Poly(3-hexylthiophene) - P3HT

(3) Poly(3-hexylthiophene) - P3HT

(4) Poly(3-hexylthiophene-*co*-methyl 3-thiophene-carboxylate) - P(3HT-*c*-M3TC) [5:1]

(5) Poly(3-hexylthiophene-*co*-methyl 3-thiophene acetate) - P(3HT-*c*-M3TA)

(6) Poly(3-hexylthiophene-*co*-thiophene-3-acetic acid) - P(3HT-*c*-T3AA)

(7) Poly(3-hexylthiophene-*co*-methyl 3-(thiophen-3-yl)acrylate) - P(3HT-*c*-M3T3YA) [1:1]

(8) P(3HT-*c*-M3T3YA) [5:1]

(9) P(3HT-*c*-M3T3YA) [10:1]

(10) Poly(3-hexylthiophene-*co*-trans-3-thiophen-3-yl-acrylic acid) - P(3HT-*c*-T3T3YAA) [1:1]

(11) P(3HT-*c*-T3T3YAA) [5:1]

(12) P(3HT-*c*-T3T3YAA) [10:1]

(13) Poly(3-hexylthiophene-*co*-N-succinimidyl 3-thiophene acetate) - P(3HT-*c*-S3TA) [1:1]

(14) Poly(3-hexylthiophene-*co*-N-succinimidyl 3-(thiophen-3-yl)acrylate) - P(3HT-*c*-S3T3YA) [1:1]

(15) P(3HT-*c*-M3TA) [1:1]

(16) P(3HT-*c*-M3TA) [5:1]

(17) P(3HT-*c*-M3TA) [10:1]

(18) P(3HT-*c*-T3AA) [1:1]

(19) P(3HT-*c*-T3AA) [5:1]

(20) P(3HT-*c*-T3AA) [10:1]

(21) P(3HT-*c*-M3T3YA) [1:1]

(22) P(3HT-*c*-M3T3YA) [5:1]

(23) P(3HT-*c*-M3T3YA) [10:1]

(24) P(3HT-*c*-T3T3YAA) [1:1]

(25) P(3HT-*c*-T3T3YAA) [5:1]

(26) P(3HT-*c*-T3T3YAA) [10:1]

(27) P(3HT-*c*-S3TA) [1:1]

(28) P(3HT-*c*-S3TA) [5:1]

(29) P(3HT-*c*-S3TA) [10:1]

(30) P(3HT-*c*-S3T3YA) [1:1]

(31) P(3HT-*c*-S3T3YA) [5:1]

(32) P(3HT-*c*-S3T3YA) [10:1]

Chapter 1
Introduction and Context

The production of flexible, printed and organic electronics (OEs) involves the combination of thin layers of material into carefully designed device architectures. Over recent decades, various classes of functional organic materials have been developed, leading to the creation of many devices e.g. organic thin-film transistors (OTFTs), organic photovoltaics (OPVs), organic light-emitting diodes (OLEDs) as well as flexible sensors. The optimisation, scale-up, and commercialisation of materials and devices remains a significant objective for both academia and industry, allowing for the alignment of common goals to boost innovation and research success.

Forecasts show the value of the organic electronics industry is expected to exceed £100 billion by 2027, with printed and flexible sensors possessing a 10% market share [1, 2]. Given the considerable commercial potential, it is no surprise there has been significant interest in the field from national research bodies and major multinational corporations e.g. BASF, Evonik, Fujifilm, Merck, Innovate UK, CEA, CSIRO, etc. The bulk of commercial value in OEs arises from flexible OLED display technology, for example, Samsung's infinity flex display, organic semiconductor materials and the photovoltaics sector. However, in the near future, the flexible and printed sensor sector is expected to see substantial growth due to the increasing prevalence of the 'Internet of Things' (IoT) and 'Industry 4.0', which will require a large network of low-cost sensors. Biosensor devices are expected to account for the largest portion of the printed sensor industry, with glucose monitoring, a prevailing use case [3].

1.1 Project Objective

The primary objective of this project was centred on the use of polymeric materials in the fabrication of a flexible biosensor device. The project aimed to develop a soluble polymer, suitable for the immobilisation of sensor bioreceptors (enzymes), thus allowing for the fabrication of a key biosensor component using solution-based deposition processes. Additionally, the polymer should possess an intrinsic ability to carry electrical charge, i.e., it

is a conductive polymer, enabling the realisation of a third-generation glucose sensor. The project intended to develop on an existing selective metallisation process utilising the elastomer polydimethylsiloxane (PDMS), exploring how PDMS can be used in the context of patterned metal deposition and sustainable method development by investigating regeneration and reuse of an otherwise single-use printing stamp. Finally, the project aimed to produce a glucose biosensor based on a flexible, gold electrode and an enzyme-polymer conjugate fabricated by UV/O_3-PDMS metal deposition and solution-processing methods.

1.2 Outline of Thesis

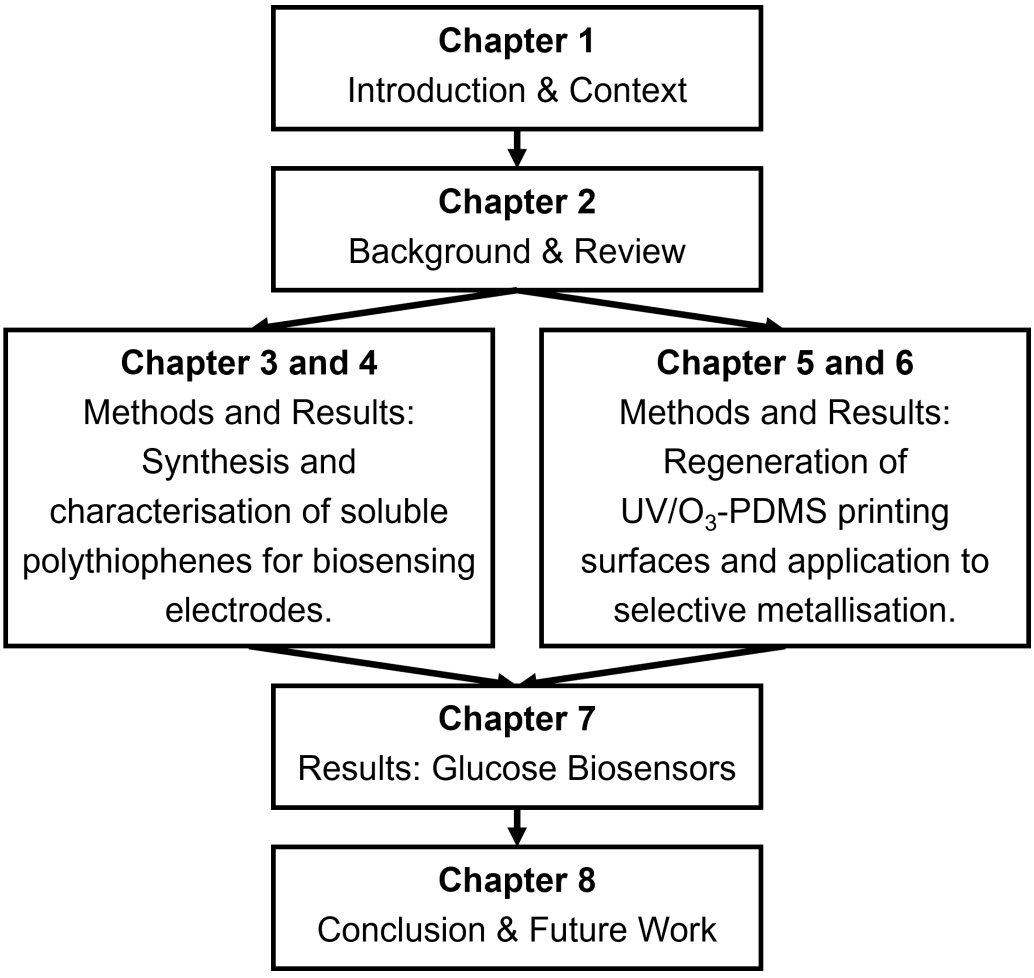

Figure 1.1: Flow diagram of thesis structure.

As outlined in Figure 1.1, the work in this thesis is structured into 8 chapters.

Chapter 1 presents a broad introduction to the commercial aspects of flexible, printed and organic electronics (OEs) and outlines the aims of this project.

Chapter 2 aims to discuss the relevant background and theory regarding enzymatic biosensor devices, polymer materials and metal deposition by selective metallisation, highlighting

recent literature and areas of focus within the field.

Chapter 3 outlines the experimental methods, including the synthetic procedures and analytical techniques, used in the production of thiophene copolymers and their application as enzyme immobilisation agents.

Chapter 4 discusses the outcome of the polythiophene synthesis experiments, and characterisation of the chemical and physical properties of the polymers.

Chapter 5 outlines the methods and techniques used in the development of UV/O_3-PDMS printing stamps, for example, the manufacturing process, surface modification and methods of regeneration as well as the operational conditions of the analytical methods used for this work.

Chapter 6 discusses the regeneration of UV/O_3-PDMS printing stamps by controlling hydrophobic and oleophobic recovery.

Chapter 7 is the final experimental chapter and outlines the application of both the synthesised polymers and novel metal deposition process in the manufacturing of a flexible, glucose biosensor electrode.

Chapter 8 discusses the potential for future work, highlighting possible areas of interest, summarising the experimental research, outcomes, and conclusion of this project.

Chapter 2
Background and Review

2.1 Enzymatic Biosensors

In 1953, Leland C. Clark published his foundational paper describing the creation of a polarographic electrochemical sensor for monitoring O_2 concentration in blood and body tissue [4]. The Clark electrode laid the groundwork for the development of the first true biosensor and by 1962 alongside Champ Lyons, Clark expanded on his previous work to conceptualise such a device [5]. Discussing the integration of enzyme-containing membranes into the oxygen electrode, they explored the detection of small molecules e.g. glucose ($C_6H_{12}O_6$) or urea (CH_4N_2O), using the enzymes' glucose oxidase (GOx) and urease (Ure).

Further developments came in 1967 when Updike and Hicks immobilised GOx into a layer of polyacrylamide (PAM) gel to realise the first functional, amperometric glucose biosensor [6]. Shortly thereafter, in 1969 Guilbault and Montalvo presented a first-of-its-kind potentiometric biosensor based on a urease-PAM gel with an ammonium cation (NH_4^+) selective electrode [7]. The culmination of academic advancements led to the commercialisation of the first blood glucose biosensor, with Yellow Spring Instruments launching the 'Model23A' in 1974, based on the principles of Clark's enzyme electrode. [8, 9].

2.2 Biosensor Devices

The International Union of Pure and Applied Chemistry (IUPAC) define the biosensor as "a device that uses specific biochemical reactions mediated by isolated enzymes, immunosystems, tissues, organelles, or whole cells to detect chemical compounds, usually by electrical, thermal or optical signals" [10]. Practically, a typical biosensor device consists of five parts as illustrated in Figure 2.1:

i) **Analyte** - The chemical of interest to be detected or quantified, e.g. glucose ($C_6H_{12}O_6$), Urea ($C_4H_4N_2O$). For enzyme-based biosensors, the term *substrate* is used interchangeably [11].

ii) **Bioreceptor/Biorecognition element** - A biological molecule that is selective to the recognition of a specific analyte, e.g. glucose oxidase (GOx), an oxidoreductase enzyme, selectively recognises the monosaccharide, β-D-Glucose.

iii) **Transducer** - Electrochemical, optical, thermal or mass-based transducers convert the analyte recognition into a quantifiable signal. It is common practice to classify a biosensor by its transduction method, for example, an amperometric electrochemical sensor detects current generated by the biorecognition event.

iv) **Electronics/Signal Processing** - Transduced signals, such as electrical currents, are processed through complex circuits and prepared for readable output. Amplification, current-to-voltage conversion and digitisation are common signal processing methods.

v) **Output** - Processed signals can be displayed to the user via a digital display or printout. Graphic figures and numerical data enable the user to easily assess and interact the biosensor results.

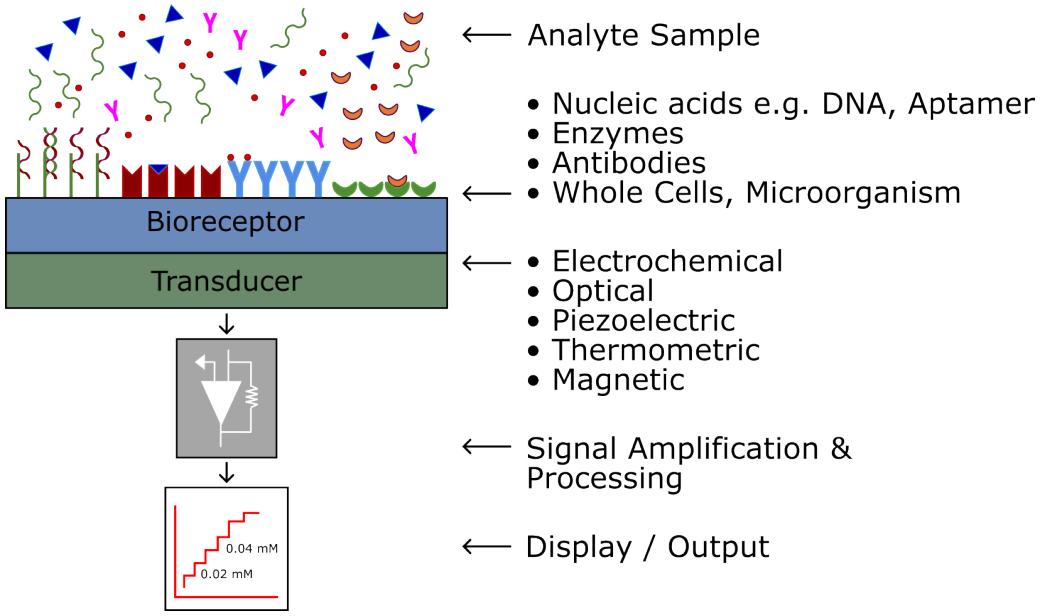

Figure 2.1: Schematic diagram depicting the general construction of a biosensor device.

2.3 Transduction

The transduction method of a biosensor is crucial for converting the signal from the biorecognition of an analyte into a measurable output. Reactions between the receptor and analyte yield a range of detectable signals in the form of electrons, light, sound and heat. Signify-

ing the importance, biosensor devices are often classified by the transduction method, with the five main classes of transducers being electrochemical, magnetic, optical, piezoelectric (mass) and thermometric (heat). This project will focus on electrochemical biosensors, specifically an amperometric transduction method.

- **Optical**: Optical biosensors measure light produced or absorbed during a biorecognition event or from a subsequent reaction involving the by-products of analyte detection [12]. The dominant optical transduction methods found in the literature are Surface Plasmon Resonance (SPR), fluorescence and chemiluminescence, each with benefits and limitations to their use. As outlined in a review paper by Kaur et al. optical transducers have been widely employed in enzymatic biosensing for detection of organophosphate pesticides e.g. parathion [13].

- **Piezoelectric**: Piezoelectric biosensors detect changes in the mass of the analyte or other reaction by-products. In certain materials e.g. quartz SiO_2, the piezoelectric effect refers to the generation of an electric potential under mechanical stress or deformation, while the converse effect refers to mechanical deformation or oscillation induced by the application of an electric field [14, 15]. For sensing applications, this phenomenon is exploited as the binding of the analyte to the surface of a piezoelectric crystal results in changes to the oscillation frequency, which is capable of being monitored [16]. Common piezoelectric materials used for sensing applications include the quartz crystal microbalance (QCM).

- **Thermometric**: Thermal and calorimetric transduction measures changes in heat [17]. Heat produced or absorbed by the bioreceptor is related to the concentration of analyte and is typically measured by metal-oxide thermistors or semiconductors e.g. Bismuth Telluride thermocouples [18–20].

For more detail on the non-electrochemical methods of transduction, e.g. magnetic, optical, piezoelectric and thermometric, *Biomaterials-Based Sensors: Recent advances and applications* by Kumar et al. provides a comprehensive summary of the topic [21].

2.3.1 Electrochemical Transducers

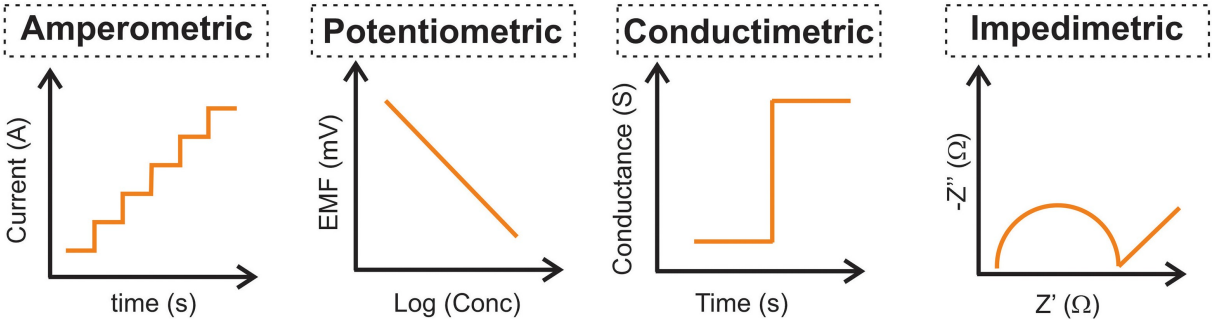

Figure 2.2: Examples of biosensor signal output from amperometric, potentiometric, conductometric and impedimetric transduced responses. Reprinted from L. C. Lopes, *Sensors and Actuators Reports*, 2022, 4, 100087, CC BY NC ND [22].

Among the various types of transducers, electrochemical methods have gained significant attention due to their high sensitivity, fast response time, and compatibility with miniaturisation into small, portable devices [22]. Electrochemical transducers are the most frequently used transducers in the literature and, alongside optical transducers, enable the widest range of receptor classes and immobilisation techniques to be used [13]. Within the electrochemical transduction category, amperometric and potentiometric transducers are the predominant methods, while studies that have used conductometric and impedimetric transducers are limited in comparison. These methods usually require the immobilisation of receptors onto an electrode's surface, where the receptor can catalyse the specific reaction with the target analyte, leading to the production or consumption of electrons. The change in current is converted into a detectable electrical signal, providing quantitative data about the analyte concentration. Amperometric biosensors measure the current generated by redox reactions in electroactive species produced during the biorecognition event. Potentiometric biosensors, on the other hand, measure changes in the potential resulting from ion concentration changes near the electrode surface due to the receptor-analyte reaction. Conductometric biosensors measure the difference in conductivity of a medium resulting from the production or consumption of ionic species in the receptor reaction while impedimetric biosensors measure changes in the electrical impedance in the medium caused by the receptor-analyte reaction, which can be correlated with analyte concentration [23].

2.3.2 Amperometric Biosensors

Amperometric biosensors operate on the simple principle that electrical current generated as a result of the biorecognition event is proportional to the concentration of the target analyte. Devices based on amperometric transduction involve the oxidation or reduction of redox-active species produced during the enzyme-substrate reaction, as maintained by the application of a potential difference. The transfer of electrons between the receptor system and a working electrode; which may occur directly with the electrode surface or indirectly via a redox mediator, produces a detectable electrical current that is proportional to the concentration of the target analyte [21, 24]. Devices based on an amperometric platform are considered to be most appropriate for commercialisation with many commercial devices already available, e.g. The Roche Accu-Chek® blood glucose meter, utilises the enzyme - glucose dehydrogenase to convert glucose into gluconic acid, generating two electrons and reducing the enzyme in the process. An electron mediator facilitates the rapid transfer of electrons from the redox centre of the enzyme to an electrode in the hand-held test device [25].

In amperometric biosensor devices, especially those utilising oxidoreductase-type enzymes, direct electron transfer between the redox centre of the enzyme and the electrode is often limited due to the insulating nature of the protein structure surrounding the redox centre. This insulating protein layer can hinder the efficient transfer of electrons between the enzyme and the electrode, affecting the sensitivity and performance of the biosensor. To overcome this limitation, various strategies are employed to facilitate electron transfer, such as using redox mediators or modifying the electrode surface to enhance enzyme immobilisation and electron transfer kinetics. These approaches help improve the efficiency of electron transfer and enhance the performance of amperometric biosensors for sensitive and accurate detection of target analytes [22, 26, 27].

2.4 Bioreceptors

Versatility in the choice of biorecognition element afforded by electrochemical biosensors enables the use of many classes of molecules if compatible with the desired method of im-

mobilisation. The receptor imparts a principal benefit of biosensors, that is, a high degree of selectivity and, ideally, true specificity towards the target analyte. The choice of bioreceptor is often based on a range of criteria such as applicable immobilisation methods, handling constraints, target analyte, local expertise and experience, etc [28]. Proteins such as antibodies [29, 30] and enzymes [23, 31], nucleic acids (e.g., DNA fragments [32], aptamers [33, 34]) and even microbial whole cells [35–37] have all been utilised in electrochemical biosensors. Among these, enzymatic sensors are the most prevalent due to their simplicity, widespread application and already successful commercialisation.

In electrochemical biosensors, catalytic bioreceptors such as the oxidoreductase (EC 1) are frequently employed, as this class of enzyme catalyses redox reactions involving the transfer of electrons between molecules. This property is particularly useful because the generated signal is directly related to the redox process, allowing for sensitive and specific detection of analytes. To a lesser extent, hydrolase enzymes (EC 3) have also seen use for the detection of analytes such as urea [38, 39], or lactose [40] but are best suited to voltammetry and potentiometric transduction as the biochemical reaction uses water to cleave chemicals.

2.5 Analyte Detection

Depending on the choice of receptor and transduction mechanism, a range of analyte compounds can be monitored using a biosensor platform. While the main commercial motivation for biosensor research is often centred on healthcare, specifically blood sugar monitoring, biosensors can be utilised for the detection of many analytes whilst maintaining a strong commercial application. Non-medical examples include food spoilage indication via detection of putrescine ($C_4H_{12}N_2$), cadaverine ($C_5H_{14}N_2$) and hypoxanthine ($C_5H_4N_4O$) or environmental monitoring such as organophosphate insecticides e.g. methyl parathion ($C_8H_{10}NO_5PS$). There is great interest in the monitoring of food quality for safety purposes and for the quantification of product freshness. Biosensors may be a highly applicable technology for this purpose, owing to high sensitivity and suitability for integration into functional packing to allow for effective monitoring of indicators.

Meat and fish products release several biogenic amines and purines following the decomposition and decay of proteins and nucleotides. In 1983, Wantabe et al. developed a flow-type

electrochemical biosensor utilising the enzyme xanthine oxidase (XOD) for the detection of hypoxanthine, a purine released during decomposition of adenosine-5'-triphosphate (ATP) in fish tissue. The method outlined by Wantabe follows a similar principle to the original Clark glucose sensor, whereby an immobilised-enzyme membrane is integrated to a Clark-type oxygen electrode. The performance of the device compared well with a conventional assay method possessing a hypoxanthine detection range of 0.06 to 1.5 mM while showcasing a high degree of reusability duration over 30-days when stored at low-temperature [41]. An almost identical sensor targeting a batch testing regime was presented by Mulchandani et al. and utilised a XOD membrane on a polagraphic electrode to indirectly measure the hypoxanthine concentration by detecting both H_2O_2 and uric acid [42]. The Mulchandani device possessed a lower hypoxanthine detection range of 0.0036 - 0.107 mM, but had limited reusability. The key difference in the works by Wantabe and Mulchandani is related to the preparation of the enzyme-containing membrane as Wantabe prepared a cellulose triacetate gel as opposed to the commercially available Nylon membrane used by Mulchandani.

In addition to the detection of purines, the sensing of biogenic amines is widely represented in the literature. Putrescine ($C_4H_{12}N_2$) and cadaverine ($C_5H_{14}N_2$) are two of the primary decomposition products from food spoilage and are some causes of the unpleasant odour from rotting animal tissue. With the same motivations as that of purine-type molecules, the detection, and monitoring of biogenic amines from the microbial decarboxylation of amino acids are of particular significance due to the toxicity of these compounds to both humans and animals [43]. Early sensors follow the common route, coupling an enzyme e.g. monoamine oxidase (MAO) or diamine oxidase (DAO) on a polyamide membrane to an oxygen electrode for the indirect measurement of the analyte [44].

The materials and methods were, again, refined and optimised to improve response time, device cost, ease-of-use such as in the electrochemical biosensor presented by Draisci et al. which is based on a H_2O_2 platinum electrode and an immobilised-DAO membrane [45]. The device successfully quantifies the concentration of several biogenic amines with a linear response of 0.1 - 2000 μM and a detection limit of ca. 0.05 μM. Other ideas in the literature include three different enzymatic biosensors described by Bóka et al. where the sensing properties of DAO, MAO and putrescine oxidase sensors are discussed [46]. Finally, a variety

of amine biosensing methodologies are described in publications by Castillo et al. [47], Luong et al. [48] and Leonardo et al. [49] as well as more recently by Amin et al. [50] and Zhao et al. [31]. These publications primarily outline the electrochemical detection of biogenic amine by novel transducer and receptor combinations, for example, in Zhao et al., the detection of H_2O_2 from the reaction of DAO and putrescine on a clay modified glassy carbon electrode is described, enabling the detection of the diamine with a 3.3 pM LoD.

2.5.1 Glucose Sensing

For the detection of glucose, the primary biological recognition element is the enzyme glucose oxidase (β-D-glucose:oxygen 1-oxidoreductase, EC 1.1.3.4). It was the enzyme used in the first devices by Clark et al., Updike et al., and has been used extensively ever since [5, 6]. Lyophilized powder forms of GOx, produced from the fungus *Aspergillus niger*, are stable, easy to store, easy to use and possess high activity[1] ($>$ 250 units mg^{-1}) [51]. Glucose oxidase is a flavoprotein that contains the active redox centre Flavinadenine dinucleotide (FAD) within its peptide structure. FAD is a prosthetic group; a bound, non-polypeptide unit, that plays a crucial role in the catalytic activity of GOx by facilitating the redox processes.

The mechanism of the biocatalysis reaction can be split into a two-step process i) GOx-FAD catalyses the oxidation of β-D-glucose to D-Glucono-1,5-lactone, reducing FAD to $FADH_2$ in the process. D-Glucono-1,5-lactone immediately hydrolyses to form gluconic acid. ii) GOx-$FADH_2$ is oxidised by molecular oxygen to give GOx-FAD and H_2O_2 [52].

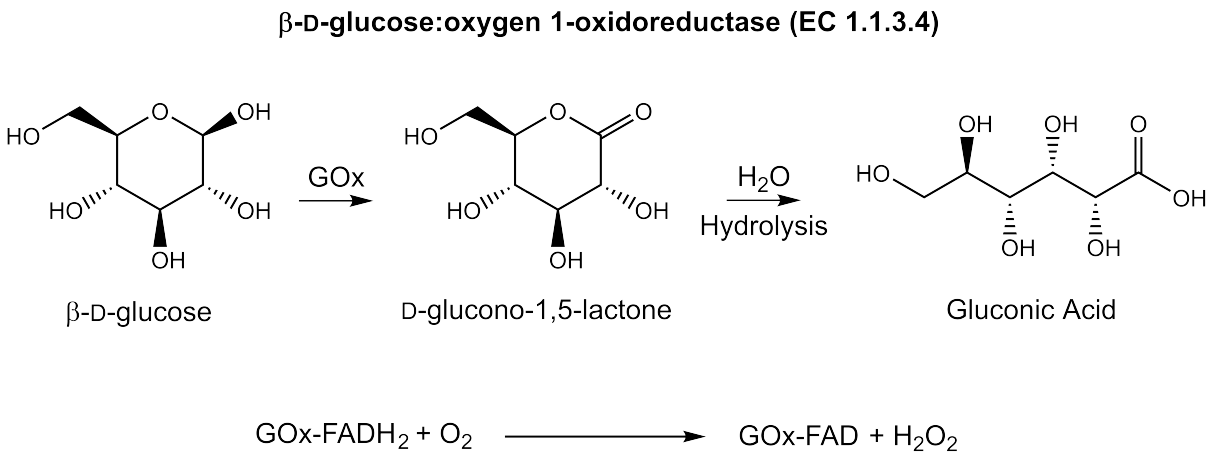

Figure 2.3: Enzyme-substrate catalysis reaction of glucose oxidase-glucose.

The structure and composition of glucose oxidase have been characterised at angstrom resolution in a range of studies [51, 52]. Glucose oxidase possesses a homodimeric structure comprised of two identical monomer sub-units, each with a single FAD cofactor. The enzyme dimer is a 'rounded rectangular prism shape' with an approximate dimension of 60 x 52 x 77 Å and possesses a molecular weight between 130 - 170 kDa [53]. Particularly relevant to the targeting of covalent cross-linking immobilisation through amide linkages, the surface of the enzyme is covered with various NH_2-containing amino acid residues, e.g. lysine (Lys) and cysteine (Cys) [54, 55].

In both the commercial and academic environment, the use of glucose-sensing technologies remains prolific for motivations specific to each field. In a commercial sense, glucose sensing and the monitoring of blood sugar is a multi-billion dollar industry, dominating the entire biosensor market and is overwhelmingly focused on healthcare for the clinical setting and for at-home self-testing. By comparison in academia, the glucose-glucose oxidase couple is a much-used model system for the development of biosensor devices due to the availability of the enzyme, low-cost associated chemistry, e.g. coupling agents, buffers, and the existence of a significant amount of well-defined results in the literature.

Recent investigations centred around glucose oxidase biosensors tend to focus on the development of immobilisation methods and accompanying materials or transduction methods. For example, an article by Somchob et al. presents the use of a zwitterionic phospholipid-like copolymer[2] as an enzyme preservation layer to further stabilise the immobilised oxidase enzymes [56]. The study highlights an interesting and non-standard application of polymer materials to increase the long-term performance of a biosensor device, and in the case of the Somchob device, the hydrogel capping enabled the retention of activity up to 49 days. Furthermore, as the copolymer layer does not chemically alter the enzyme layer, this application of such material has the potential to be universally applied to other enzyme-based biosensors.

The design of signal processing electronics and the implementation into real devices for commercial applications also remains a present point within the literature. Studies include the fabrication of a complete glucose biosensor platform by Promsuwan et al., which utilises a commercial near-field communication (NFC) potentiostat controlled by a smartphone [57].

The sensing element within the device consists of a GOx/gold nanoparticle/PEDOT:PSS enzyme layer with a Prussian blue redox mediator, allowing for portable glucose detection via a single drop test sample. The NFC glucose biosensor device possesses a linear response between 0.5 - 500 μM and a LoD of 0.15 μM as well as a reported high-degree of device selectivity vs common interferents e.g. uric acid. Finally, Zhang outlines the development of a flexible, organic thin-film transistor transimpedance amplifier (OTFT-TIA) for the processing and conditioning of sensor signals [58]. Paired with a suitable sensing element, the OTFT-TIA circuit, which is manufactured using high-throughput roll-to-roll manufacturing techniques such as vacuum web coating, offers a pathway towards a mass-produced generalised sensing platform as demonstrated. In a related article by Chen et al. the same amplifier is utilised in a wearable pH sensor configuration [59], while Zhang highlights the potential for operation in a glucose oxidase biosensor [58].

Notes

[1]one GOx unit will oxidise 1 μM of β-d-glucose to gluconic acid and H_2O_2 per minute at pH 5.1 and 35°C.

[2]poly(2-methacryloyloxyethyl phosphorylcholine-*co*-N-methacryloyloxyethyl tyrosine methylester)

2.5.2 Glucose Biosensors

Depending upon the electron transfer mechanism employed in the biosensor, amperometric glucose sensors can be classified into four generations, as illustrated in Figure 2.4:

First-generation: The first-generation devices indirectly measure the glucose concentration by monitoring the generation of H_2O_2 or consumption of O_2. These sensors utilise the biocatalytic redox reactions inherent to glucose oxidase and require a high operating potential to electrochemically oxidise H_2O_2 or reduce O_2 at the electrode surface to produce a detectable flow of electrons. While 1st-generation devices allow for simplicity in the biosensor design, high operating potentials and the requirement for O_2 as a secondary substrate hinder their application. The dependency on O_2 limits application in environments with low O_2 concentration due to a detrimental effect on response linearity [60–64].

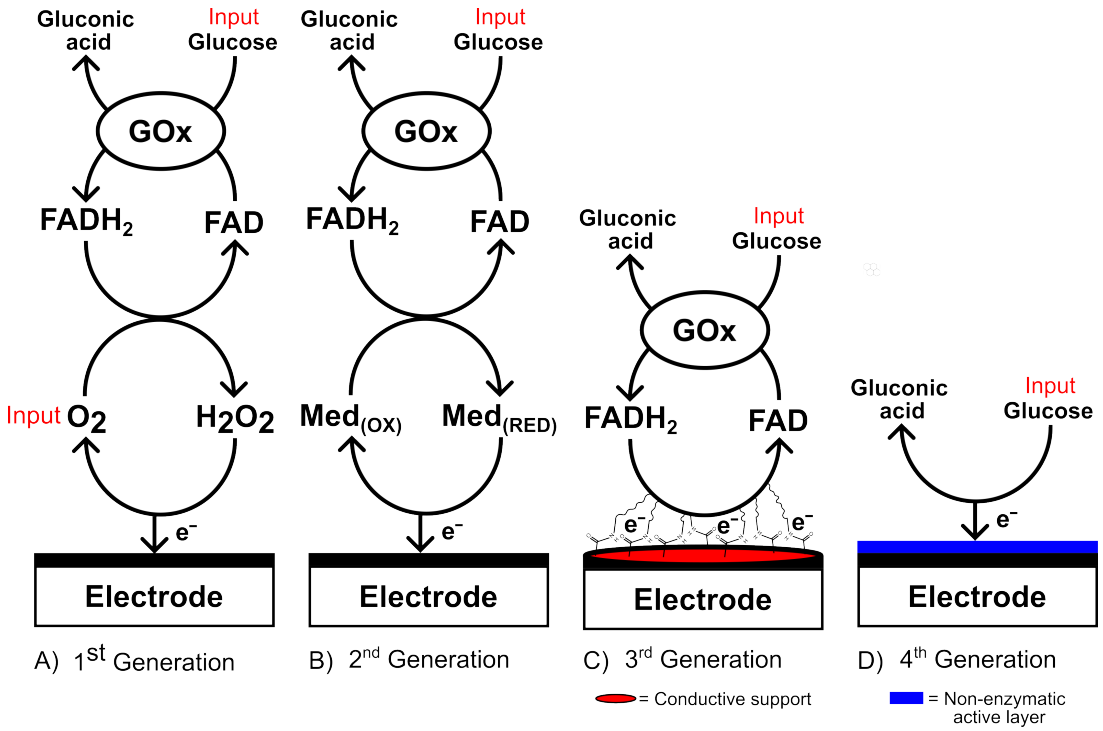

Figure 2.4: Representation of different amperometric glucose biosensor device generations. A) 1st-generation biosensor measuring the production of H_2O_2, B) 2nd-generation biosensor utilising a redox mediator to shuttle electrons, C) 3rd-generation biosensor with enzyme immobilised onto conductive support, and D) 4th-generation non-enzymatic glucose sensor.

Second-generation: Second-generation glucose sensors utilise redox mediators that are capable of transferring electrons between the active centre of GOx to the electrode. The use of mediators has the primary benefit of reducing the operating voltage as these compounds possess low redox potentials, readily facilitating the oxidation of GOx-$FADH_2$ centre. Mediators also reduce the dependency on O_2 while limiting the impact of interferents due to the lower operation potentials [65]. In GOx biosensors, common mediators include ferrocenes, ferricyanide and quinones e.g. *p*-benzoquinone [66, 67]. As the mediators are often low-molecular-weight molecules, leaching from the electrode is a present issue. This affects the viability of mediated-glucose biosensors in long-term, biologically sensitive applications, e.g. *in vivo*, therefore, immobilisation of the mediator is often required [68, 69].

Third-generation: Removal of the mediator from the biosensor system and targeting the direct electron transfer from the enzyme's redox centre to the electrode is the key identifier of a third-generation device [70]. With a direct electron transfer (DET) biosensor, it is possible to greatly reduce the operation potential, improving selectivity by eliminating competition from interfering species, e.g. urea, uric acid. [71]. It is essential for the mate-

rial used to connect the enzyme to the electrode to possess a high conductivity and suitable processability. In the effort to develop a DET, third-generation biosensor [72], conductive materials, e.g. carbon nanotubes, polythiophene, and polyaniline, can be modified to be used for enzyme immobilisation with the aim of linking the redox centres to the electrode [73–75].

Fourth-generation: Fourth-generation or non-enzymatic glucose biosensors target the electrochemical oxidation of glucose to gluconic acid using a nanomaterial/electrode interface, forgoing the enzyme biocatalysis entirely. Studies developing non-enzymatic devices have become more prevalent in recent years due to the perceived benefits of such a device, e.g. very low cost, simple design, and high stability. However, the lack of a highly specific biological recognition element means 4^{th}-gen glucose sensors are generally considered to be less selective and specific towards glucose, a major factor currently restricting viability in a commercial setting. A comprehensive summary of recent advances in fourth-generation, non-enzymatic glucose sensing can be found in reviews by Naikoo et al. and Wei et al. [76, 77].

2.6 Immobilisation of Enzyme

When pursuing the development of a functional biosensor platform, it is imperative for the biological catalysts to be immobilised to a solid support, as anchoring the enzyme to a support matrix or electrode ensures operational stability, improved reusability, better storage capability and enhanced performance [54]. Immobilisation has been shown to improve the performance of the enzyme, increasing the resistance of the biomolecule to changes in environmental conditions such as pH and temperature; therefore, recent advances in polymer science, nanotechnology, and bioengineering have the potential to result in big improvements [78–80]. The term immobilisation regards a process where enzymes are physically confined by fixation or trapping to a defined region while retaining enzyme activity [81]. As the stability of the enzyme and retention of activity are of significant importance to sensing applications, changes to the chemical and physical properties of the enzyme may occur as a result of immobilisation. Thus, it is important to consider the material choice, reaction conditions and mode of attachment.

Given the intricate nature of enzymes, there is no universal matrix or support system suitable for all biomolecules. Immobilisation materials must meet exhibit particular characteristics. These include having a high affinity for binding with the enzyme, being processable, environmentally and chemically stable, containing reactive binding sites, and not acting as inhibitors or toxic substances to the enzyme. Various suitable materials are being developed for enzyme binding, including inorganic solids like silica [82, 83] and alumina [84], synthetic organic polymers (e.g. resins and intrinsically conductive polymers [85–87]), biopolymers such as polysaccharides [88], and nanomaterials like modified carbon nanotubes (CNTs) and metal nanoparticles (NPs) [89–92]. Along with material choice, the mode of attachment is also crucial to effective immobilisation. Major immobilisation methods include reversible and irreversible approaches; reversible methods encompass physical adsorption, ionic bonding, and affinity bonding, while irreversible methods include covalent attachment, cross-linking, encapsulation, and physical entrapment.

2.6.1 Reversible Immobilisation

2.6.1.1 Physical Adsorption

Physical adsorption serves as a non-covalent approach, offering a simple and reversible mode of attachment. This method relies on interactions between the enzyme and a solid support matrix, such as intermolecular Van der Waals forces, hydrogen bonding, and electrostatic forces [93]. However, due to the weak nature of these bonding forces, the enzyme is prone to loss and leaching from the support. Consequently, there exists a trade-off between factors like cost, ease of implementation, and mild reaction conditions versus the challenge of low stability, which results in rapid enzyme loss [55, pp. 20–26]. Numerous organic and inorganic materials have been utilised as adsorption supports, with silica-based compounds receiving most of the interest in the literature due to its ability to easily control the surface area, pore size, pore structure and surface functionalisation [83, 94, 95].

2.6.1.2 Affinity Binding

Affinity immobilisation harnesses principles from protein purification techniques like affinity chromatography. There are two primary methods for achieving affinity immobilisation:

using support matrices with ligands or functionalisation that exhibit high affinity towards the enzyme, or use of an affinity-tagged enzyme to create a bond between the enzyme and the support matrix [78]. When the enzyme encounters the support, it selectively binds to the motifs via complementary binding sites, anchoring the enzyme onto the support surface. This non-covalent affinity interaction yields strong yet reversible immobilisation, ensuring control of enzyme orientation and retaining high activity levels [96, pp. 97–128]. Various binding technologies have been developed, with standout methods including polyhistidine-tagged enzymes for binding to nitrilotriacetic acid or metal chelate functionalised supports [97] and the well-developed biotin-avidin/streptavidin method, where the enzyme is biotinylated with a biotin tag or conjugated to an avidin tag and bound to avidin/streptavidin or biotin modified support matrices [98]. Considering the support material, polymers, nanomaterials, and inorganic materials, such as siloxanes, have all been employed for the immobilisation of enzymes by affinity binding [79, 99, 100].

2.6.2 Irreversible Immobilisation

2.6.2.1 Covalent Attachment

Turning to irreversible immobilisation methods, the formation of strong and stable covalent bonds between the biomolecule and support matrix offers many benefits over reversible methods, including the permanent anchoring of the enzyme and minimisation of leaching. Compared to the simplicity afforded by physical adsorption, the need to alter an enzyme's chemical structure to form the covalent bonds increases the complexity of the system, but significantly elevated stability, better sensor reusability, increased storage capability and improved device reproducibility are key driving forces to achieve covalent immobilisation. The primary method of achieving covalent immobilisation is through the targeting of amino acid residues on the enzyme surface. The ε-amino group of lysine ($R-NH_2$), arginine ($R-NH-CNH-NH_2$), the thiol of cysteine ($R-NH_2CH_2SH$) and carboxylic acid residues e.g. aspartic ($R-CH_2-COOH$) and glutamic acid ($R-(CH_2)_2-COOH$) are favoured due to their prevalence at the surface as well as their ability to form strong linkages e.g. amide ($R-CONH-R$), carbamates ($R-CO-NR_2$), sulfides ($R-S-R$) via a range of routes under mild reaction conditions. However, as a variety of amino acid residues can be targeted for

immobilisation, it is important to consider which residues may be essential for enzyme function and to design reactions that target the formation of specific bond types [55, pp. 15–31].

Polymer support materials are particularly suited for covalent immobilisation as the integration of specific reactive groups into the backbone, enabling enzyme-polymer conjugation, can be performed using well-understood carbonyl and amine chemistry. The reactive residues on the surface of an enzyme can be attached to polymers by bonding to single chains or a network of multiple chains via different methodologies.

For example, analogous to the formation of a graft copolymer, covalent immobilisation may follow a grafting-from or grafting-to process. As described by Rodrigeuz-Abuzeox et al., grafting-from methods involve the attachment of initiators to the enzyme prior to an in-situ polymerisation to form the enzyme-polymer conjugate, whereas a grafting-to approach targets enzyme immobilisation via the use of a functionalised polymer backbone with side groups that react with residues of the enzyme [101]. A grafting-from method requires mild reaction conditions so that the enzyme is not denatured during polymerisation, thereby restricting which polymer can be used. On the other hand, a grafting-to approach can enable a wide range of polymers, including intrinsically conductive polymers, which often require the use of solvents e.g. $CHCl_3$ and THF, oxidants $FeCl_3$, elevated temperature and non-physiological pH values that may negatively impact the enzyme.

In the grafting-to approach of covalent immobilisation, various studies have explored the use of polymeric materials as effective support matrices. Along broad terms, these polymers can be categorised into three main types:

1. **Non-conductive organic polymers**, such as nylon [102], poly(latic acid) [103], poly(styrene) [104] or glyoxyl agarose; a polysaccharide [88, 105].
2. **Conductive organic polymers**, including polythiophene derivatives [27, 38, 68, 106–112] and poly(aniline) [39, 113, 114].
3. **Inorganic polymers**, for example, polysiloxanes [115–117], and polyphosphazene [118–120].

A specific example of a polymer immobilisation agent is described by Pilo et al. where a film of electrochemically prepared poly(4,4'-bis(2-methyl-3-butyn-2-ol)-2,2'-bithiophene) was used to effectively immobilise glucose oxidase using a carbodiimide coupling reaction [27]. The biosensor fabricated in the work, had typical performance metrics for a glucose sensor, giving a linear response between 0.15 - 5.20 mM, a limit of detection of 0.03 mM and a 20 s initial response time. Additionally, the Pilo device remained stable over successive test for over 30 days highlighting the strong enzyme immobilisation arising from use of the thiophene support. Moreover, in a recent paper by Jose et al. the enzyme laccase (EC 1.10.3.2) was covalently immobilised to an electropolymerised poly(anthranilic acid) on a carbon fibre paper electrode [121]. Enabling the detection of a potent endocrine disruptor, p-nonylphenol, laccase is immobilised via an 1-ethyl-3-(3-dimethylaminopropyl) carbodiimide (EDC) and N-hydroxysuccinimide (NHS) coupling pathway. The CFP/PAA/Lac device possesses a wide linear range between 5 - 250 nM with a LoD of 1.7 nM following optimisation of operation conditions and is capable of determining the concentration of p-nonylphenol in real-world water samples. It becomes evident that a significant disparity exists within the literature regarding electropolymerised and chemically polymerised materials for biosensor devices. The vast majority of studies tend to utilise electrochemically prepared materials which is likely due to the facile nature of how conductive polymers can be prepared by simple electrochemical methods and the simplicity of being able to prepare and characterise a novel biosensor device using a single potentiostat. In a highly-cited article by Lai et al., poly(3-hexylthiophene-*co*-thiophene-3-acetic acid) was prepared by chemical oxidative polymerisation, affording a soluble material capable of solution-processing [38]. Lai fabricated a potentiometric urea biosensor on Indium-Tin-Oxide (ITO) using P3HT-*c*-T3AA to covalently immobilise the hydrolase enzyme - urease (EC 3.5.1.5) via the familiar EDC-NHS coupling reaction. The performance metrics for the Ure/polymer/ITO device aligned well with the real-world application of urea sensing in blood, giving a linear response between 0.99 - 4.97 mM for concentrations of urea, testing in an aqueous solution.

2.6.2.2 Encapsulation and Entrapment

Encapsulation and entrapment techniques are also commonly employed to immobilise enzymes within the interior of a support matrix. Both limit the enzyme's exposure to the surrounding environment, reducing mechanical stress and solvent effects. However, this confinement introduces mass transfer phenomena, such as depth-dependent diffusion of analyte molecules, and limits the enzyme loading capacity [122]. The fixation of enzymes within the matrix can occur via covalent or non-covalent bonding, depending on the material choice. However, the loss of enzymes through leaching is closely linked to matrix pore size; thus, control over this property is crucial [55, 123].

Entrapment involves physically trapping the enzyme within a fibre network. Since the enzyme does not directly interact with the support material, it retains the ability to function as a free molecule in solution. In contrast, encapsulation involves the formation of a membrane-like structure or shell around the enzyme, creating a localised microenvironment. This allows small analyte molecules to pass through towards the enzyme's active site while anchoring the biomolecule within the matrix. Gel methods such as sol-gel, hydrogels, and aerogels are the most common approaches to achieve immobilisation by encapsulation and entrapment, employing silane gels to create a highly controlled membrane [124–126]. Organic polymer films produced via electrospun and electropolymerisation have also been employed for this method of immobilisation [102, 127, 128], for example, use of an electrospun poly(vinyl alcohol) network for the entrapment glucose oxidase and hexokinase [129] or the immobilisation of lactase onto an electropolymerised film on poly(pyrrole) [130].

2.7 Polymers in the Fabrication of Flexible Electronics

Polymers are aptly suited for use in printed and flexible organic electronics (OEs) due to their favourable processability, mechanical flexibility, cost, and tunability. Polymers find application through integration into the device stack or through the use in components of manufacturing systems [131–134], deposition processes [135, 136], and testing apparatus [137–139]. Polymeric materials have been employed in sensing platforms such as enzymatic biosensors, where bioreceptors are immobilized onto electrode surfaces by polymer

supports [55, 79, 102, 127, 140], in electrochemical sensors that utilise molecularly imprinted polymers (MIPs) as a non-biological recognition layer [141–143], or in membranes that act as selective diffusion barriers to improve sensor performance [144, 145].

Comprised of a repeating and macromolecular structure with a high molecular weight, polymers are made up of short, low molecular weight monomer units. Polymerisation is the process in which monomers are converted into a polymer, and occurs both naturally and synthetically to produce many types of polymer materials. For example, in trees, monolignols are polymerised to form lignin; a natural polyphenol and major component of wood [146], while the hydrocarbon ethene is polymerised using the Ziegler-Natta process to produce the olefin thermoplastic polyethylene [147]. Typically, polymers are classified based on their monomer composition (homo- vs. co-polymer), structure (linear vs. cross-linked), polymerisation method, origin (natural vs. synthetic), and properties (conductors vs. insulators), among others.

Within the scope of this project, two polymer types have been investigated: **Polythiophenes** are a well-studied class of organic conductive polymer based on the heteroaromatic molecule, thiophene (C_4H_4S). Figure 2.5 depicts structures of poly(thiophene-2,5-yl) (PTh) and its derivatives e.g. poly(3-hexylthiophene) (P3HT) and poly(3,4-ethylenedioxythiophene) (PEDOT) which are some of the most utilised conductive polymers with frequent application in organic photovoltaics (OPV) and organic thin-film transistors (OTFT) [148–152].

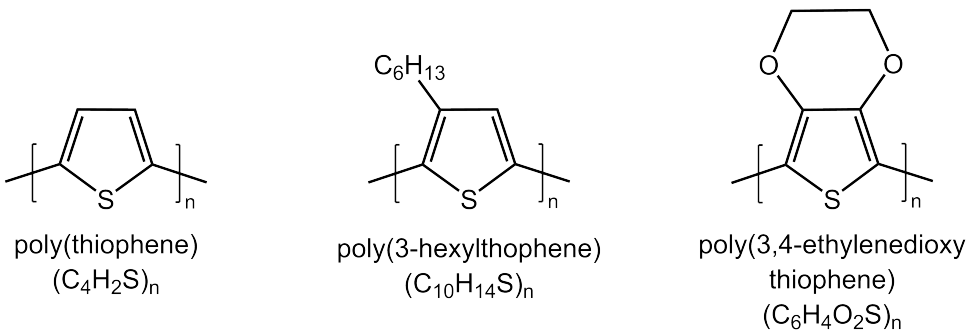

Figure 2.5: Chemical structures of polythiophene and derivatives.

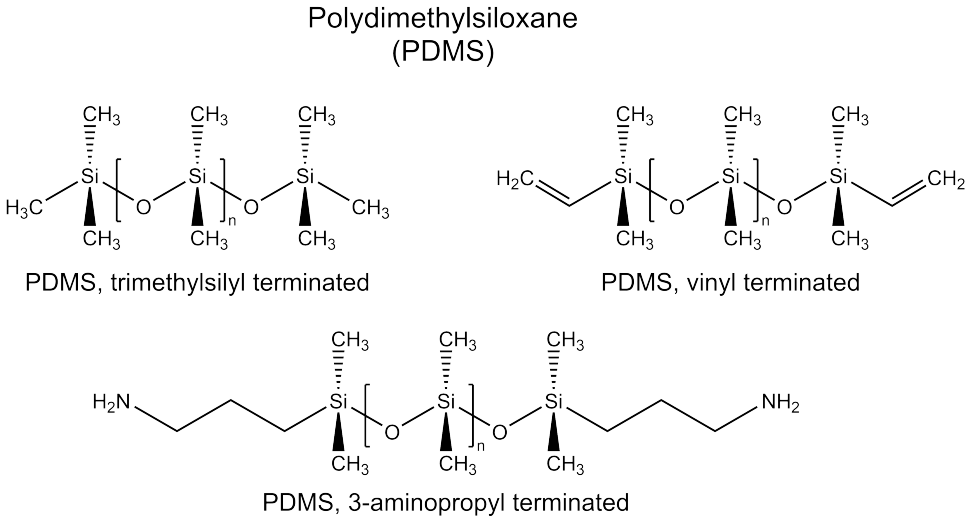

Figure 2.6: Chemical structures of polydimethylsiloxanes.

Polydimethylsiloxane belongs to a class of inorganic polymers known as the polysiloxanes or silicones and possesses a silicon-oxygen backbone. PDMS is a rubber-like, elastic material that has become one of the most common elastomers owing to its versatility and ease of preparation, finding extensive use in microfluidics, soft lithography, and sensing [153–158].

In most cases, PDMS is prepared as a transparent solid by the thermal crosslinking of a commercial two part kit (e.g. Sylgard 184), which consists of a vinyl terminated PDMS base and a platinum catalysed curing agent [159]. Many unique applications, for example, polymer-based explosives [160] or implantable bioelectronics [161] arise from the ability to terminate PDMS with different end groups e.g. vinyl ($RC{=}CH_2$) and 3-aminopropyl (RC_3H_8N) as shown in Figure 2.6. The choice of end group can influence the physical properties, e.g. viscosity, as well as the curing mechanism and curing temperature [160, 162].

2.8 Conductive Polymers

Conductive polymers (CPs) possess an intrinsic ability to transport electrical charge. These long-chain organic molecules exhibit the physical and mechanical properties of plastic-like polymers, such as solution processability and environmental stability, while also possessing electrical properties similar to those of a metal e.g. Ag, or metalloid e.g. Si [149, 163].

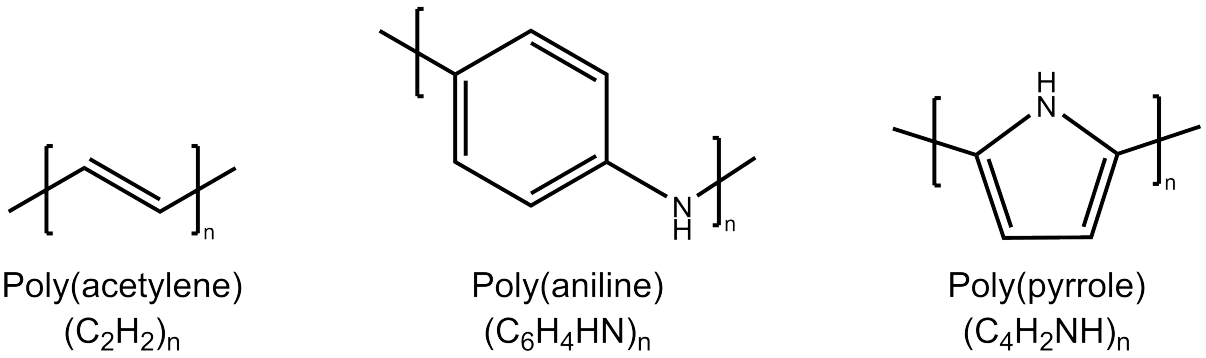

Figure 2.7: Chemical structures of widely-researched, non-thiophene conductive polymers - polyacetylene, polyaniline and polypyrrole.

Highlighting the significance of their work during the 1960s and 70s, in 2000, Alan Heeger, Alan MacDiarmid, and Hideki Shirakawa were jointly awarded the Nobel Prize in chemistry for the discovery and development of electrically conductive polymers such as those given in Figure 2.7. Building upon decades of research following the initial determination of the charge-carrying ability of polyacetylene (PA) by Hatano et al. [164]. In 1977, a highly conductive polyacetylene was reported following oxidation of the polymer by exposure to halogen gas i.e. doping [165, 166]. The chemically doped films of *trans*-polyacetylene resulted in a substantial conductivity increase from $4.4 \times 10^{-5}\,\mathrm{S\,cm^{-1}}$ to a reported value of $38\,\mathrm{S\,cm^{-1}}$. Expanding on the preliminary works by comparing the p-type doping (oxidation) using halogen vapour and n-type doping (reduction) using Li, Na, and K, Chiang reported a maximum conductivity of $560\,\mathrm{S\,cm^{-1}}$ for an arsenic pentafluoride (AsF_5)-doped *cis*-polyacetylene [167–169]. The subsequent development of new polymers and doping processes ushered in the creation of many new areas of research [170]. For example, in the 1980s, a photoelectrochemical solar cell using PA was described by Chen et al. [171], thin-film field-effect transistors based on polythiophene were first presented by Tsumura et al. [172], and Bidan et al. showed the application of polypyrrole composites in pH and water sensors [173]. Development and device optimisation rapidly increased in the 1990s and 2000s, for instance, in 1990 a polymer light-emitting diode utilising a film of poly(*p*-phenylene vinylene) (PPV) was reported by Burroughes et al. [174], the first polymer-fullerene bulk heterojuction OPV devices were reported by Yu et al. in 1995. [175] while many conductive polymers have been applied in biosensing [75].

More recently, conductive polymers prepared using optimised processes now possess metal-

like conductivities on the order of $\sim 10^5\,\mathrm{S\,cm^{-1}}$. For example, in 2016 PEDOT:PSS films treated with H_2SO_4 were reported to have a conductivity of $4829\,\mathrm{S\,cm^{-1}}$. This is in addition to the development of new types of semiconducting polymer with highly refined and tunable properties such as defined band gaps, colour, and high carrier mobilities [176]. Examples of such materials are given in Figure 2.8 i.e. F8BT used in green OLED devices [177], PEDOT:PSS [178], and PSEHTT[3] for photovoltaics [179, 180].

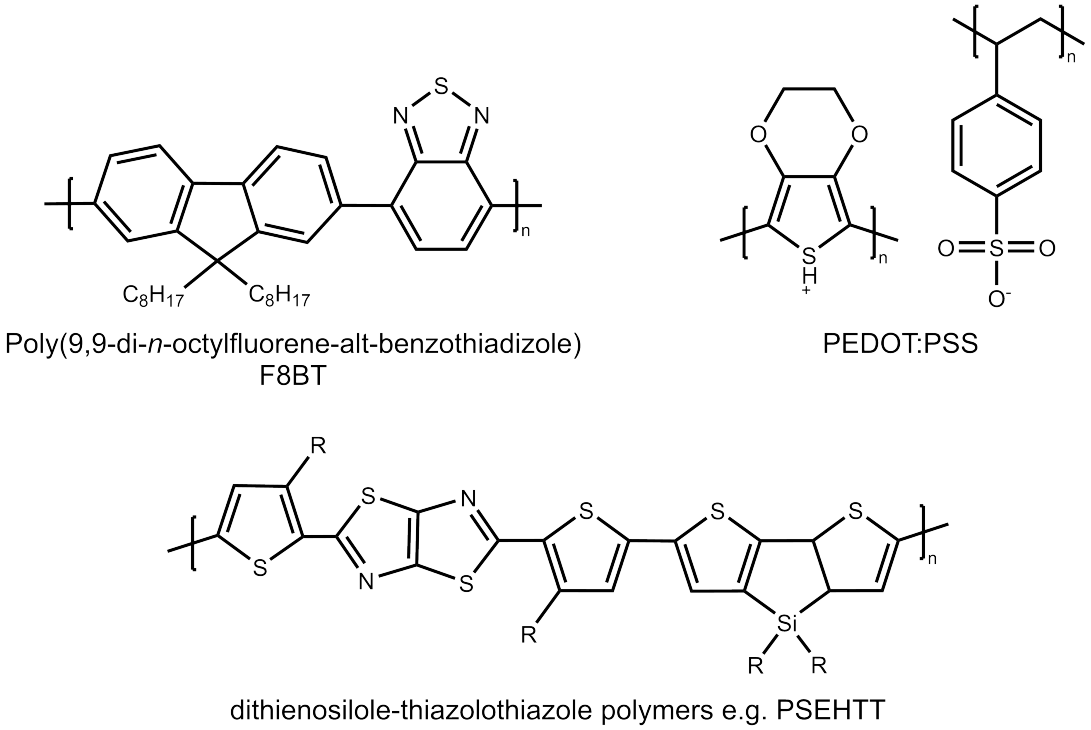

Figure 2.8: Chemical structures of modern conducting and semiconducting polymers and mixtures.

Notes

[3]poly[(4,4'-bis(3-(2-ethylhexyl)dithieno[3,2-b:2,3-d]silole)-2,6-diyl-alt-(2,5-bis(3-(2-ethylhexyl)thiophen-2yl)thiazolo[5,4-d]thiazole)]

2.9 Polythiophenes

During the same period of the early investigations into polyacetylene, various works on the synthesis and electronic properties of polymers based on the 5-membered heterocyclics e.g. thiophene (C_4H_4S) and pyrrole (C_4H_4NH) were also being reported [181, 182]. The initial attempts of synthesising polythiophene as described by Meisel et al. and Armour et al., yielded short thiophene oligomers with < 5 monomer units [183, 184]. However, by 1980

the synthesis of a long-chain poly(thiophene-2,5-diyl) with a regular repeating unit was first reported by Yamamoto et al. [185] and followed shortly by Lin et al. [186].

2.9.1 Conjugation and Conductivity

Electrical resistivity (ρ) is an intrinsic property and measure of a material's opposition to electric current. By definition, conductivity (σ) is the reciprocal of resistivity and describes a material's ability to conduct electrical current. The units of resistivity and conductivity are $\Omega.m$ and $S.m^{-1}$, respectively. Conductivity is influenced by the charge carrier mobility (μ) and charge carrier concentration (n) as described in Equation 2.9.1

$$\sigma = q(\mathrm{n_e}\mu_e + \mathrm{n_h}\mu_h) \tag{2.9.1}$$

where q = elemental charge of carrier, n = carrier concentration of electrons (e) and holes (h) and μ = mobility of the respective charge carrier.

For the practical implementation to a material with a specific geometry, resistance (R) and conductance (G) are determined. As shown in Equation 2.9.2, resistance (R) is directly proportional to a material's resistivity, normalised to the geometric dimensions of the object whereas conductance (G) is the reciprocal of R, directly proportional to conductivity (σ) and inversely proportional to resistivity (ρ).

$$R = \rho \frac{\mathrm{L}}{\mathrm{A}} \qquad\qquad G = \sigma \frac{\mathrm{A}}{\mathrm{L}} \tag{2.9.2}$$

where R = resistance (Ω), G = conductance (S), ρ = resistivity ($\Omega.m$), σ = conductivity ($S.m^{-1}$, A = cross-sectional area of object (m^2) and, L = length of object (m).

In conducting and semiconducting polymers, the ability to conduct electricity arises from their chemical structure, with conjugation across the polymeric chain a defining feature. In polyacetylene (Figure 2.9), the continuous chain of alternating single and double carbon-carbon bonds i.e. sp^2 hybridised carbon atoms, imparts conjugation due to the overlapping

p-orbitals and subsequent delocalisation of π-electrons. In polythiophene, significant overlap of p-orbitals in the extended aromatic π-system allows for delocalisation, contributing to its conductivity. Conversely, insulating polymers typically lack conjugation, with saturated bonds present across all or some of the molecule. Considering polypropylene shown in Figure 2.9, all carbons in the backbone are sp^3 hybridised, connected by single C−C bonds with no conjugation. Similarly, polyisoprene also lacks conjugation, as the C=C double bond is isolated and not part of a continuous system.

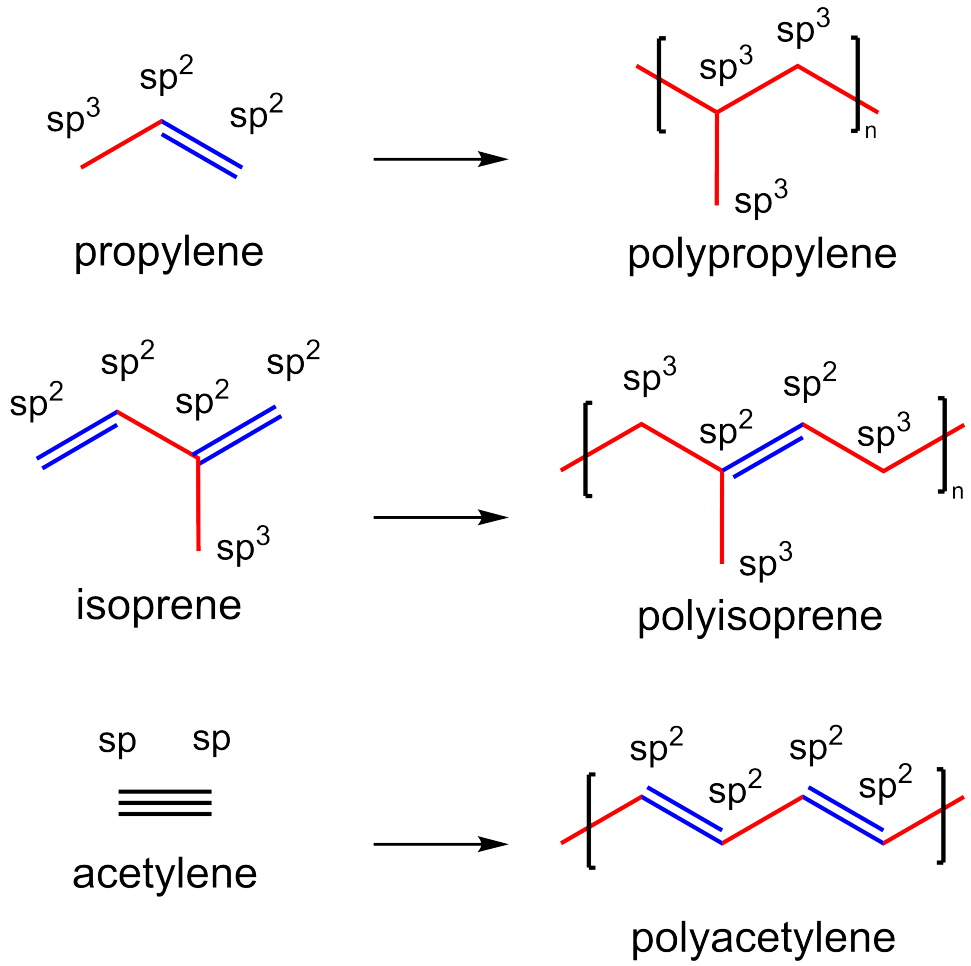

Figure 2.9: Hybridisation of carbon atoms for polyacetylene, polypropylene, and polyisoprene.

The conjugated π-system across the polymer leads to a state with a filled or partially filled π-bonding orbital (HOMO) and an empty or partially empty π*-antibonding orbital (LUMO). Referring to band theory, electrical conduction in an organic polymer is the result of electrons from a band of bonding orbitals (the valance band) moving to the higher energy conduction band by thermal activation, photo excitation or through the application of an

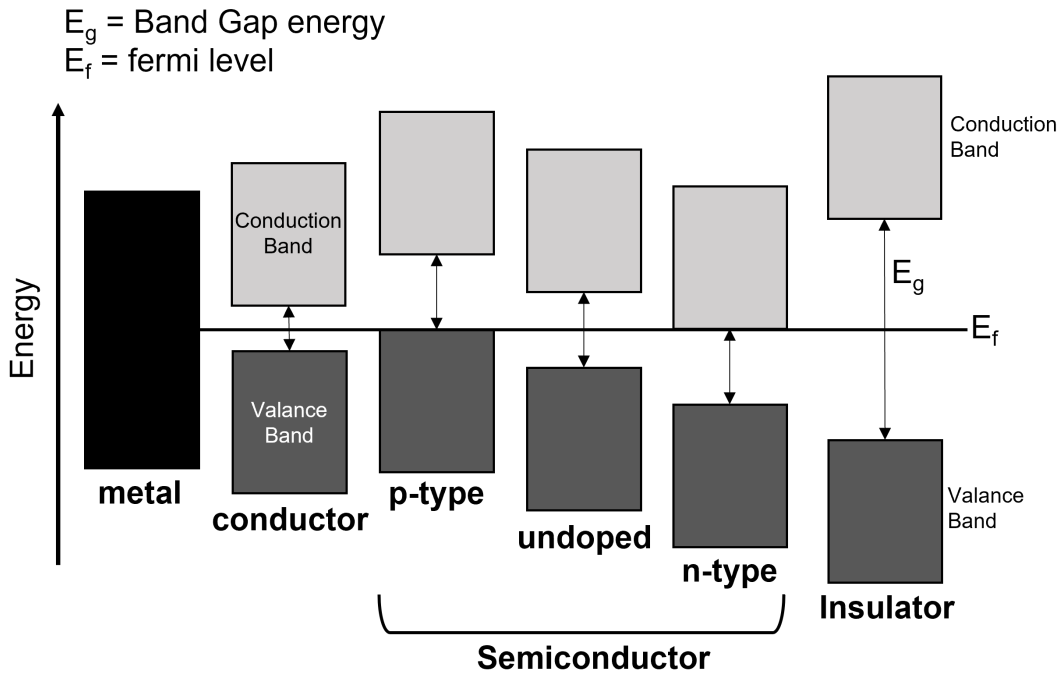

Figure 2.10: Energy band diagram for a metal, p-type, ambipolar, n-type semiconductors and an insulator.

external potential [187]. The energy difference between the valence and conduction band is known as the band gap (E_g) as shown in Figure 2.10 for various material types. E_g relates to the minimum energy required to excite an electron across the forbidden energy gap and contribute to conduction. As a result, the size of the band gap has a significant impact on conductivity. One of the motivations for using organic semiconductors is that E_g can be tuned by modifying the polymer's structure, such as by introducing substituents or co-monomers [188, 189]. While delocalisation of electrons across the polymer and the resultant bands help explain the ability to conduct electrical charge, the transport of charge in semiconductors is performed by charge carriers (holes in p-type and electrons in n-type semiconductors). These carriers possess the ability to propagate across the polymer chains through a variety of proposed inter and intramolecular mechanisms such as the formation of polarons, chain hopping [190], percolation [191], band-like transport [192].

Charge transport mechanisms are a complex and often contentious topic due to the large variety that have been proposed in the literature, therefore a detailed description is ultimately beyond the scope of this work. However, to summarise, the mechanisms used to describe charge transport in organic semiconductors are influenced by multiple factors such as; crystallinity, molecular ordering, molecular packing, impurities and defects, charge-carrier

density, electric field and temperature [192–194]. In reference to poly(3-alkylthiophenes) e.g. poly(3-hexylthiophene), the asymmetry of the 3HT monomer leads to a number of possible coupling configurations during polymerisation, for example, a 3HT-3HT dimer can have a head-head (HH), head-tail (HT), and tail-tail (TT) linkage as shown in Figure 2.11. Regioregularity (RR) has a significant impact on the packing and molecular ordering of the polymer chains during the formation of a thin film [195]. HH and TT linkages lead to increased steric twisting of the ring, reducing the ordering and close packing required for efficient and fast transport of charge carriers. A high percentage of the head-tail (HT) configuration enhances packing, planarity and regularity of the polymer chains, improving electronic performance of the film by promoting π-π stacking and increasing conjugation [149]. As such, regioregularity refers to the percentage of HT coupling. In practical terms, control of regioregularity occurs during synthesis with certain polymerisation methods favouring the generation of high HT percentage, for example, Grignard metathesis (GRIM) polymerisation can produce > 99% HT couplings while oxidation polymerisation methods are typically limited to 80 - 90% RR [196, 197].

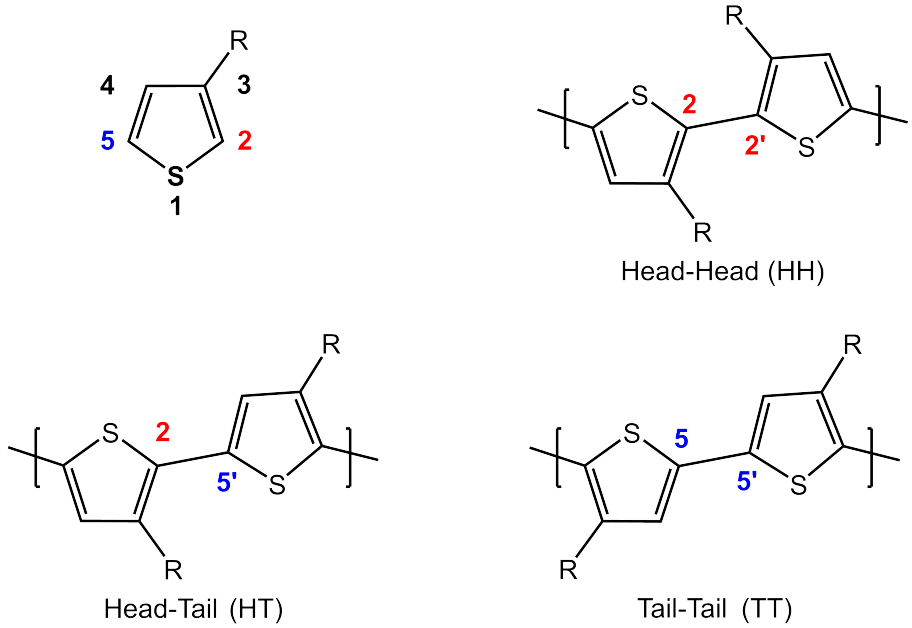

Figure 2.11: Coupling configurations for a dimer of a 3-substituted thiophene.

2.9.2 Solubility and Processing

Unsubstituted polythiophene has significant processability issues due to insolubility in all common organic solvents, regardless of polarity and proticity. Strong intermolecular π-π

stacking, a highly rigid and regular backbone and a lack of favourable interaction with the solvent prevents dissolution, rendering solution-processing of PTh largely unfeasible [198]. Due to the promising properties polythiophene exhibited in its early development, i.e., environmental stability, conductivity, and thermal stability, immediate efforts were made to enhance its processability. This led to the creation of the 3-alkylthiophene polymer series (P3ATs). By 1986, both Elsenbaumer et al., and Sugimoto et al. reported the chemical synthesis of soluble polythiophene derivatives with electronic properties comparable to that of PTh (Conductivity of I_2-doped P3ATs = 1-10 $S\,cm^{-1}$) [199, 200]. Introducing aliphatic pendant groups equal to or greater than 4 carbons in length (i.e. $\geq$ butyl $R{-}C_4H_9$) to the 3-position of the thiophene ring (shown in Figure 2.5) drastically improves solubility in organic solvents. The long alkyl chains disrupt π-π stacking inherent to the thiophene polymer backbone and increases chain flexibility, allowing solvent molecules to solvate and dissolve the polymer by promoting Van der Waals interactions between the solvent molecules and the polymer and reducing interchain interaction [201, 202]. This improvement in solubility allows for deposition of the polymer films via solution-processing methods e.g. spin-coating, printing, etc.

Two of the most well-studied solution-processable thiophene derivatives are poly(3-hexylthiophene), a P3AT soluble in organic solvents, and poly(3,4-ethylenedioxythiophene):poly (styrene sulfonate) (PEDOT:PSS), an ionomer blend capable of forming a colloidal dispersion in water and certain solvents e.g. toluene. Poly(3-hexylthiophene) (P3HT) is a widely used conductive polymer that is highly soluble in chlorinated solvents, possesses a low-band gap ($\sim$2 eV) and finds extensive application in organic and optoelectronics e.g. photovoltaics as an electron donor and hole transport material [203–205] or in OTFT devices as a polymer semiconductor [206, 207]. Alongside highly-refined and well-understood physical and electronic properties, P3HT is also favoured for its compatibility with multiple print deposition methods and scalability through low-cost synthetic routes.

PEDOT-based conductive inks are arguably the most successful commercialised conductive polymer due to ease of processability and favourable mechanical properties. Similar to unsubstituted polythiophene, PEDOT is insoluble, however polymerisation of its monomer; 3,4-ethylenedioxythiophene (EDOT), with polystyrene sulfonate (PSS) yields a highly con-

ductive, optically transparent polymer mixture. PSS is a polymer surfactant, ionic dopant and anodic counter ion which allows PEDOT:PSS to form a stable dispersion in water, enabling solution-deposition processes. As with many thiophene-based conductive polymers, PEDOT:PSS is used extensively in the usual opto- and organic electronics, however the optical transparency and very high conductivity has enabled use as a transparent organic electrode to rival the traditional transparent conductive oxide e.g. Indium-Tin-Oxide (ITO).

One of the main motivations for the use of soluble and solution-processable conductive polymers is the deposition of polymer films and device layers by high-throughput methods such as printing. High-throughput production methods for flexible and organic electronics has gathered considerable attention due to the potential for manufacturing cost reduction and improvements to sustainability through reductions in the amount of materials used [208, 209]. Highlighting the processing versatility of polythiophenes, it has been shown that thin-films (<50 nm) of PTh can be depositied via thermal evaporation; a relatively low throughput process frequently used for the processing of small-molecule organic semiconductors [210]. Kovacik et al. outlines that high vacuum (5×10^{-5} mbar), low temperature (300 °C) and low rate (1 nm min^{-1}) vacuum thermal evaporation of polythiophene allows for the preparation of a functional, highly crystalline thin-film that possesses suitable properties for the fabrication of an operational OPV cell. Vacuum thermal evaporation is a useful technique, however, it is not generally suited for high-throughput polymer film deposition and is typically limited to small molecular organic semiconductors capable of forming crystalline structures that favour fast charge transport and carrier mobility e.g. pentacene, DNTT, etc [211].

2.9.3 Thiophene Polymerisation Methods

While the methods by which the polymers are processed is an important consideration with any organic electronic device, the synthesis method of the functional material is similarly critical, as the choice of synthetic pathway will affect the final application and processing conditions. Restricting the scope to soluble thiophene derivatives, the three main approaches have been metal-catalysed cross-coupling, oxidative coupling and electrochemical polymerisation. For details beyond the descriptions below, many reviews for this topic exist

in the literature, for example, Osaka et al. [212], Ding et al. [213], and Chan et al. [214].

Metal-Catalysed Cross-Coupling: involves the use of transition metal catalysis to form the C−C bonds between thiophene monomers. These methods often utilise organonickel, organopalladium and Rieke metal catalysts to produce polymers with high regioregularity and defined properties e.g. optimal band gaps and low polydispersity. In 1999 the development of Grignard Metathesis polymersisation (GRIM), also called kumada catalyst transfer polycondensation (KCTP) signified a large advancement in the synthesis of regioregular P3ATs [149, 197]. A type of chain-growth polycondensation, GRIM/KCTP involves the formation of a Grignard monomer followed by polymerisation in the presence of a nickel catalyst e.g. Ni(dppp)Cl_2 [215]. Owing to a high degree of control over the molecular weight and regioregularity, the GRIM/KCTP route has become one of the standard approaches for producing polythiophenes used in organic electronic applications. Catalysis-transfer polycondensation reactions involving palladium-catalysis such as Stille coupling and Suzuki coupling have also emerged as effective thiophene polymerisation methods [212, 213, 216].

Chemical Oxidative polymerisation: refers to another class of methods that were originally pioneered in the 1980s by Yoshino and Sugimoto [217]. This simple method involves the use of an oxidant, typically $FeCl_3$, in an anhydrous solvent and leads to a high molecular weight polythiophene with a fairly broad polydispersity (PDI). The basic principles of this method are still widely utilised due to its simplicity, scalability, and ability to produce polymer in a powder form following precipitation in a nonsolvent such as methanol [218]. Oxidative polymerisation is the method used to produce P3HT copolymers in this project. Further detail and review of this process is outlined in Chapter 4.

Electrochemical polymerisation: has been explored as an alternative method to organic synthesis. Application of an electric potential to an electrolyte solution containing thiophene monomers, results in oxidation and subsequent polymerisation at the surface of the working electrode. Electrochemical polymerisation allows for the preparation of an on-electrode polymer film with a high degree of control over the thickness and morphology, as dictated by the applied potential range and polymerisation time [67, 86]. The electrochemical approach is typically performed using a three-electrode cell employing standard electrode choices e.g. Pt, Au, glassy carbon, Ag/AgCl, saturated calomel in solvents such as

acetonitrile and propylene carbonate with supporting electrodes like tetrabutylammoinium percholate, lithium perchlorate, etc [67].

The continuous development of polymerisation methods for soluble polythiophene derivatives has advanced the field of conductive polymers. Each method offers unique advantages, allowing researchers to tailor the properties of the polymer to the specific application, e.g. flexible biosensor devices or organic thin-film transistors. The choice between the various transition-metal catalysis polymerisation methods, oxidation polymerisation routes and electrochemical approaches are a matter of matching the requirements of regioregularity, molecular weight, and polydispersity with reagent availability, suitability of the process conditions (e.g. temperature), yield and quantity, and importantly the compatibility for polymerising monomers with the functionality to directly bind biomolecules e.g. thiophene carboxylic acids.

2.9.4 Copolymerisation

A copolymer may form during a polymerisation reaction that contains two or more different monomers. The materials formed during copolymerisation possess properties similar to the related homopolymers, with the structure or sequence of the monomers across the polymer chain also contributing to properties such the glass transition temperature or the ability to undergo microphase separation [219, 220]. Copolymers are often classified according to their monomer sequence under two broad categories; i) linear copolymers that are comprised of a single macromolecule chain and ii) branched copolymers that possess polymeric side chains. Polythiophenes typically form linear polymers through C-C couplings at the 2- and 5-positions on the thiophene ring. In P3HT, the steric effects of the alkyl chain at the 3-position further enforce this coupling, reducing the likelihood of side reactions at the 4-position, which could lead to a branched structure. Focusing on linear copolymers, given the relevance to polythiophenes, a variety of structure can be formed during copolymerisation:

- Alternating copolymer (-ABABABAB-),
- Block copolymer (-AAAABBBB-),
- Statistical/Random copolymer (-AABABBAB-),

- Periodic copolymer (-AABBAABB-).

The formation of linear copolymers and resultant monomer sequences are governed by several factors including, the monomer structure and compatibility, reaction mechanism, and synthetic conditions [221]. Moreover, as described by the copolymer (Mayo-Lewis) equation, the copolymer structure is heavily influenced by reaction kinetics such as monomer reactivity ratios (r_i) that describes a ratio of rate constants (k_{ii}) for the propagation of the polymer chain ($M_A^\bullet, M_B^\bullet$) with one of the monomers (M_A, M_B) [222]. The monomer and reactive chain end interaction is summarised below in Equation 2.9.3.

$$\begin{aligned} M_A^\bullet + M_A &\xrightarrow{k_{AA}} M_A^\bullet M_A \\ M_A^\bullet + M_B &\xrightarrow{k_{AB}} M_A^\bullet M_A \\ M_B^\bullet + M_A &\xrightarrow{k_{BA}} M_B^\bullet M_A \\ M_B^\bullet + M_B &\xrightarrow{k_{BB}} M_B^\bullet M_B \end{aligned} \tag{2.9.3}$$

where the reactivity ratios are defined as $r_A = k_{AA}/k_{AB}$ and $r_B = k_{BB}/k_{BA}$.

Alternating copolymers form when the monomers preferentially react with each other ($r_1, r_2 \approx 0$) i.e. $R-A^\bullet$ or $R-B^\bullet$ will react with monomer B or A, respectively. Examples of alternating copolymers include poly(styrene-*co*-maleic anhydride) synthesised via a free radical approach [223], and poly(3-hexylthiophene-*co*-3-hexylfuran) produced using catalyst transfer polycondensation (CTP) as outlined by Qiu et al. [224]. In contrast, statistical copolymers e.g. poly(styrene-*co*-acrylonitrile) are characterised by a random monomer sequence that follows a statistical distribution [10, 225]. These are formed during chain propagation when $r_1, r_2 > 0$ meaning $R-A^\bullet$ or $R-B^\bullet$ may react with either monomer A or B. The polymers synthesised in this project possess a statistical/random monomer sequence [149, 226].

Copolymerisation is a useful method for designing functional materials, therefore the sequence and structure of copolymers is an important consideration. By copolymerising monomers with desirable characteristics such as the solution-processability of 3HT polymers and the amine reactivity of R−COOH groups in thiophene-3-acetic acid (T3AA) polymers, it is possible to create novel materials suited to a wide range of applications. including biosen-

sors [68]. For instance, Lai et al. outlines the synthesis and characterisation of 3HT-T3AA copolymers, enabling the development of a potentiometric urease-urea biosensor [38].

2.10 Solution-processing of Polymer Materials for Flexible Electronics

Using mass-print deposition methods in the production of flexible and organic electronics has gathered considerable attention due to the potential for reductions in manufacturing costs and unmatched scalability. Specifically, there is much interest in the use of both contact print techniques such as Gravure, flexography, and offset [227, 228] and non-contact techniques, mainly inkjet (IJP) and aerosol jet (AJP) [229], to realise the high-throughput device fabrication, which is ultimately key to unlocking the potential of flexible electronics on a commercial level [230].

The industrial fabrication of organic electronics involves the use of solution-based processes with a focus on wide-area deposition of device layers using various high-throughput roll-to-roll (R2R) print methods. In contrast, silicon-based electronics e.g. metal-oxide-semiconductor field effect-transistors (MOSFETs), are fabricated using a combination of additive and subtractive deposition steps in which materials are deposited by standard thin-film processes e.g. physical vapour deposition (PVD), atomic layer deposition (ALD) then patterned using photolithography and chemical etching methods to produce the desired features. Printing is an additive process where a patterned layer of material is selectively deposited onto a substrate. Described by the organic and printed electronics association (OE-A) as an 'enabling technology', printing allows for the simplification of manufacturing processes by reducing process complexity [231].

Seizing upon the solution processability of oils, polymer semiconductors, nanoparticle solutions, a variety of printing techniques have been developed and investigated in recent years for use in the fabrication of flexible organic electronics. As previously mentioned, printing methods are often divided into two categories, that is, non-contact and contact. In Table 2.1, some of the purported benefits and drawbacks described in the literature are outlined for a variety of common techniques.

Table 2.1: Table of advantages and drawbacks for common contact and non-contact printing methods.

Technique	Advantages	Drawbacks
Inkjet (Non-contact)	Rapid single-pass print speed [227]. Minimal material waste [232]. Insensitive to substrate defects [233]. Very high resolution (1-50 μm).	Complex inks with narrow viscosity range [234, 235]. Nozzle clogging. Low throughput [228]. Poor device performance beyond laboratory-scale [232].
Aerosol Jet (Non-contact)	Digital print method. Wide range of ink viscosity (1-2500 cP) [236]. Use of non-planar substates possible. Low processing temperature.	Relatively low throughput. Material/pattern overspray [228, 237].
Screen Printing (Contact)	Suitable for large-area printing [132]. Mature technique for deposition of metal pastes [238]. Good lateral resolution ($\sim$ 10 μm) [239].	Significant material waste [240]. High viscosity paste-like inks required [241]. Layer thickness limits application in organic electronics (100-1000 μm). Print quality highly dependent on screen quality [239].
Gravure (Contact)	Very high throughput (100 m min^{-1}) [194]. High lateral resolution (2-50 μm) and thickness uniformity [242]. Highly scalable [243].	High initial costs. Fixed pattern choice (Engraved metal print cylinders). Significant process optimisation required [242]. Poor print cylinder lifetime [240]. Coffee-staining prominent.
Flexography (Contact)	Wide range of low-viscosity and quick drying inks available [241]. High throughput [244]. Low-cost patterned print plates [240]. High thickness resolution (100 nm) [245]. Low printing pressure prevents layer destruction.	Quality of printing plate has large impact on print quality [246]. Deposition of very thick films (10s μm) requires multiple print passes. Potential for issue with layer registration (e.g. misregistration, ghosting) [247].

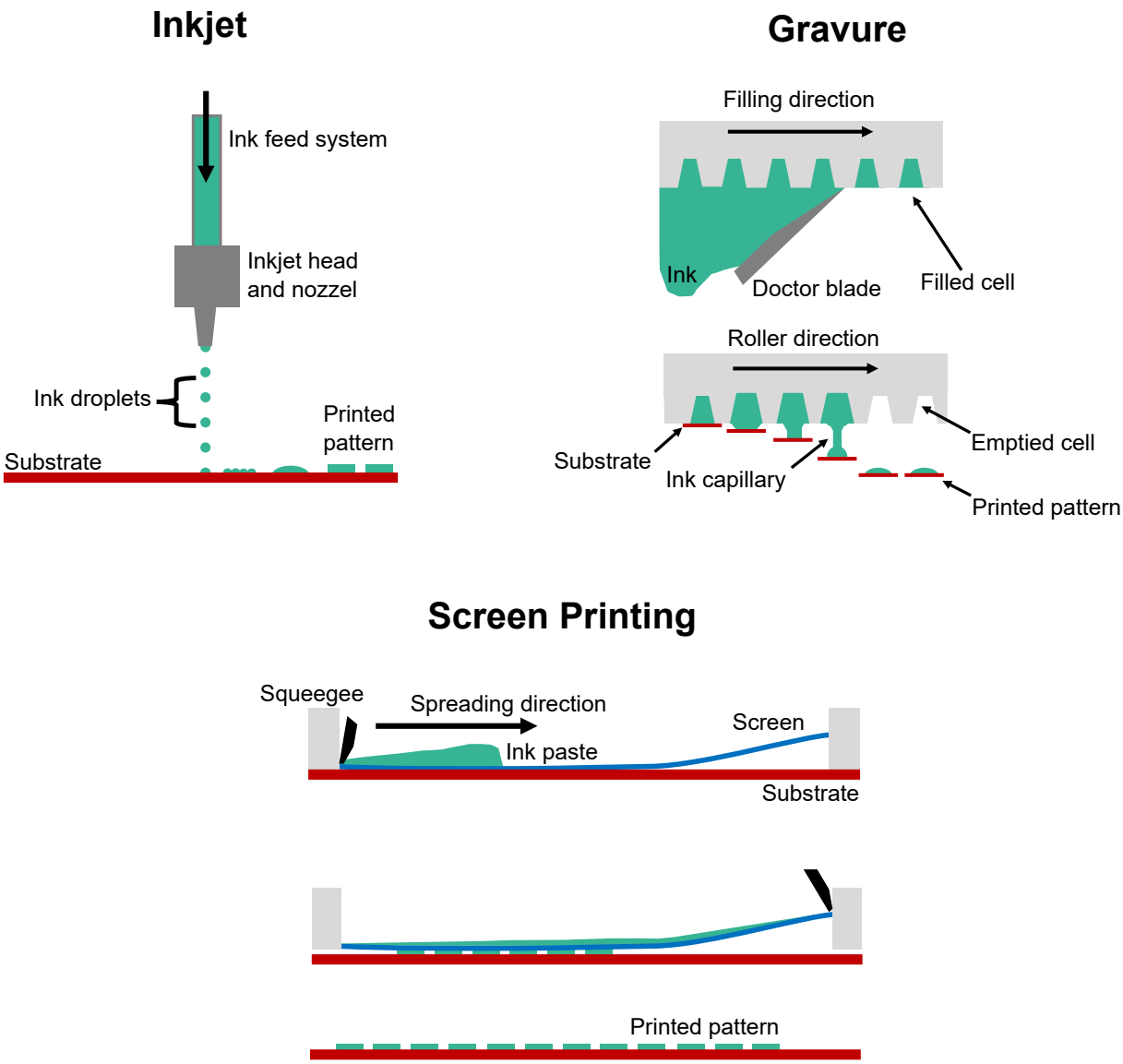

Figure 2.12: Schematic representation of common printing methods for flexible electronic fabrication: Inkjet, Gravure and Screen Printing.

In the context of solution-processable flexible electronics, an ink refers to a solution or suspension containing a functional material. These inks can be as simple as an organic semiconductor dissolved in solvent, a metal nanoparticle suspension, or a multi-component formulation comprising an active material, surfactant, rheological modifier, a complex solvent system, additive, etc [248]. As represented in Figure 2.12, contact printing differs from non-contact methods, as the substrate comes into direct contact with the ink transfer mechanism. Screen printing is a contact print method utilised extensively in the production of photovoltaic cells and the circuit board industry [238]. Layers are deposited onto a substrate by pushing ink through a patterned mesh screen using a squeegee. Screen printing requires viscous paste-like inks, therefore formulation of such high viscosity inks may limit

the use of some materials due to solid loading requirements [249]. In cases where low solubility of the active material may prohibit high solid loading, the inclusion of binders can increase this viscosity [241]. The schematic in Figure 2.12 depicts a flat screen process, however integration of screen printing into a rotary form is widespread and has been shown to be a good technique for flexible electronics. For example, Carlos et al. has reported the fabrication of a flexible metal oxide diode in which a PEDOT:PSS electrode was printed by rotary screen [250].

Rotary print methods such as gravure and flexography share the common principle that ink is transferred from source to substrate via a series of rotating cylinders, however the mechanism by which the ink is deposited varies [132]. For example, in gravure, ink is filled into the cells on an engraved cylinder before it is transferred onto a substrate through direct contact with the patterning surface whereas flexography utilises patterned photopolymer printing plates with raised features. In a flexo system, ink is first loaded onto an anilox cylinder before the printing plate is coated with a thin ink layer upon anilox-plate contact. For gravure, the ink is dispensed onto the patterning cylinder and spread into the cells with assistance from a doctor blade [242]. Roll-to-roll contact printing techniques have a number of noteworthy benefits, namely the reductions in costs owing to fewer process steps, lower overall equipment prices, high product throughput and less material wastage due to selective deposition [251].

On the lab scale, it is common for organic electronic devices to be fabricated using processes such as spin-coating, blade-coating, physical vapour deposition. As such, it has been noted that scaling from the laboratory to a commercial scale using high-throughput R2R systems is a difficult process [252]. As discussed in a recent review by Luo et al., the scaling of flexible sensor technologies is hampered by ink formulation challenges, stability of functional materials, restrictive regulatory requirements and device integration, among others [253]. The difficulty facing printed electronics due to functional ink formulation is a common topic in the literature, for example Grau et al. the importance of optimised ink characteristics i.e., viscosity, solvent evaporation rate for gravure printing is described [242]. In Sheats et al. a review on the manufacturing and commercial scale up of OEs is presented with the author noting that optimisation of an ink's rheological properties and surface tension is key

to the fabrication of quality devices but that modification of an ink's deposition characteristics through the inclusion of additives may be detrimental to the electronical and optical properties of the functional organic polymer [254].

2.10.1 Introduction to Flexography

Flexography is a contact printing technique that makes use of reusable printing plates with raised feature (relief) to transfer a patterned layer of ink onto a substrate. This technique offers good lateral resolution (20 - 50 μm) and a large range of printable thicknesses (0.1 - 5 μm) appropriate for the production of features for organic electronics, i.e. metal electrodes.

As shown in Figure 2.13, a standard flexography system consists of:

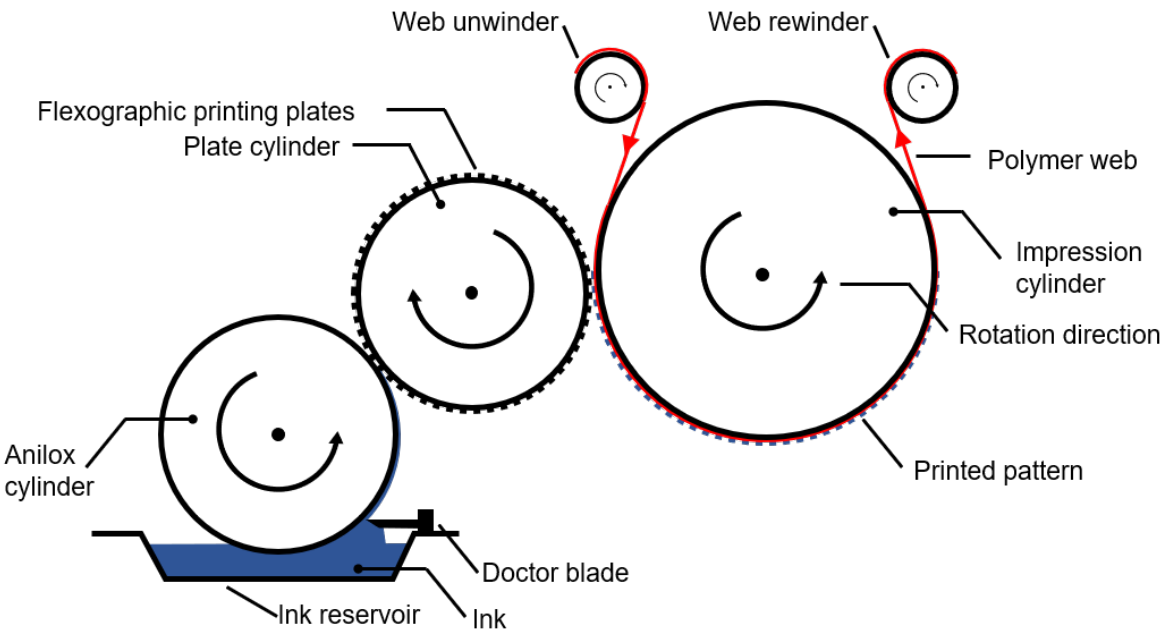

Figure 2.13: Diagram of a typical flexographic print system.

1. **Anilox system - ink reservoir, anilox cylinder and doctor blade**: The anilox system is used to deliver a pre-determined amount of ink onto the flexographic printing plate [247]. The anilox cylinder is the only rotary component in direct contact with the ink source/reservoir, therefore, it is typically constructed from a hard metal or ceramic to ensure roller durability and solvent resistance.

2. **Substrate feed system - winders, polymer substrate and impression cylinder**: The impression cylinder is constructed from a durable material e.g. polished stainless

steel, so that the surface offers a consistent pressure across the substrate and printing plate. This roller is used to support the substrate as it comes into contact with the printing plate. A variety of polymer substrates; known as webs, can be utilised in flexography. Common choices include; polyethylene naphthalate (PEN), polyethylene terephthalate (PET), and biaxially orientated polypropylene (BOPP) as they are lightweight, flexible, transparent and offer good chemical compatibility [255]. Macdonald et al. summarises the chemical, mechanical and optical properties of PET and PEN [256] and outlines why polyester substrates are particularly suited for organic electronic applications.

3. **Plate cylinder and flexography (relief) print plates**: The plate cylinder is a generic hard metal roller i.e. stainless steel, that is used to hold an external sleeve; known as the flexographic printing plate, via a pressure fit or by using a mechanism such as magnets or mounting tape. Flexographic printing plates are relief style printing plates used to transfer ink from the anilox system onto the substrate. The term *relief* describes a printing method where ink is only applied to the raised features of a patterned printing plate before it is contacted onto a substrate, thus yielding an ink pattern. As discussed in a review by Lui et al., flexo plates are made from materials such as, nitrile rubbers and photopolymers [246]. Different applications warrant the use of the different plate materials, however synthetic photopolymers, e.g. styrene-acrylate polymer blends, tend to dominate due to high resolution capabilities. On the lab scale, polydimethylsiloxane (PDMS) has also been utilised as a low cost plate material due to unmatched fabrication speeds and the ability to lean on the extensive learnings from microcontact printing (μCP) [156, 257]. For example, Maksud et al. describes a process for producing a PDMS flexo plate by 3D printing and demonstrates capability to produce $\sim$100 μm line width features [258], furthermore, Hassan et al. outlines a proof of concept method for the deposition of water-based carbon nanotube inks using a μCP-type plate production process [259].

2.11 Metal Deposition

Where flexographic printing is a technique that can be utilised for patterned deposition of inks e.g. a patterned oil mask, physical vapour deposition (PVD) techniques provide the route to metallisation and the fabrication of electrical contacts for use in organic electronic devices. PVD techniques encompass a broad class of thin film deposition processes in which a solid or liquid compound is sublimed or vaporised and transported through a vacuum, low pressure or plasma environment onto a substrate where condensation occurs, and a film is formed [260]. Throughout both industry and academia, PVD techniques are utilised extensively for the production of optically active coatings, barrier and passivation layers, electrical conductors, hydrophobic coatings, etc [261].

In this DPhil project, the PVD method vacuum thermal evaporation (VTE) was employed for the deposition of metal thin-films. Lab-scale thermal evaporation is an extremely common technique, however, as more focus is placed on higher-throughput deposition and high production rates, the integration of VTE into a roll-to-roll format is becoming ever more prominent [262, 263]. Roll-to-roll in-vacuum evaporation, also called vacuum web-coating, is one method that allows for high-speed deposition of metal layers without the need for printing of nanoparticle-based inks. Vacuum web-coating has been used commercially in applications such as the deposition of decorative metal films on paper boxes or barrier layers for food packaging, but the use in the production of high-quality metal electrodes for flexible electronics is a recent innovation [262]. For an overview of vacuum web-coating, Kukla et al. describes the basics of a web-coater system and their application in a commercial setting [255]. In the evaporator system, the metal sample, substrate, and vacuum chamber are prepared to obtain a high vacuum ($<1\times10^{-5}$ mbar) as this is crucial for ensuring that the mean free path is large enough to allow collision-free travel between thermal source and substrate. It is common for a refractory metal or ceramic boat to be used for the resistive heating, as these materials are capable of reaching the high temperatures required to process the metal samples. Through the application of an electric current across the boat, the metal sample is heated to result in the release of gaseous atoms through the vacuum, towards the substrate. Upon reaching the substrate, the metal vapour condenses, forming

a metal thin-film [260].

For finer applications of thermal evaporation, users require deposition of patterned features, for example the source-drain electrodes of an OTFT device [264]. In low throughput fabrication, patterned thin-film deposition is often achieved by evaporation through a shadow mask or use of photolithography, however, when focusing on high-throughput R2R processes, the options available to achieve patterned metal deposition are limited. As discussed by Bishop in *Vacuum Deposition onto Webs, Films and Foils*, for R2R in-vacuum metallisation, there are two practical masking options: Shadow/stencil masking and oil masking [265]. Shadow masking refers to the use of a solid stencil mask to cover areas of the substrate in order to prevent deposition. Their use is wide-spread throughout the field [266–268] owing to a plethora of benefits, for example, lithographic resists are not required to produce patterns, the masks are reusable and durable and importantly, implementation into existing processes is trivial. However, shadow masking is not without issue with shadowing effects and limited scalability noted problems.

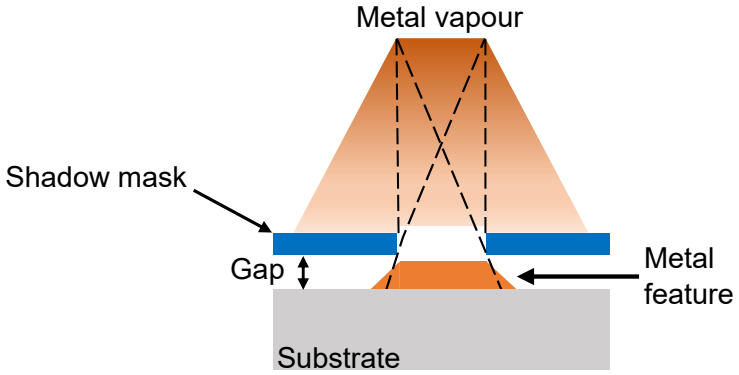

Figure 2.14: Schematic representation of the shadowing effect during thermal evaporation.

Due to the unavoidable shadow mask-substrate gap, represented in Figure 2.14, metal can be deposited through the mask at an angle. This causes a reduction in pattern edge sharpness, which can be detrimental to feature quality and electrical performance depending on the extent of the effect [269]. In terms of scalability, fixed shadow masks are used primarily in small-scale VTE processes, as it is not feasible to use in large-scale R2R processing due to shadowing and the continual build-up of material over the duration of a deposition process [265].

2.12 Selective Metallisation

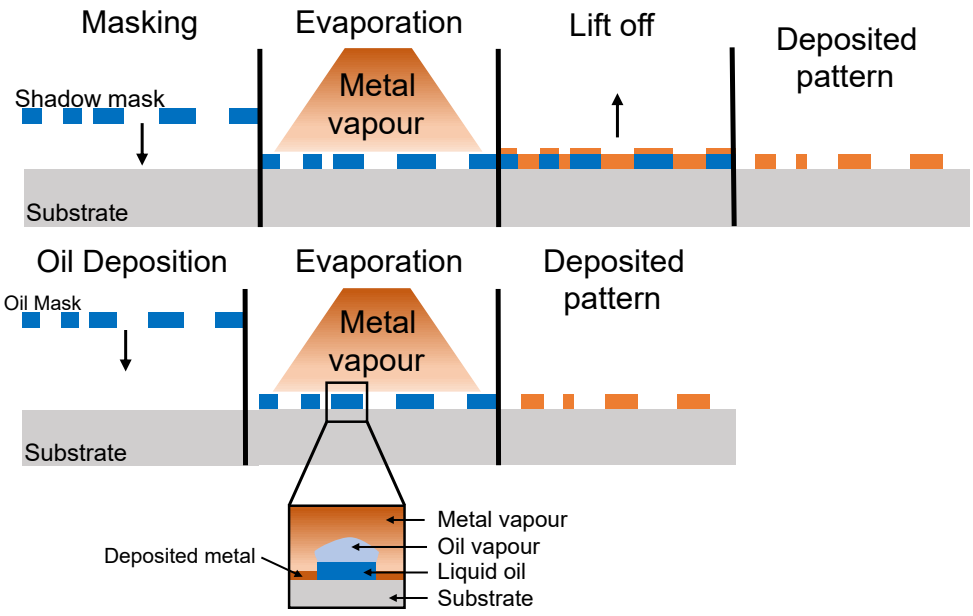

Figure 2.15: Process steps for shadow mask (top) and oil mask (bottom) metal deposition.

The term selective metallisation refers to a number of processes used for the deposition of patterned metal layers. In most cases, this is achieved by masking during physical vapour deposition (PVD) [265, 270, 271] or by laser-assisted and print-assisted chemical methods, e.g. electroless deposition [240, 272, 273]. In the context of this project, selective metallisation specifically refers to a PVD process in which, a sacrificial mask of Krytox1506 perfluoropolyether (PFPE) vacuum pump oil is employed to prevent metal deposition as illustrated in Figure 2.15 which compares selective metallisation using a shadow mask vs an oil masking approach.

This type of method for patterned metal deposition has seen use in industry due to the compatibility with R2R manufacturing processes, for example, vacuum web coating, where other patterning methods are limited by throughput and print quality [274]. Oil masking originated from an observation that metal vapour shows poor adhesion to vacuum oil after a polymer web was contaminated with back-streamed pump oil [265]. A thin film of vacuum compatible oil, e.g. Krytox1506, can therefore be purposefully used to prevent deposition on specific areas of the substrate. This technique has been in use for a number of decades, as identified by patents from the 1970's and 80's [275, 276].

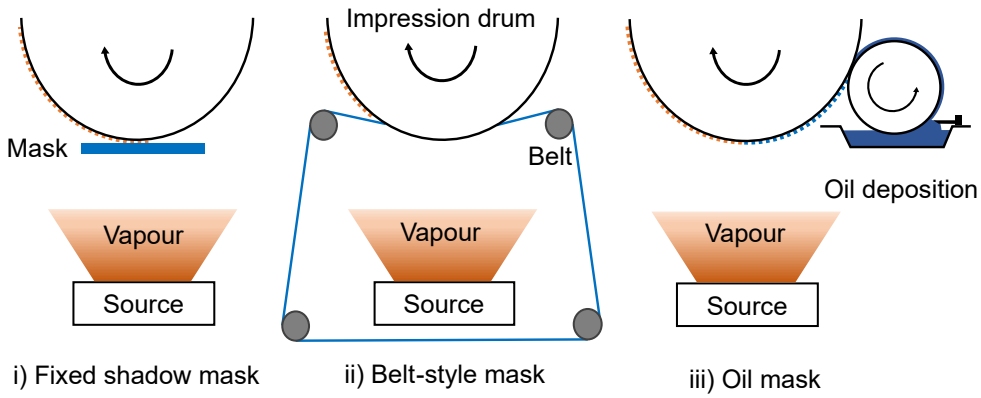

Figure 2.16: Schematics of in-line patterning techniques i) Fixed shadow mask, ii) Belt-style masks, iii) Oil masking.

As shown in Figure 2.16, the metallisation process begins with deposition of a thin film of patterned vacuum oil onto a polymer substrate. Various techniques can be used to deposit this film, for example, oil boiler systems, inkjet/spray systems or contact print systems (flexography) [244]. Following oil deposition, the substrate can be exposed to a thermal evaporation source where metal vapour sticks to the non-oil coated areas. Simultaneously, the oil mask is removed from the substrate due to the radiant heat of the thermal source, leaving a high-quality metal pattern. Various studies have discussed similar processes for patterned metal deposition using a sacrificial Krytox1506 oil mask. Cosnahan et al. outlines the optimisation of a R2R PVD process using in-house fabricated, relief-style PDMS print plates for in-line deposition of the patterned oil mask [270]. Cosnahan presents several factors that influence the print system and final deposition quality, for example, the volume (thickness) of Krytox1506 oil on the substrate, the physical properties of Krytox1506 that control vaporisation as well as the amount of radiative heating from the thermal evaporation source. Later, Stuart et al. presented a comprehensive overview of R2R vacuum deposition of patterned aluminium, copper, and silver layers by the flexographic printing of a sacrificial Krytox1506 oil mask [271]. Showcasing the versatility of sacrificial oil masking for in-line patterning of common metals found in flexible and printed electronics, Stuart demonstrates the capability of a vacuum R2R system to deposit thin (<50 nm) patterned metal layers over a range of print speeds (1 - 25 m min^{-1}) using traditional photopolymer flexographic print plates.

The combination between vacuum thermal evaporation, a selective metallisation process in oil masking and a means to deposit the oil mask by high-speed, high-resolution flexographic

printing offers a potential route to produce large-area yet high-quality patterned metal electrodes for flexible electronics, thus enabling the production of low-cost functional devices e.g. flexible sensors and large-area OTFTs or OPVs.

2.13 Polydimethylsiloxane-Based Flexo Plates

Polydimethylsiloxane (PDMS) is a polymeric organosilicon; a silicone, that is used in the medical industry [277], in soft lithography (microcontact printing) [257] and microfluidics [157]. The widespread application of cured PDMS is a result of its properties, for example, it is non-toxic and biocompatible, chemically resistant, simple to prepare, optically transparent, flexible, stretchable, etc [158, 278].

A novel approach to flexographic printing plate production has recently been presented by Francis et al. [136]. The process involves the application of area selective oxidation onto planar, i.e. non-relief patterned, PDMS plates. It has been shown that oxidising the surface of PDMS with ultraviolet/ozone can result in controllable wetting and dewetting of Krytox1506 oil. The ability to control local dewetting of the oil is crucial to the patterning of features on the plate surface and subsequent deposition of a patterned oil layer. In the publication, Francis outlines the development and refinement of the casting, oxidation process and oil coating, enabling the deposition of patterned metal features with a thickness of ~500 nm and a lateral resolution <20 μm.

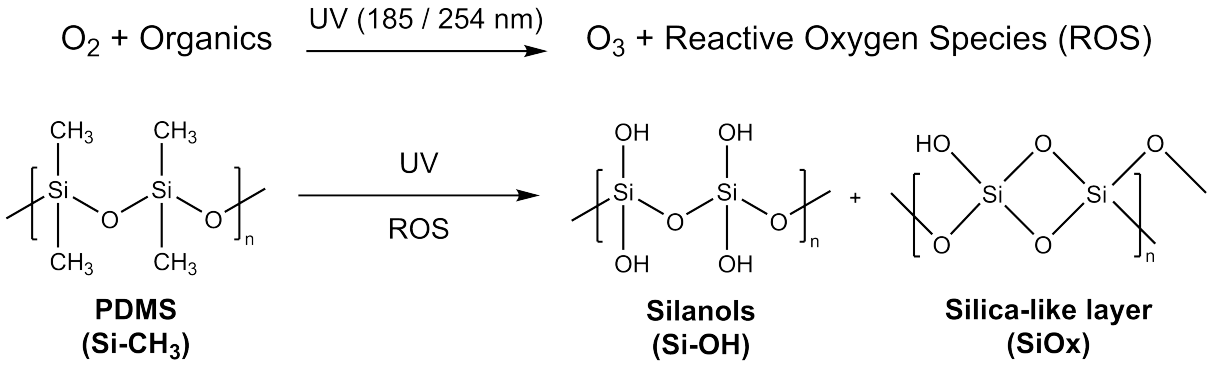

Figure 2.17: Reaction scheme for the photo-oxidation of PDMS by UV/Ozone.

The production of hydrophilic groups by oxidation of the PDMS surface increases surface free energy and results in the formation of a low-contact angle, dewetting surface state. As outlined in the literature, oxidised-PDMS may be produced upon treatment by a range of

processes, including plasma [279], corona discharge [280], photo-oxidation (UV/O_3) [136] and chemical treatment [281]. With specific reference to oxidation of PDMS by UV/O_3, the primary mechanism for the hydrophilisation process is shown in Figure 2.17. Firstly, UV light interacts with O_2 to produce ozone O_3. The ozone molecules decompose further due to the UV light, yielding various reactive oxygen species (e.g. $^1O_2$, $OH^\bullet$) which attack the PDMS. The hydrophobic and silicon-bound methyl groups ($Si-CH_3$) are oxidised by the reactive oxygen species, forming hydrophilic silanol groups ($Si-OH$) on the surface. A sustained exposure to UV/O_3 allows for further oxidation of the silanols and $Si-O$ backbone, promoting crosslinking reactions which leads to the formation of a network of $Si-O-Si$ [159]. Over time, a thin, brittle and oxygen-rich layer resembling silica forms [279]. This layer is often referred to as a silica-like (SiOx) due to similarities in its chemical composition and properties to silicon dioxide.

Further discussion on the use of UV/O_3-PDMS in the context of patterned metal deposition by selective metallisation and the proposed theoretical basis behind the control of Krytox1506 wetting and the intrinsic recovery of hydrophobicity is presented in Chapter 6.

Chapter 3
Experimental Methods - Polymer Synthesis and Biosensors devices

This chapter covers the experimental methods utilised during the project, specifically, the synthesis of thiophene polymers, the characterisation of synthesised materials as well as the fabrication and analysis of biosensor devices. The operational conditions for various analytical techniques, such as Attenuated total reflectance - fourier transform infrared spectroscopy (ATR-FTIR), Ultraviolet-visible (UV-Vis) spectroscopy, and Chronoamperometry (CA) are also discussed.

Table A.2 contains a list of reagents, chemical formulae and product purity/grades of those described in Chapters 3, 4 and 7. This can be found in Appendix A *Chemicals and Solvents*.

3.1 Thiophene Ester Monomers

Five monomers were prepared from known synthetic routes to facilitate the production of polythiophenes. Due to the high susceptibility of oxidative decomposition and degradation, carboxylic acid-functionalised thiophene monomers are not compatible with direct use in $FeCl_3$ oxidation polymerisation reactions [282]. This inability to undergo polymerisation necessitates that protection of the R−COOH moiety is performed. In this project, ester monomers of methyl 3-thiophene carboxylate (M3TC), methyl 3-thiophene acetate (M3TA) and methyl 3-(thiophen-3-yl)acrylate (M3T3YA) were synthesised from the corresponding thiophene carboxylic acid using a Fischer esterification reaction as outlined in Kim et al. and Bertran et al. [283, 284].

The following reactions are representative examples of synthetic procedures used for the preparation of thiophene methyl and N-succinimidyl esters. While the exact quantities of starting materials may be different between individual batches, the procedure and molar stoichiometry remained the same throughout.

3.1.1 Esterification of thiophene-3-carboxylic acid

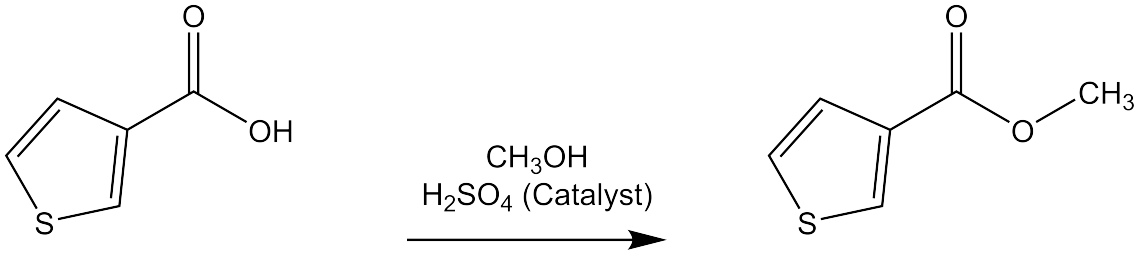

thiophene-3-carboxylic acid
T3CA
$C_5H_4O_2S$
128.15 g mol^{-1}

methyl 3-thiophene carboxylate
M3TC
$C_6H_6O_2S$
142.17 g mol^{-1}

Figure 3.1: Reaction scheme for esterification of thiophene-3-carboxylic acid (T3CA).

As outlined in Figure 3.1, thiophene-3-carboxylic acid (1.0050 g, 128.15 g mol^{-1}, $C_5H_4O_2S$) was dissolved in 20 mL of methanol (CH_3OH) along with a catalytic amount of concentrated sulfuric acid ($H_2SO_{4(aq)}$). The mixture was heated to reflux for 24 hr before concentrating *in vacuo*, followed by liquid-liquid extraction with 2 x 20 mL ethyl acetate ($C_4H_8O_2$). The ethyl acetate layer was washed with 2 x 10 mL deionised water (H_2O) before drying over anhydrous magnesium sulfate ($MgSO_4$) then filtering. Removal of the remaining solvent gave a pale yellow liquid - methyl 3-thiophene carboxylate (0.6553 g, 142.17 g mol^{-1}, $C_6H_6O_2S$) at a yield of 58.8%. The characterisation of synthesised materials is discussed in Chapter 4.

3.1.2 Esterifcation of thiophene-3-acetic acid

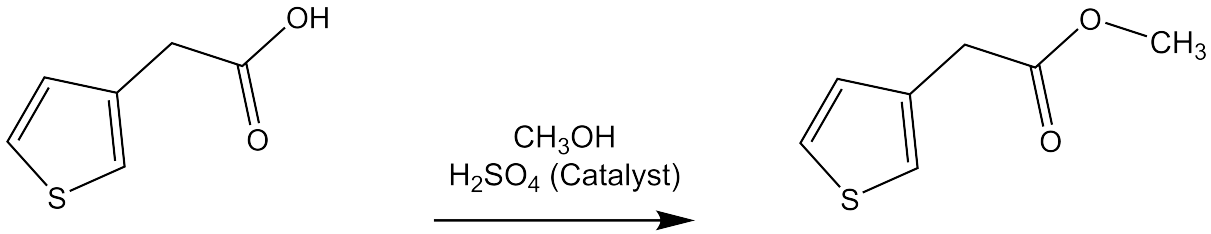

thiophene-3-acetic acid
T3AA
$C_6H_6O_2S$
142.17 g mol^{-1}

methyl 3-thiophene acetate
M3TA
$C_7H_8O_2S$
156.20 g mol^{-1}

Figure 3.2: Reaction scheme for esterification of thiophene-3-acetic acid (T3AA).

The synthesis of methyl 3-thiophene acetate given in Figure 3.2, follows the same procedure as the esterification of T3CA, as described in section 3.1.1. Thiophene-3-acetic acid (2.0036 g, 142.17 g mol^{-1}, $C_6H_6O_2S$) was converted into methyl 3-thiophene acetate (1.2835 g, 156.20 g mol^{-1}, $C_7H_8O_2S$). The reaction yield was 58.3%, and the product had the appearance of a light-brown crystalline solid.

3.1.3 Esterification of trans-3-thiophen-3-yl-acrylic acid

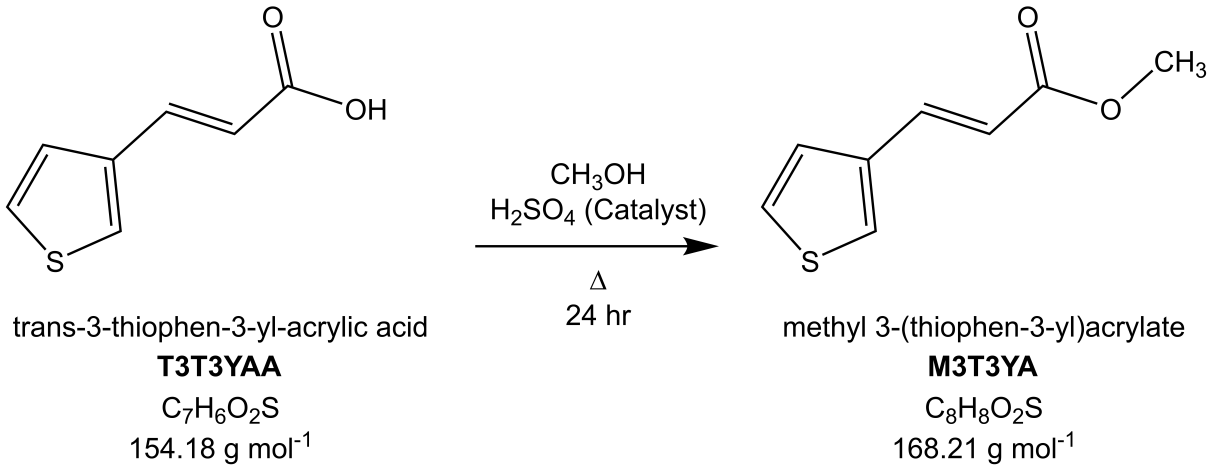

Figure 3.3: Reaction scheme for esterification of trans-3-thiophene-3-yl-acrylic acid (T3T3YAA).

The esterification of trans-3-thiophen-3-yl-acrylic acid (2 .0148 g, 154.18 g mol^{-1}, $C_7H_6O_2S$) shown in Figure 3.3 afforded the ester - methyl 3-(thiophen-3-yl)acrylate (1.9690 g, 168.21 g mol^{-1}, $C_8H_8O_2S$) as a champagne-coloured solid. Yield 89.6%.

All the synthesised methyl ester monomers possessed a strong, astringent scent. As such, they were stored in film-wrapped vials in a low-moisture, dark environment to minimise their apparent volatility until needed.

3.2 Thiophene N-succinimidyl Ester Monomers

The irreversible attachment of biomolecules via covalent immobilisation greatly enhances biosensor performance and device longevity. Functionalised polymers enable this process by facilitating the formation of covalent bonds between the amine-containing residues of enzyme and the complimentary reactive groups on the polymer. This can be achieved through

various chemical pathways, including glutaraldehyde-mediated or N-hydroxysuccinimide-carbodiimide (NHS-EDC) immobilisation reactions [285, 286].

Following deposition of thin-films onto the electrode surface, carboxylic-acid functionalised polymers required activation of the COOH group to enable enzyme cross-linking. A common method involves activation via a carbodiimide coupling reaction e.g. NHS-EDC, where the COOH group reacts with EDC to form an amine-reactive O-acylisourea intermediate. The nucleophilic amine group of an amino acid residue on the enzyme displaces the intermediate species, resulting in the formation of an amide linkage between the polymer and the enzyme [287]. The use of NHS-EDC reactions are favoured due to their mild, aqueous reaction condition and biocompatibility towards the bioreceptor, retaining the enzyme structure and activity [286]. Building on these principles, thiophene carboxylic acid derivatives can be pre-activated to simplify the fabrication of biosensor devices. It has been shown that pre-activation of carboxylic acid-containing monomers (e.g. T3AA, T3T3YAA) by an NHS-carbodiimide reaction generates stable thiophene N-succinimidyl esters that are capable of polymerisation [288, 289]. Therefore, it is proposed that copolymerisation of such monomers with 3-hexylthiophene may yield a polymer that is both solution-processable and capable of directly immobilising bioreceptors without the need for additional activation reactions [67].

Thiophene N-succinimidyl esters were generated from the corresponding thiophene carboxylic acid using N-hydroxysuccinimide (NHS) with Dicyclohexyl-carbodiimide (DCC) as a coupling agent. A general synthetic procedure has been outlined by Baüerle et al. and Kim et al. with a specific process for the synthesis of S3T3YA discussed by Clayton (2011) [67, 290, 291].

3.2.1 Synthesis of N-succinimidyl 3-thiophene acetate

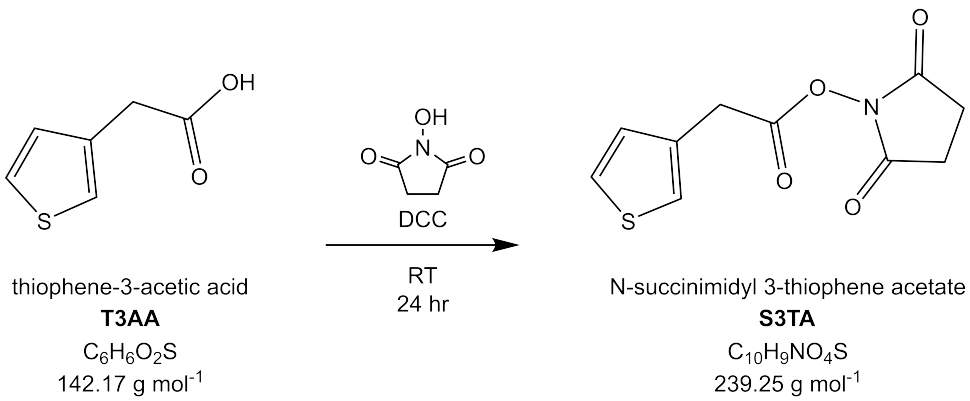

Figure 3.4: Synthesis of N-succinimidyl 3-thiophene acetate from T3AA.

As described in Figure 3.4, an equimolar ratio of T3AA (10 mmol, 142.17 g mol^{-1}), NHS (10 mmol, 115.09 g mol^{-1}) and DCC (10 mmol, 206.33 g mol^{-1}) was added to 90 mL of dry acetonitrile (CH_3CN) and stirred at room temperature for 24 hr. Filtering followed by removal of solvent via rotary evaporation yielded a dark, viscous oil. The crude compound was purified by column chromatography (silica, ethyl acetate/hexane [9:1] v/v). N-succinimidyl 3-thiophene acetate (1.7031 g, 239.25 g mol^{-1}, $C_{10}H_9NO_4S$) was isolated as an off-white solid. Yield 70.6%.

3.2.2 Synthesis of N-succinimidyl 3-(thiophen-3-yl)acrylate

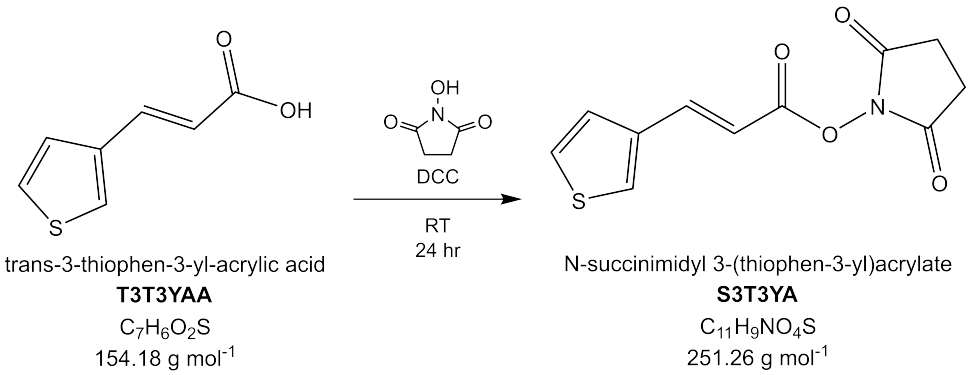

Figure 3.5: Synthesis of N-succinimidyl 3-(thiophen-3-yl)acrylate from T3T3YAA.

Synthesis of N-succinimidyl 3-(thiophen-3-yl)acrylate from T3T3YAA, NHS and DCC as outlined in Figure 3.5 followed an identical procedure to N-succinimidyl 3-thiophene acetate

described in 3.2.1. Purification by column chromatography, afforded N-succinimidyl 3-(thiophen-3-yl)acrylate as an off-white solid (2.1511 g, 251.26 g mol^{-1}, $C_{11}H_9NO_4S$). Yield 85.5%.

Characterisation of the synthesised monomers; M3TC, M3TA, M3T3YA, S3TA and S3T3YA is discussed in Chapter 4 - *Synthesis of Thiophene Copolymers for the Immobilisation of Biomolecules*.

3.3 Oxidative Polymerisation of Thiophene Monomers

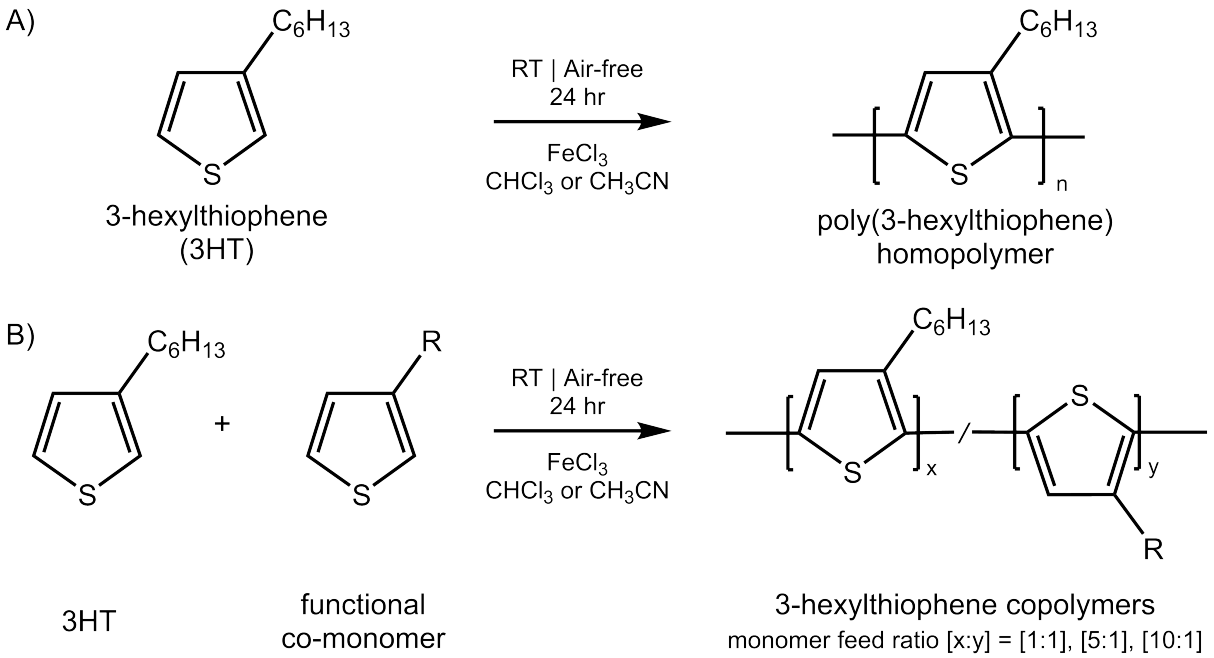

where R =
methyl 3-thiophene carboxylate : $-CO_2CH_3$
methyl 3-thiophene acetate : $-CH_2CO_2CH_3$
methy 3-(thiophen-3-yl)acrylate : $-CH{=}CHCO_2CH_3$
N-succinimidyl 3-thiophene acetate : $-CH_2CO_2N(CH_2CO)_2$
N-succinimidyl 3-(thiophen-3-yl)acrylate : $-CH{=}CHCO_2N(CH_2CO)_2$

Figure 3.6: Reaction scheme for the chemical oxidative polymerisation of thiophene monomers. A) Homopolymer synthesis, and B) Copolymer synthesis.

A chemical oxidative polymerisation reaction was utilised to produce the thiophene copolymers in this project. Likely due to its low cost, availability and ease of handling, iron(III) chloride ($FeCl_3$) is the most common oxidant choice in the literature, however as discussed in the original papers on the preparation of 3-alkylthiophenes by Yoshino and Sugimoto, other anhydrous oxidants e.g $MoCl_5$ and $RuCl_3$ can also be used [149, 217]. In this work,

$FeCl_3$ has been used exclusively in all polymerisation reactions.

At a variety of molar ratios, the majority monomer, 3-hexylthiophene, was polymerised in the presence of a 'functional' co-monomer, that is, a thiophene methyl ester ($R-CO_2CH_3$) or N-succinimidyl ester monomer ($R-CO_2N(CH_2CO)_2$). For homopolymer generation, thiophene (C_5H_4S) or 3-hexylthiophene ($C_{10}H_{16}S$) were used as purchased without additional purification and polymerised using the same oxidative process without the inclusion of a secondary monomer.

As shown in Figure 3.6, monomers were dissolved in ca. 15 mL of dry solvent (chloroform $CHCl_3$ or acetonitrile CH_3CN) and degassed by N_2 sparging. Using a four-fold molar equivalent, iron(III) chloride ($FeCl_3$) was dissolved in additional dry solvent (50 - 80 mL), then degassed by the freeze-pump-thaw (FPT) method. Under an inert N_2 environment with vigorous stirring, the monomer mixture was slowly added to the oxidant (dropwise, 1 - 2 hr controlled addition). The reaction mixture was continuously stirred for 24 hr at room temperature.

The polymer was precipitated when the reaction mixture was poured into a large excess of methanol (> 400 mL), gathered by vacuum filtration and washed repeatedly with CH_3OH and deionised H_2O. Further purification by CH_3OH Soxhlet extraction was performed to remove the remaining, residual $FeCl_3$ before drying under reduced pressure (24 - 74 hr, 35 °C).

3.4 Alkaline Hydrolysis of methyl ester copolymers

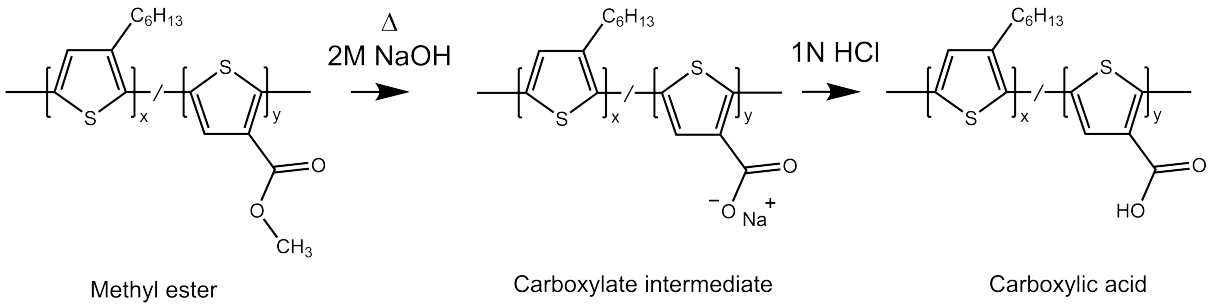

Figure 3.7: Reaction scheme overview for the hydrolysis of a thiophene methyl ester polymer (deprotection).

In order to obtain the appropriate enzyme binding groups, reformation of the carboxylic acid

groups from the methyl ester-protected polymers is required. As covalent immobilisation between the amine-containing residues on the enzyme and carboxylic acids in the polymer immobilisation matrix is targeted, this necessitates deprotection. The reaction scheme in Figure 3.7 shows that hydrolysis of the methyl ester ($R-CO_2CH_3$) under basic conditions affords a sodium carboxylate ($R-COO^{\ominus}Na^{\oplus}$) which upon acid workup gives the desired carboxylic acid ($R-COOH$). In this project, 100 - 200 mg of methyl ester copolymer was added to a five-fold excess of 2 M methanolic sodium hydroxide (NaOH(aq) in CH_3OH/H_2O [4:1]). Under stirring, the reaction mixture was refluxed for 24 hr. After cooling to room temperature, precipitation of the COOH-copolymer was achieved by the slow addition of 1 M hydrochloric acid (HCl) until the reaction mixture became acidic (<2 pH). Polymer products were collected via vacuum filtration, washed with 1 M HCl, deonised H_2O and CH_3OH before drying under reduced pressure (24 - 74 hr, 35 °C).

A select number of ester deprotection reactions were performed using a basic mixture of tetrahydrofuran (THF) and sodium hydroxide (C_4H_8O/4M NaOH(aq) [4:1] v/v). This was intended to better suspend the polymer in solution with the aim of making the ester more susceptible to hydrolysis.

3.5 Gel Permeation Chromatography

Gel Permeation Chromatography (GPC) allowed for the determination of polymer molecular weight (M_W) and polydispersity index (PDI). Approx. 3 mg of polymer was dissolved in 1 - 2 mL of inhibitor-free, HPLC-grade, tetrahydrofuran before filtering through a 0.2 μm PTFE membrane syringe filter. Using a Shimadzu LC-20AD SEC instrument calibrated against a narrow molecular weight polystyrene standard (eluent: HPLC-grade THF), the polymer samples were analysed using a default program for monomodal or bimodal distributions.

3.6 Deposition of Polymer Films

3.6.1 Polymer Spin-coating Solutions

After the synthesis of soluble materials, it became possible to conduct analysis by UV-Vis spectroscopy and to produce biosensor electrodes for glucose testing. The preparation of

particle-free polymer solutions required for spin-coating was therefore necessary. This was achieved by the dissolution of soluble solids in a chloroform/chlorobenzene solvent mixture ($CHCl_3$:C_6H_5Cl [8:2] v/v) to a concentration of 15 mg ml^{-1}.

To ensure complete dissolution, the polymer solutions were heated to 50 °C for 1 - 3 hrs, then maintained at 30 °C until use to prevent aggregation. Throughout the dissolution process, the solutions were continually stirred at high rpm.

3.6.2 Substrate Preparation

Various substrates were used in the project to meet different test requirements. Microscope slides (soda-lime glass) were utilised for basic solubility testing via drop-casting or spin-coating of solutions. Sapphire and Indium-Tin-Oxide (ITO)-glass substrates were employed for UV-VIS spectroscopy and enzyme immobilisation testing, respectively. Flexible biosensor electrodes were fabricated by evaporating 99.99% gold onto plastic substrates before deposition of a thin polymer (∼100 nm) film.

Transparent Substrates: ITO-glass, single crystal sapphire (AL_2O_3) and glass substrates were subjected to following cleaning regime prior to use;

1. Sonication in hot solution of detergent e.g. Alconox® (60 °C, 5 min),
2. Sonication in deionised water (5 min),
3. Sonication in ethanol (25 °C 5 min),
4. Sonication in acetone (25 °C, 5 min),
5. Sonication in isopropanol (25 °C, 5 min),
6. UV-Ozone treatment (25 °C, 10 min).

NB: sonicator operating power = 300 W, frequency = 32 - 38 kHz.

Gold on Polyethylene terephthalate (PET): Gold electrodes were prepared in-house to allow for customisation and optimisation of the spin-coating process. The gold layer was deposited onto laser-cut PET substrates (30 x 30 x 0.125 mm, DuPont Teijin Films™ Melinex®) via vacuum thermal evaporation (2×10^{-4} mbar, 0.5 nm s^{-1}, 99.99% purity). The thickness of the gold layer was 75 nm as monitored by quartz crystal microbalance (QCM).

3.6.3 Film Deposition

Polymer thin-films were deposited via spin-coating using a Laurell WS-650SZ-6NPP/LITE coater. 150 - 300 μL of polymer solution was dynamically dispensed at 1500 rpm (30 s spin duration) onto the substrate surface. A post-deposition anneal was performed on all films to allow for complete evaporation of the carrier solvent and improved substrate adhesion.

For ITO or sapphire, a 15 min, 120 °C anneal was performed and for Au on PET, a 15 min, 90 °C anneal was employed with the reduced anneal temperature due to limited thermal stability of plastic substrates [256]. All polymer films were stored in a low-moisture, dark store until use (ca. 13% Relative Humidity).

3.7 Enzyme Immobilisation

A common N-hydroxysuccinimide-carbodiimide (NHS-EDC) coupling pathway was employed to immobilise the enzyme bioreceptor to the electrode via covalent attachment to the conductive polymer support [286, 292–294]. Thin films of carboxylic acid-functionalised polymer were deposited onto ITO or gold substrates and immersed in a 0.01 M phosphate-buffered saline[4] (PBS) solution with 60 mmol N-hydroxysuccinimide (NHS) and 30 mmol 1-ethyl-3-(3-dimethylaminopropyl) carbodiimide (EDC). After 3 hr of gentle agitation on a shaker, the activated films were exposed to a 5 mg ml^{-1} glucose oxidase (GOx) enzyme solution in PBS, for 6 hr to allow for the immobilisation.

For N-succinimidyl ester-functionalised polymers, films were exposed to the enzyme solution only (6 hr, GOx in 0.01 M PBS, 5 mg ml^{-1}). Following the enzyme exposure step, the films were rinsed with PBS and then stored in PBS at 4 °C until use. All enzyme immobilisation reactions were performed at room temperature with PBS (pH 7.3 - 7.7).

Notes

[4]Phosphate-buffered saline is a isotonic buffer consisting of 137 mM NaCl, 2.7 mM KCl, 10 mM Na_2HPO_4 and 1.76 mM KH_2PO_4

3.8 UV-Vis Spectroscopy

Ultraviolet-visible (UV-Vis) spectroscopy is a useful tool for the development of conductive polymers and enzymatic biosensor devices. It efficiently probes strong ultraviolet (∼100 - 400 nm) and visible (∼400 - 800 nm) absorptions, providing valuable insights into the electronic structure and conjugation length of conjugated polymers through analysis of $\pi - \pi^*$ transitions as well as the confirmation of enzyme immobilisation via assays.

UV-Vis was performed using an Agilent Cary 5000 UV-Vis-NIR Spectrophotometer. During the project, two operational modes were utilised for the collection of spectral information. Firstly, using a fixed wavelength kinetic mode, spectrophotometric (colorimetric) assays were measured (fixed wavelength, absorbance vs time) to determine the successful immobilisation of glucose oxidase. Absorption spectroscopy (absorbance vs wavelength) was also performed to analyse the synthesised polymer materials.

3.8.1 UV-Vis absorption spectroscopy

Absorption spectra were obtained for polymer films deposited on sapphire substrates by scanning wavelengths from 800 to 200 nm using the instrument's default 'scan' method. Additionally, a zero baseline correction was performed prior to each measurement using a clean substrate (100% Transmission) and beam block (0% Transmission).

3.8.2 Spectrophotometric Assay

As described in *Methods of Enzymatic Analysis* by H. Bergmeyer, the activity of GOx can be determined using a spectrophotometric assay [295]. Utilising an o-dianisidine/peroxidase/glucose assay system, the increase in absorbance at 470 nm is monitored. The reaction scheme in Figure 3.8 illustrates that upon addition of glucose oxidase to the system, the generation of H_2O_2 and subsequent oxidation of the colourless o-dianisidine ($C_{14}H_{16}N_2O_2$) results in the formation of an oxidised orange-brown chromophore. The UV-Vis spectrophotometer is operated at a fixed wavelength of 470 nm with the absorbance measured against time (min).

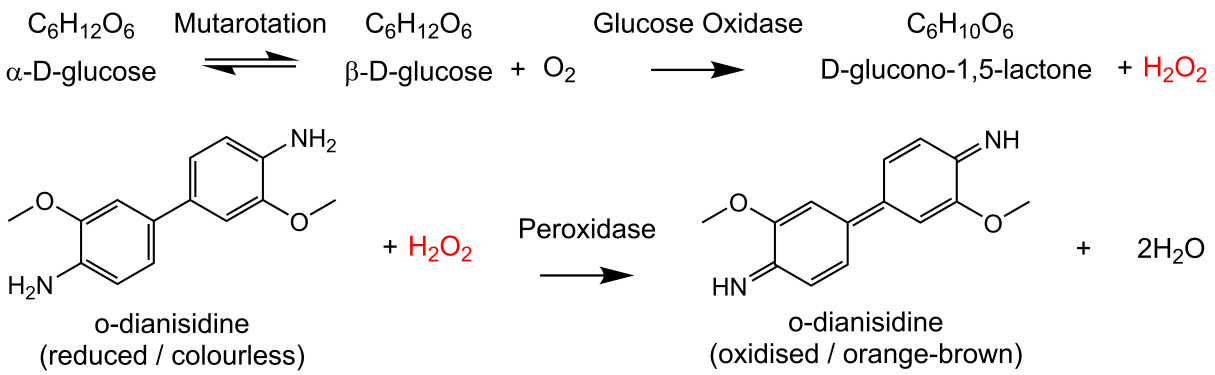

Figure 3.8: Spectrophotometric assay for the detection of glucose oxidase.

Assay system:

2.5 mL of 0.083 % w/v o-dianisidine in deionised H_2O (oxygenated), 0.3 mL of 18 % w/v d-glucose in 0.01 M PBS, 0.1 mL of 0.02 % w/v horseradish peroxidase (HRP), and 0.3 mL 0.05 % w/v glucose oxidase (GOx) in 0.01 M PBS (assay reference) or enzyme-immobilised polymer film (10 min exposure to assay system).

3.9 Infrared Spectroscopy (ATR-FTIR)

Attenuated total reflectance - fourier transform infrared spectroscopy (ATR-FTIR) was utilised extensively for the analysis of both purchased and synthesised monomers, as well as polymer materials. In absorbance mode, spectra were recorded using a Varian Excalibur FTS 3500 FT-IR or Shimadzu IRSpirit (Range: 3750 - 600 cm^{-1}, Scans: 64). Both instruments were equipped with a diamond single-reflection ATR-FTIR attachment. Characteristic vibrations within the spectra of synthesised materials were compared to known values and spectra from commercial and literature sources to allow for accurate assignment. [38, 226, 284, 296–306].

3.10 Nuclear Magnetic Resonance Spectroscopy (NMR)

Proton ^1H NMR spectroscopy was performed on synthesised monomers and polymers to allow for further confirmation of chemical structure. NMR spectra were collected using either a 60, 400 or 500 MHz NMR spectrometer with ppm values (δ) referenced against $CDCl_3$ or a tetramethylsilane (TMS) standard. Polymer solids were dissolved in deuterated chloroform ($CDCl_3$) before filtering into a 5 mm thin wall NMR tube through a KimTech

tissue to remove any undissolved particles. All NMR data in this project was analysed using Mestrelab MNova.

3.11 Electrochemical Testing

With reference to Chapter 7 - *Glucose Biosensor Electrodes: Fabrication, Immobilisation and Analysis*, electrochemical testing of glucose biosensor electrodes was performed to probe the effectiveness and performance of the synthesised polymer materials as enzyme-immobilisation agents. For amperometric biosensors, two electrochemical testing methods were employed to analyse fabricated devices.

Using a three-electrode electrochemical cell, cyclic voltammetry (CV) and constant potential chronoamperometry (CA) were performed to determine the electrochemical devices behaviour and response to glucose. Electrochemical testing was performed in a 50 mL vessel containing 30 mL of degassed 0.01 M PBS solution + 0.05 M potassium chloride (KCl) as an additional electrolyte. A typical electrode setup of a $Ag_{(s)}|AgCl_{(s)}|KCl_{(sat)}$ reference electrode, a platinum wire counter electrode and a PET/Au/Polymer/GOx working electrode was utilised throughout the project.

3.11.1 Cyclic Voltammetry

All CV measurements were performed using an Ossila T2006A1 potentiostat. Voltammograms at scan rates of 50, 100, 150 and 200 mV s^{-1} were gathered, commencing in an anodic direction between a potential range of approx. -1.5 to +1.0 V (start: -1.5 V). Before each CV experiment, the integrity of potentiostat equipment was verified using a test device supplied by Ossila.

3.11.2 Chronoamperometry

An electrochemical testing setup comprised of a Keithley2400 Source Measure Unit (SMU) and three-electrode cell was used for the assessment of amperometric response to glucose following fabrication of biosensor devices described above. The 2400 SMU is capable of sourcing a constant potential while simultaneously measuring current to a high degree of

accuracy (Source accuracy: 0.02% + 600 μV, Current measurement accuracy: 0.027% + 60 nA) allowing for determination of device performance. The current response resulting from the addition of β-D-glucose was measured at a constant potential of 0.7 V over a 6 min period. A 1 mM β-D-glucose aliquot was dispensed into the PBS saline electrolyte solution every 15 s, accounting for the stabilisation of the current signal.

For each polymer, 2 sets of 3 sensing electrodes were fabricated and analysed by amperometry. A 'daily' set of electrodes was tested 3 times over 48 hr (hours 0, 24 and 48), while the 'weekly' set was tested every 7 days over a period of 21 days (days 0, 7, 14 and 21). This testing regime allowed for the determination of linear response, response time, device reproducibility and reusability (RSD/CV%). The amperometric response to urea (0.3 M) was examined to analyse the selectivity of select polymer-enzyme sensors.

Chapter 4
Synthesis of Thiophene Copolymers for the Immobilisation of Biomolecules

This chapter outlines the synthesis of 3-hexylthiophene-based copolymers, as well as the analysis of synthesised monomers and polymer materials by a range of molecular spectroscopy techniques.

In the following work, the primary motivation centres on the production of soluble polymers designed to possess specific chemical and physical properties. At a minimum, the material must meet the following criteria;

1. Soluble in solvents typically used in solution deposition processes, e.g. chloroform ($CHCl_3$), chlorobenzene (C_6H_5Cl).
2. Suitable for deposition of thin films by solution processing methods, e.g. spin-coating.
3. Capable of immobilising enzymes through covalent binding.
4. Electrically conductive.
5. Capable of gram-scale production by a facile and low-cost synthetic chemistry approach.

Thiophene polymers and their derivatives are well-studied with the general prerequisite properties; that is, they are known to be intrinsically conductive materials with many established synthetic pathways. As such, polythiophenes possess a clear capacity for the production of materials that are soluble and possess the functionalities to bond to a bioreceptor. As outlined in Figure 3.6, all polymers outlined in this forthcoming chapter were prepared via chemical oxidative polymerisation employing iron(III) chloride ($FeCl_3$) as the oxidant. Anhydrous $FeCl_3$ can be purchased in large quantities at a low cost ($1\,kg \approx £30$). Given the polymerisation reaction proceeds at room temperature in a limited volume of common solvent (chloroform or acetonitrile), this class of polymerisation makes for a simple and 'cheap' method when preparing 3-hexylthiophene copolymers and despite challenges, the organic synthesis methods are the most suitable for gram-scale production when compared to electrochemical approaches [86, 307].

The solubility of the proposed copolymer materials in solvents such as chloroform and chlorobenzene is crucial to achieving the goals of this project. These solvents are particularly well-suited for solution-processing methods, such as spin-coating and printing techniques, e.g. gravure. Chloroform, in particular, is used extensively when preparing solutions and inks containing soluble conductive polymers due to its desirable properties relevant to solution deposition. For example, a low boiling point (61°C) facilitates the formation of uniform thin films, allowing for a quick removal of the solvent post-deposition while the miscibility of such solvents enables the creation of multi-solvent systems which are often required for the optimisation of process conditions and film quality.

4.1 Poly(3-hexylthiophene)

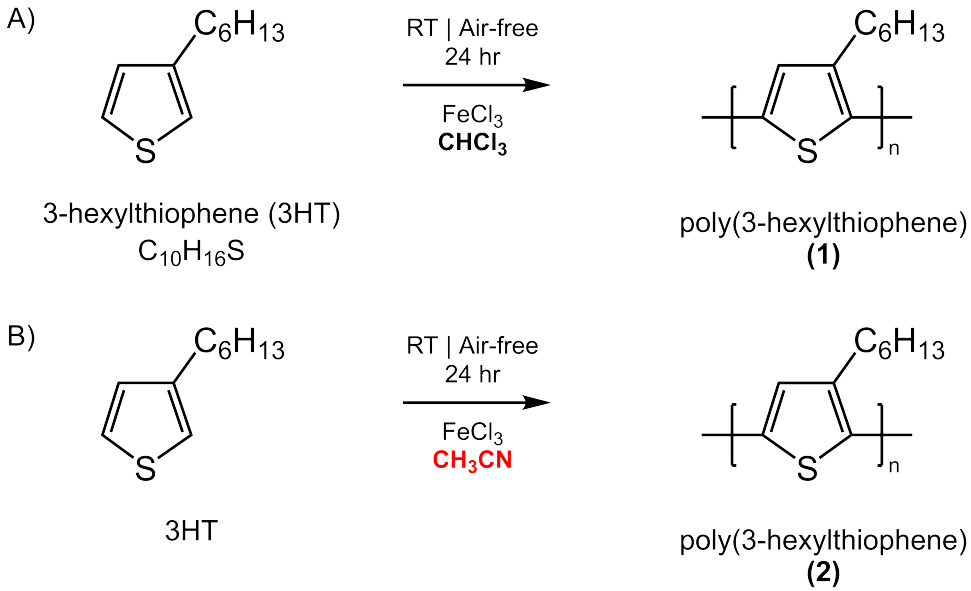

Figure 4.1: Reaction scheme for poly(3-hexylthiophene) synthesised in reaction solvent A) chloroform **(1)** and B) acetonitrile **(2)**.

Prior to the investigation of novel materials, poly(3-hexylthiophene) was prepared to test the condition of available equipment, mainly the vacuum-gas manifold, the quality of purchased $FeCl_3$ oxidant and to aid in determining which solvent ($CHCl_3$ or CH_3CN) is most suitable for the synthetic route.

Figure 4.2: Image of poly(3-hexylthiophene) **(2)** solids.

Following the reaction scheme in Figure 4.1, poly(3-hexylthiophene) **(1)** and **(2)** were produced by the chemical oxidative polymerisation of 3-hexylthiophene in $CHCl_3$ and CH_3CN, respectively. As shown by the photographed example in Figure 4.2, the products of both reactions were collected as dark red-brown solids.

Consistent with similar homopolymerisation reactions using unsubstituted thiophene (see Appendix B, Figures B.1 & B.2 for the IR spectra of polythiophene), the polymerisation reaction of 3HT in $CHCl_3$ **(1)** yielded a higher quantity of product at ca. 70% while the percentage yield for P3HT from CH_3CN **(2)** was lower at 43%. Expectedly, both of the synthesised P3HT were soluble in chloroform and chlorobenzene at 20 mg ml^{-1}, however at this concentration, P3HT **(2)** gave a dark-orange solution that was particle free, while P3HT **(1)** gave a turbid/cloudy orange solution with undissolved solids still present despite extended heating and vigorous stirring. The difference in solubility behaviour between P3HT **(1)** and **(2)** may be due to variations in polymer molecular weight (M_W) and the degree of doping/oxidation of the polymer, which arise from the use of different reaction solvents. Moreover, the variation in $FeCl_3$ solubility for $CHCl_3$ and CH_3CN likely contributes considerably. The oxidant is only partially dissolved in the $CHCl_3$ yet fully dissolved in CH_3CN, as such the polymerisation reactions in the two solvents will proceed at different rates and to varying extents [308].

The partial solubility of P3HT **(1)** suggests that polymerisation reactions performed in $CHCl_3$ produce a high M_W polymer, as well as a higher yield, with a greater proportion of oxidised

P3HT species that exhibit more double bond character along the backbone. In contrast, the reaction in CH_3CN produces a lower-yielding product with a lower molecular weight. Under the assumption the P3HT synthesised in this project is of reasonable purity and quality, the relationship between M_W and solubility aligns with commonly accepted knowledge in the literature and helps to explain the observed trends [309, 310].

It is possible a distribution of molecular weights were present in the crude polymer **(1)** as a soluble component was collected following Soxhlet extraction with boiling $CHCl_3$. Removal of the solvent from extract via simple evaporation yielded a fully-soluble component of **(1)** that could be used in film deposition and for further analysis. The total yield of processed and soluble P3HT **(1)** was 36.6%, that is, approximately half of the crude product was soluble.

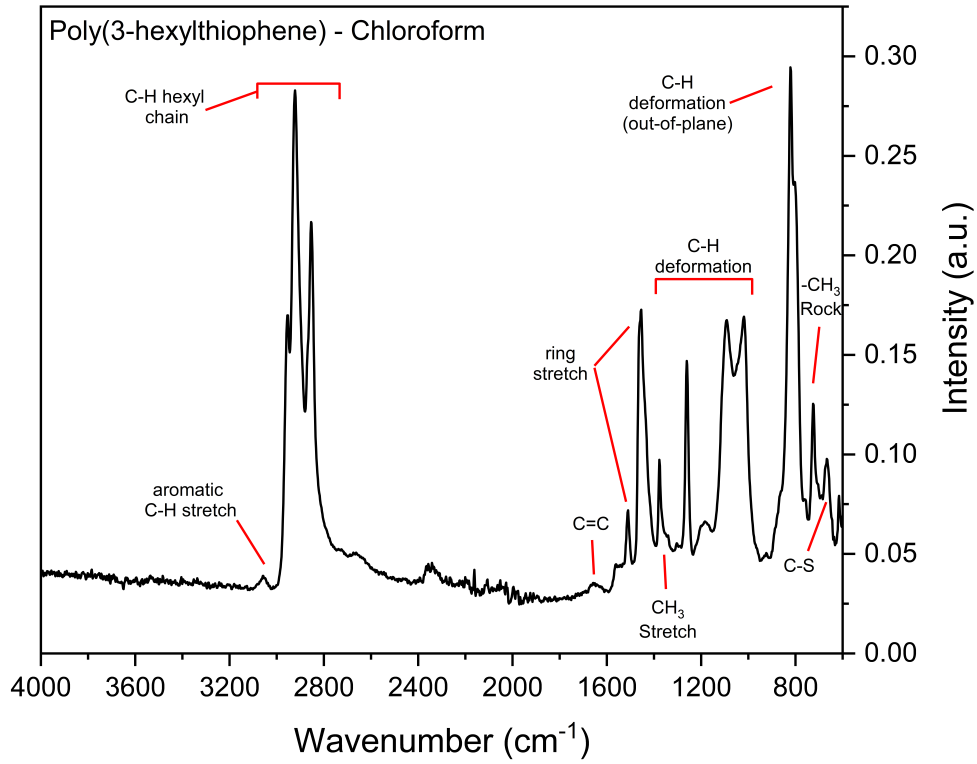

Figure 4.3: IR spectrum of Poly(3-hexylthiophene) (P3HT) from $CHCl_3$**(1)**.

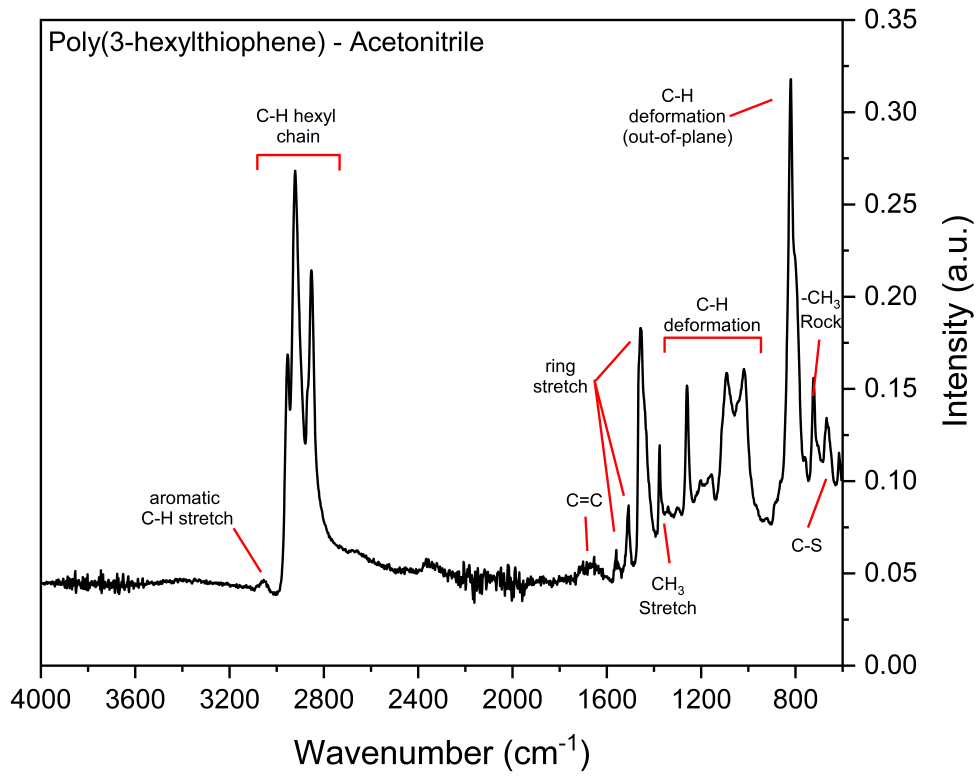

Figure 4.4: IR spectrum of Poly(3-hexylthiophene) (P3HT) from CH_3CN **(2)**.

Characterisation of synthesised P3HT **(1)** and **(2)** was achieved by ATR-FTIR and ^{1}H NMR. The typical characteristic vibrations of P3HT were presented in both IR spectra (Figures 4.3 and 4.4). The small peak at ∼3060 cm^{-1} corresponds to the aromatic C−H stretch from the lone ring-bound hydrogen while the distinctive, three sharp peaks at 2953, 2922 and 2855 cm^{-1} are indicative of the aliphatic C−H stretches from the hexyl ($-C_6H_{13}$) chain. The ring stretching peaks between 1510 and 1450 cm^{-1} are present, while the sharp peak located at 1377 cm^{-1} represents a methyl ($-CH_3$) umbrella vibrational mode at the end of the $-C_6H_{13}$ chain. Within the fingerprint region, a C−H out-of-plane bending deformation is seen at ∼820 cm^{-1}, a methyl ($-CH_3$) rock is located at 725 cm^{-1} and C−S vibration at ∼670 cm^{-1} can also be observed.

^{1}H NMR of P3HT **(1)** and **(2)** allowed for further classification of the chemical structure, structural connectivity and quantification of the regioregularity (RR) via comparison of the peak integrals from the methylene ($-CH_2-$) group directly attached to the thiophene ring (2.80 / 2.40 ppm).

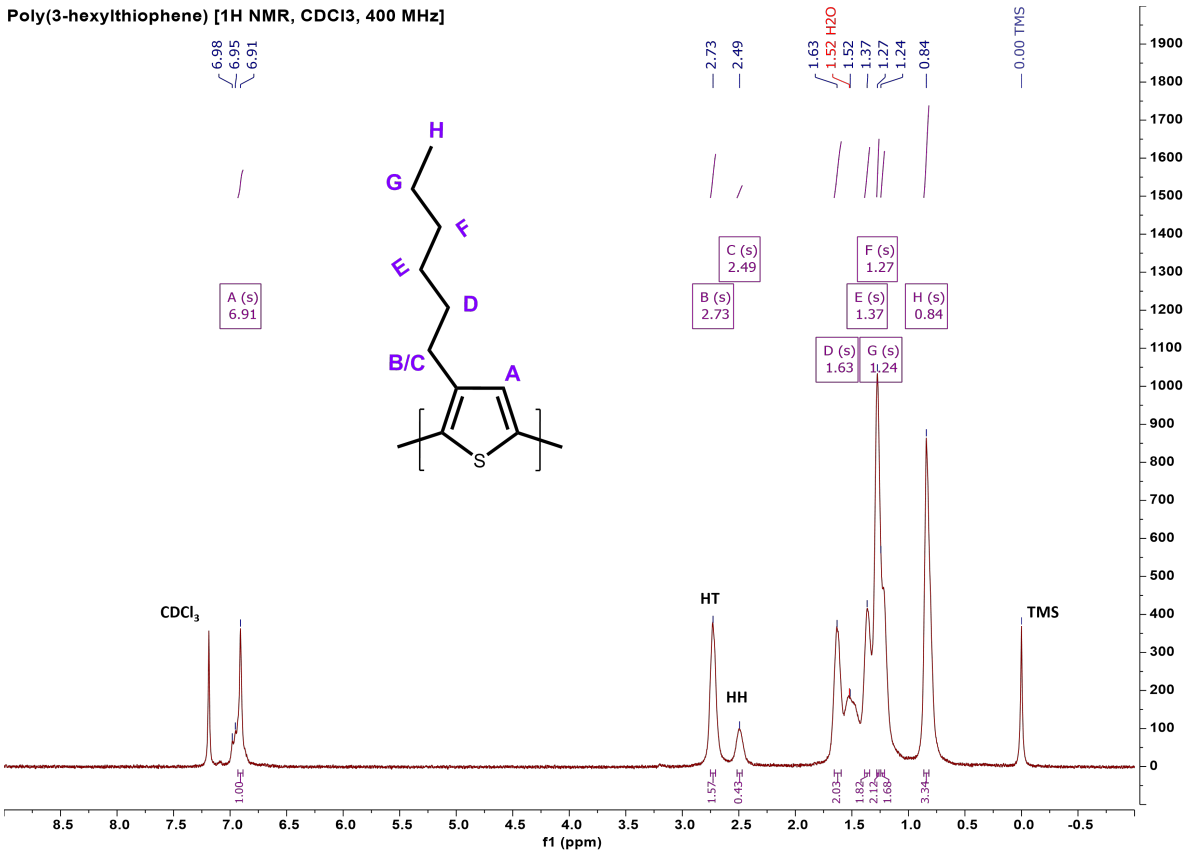

Figure 4.5: ^{1}H NMR spectrum of P3HT from $CHCl_3$ **(1)**.

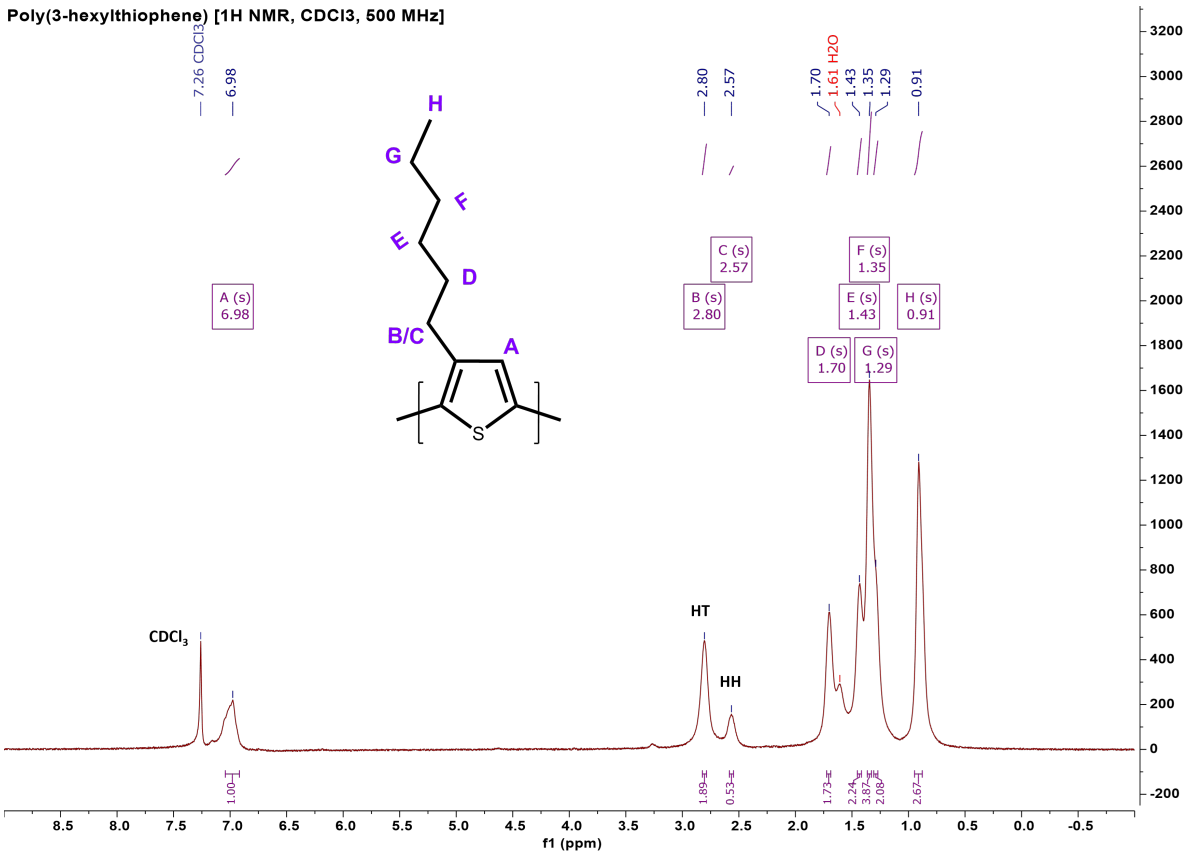

Figure 4.6: ^{1}H NMR spectrum of P3HT from CH_3CN **(2)**.

The combination of IR and ^{1}H NMR spectra provides evidence that 3-hexylthiophene polymers can be prepared with the available equipment and that the synthesised P3HT possesses the expected characteristics and structure. Analysis of the NMR spectra in Figures 4.5 and 4.6 indicates the synthesis P3HT matches the literature [311, 312], giving the expected chemical shift values: P3HT **(1)** - ^{1}H NMR (400 MHz, CDCl3) δ 6.98-6.91 (s, 1H), 2.73 (s, 2H), 2.49 (s, 0H), 1.63 (s, 2H), 1.37 (s, 2H), 1.27 (s, 2H), 1.24 (s, 2H), 0.84 (s, 3H).
P3HT **(2)** - ^{1}H NMR (500 MHz, CDCl3) δ 6.98 (s, 1H), 2.80 (s, 2H), 2.57 (s, 1H), 1.70 (s, 2H), 1.43 (s, 2H), 1.35 (s, 4H), 1.29 (s, 2H), 0.91 (s, 3H).

As shown by the annotated chemical structures in Figures 4.5 and 4.6, the peaks at 6.98-6.91 ppm (A) represent the aromatic hydrogen of the thiophene ring (integral values referenced to this proton). The two peaks located between 2.8 and 2.40 ppm (B/C) arise from the deshielded hydrogens close to an aromatic centre. The methylene ($-CH_2-$) groups of the hexyl chain can be assigned to the cluster of peaks between 1.70 to 1.20 ppm (D to G) and finally, the terminal methyl protons ($-CH_3$) give the sharp singlet located at 0.91/0.84 ppm (H). By comparing the ratio of peak integral for the deshielded chain protons (B/C), the regioregularity of P3HT **(1)** was calculated as 78.5 % Head-Tail to 21.5 % Head-Head and for P3HT **(2)** it was determined to be 78.1 % HT and 21.9 % HH. Therefore, polymers **(1)** and **(2)** are largely regiorandom, but possess RR% values that match P3HT preparations found in the literature that have been synthesised using the same chemical oxidative polymerisation method [311, 313, 314].

Overall, ATR-FTIR and ^{1}H NMR of reaction products **(1)** and **(2)** confirms the successful chemical oxidative polymerisation of P3HT at quality comparable to that synthesised in the literature. While these materials are not new and represent a reproduction from the literature, collection of spectroscopic data will enable comparative analysis between the synthesised P3HT homopolymers and novel copolymer materials presented in this chapter. Further characterisation of P3HT **(1)** and **(2)** by UV-Vis spectroscopy is discussed later in Section 4.4.

4.2 Synthesis of 3-hexylthiophene Copolymers

This section will focus on the preparation of functionalised thiophene monomers, the synthesis of 3-hexylthiophene copolymers by chemical oxidative polymerisation, and the characterisation of synthesised materials using molecular spectroscopy techniques. All copolymers explored in this section use 3-hexylthiophene (3HT) as the principle monomer, i.e. in excess or equal quantity relative to the functional monomer component. Initially, a selection of copolymer reproduced from the literature are presented. This is followed in later Section 4.3.2 with novel materials that have not been previously synthesised.

4.2.1 Poly(3-hexylthiophene-*co*-methyl 3-thiophene carboxylate)

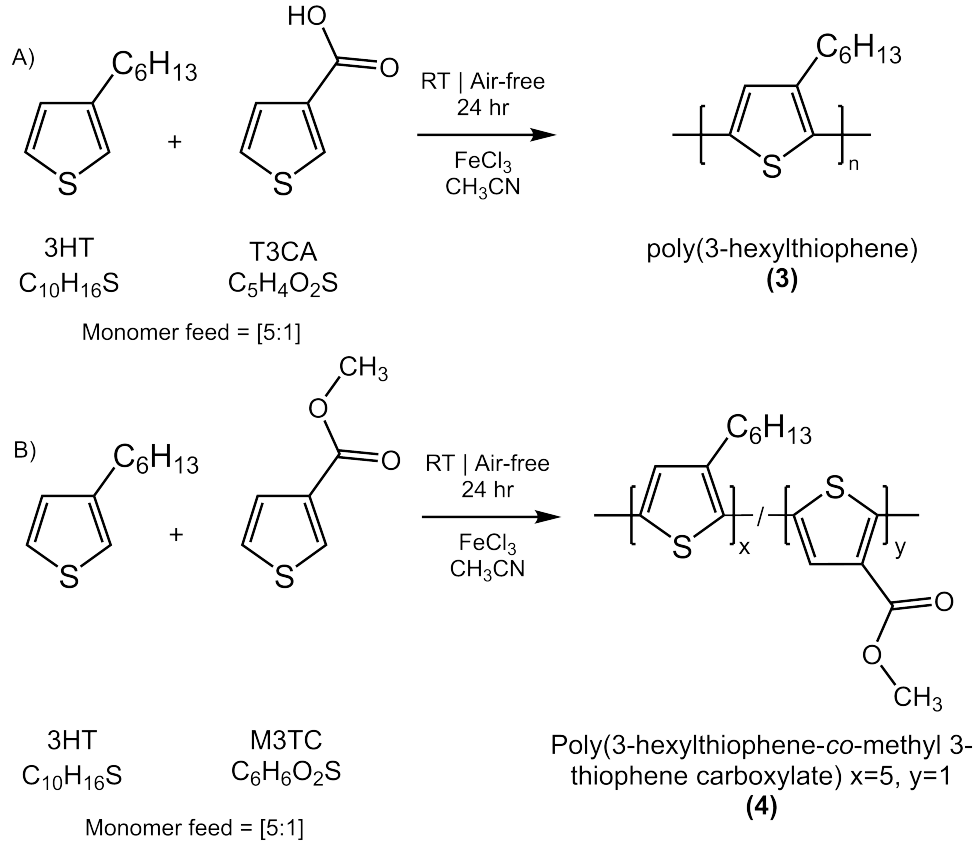

Figure 4.7: Reaction scheme for polymerisation of A) 3HT + T3CA yielding P3HT **(3)**, and B) 3HT + M3TC yielding P(3HT-*c*-M3TC) **(4)**.

Incorporating a carboxylic acid functionalisation onto the polymer backbone provides a simple yet effective approach to enable the immobilisation of biomolecules. By synthesising materials to include R−COOH moieties, appropriate binding sites for covalent immobilisation become available. This subsequently allows for the formation of amide linkages between

the (R−COOH) of the polymer and amine-containing residues (R−NH_2) of an enzyme via carbodiimide coupling chemistry. Considering COOH-functionalised thiophene polymers, thiophene-3-carboxylic acid (T3CA) is the smallest, most simple acid available and was the first comonomer explored. In this instance, the choice of T3CA relates to i) a desire to repeat procedures and methods found in the literature, for example, in He et al. where 3HT and T3CA are directly copolymerised without modification [315], and ii) there are no examples outlining use of P(3HT-*c*-T3CA) for enzyme immobilisation and biosensing applications in the literature at present.

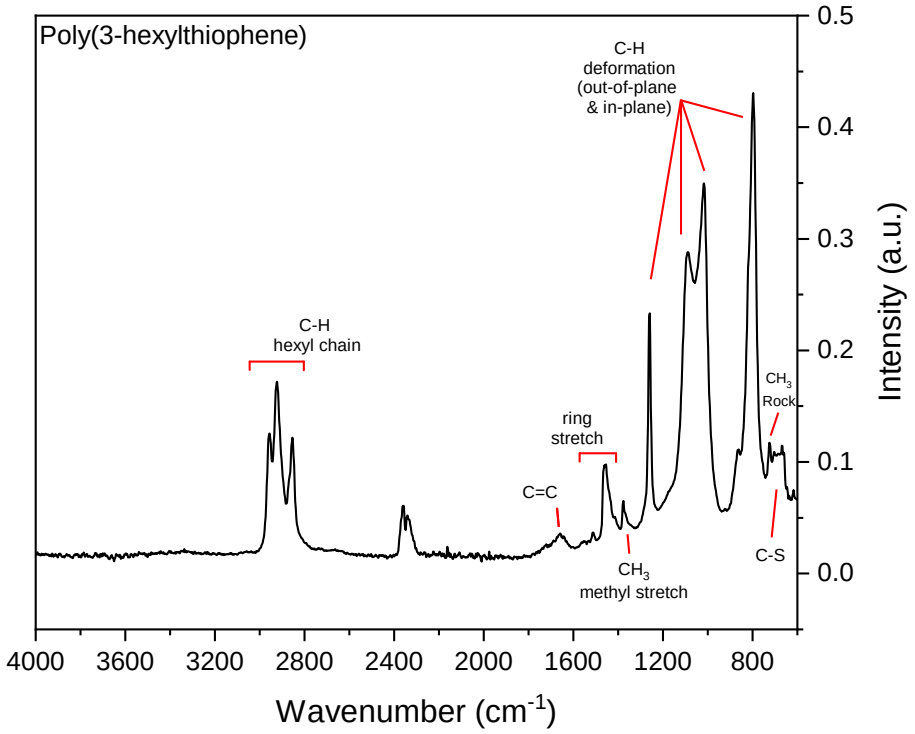

Figure 4.8: IR spectrum of P3HT **(3)** - failed copolymerisation of 3HT and T3CA.

In order to establish that protection of the carboxylic acid is required, a polymerisation reaction between 3HT and T3CA was attempted. Analysis of Figure 4.8 shows the reaction product polymer **(3)**; the compound obtained in the polymerisation between as-purchased 3HT and T3CA, was a P3HT homopolymer. The IR spectrum matches with that in Figures 4.3 and 4.4 while missing the expected broad peak of an O−H stretch between 3500 - 2500 cm^{-1} and a sharp carbonyl stretch C=O located around ca. 1700 cm^{-1} which would arise due to the presence of T3CA monomers. The double peak at 2350 cm^{-1} is due to the asymmetric stretch of CO_2 in the atmosphere, it is not part of the polymer structure and can be observed in many of the ATR-FTIR spectra collected during this project.

The synthesis of P3HT during this attempted copolymerisation contrasts with the result presented by He et al., who show direct oxidative polymerisation of 3HT and T3CA [315]. Questions can be raised about the IR analysis in the article that, in part, leads to the characterisation of P(3HT-*c*-T3CA), for example, assignment of a sharp R−OH stretch more commonly associated with aliphatic alcohols to the carboxylic acid. The ambiguity surrounding the formation of P(3HT-*c*-T3CA) in the study could be clarified by ^{13}C NMR spectroscopy as the carbon of the carboxylic acid would present at 160 - 180 ppm due to strong deshielding however this has not been carried out by the authors. The inability to directly copolymerise the carboxylic acid, highlights the requirement to protect the acid group and as described in Section 3.1.1, this was achieved by conversion of the carboxylic acid (R−COOH) into a methyl ester (R−COOCH$_3$) via Fischer esterification. Successful conversion of the acid to a methyl ester is outlined by IR spectroscopy in Figure 4.9 where complete loss of the O−H stretch and strengthening of the C=O to a higher wavenumber is observed.

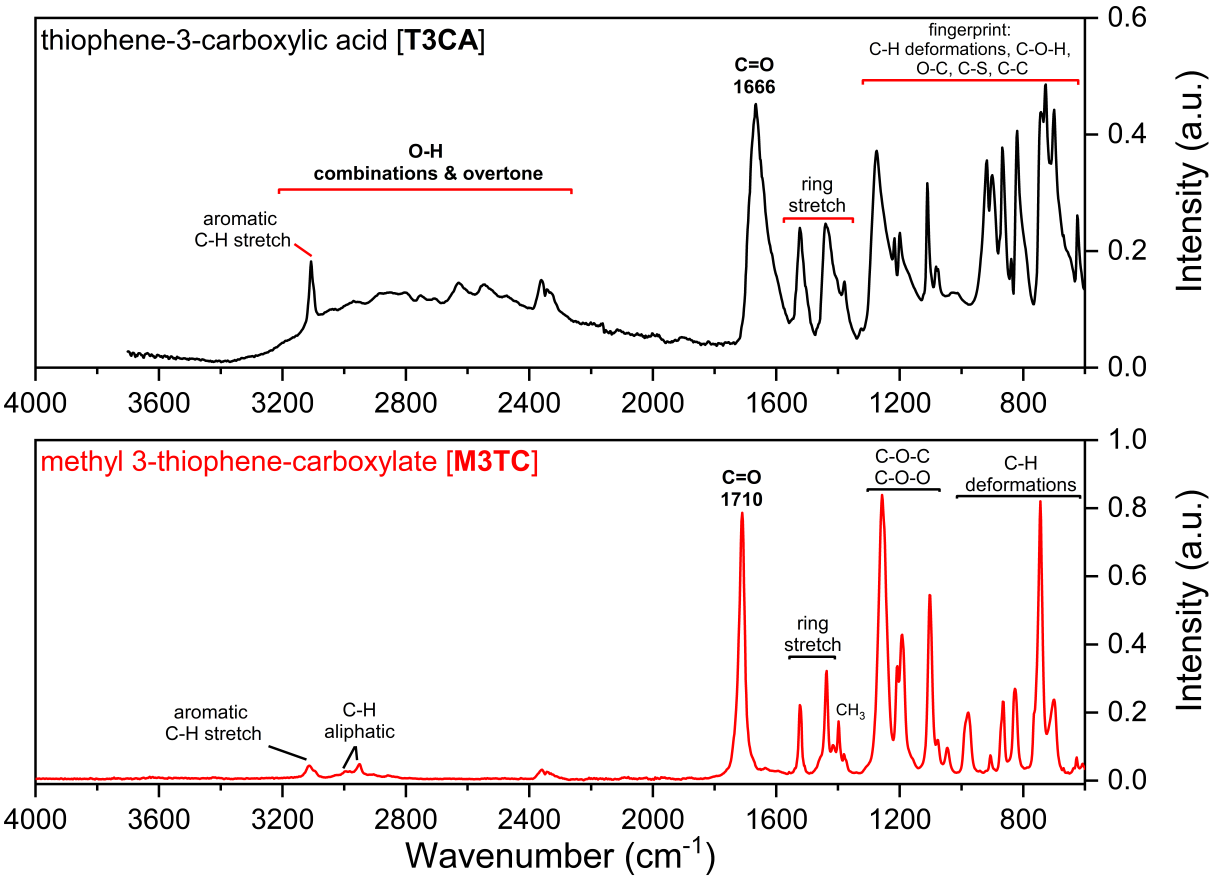

Figure 4.9: IR spectra of thiophene-3-carboxylic acid and synthesised methyl 3-thiophene carboxylate monomers.

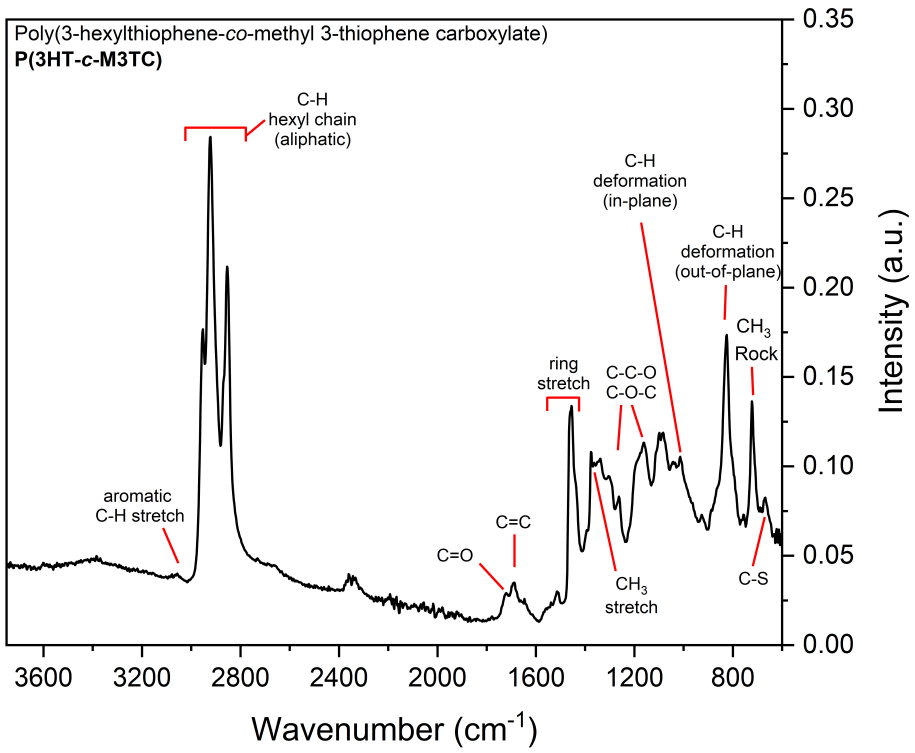

Figure 4.10: IR spectrum of P(3HT-*c*-M3TC) **(4)**.

Represented in the reaction scheme (Figure 4.7), 3HT and M3TC in a [5:1] monomer feed ratio was successfully copolymerised, yielding **(4)**: poly(3-hexylthiophene-*co*-methyl 3-thiophene carboxylate) - P(3HT-*c*-M3TC) as a dark solid (19%). Although weak, ATR-FTIR of polymer **(4)** in Figure 4.10 shows a C=O stretch at 1720 cm^{-1} as well as increased complexity in the fingerprint region arising due to the presence of ester vibrations of C−O−C and C−C−O from the M3TC monomer. Compared to P3HT IR spectra in Figures 4.3, 4.4 and 4.8, the differences in the spectral makeup paired with the presence of characteristic vibrations for the aliphatic C−H of 3HT and those from the methyl ester suggests copolymer formation.

P(3HT-*c*-M3TC) **(4)** exhibited minimal solubility in common spin coating solvents, e.g. chloroform, chlorobenzene, and THF. This was observed despite the synthesis i) being performed in acetonitrile, which had yielded highly soluble P3HT homopolymers (**(2)** and **(3)**) and ii) using a monomer feed ratio of [5:1], thus favouring the soluble majority monomer 3-hexylthiophene.

One of the primary objectives of this project is to produce soluble polymers to enable solution processing and mass fabrication of sensor devices. Given that methyl 3-thiophene

carboxylic acid possesses a rigid structure, it is likely that the structure of M3TC within the polymeric chain contributes to the lack of solubility. Moreover, once the ester is deprotected by hydrolysis, reformation of the carboxylic acid will likely reduce solubility further due to the presences of carboxylic acid groups capable of forming strong interchain hydrogen bonds. In P(3HT-*c*-M3TC), the π-interactions may hinder solvation and dissolution, leading to insolubility.

As the polymer was insoluble, it was decided to cease further work on T3CA/M3TC due to these proposed structural limitations. This brings about a clear reason as to why a large proportion of the literature for COOH-containing thiophene polymers focuses on electropolymerisation, as the need for processing and deposition of the polymer onto an electrode is avoided.

4.3 Thiophene Polymerisation in Chloroform ($CHCl_3$)

The following work describes polymer materials synthesised in chloroform ($CHCl_3$) exclusively. At the time of this work, the rationale for using $CHCl_3$ over CH_3CN was to push for the production of low-cost, gram-scale quantities of product by exploiting the higher-yielding reaction in $CHCl_3$. Additionally, the use of $CHCl_3$ will aid comparison to the literature, as it is the most common reaction solvent used in $FeCl_3$ chemical oxidative polymerisation of Poly(thiophene) (PTh), Poly(3-hexylthiophene) (P3HT), etc.

4.3.1 Poly(3-hexylthiophene-*co*-thiophene-3-acetic acid)

Thiophene-3-acetic acid (T3AA) represents the next logical monomer to explore, possessing one additional methylene ($-CH_2-$) group when compared to T3CA. The extra carbon spacer can increase the flexibility of the acid pendant group, reducing the π-stacking interactions, and may improve the solubility characteristics. Furthermore, as outlined by Lai et al. a copolymer of 3HT and T3AA can be produced using chemical polymerisations methods to yield a chloroform-soluble material [38]. In general, copolymers of T3AA are more present in the literature [38, 226, 316, 317], however the studies are overwhelmingly focused on electrochemical polymerisation, are limited in terms of chemical copolymerisation with 3HT and application to biosensing. Given the previous synthesis of this particular polymer via

both chemical and electrochemical polymerisation methods, the work outlined in the thesis is a reproduction from the literature and serves the purpose of generating a useful material with a set of known properties i.e., it is a soluble, 3-hexylthiophene copolymer with application for enzyme immobilisation [38]. As such, the production of P(3HT-*c*-T3AA) will enable comparison and assist with the characterisation of the novel polymers described later in this chapter.

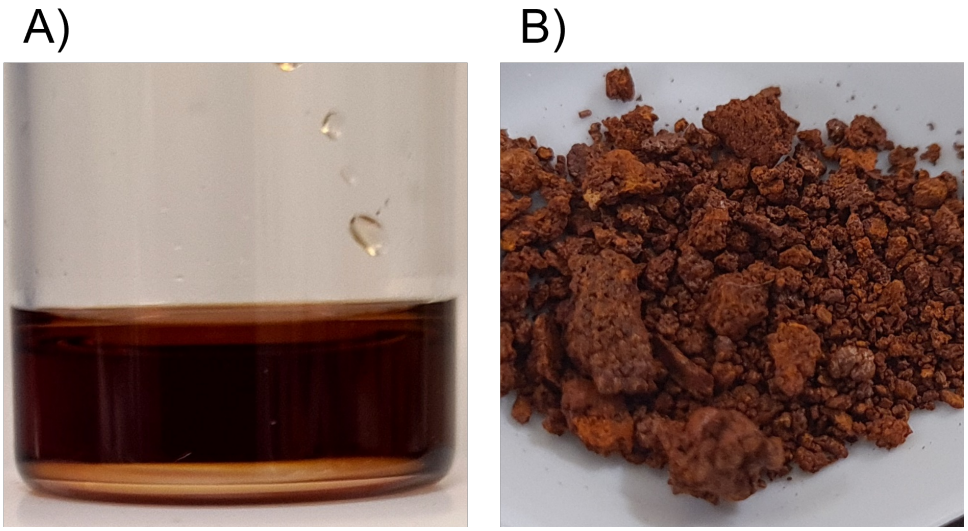

Figure 4.11: Images of A) methyl 3-thiophene acetate monomer and B) poly(3-hexylthiophene-*co*-methyl 3-thiophene acetate) **(5)**.

Prior to polymerisation, the synthesis of methyl 3-thiophene acetate from T3AA following the method in Section 3.1.2 is evidenced by infrared and NMR spectroscopy in Figures 4.12 and 4.13, respectively.

Considering the IR spectra (Figure 4.12), formation of methyl 3-thiophene acetate is clear. The disappearance of the O−H broad combination bands and overtones between 3200 - 2400 cm^{-1} shows total loss of the alcohol, and shifting of the carbonyl stretch from 1666 to 1734 cm^{-1} indicates ester formation. The stretching frequency of C=O is particularly sensitive to its surrounding molecular environment and can be used to distinguish between carboxylic acids and the acid derivatives effectively.

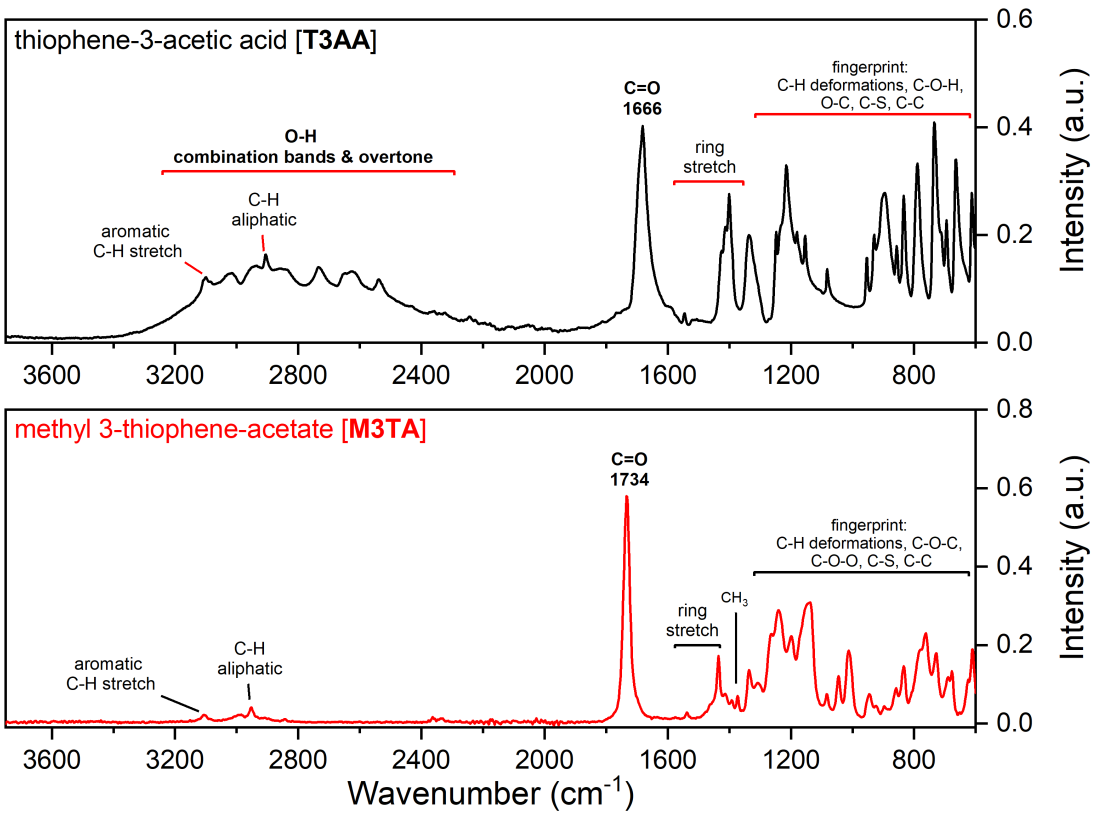

Figure 4.12: IR spectra of thiophene-3-acetic acid and synthesised methyl 3-thiophene acetate monomers.

In general, esters possess an increased C=O frequency as the negative induction of a R−OCH_3 group withdraws electrons from the π-orbital of the carbonyl, shortening and increasing the π-bond strength. A π-bond with more double bond character will possess a higher IR frequency when compared to the π-bond of a typical carboxylic acid [216]. ^{1}H NMR provides final confirmation for the formation of M3TA with analysis in Figure 4.13 showing 3 aromatic protons of the ring at 7.29, 7.15 and 7.04 ppm, the methyl group of the ester chain at 3.71 ppm and finally, the 2 protons of the methylene group at 3.67 ppm. The integrated intensity of the NMR signals matches with the expected number of protons in the M3TA monomer structure: ^{1}H NMR (500 MHz, CDCl3) δ 7.29 (dd, J = 4.9, 3.0 Hz, 1H), 7.15 (dq, J = 3.1, 0.9 Hz, 1H), 7.04 (dd, J = 5.0, 1.3 Hz, 1H), 3.71 (s, 3H), 3.67 (s, 2H).

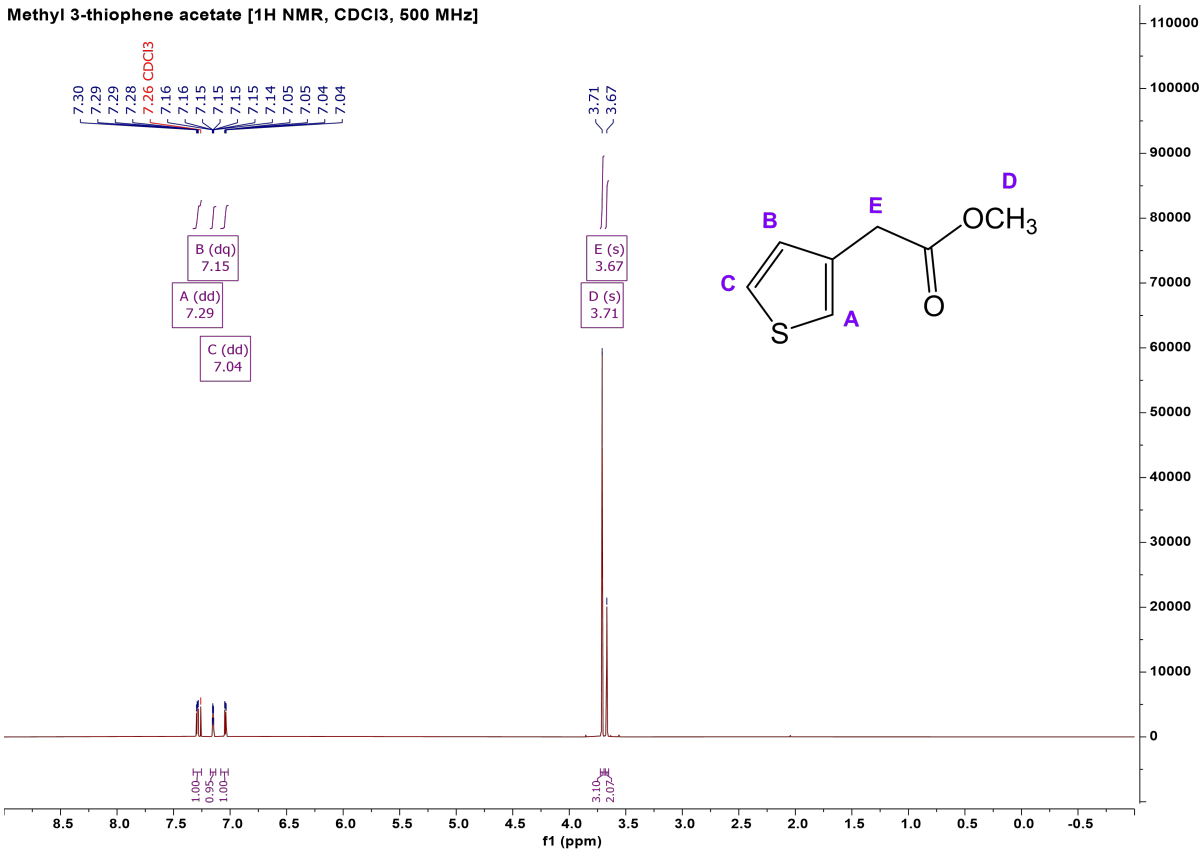

Figure 4.13: ^{1}H NMR Spectrum of synthesised M3TA monomer.

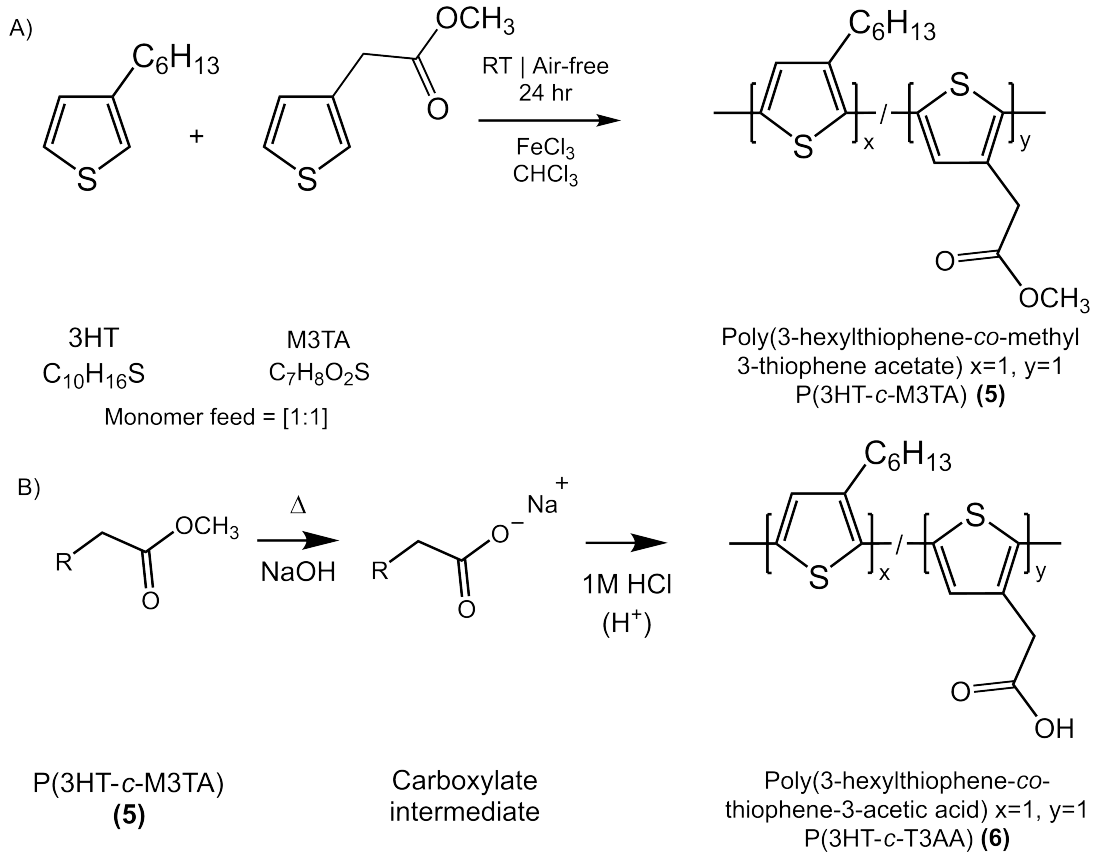

Figure 4.14: Reaction schemes for A) polymerisation of 3HT and M3TA, and B) Hydrolysis of P(3HT-*c*-MT3A) **(5)** to P(3HT-*c*-T3AA) **(6)**.

The polymerisation (Figure 4.14) of 3HT and methyl 3-thiophene acetate (M3TA) proceeded in an equal [1:1] monomer feed ratio without issue, producing an orange/brown solid (see Figure 4.11) of poly(3-hexylthiophene-*co*-methyl 3-thiophene acetate) - P(3HT-*c*-M3TA) at a yield of 56.2%. Primary analysis by ATR-FTIR in Figure 4.15 shows the triple peak of the aliphatic C−H at 2949, 2926 and 2853 cm^{-1}, a sharp ester carbonyl C=O peak at 1737 cm^{-1} and two ester peaks centred on ca. 1200 cm^{-1} to confirm the presence of both monomers in the product.

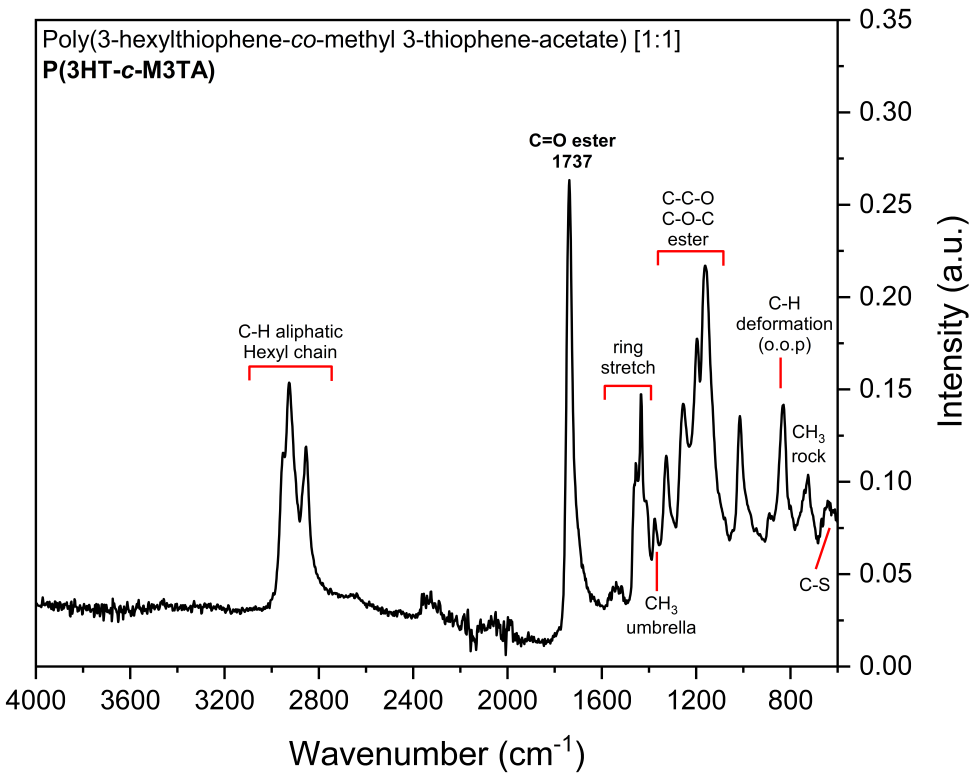

Figure 4.15: IR spectrum of poly(3-hexylthiophene-*co*-methyl 3-thiophene acetate) [1:1] **(5)**.

The methyl acetate copolymer **(5)** was mostly soluble in chloroform as ascertained from visual inspection. Following a review of the literature focusing on the hydrolysis methods of thiophene methyl esters, the predominant method for deprotection of the acid was identified as alkaline hydrolysis using 2M Sodium Hydroxide (NaOH) followed by workup with a weak, monoprotic acid e.g. 1M HCl.

Over the course of several preliminary deprotection reactions performed on methyl ester copolymers e.g. polymer **(5)**, the hydrolysis did not proceed as expected. There were two outcomes: either a white, salt compound precipitated (likely NaCl - See Figure B.3 in Appendix B) or recollection of the starting ester polymer. The reason for the failed hydrolysis

is difficult to theorise as the literature provides clear evidence the reaction should proceed readily. Bertran et al. and Fernando et al. performed the deprotection step in 2M NaOH(aq) for 24 hr before acid workup in 1 M HCl on M3TA containing polymers [301, 305]. Further to this, Lai et al. successfully produced P(3HT-*c*-T3AA) from P(3HT-*c*-M3TA) using the same process [38]. Considering the possibility of a slower rate of hydrolysis to the literature materials, a number of reactions were performed with an extended reflux step (72 hr) to ensure the methyl ester ($R-COCH_3$) is converted to the carboxylate ($R-COO^-Na^+$); however the extended reflux did not change the outcome as deprotection of the ester was again unsuccessful. In Shit et al., a 72 hr reflux had been successfully employed for deprotection of P3HT-*c*-M3TA as such, the outcome is surprising given the evidence for this method being suitable for the hydrolysis of the acetate polymer [226].

A new approach was needed; thus, consultation and further investigation of the literature and patent documents provided two additional hydrolysis procedures using concentrated NaOH i) in methanol / water, or ii) in tetrahydrofuran / water. Conversion from the methyl acetate to the acetic acid occurred using either of these methods, giving poly(3-hexylthiophene-*co*-thiophene-3-acetic acid) - polymer **(6)**. The percentage yield for the ester hydrolysis using methanolic NaOH was 67.3% while the reaction in THF/4 M NaOH(aq) was much lower at 11.3%. The difference in yield can be assigned to limited reprecipitation of the P(3HT-*c*-T3AA) upon neutralisation by HCl for the reaction in THF.

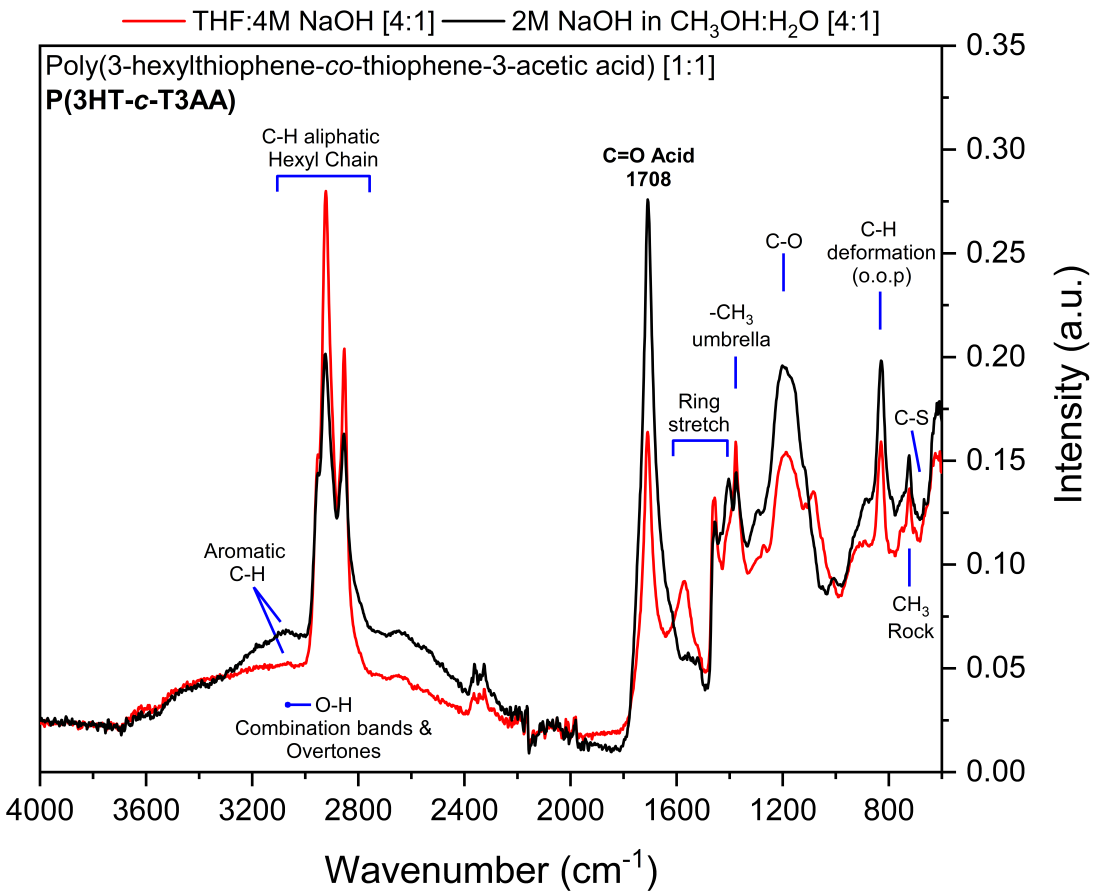

Figure 4.16: IR spectra of P(3HT-*c*-T3AA) **(6)** from hydrolysis of **(5)** in THF/4M NaOH [4:1] or 2M NaOH in CH_3OH/H_2O [4:1].

Figure 4.16 shows IR spectra of the hydrolysed polymers **(6)** following the reaction conditions described in Section 3.4. Reformation of the carboxylic acid moiety becomes apparent by the appearance of a broad O−H stretch between 3600 - 2400 cm^{-1} and weakening of the carbonyl peak from 1737 cm^{-1} in polymer **(5)** to 1708 cm^{-1} in polymer **(6)**.

^{1}H NMR spectra for P(3HT-*c*-M3TA) - **(5)** and P(3HT-*c*-T3AA) - **(6)** following ester hydrolysis (2M NaOH(aq)) in CH_3OH/H_2O as shown in Figures 4.17 and 4.18 provides further evidence of successful deprotection. The signals arising from the proton environments of the methyl acetate ($R-CH_2-COOCH_3$) or acetic acid groups ($R-CH_2-COOH$) will be present between a chemical shift range of 3.7 - 3.4 ppm.

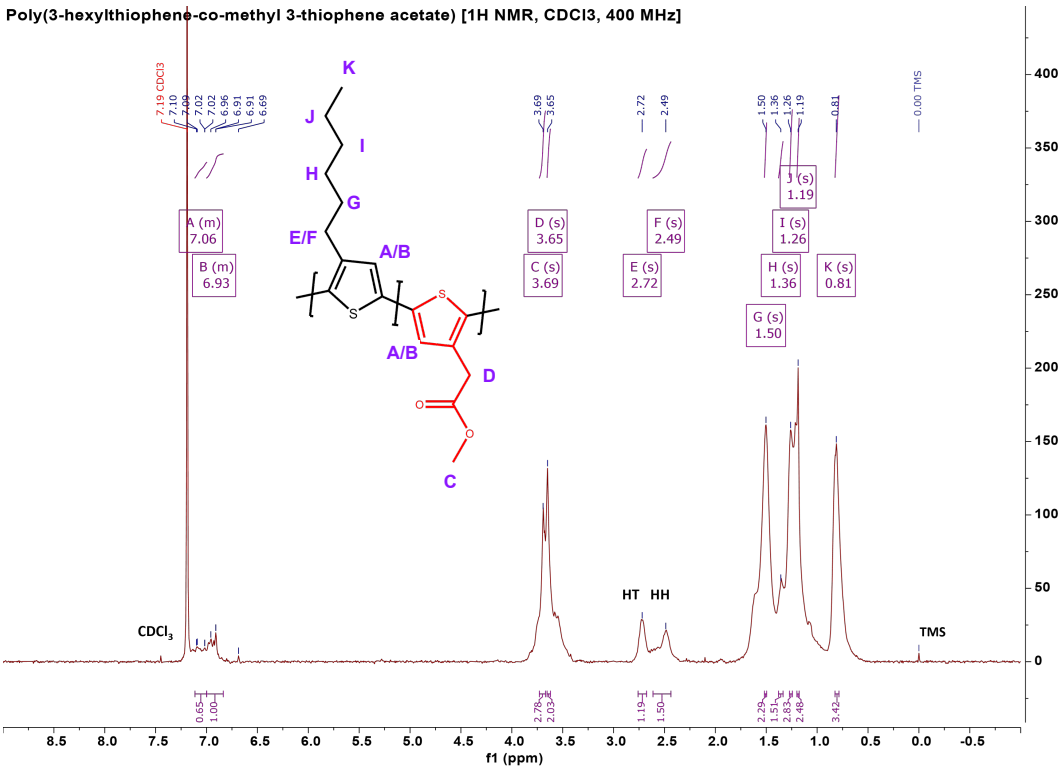

Figure 4.17: ^{1}H NMR spectrum of P(3HT-*c*-M3TA) [1:1] **(5)**.

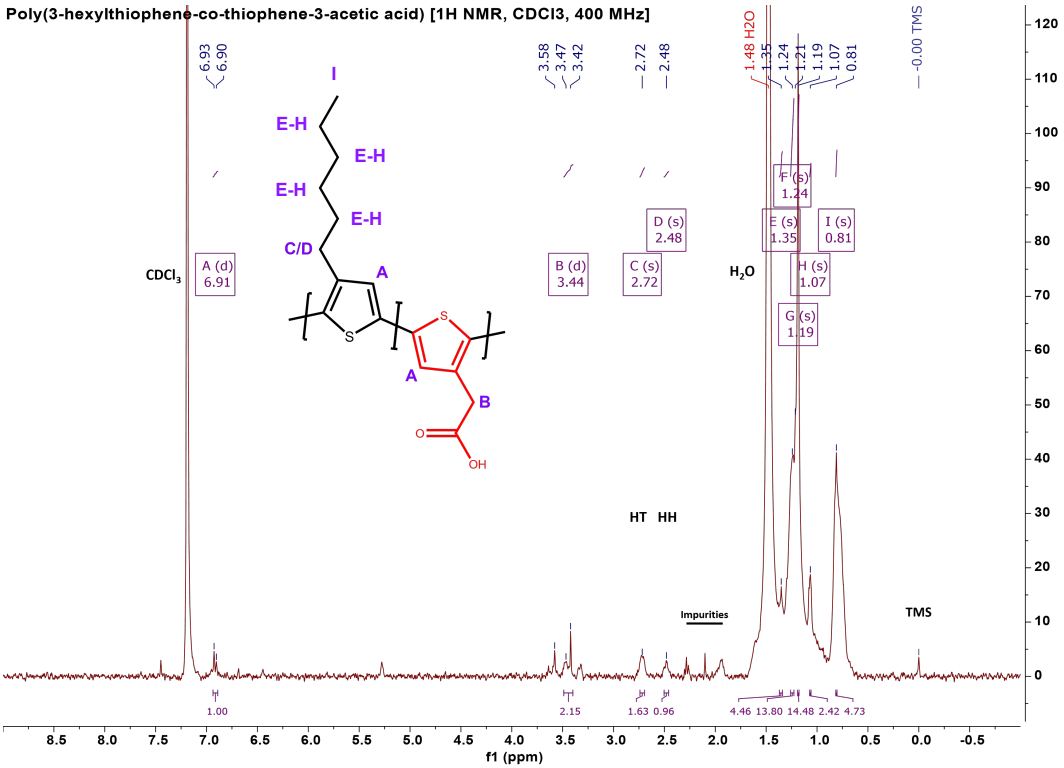

Figure 4.18: ^{1}H NMR spectrum of P(3HT-*c*-T3AA) [1:1] **(6)**.

The deshielding environment of the ester carbonyl, shifts the NMR signal downfield to a higher PPM value when compared to the comparable methylene group of the hexyl alkane chain. Simple differentiation between the two monomers of the copolymer is enabled as

3HT and C=O functionalised thiophene possess distinctly different proton environments. In Figure 4.17, the terminal methyl group ($R-OCH_3$) of the ester gives a strong singlet peak at 3.69 ppm, paired with an obscured peak at ca. 3.65 ppm for the methylene ($-CH_2-$) groups, accounts for the remaining protons of the acetate. P(3HT-*c*-M3TA): 1H NMR (400 MHz, CDCl3) 7.11 7.00 (m, 1H), 7.00 6.84 (m, 1H), 3.69 (s, 3H), 3.65 (s, 2H), 2.72 (s, 1H), 2.49 (s, 1H), 1.50 (s, 2H), 1.36 (s, 2H), 1.26 (s, 3H), 1.19 (s, 2H), 0.81 (s, 3H).

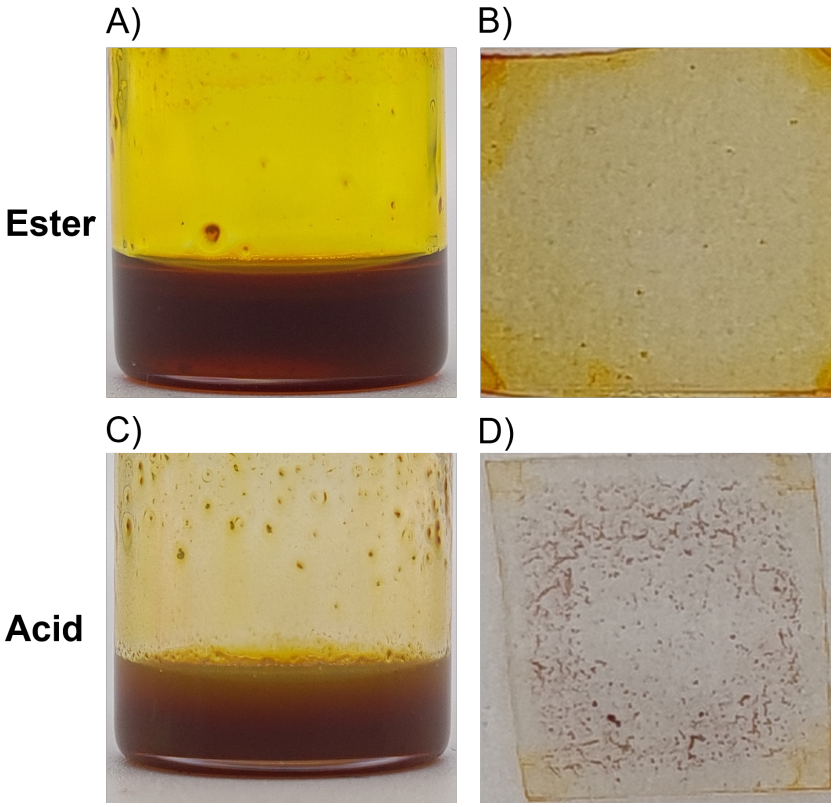

Figure 4.19: Images of A) P(3HT-*c*-M3TA) [1:1] **(5)** solution in $CHCl_3$:C_6H_5Cl, B) thin film of **(5)** on Al_2O_3 sapphire substrate deposited via spin-coating, C) spin coating solution of P(3HT-*c*-T3AA) **(6)** and D) thin film of P(3HT-*c*-T3AA) **(6)** on Al_2O_3 substrate.

Conversely, in Figure 4.18, there is a large reduction in signal intensity at 3.69 ppm, indicating loss of the methyl group following hydrolysis. P(3HT-*c*-T3AA): 1H NMR (400 MHz, CDCl3) 6.91 (d, J = 9.0 Hz, 1H), 3.44 (d, J = 18.1 Hz, 2H), 2.72 (s, 2H), 2.48 (s, 1H), 1.35 (s, 4H), 1.19 (s, 14H), 1.07 (s, 2H), 1.24 (s, 14H), 0.81 (s, 5H). Typically, the carboxylic acid proton (R-COOH) is expected between 10 - 13 ppm; however, no signal is observed within this range. Given the presence of the alcohol ($O-H$) in the IR spectra (Figure 4.16), the lack of signal is likely due to proton exchange between the acidic proton of $R-COOH$ and deuterium in $CDCl_3$. As the yield for hydrolysis of polymer **(5)** in methanolic base was significantly higher than the reaction in THF, hydrolysis utilising methanolic sodium hydroxide

became the condition of choice for the remainder of the project.

Solubility of polymer **(6)** was investigated by dissolving the solids in a spin-coating solvent mixture $CHCl_3$:C_6H_5Cl at 15 mg mL^{-1} as well as other solvents and solvent mixtures such as THF and toluene at 5 mg mL^{-1} (See Appendix A, Figure A.1 for more images of dissolutions.). As illustrated in Figure 4.19, from the visual inspection of the solution and spin-coated thin film as well as by determination of turbidity using UV-Vis, it is clear that polymer **(6)** is much less soluble than polymer **(5)** with many undissolved particles in both solution and film. This difference in solubility in organic solvents, e.g. chloroform, also appears in the literature looking at the homopolymers of thiophene esters and carboxylic acids e.g. poly(thiophene-3-acetic acid) and poly(methyl-3-thiophene acetate) [284, 301, 318–320]. As outlined by Della Casa et al. and Mescoloto et al., it is thought the reintroduction of the polar and hydrophilic R−COOH group, allows for the formation of strong intermolecular forces, mainly hydrogen bonding, between polymer chains [321–323]. This has the effect of reducing solubility in non-polar solvents, such as $CHCl_3$. Carboxylic acid groups may improve solubility in polar, aqueous solvents, such as H_2O, but in polymers like **(6)**, this would be completely negated by the presence of the non-polar hexyl chain [283, 317].

4.3.2 Poly(3-hexylthiophene-*co*-trans-3-thiophen-3-yl-acrylic acid)

Trans-3-thiophen-3-yl-acrylic acid (T3T3YAA) is another readily available thiophene acid monomer. Compared to both T3CA and T3AA, trans-3-thiophen-3-yl-acrylic acid possesses a longer chain length with an acrylic acid group as shown by the structure in Figure 3.3. Several factors influenced the decision-making process when determining which functional monomers to pursue. As mentioned, one factor was materials cost, which T3T3YAA satisfies at £5 per gram. The functionality of the monomers is, however, the most important consideration. The monomer must be capable of forming a bond with the enzyme; in this case via the carbodiimide coupling pathway, without modifying the desirable solubility of P3HT polymers. It was thought the increased chain length would aid the solubility issue by altering overall polymer polarity.

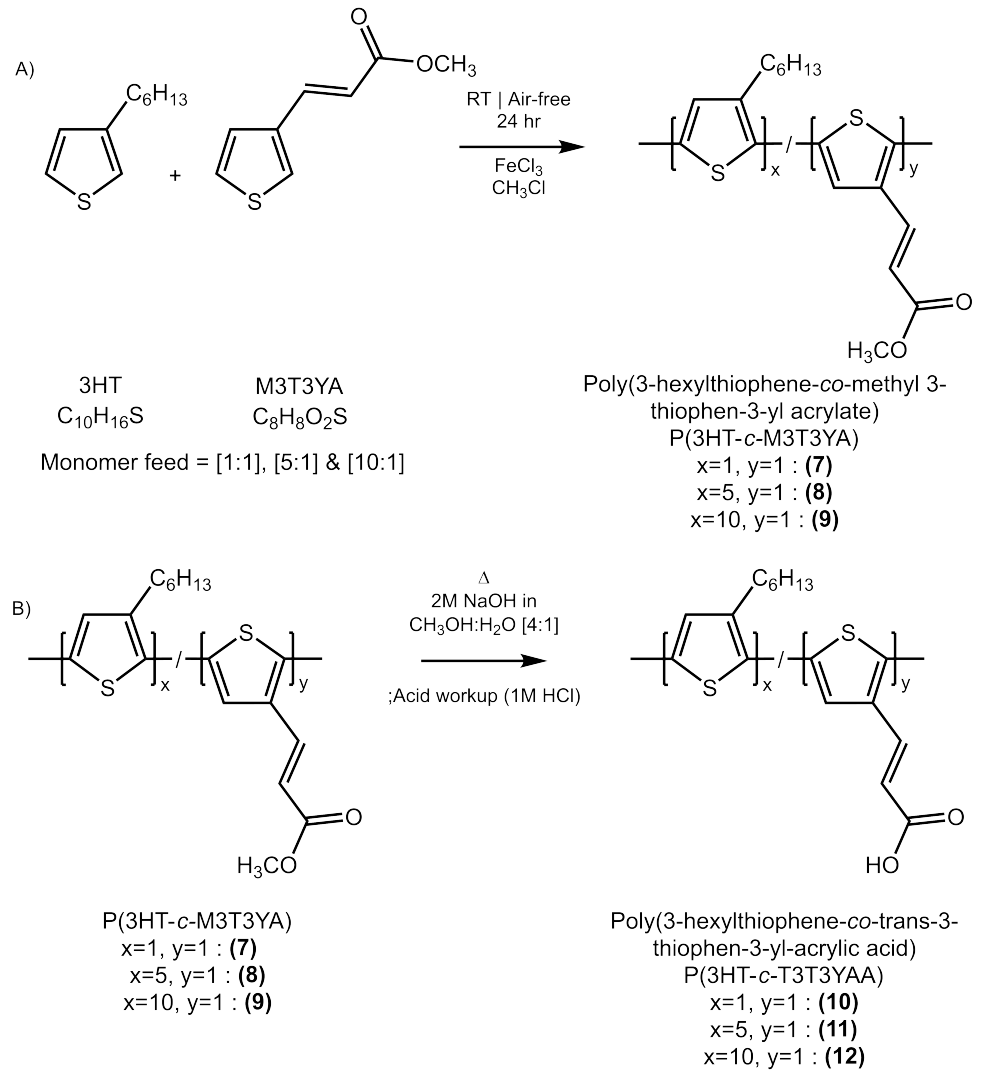

Figure 4.20: Reaction scheme for A) polymerisation of 3HT and M3T3YA and B) hydrolysis of P(3HT-*c*-M3T3YA) **(7)** - **(9)** to P(3HT-*c*-T3T3YAA) **(10)** - **(12)**.

The use of a double bond containing acrylic acid over a long chain thiophene carboxylic acid, such as 3-(thiophen-3-yl)propanoic acid ($C_7H_8O_2S$), is expected to enlarge conjugation from the π-system of the polymer backbone along the acid substituent enhancing electron transport characteristics of the enzyme-binding group, as described in a study on the structural and electronic properties of poly(T3T3YAA) by Bertran et al. [301]. Furthermore, the added length of the side chain in T3T3YAA has the potential to increase the availability of the enzyme binding sites by reducing steric interference of the backbone and 3HT comonomer while further improving sensor quality. As discussed by Clayton (2011), an improvement in sensor reproducibility and reduction of signal variation was seen in an electropolymerised poly(3-methylthiophene-*co*-trans-3-thiophen-3-yl-acrylic acid) platinum disk electrode [67]. Additionally, in Clayton (2011), the versatility of T3T3YAA is

highlighted further by the conversion of the acid to an N-succinimdyl ester type moiety and subsequent electropolymerisation with 3MT. The copolymerisation of N-succinimidyl esters with 3-hexylthiophene for the production of solution-processable materials will be discussed in 4.3.3 and 4.4.2.

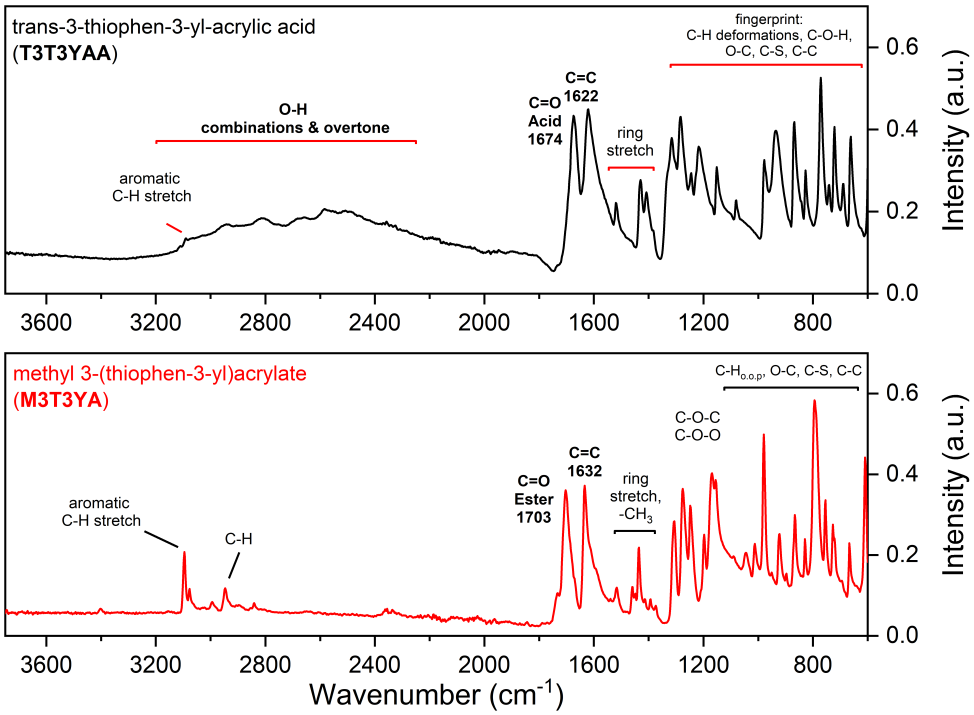

Figure 4.21: IR spectra of trans-3-thiophen-3-yl-acrylic acid and synthesised methyl 3-(thiophen-3-yl)acrylate monomers.

Similar to the previous esterification reactions, conversion of T3T3YAA to M3T3YA was performed with relative ease to high yields ($\geq 85\%$). In Figure 4.21, a comparison of IR spectra of the starting acid vs the product of esterification shows the expected loss of the broad $-$OH peak, strengthening of the carbonyl C=O due to ester formation (1674 to 1700 cm^{-1}) as well as many changes to the fingerprint region of the spectra.

In agreement with the IR spectra, the ^{1}H NMR data presented in Figure 4.22 shows a sharp singlet peak with an integration value of 3 is present at ca. 3.72 ppm and represents the methyl group (R$-$CH$_3$) of the ester.

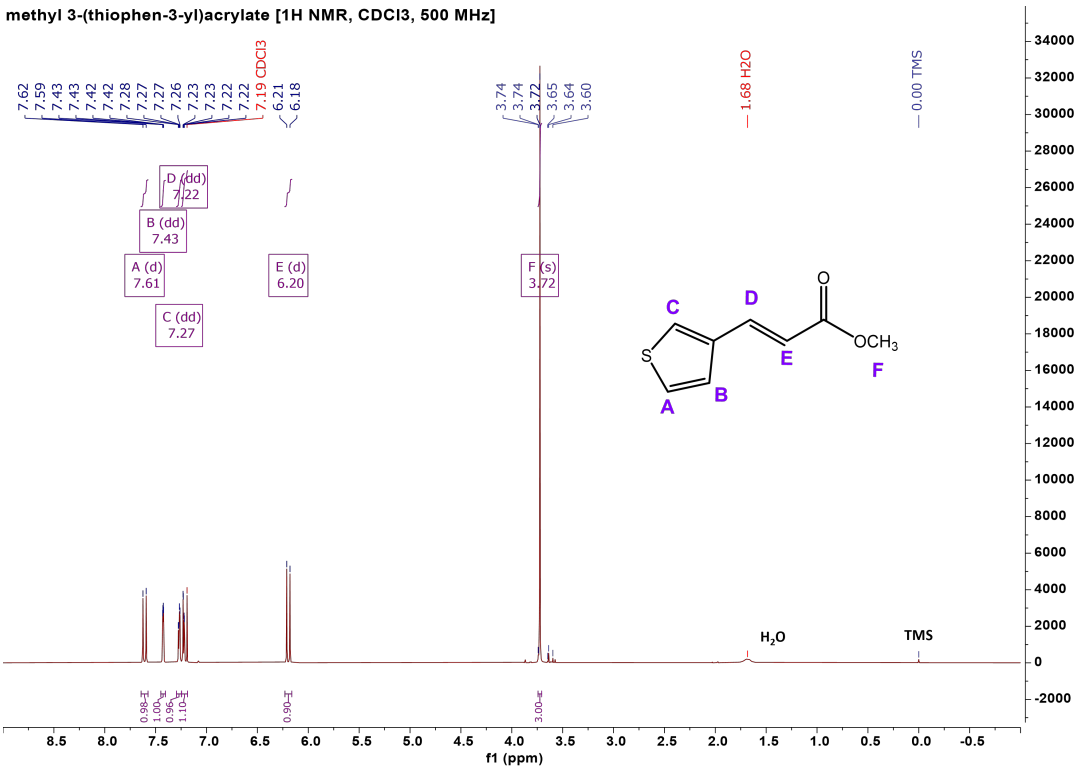

Figure 4.22: ^{1}H NMR spectrum of synthesised M3T3YA monomer.

The alkene of the chain gives two distinct proton environments, with the deshielded proton next to the thiophene at ca. 7.61 ppm compared to the signal ca. 6.20 ppm of alkene proton closest to the C=O. M3T3YA Monomer: 1H NMR (500 MHz, CDCl3) 7.61 (d, J = 15.9 Hz, 1H), 7.43 (dd, J = 3.0, 1.2 Hz, 1H), 7.27 (dd, J = 5.1, 2.9 Hz, 1H), 7.22 (dd, J = 5.1, 1.3 Hz, 1H), 6.20 (d, J = 15.9 Hz, 1H), 3.72 (s, 3H).

As represented in Figure 4.20, three polymers of 3HT and M3T3YA were prepared at monomer feed ratios of [1:1], [5:1] and [10:1] before hydrolysis to yield the acrylic acid containing P(3HT-*c*-T3T3YAA). Similar to the copolymerisations of 3HT with M3TC or M3TA, the use of chloroform as the solvent gave high-yielding reactions. A summary of reaction yield for P(3HT-*c*-M3T3YA) and P(3HT-*c*-T3T3YAA) is given in Table 4.1.

Table 4.1: Table of reaction yield (%) for preparation of P(3HT-*c*-M3T3YA) and P(3HT-*c*-T3T3YAA).

Monomer Ratio	P(3HT-*c*-M3T3YA) Yield	P(3HT-*c*-T3T3YAA) Yield
1:1	**(7)** - 69.3%	**(10)** - ~90%
5:1	**(8)** - 60.3%	**(11)** - 85.9%
10:1	**(9)** - 43.3%	**(12)** - ~88%

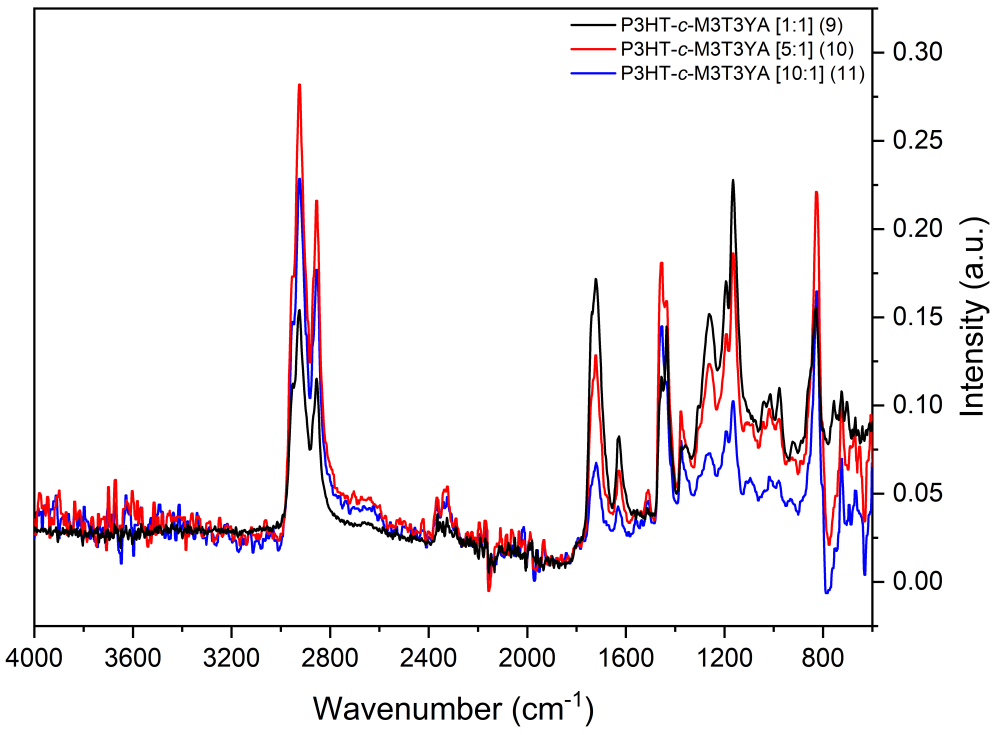

Figure 4.23: IR spectra of P(3HT-*c*-M3T3YA) **(7)** [1:1], **(8)** [5:1] and **(9)** [10:1].

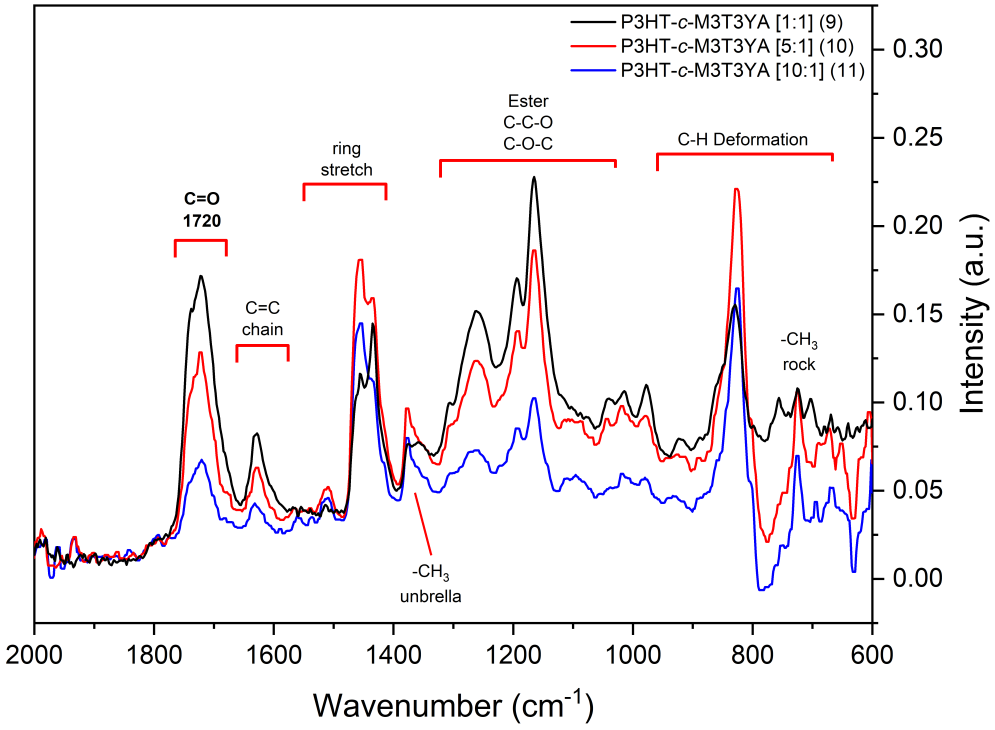

Figure 4.24: Fingerprint IR spectra of **(7)**, **(8)** and **(9)** - 2000 to 600 cm^{-1}.

Once again, IR and ^{1}H NMR were utilised for the determination of polymer structure. As outline in Figures 4.23 and 4.24, for polymers **(7)**, **(8)** and **(9)**, confirmation of successful copolymerisation is evidenced by the presence of both the strong aliphatic C−H peaks at 2953, 2922 and 2855 cm^{-1} and ester carbonyl (C=O) at 1716 cm^{-1}. The C=C vibration at

ca. 1625 cm^{-1} further highlights the presence of the acrylate chain. When possible, given clear separation of certain signals, the monomer ratio can be determined by comparison of NMR peak integrals.

Focusing on the two regions $-OCH_3$ at ca. 3.69 ppm and $-CH_2-$ between 2.8 - 2.5 ppm then determining the ratio of relative monomer % gave a reasonable matching to the monomer feed **(7)** with 52.8% 3HT to 47.2% M3T3YA or $(C_{10}H_{16}S)_{1.12}(C_8H_8O_2S)_{1.00}$. Moreover, when considering the difference between IR spectra and the relative intensities for the C-H stretches at 2900 cm^{-1} and the carbonyl (C=O) for polymers **(7)**, **(8)** and **(9)**, it becomes clear the monomer feed ratio has affected the final polymer composition. Qualitatively speaking, the C-H and C=O peaks for **(7)** are of equal intensity which corresponds to the [1:1] monomer feed ratio however for **(10)** where the 3HT:M3T3YA ratio is [10:1], the increase in 3HT content in the monomer feed has resulted in a corresponding decrease to the intensity of the C=O stretch while the C-H stretch intensity has increased. In Figure 4.25, analysis of the proton NMR spectrum for the polymer **(7)** provides additional confidence P(3HT-*c*-M3T3YA) has been synthesised[5].

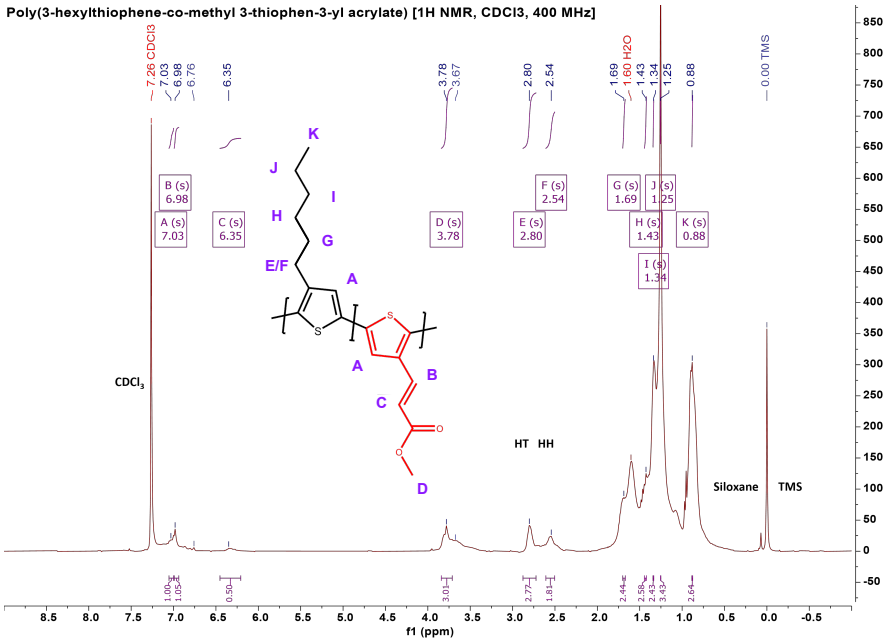

Figure 4.25: ^{1}H NMR spectrum of P(3HT-*c*-M3T3YA) [1:1] **(7)**.

The peak at 0.88 ppm represents the terminal methyl group ($-CH_3$) of the hexyl chain. The mixture of peaks between 1.25 - 1.69 ppm arise due to the methylene groups ($-CH_2-$) of the chain, and the distinct peaks at 2.88 and 2.55 ppm are typical of the deshielded protons

of the hexyl chain. The primary signal of the ester is found at ca. 3.78 ppm followed by the protons of the alkene and aromatic thiophene ring at 6.35, 6.98 and 7.03 ppm, respectively. P(3HT-*c*-M3T3YA): 1H NMR (400 MHz, CDCl3) 7.03 (s, 1H), 6.98 (s, 1H), 6.35 (s, 1H), 3.78 (s, 3H), 2.80 (s, 1H), 2.54 (s, 1H), 1.69 (s, 2H), 1.43 (s, 3H), 1.34 (s, 2H), 1.25 (s, 3H), 0.88 (s, 3H).

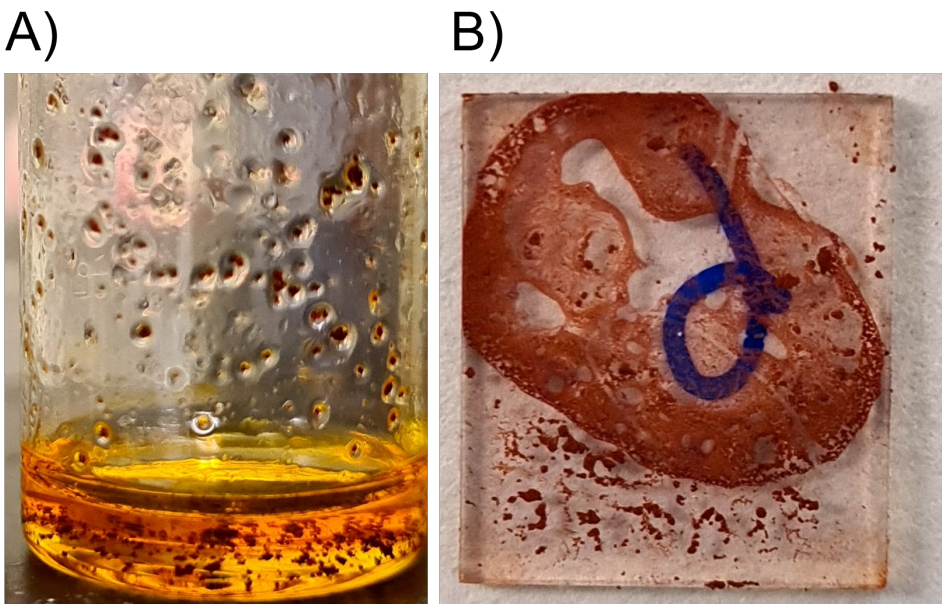

Figure 4.26: Image of A) P(3HT-*c*-T3T3YAA) [1:1] **(10)** exhibiting partial solubility when dissolved in $CHCl_3$ (20 mg mL^{-1}) and B) Thin Film of **(12)** on an ITO-glass substrate.

Deprotection of polymers **(7)**, **(8)** and **(9)** using 2M NaOH in CH_3OH:H_2O [4:1] yielded poly(3-hexylthiophene-*co*-trans-3-thiophen-3-yl-acrylic acid) - polymers **(10)**, **(11)** and **(12)**. The successful hydrolysis or deprotection is shown by weakening of the C=O from ca. 1720 to 1693 cm^{-1} as well as changes in the composition of the fingerprint region, e.g. loss of the ester peaks (C−C−O, C−O−C) in Figures 4.27 and 4.28. In the IR spectrum of polymer **(10)**, reappearance of the broad alcohol vibration (R−OH) is also observed.

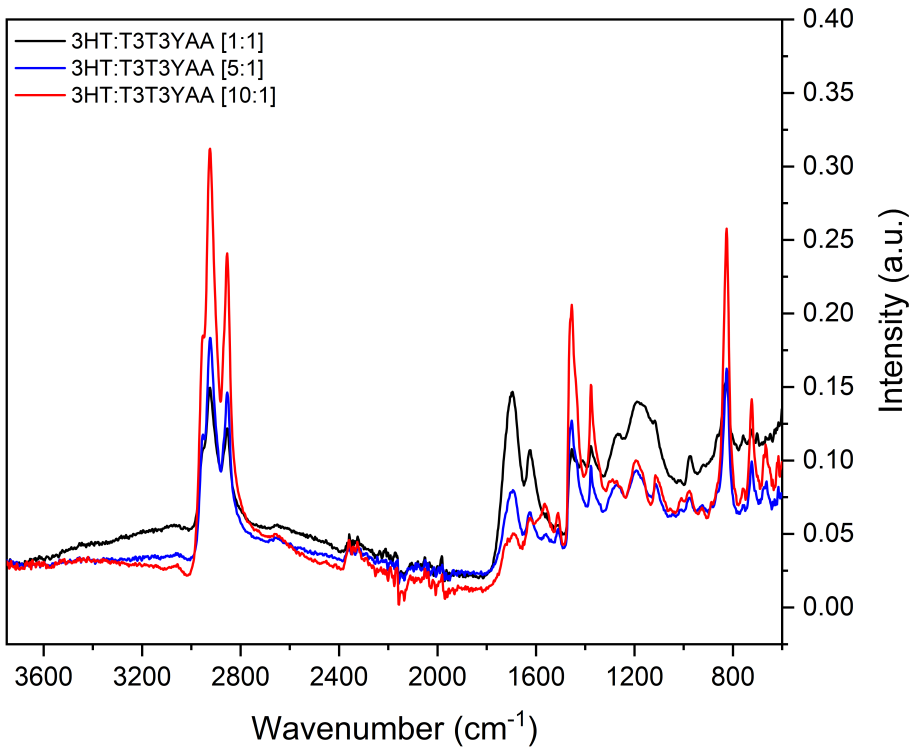

Figure 4.27: IR spectra of P(3HT-*c*-T3T3YAA) - **(10)**, **(11)** and **(12)**.

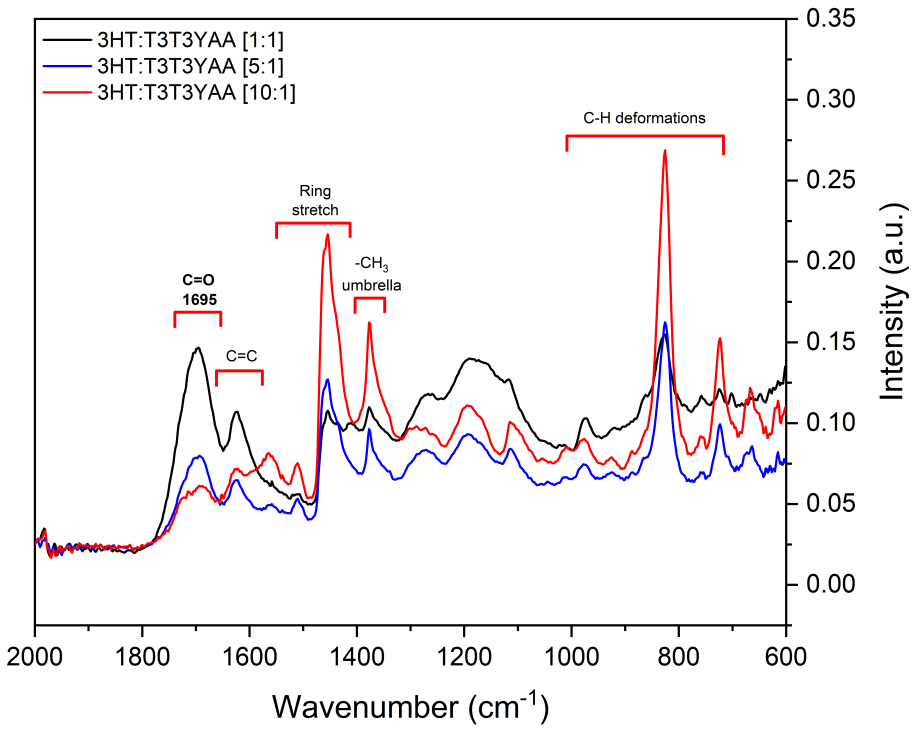

Figure 4.28: IR spectra of P(3HT-*c*-T3T3YAA) - **(10)**, **(11)** and **(12)** - 2000 to 600 cm^{-1}.

Prior to ^{1}H NMR, the P3HT-**c**-T3T3YAA compounds **(10)**, **(11)** and **(12)** were assessed for solubility by dissolution in chloroform. After only partially dissolving in the solvent, it was clear from visual inspection and UV-Vis turbidity measurements, these polymers were again

much less soluble than their methyl ester versions, i.e. polymers **(7)**, **(8)** and **(9)**. The images in Figure 4.26 show the poor solubility of these materials. Specifically, as observed in Figure 4.26.B, the presence of undissolved particles in the polymer solution leads to a non-uniform film. This issue is compounded by limited solubility in general, as the polymer begins to immediately crash-out when the carrier solvent evaporates, resulting in the film having a powdery appearance. If the polymer had good solubility, the spin-coating solution would spread out evenly across the substrate, before thinning and solvent evaporation to give uniform, and continuous thin polymer film.

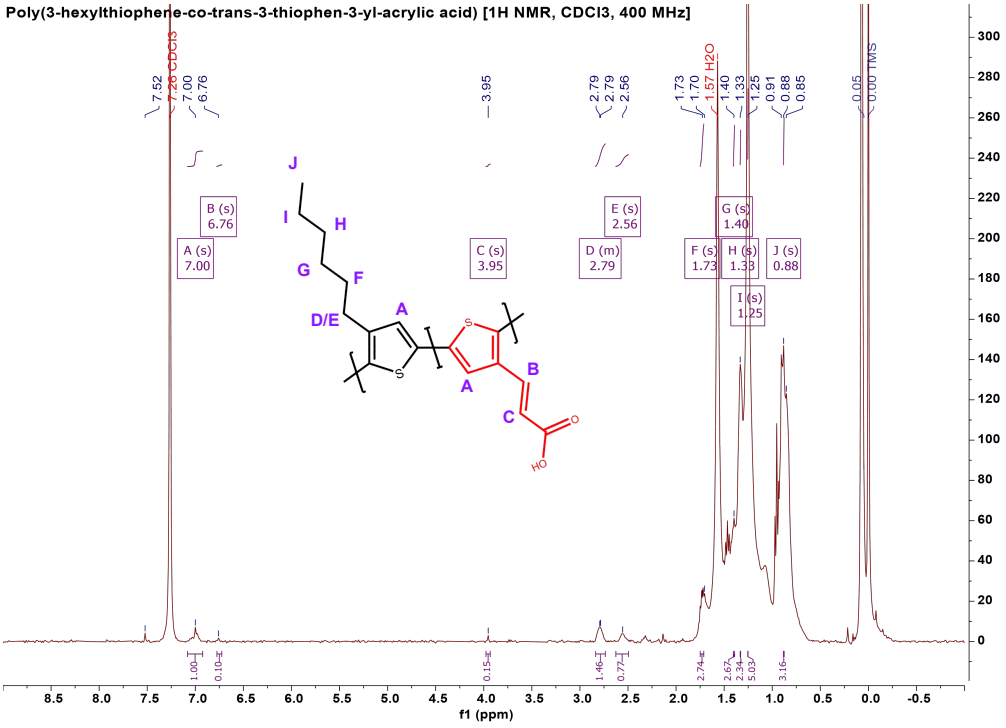

Figure 4.29: ^{1}H NMR spectrum of P(3HT-*c*-T3T3YAA) [1:1] **(10)**.

As with P(3HT-*c*-T3AA) **(6)**, it is likely the reduction in solubility is due to changes in polarity between the acrylate/acrylic acid side chain. The molecular weight of the polymers is also likely to contribute to the observed solubility behaviour. Considering the proton NMR of polymer **(10)**, the spectrum in Figure 4.29 appears to show no T3T3YAA comonomer present in the polymer with the lack of an obvious signal from the alkene proton closest to the carbonyl. It is therefore possible that the component dissolving into solution is a P3HT homopolymer present in the solid product whereas it is the P(3HT-*c*-T3T3YAA) copolymer which remains largely insoluble, producing the undissolved particles seen in the solution and film in Figure 4.26. As such, this insoluble component of polymer **(10)** is capable of

identification using ATR-FTIR as shown in Figures 4.27 and 4.28 but is not effectively able to be characterised by ^{1}H NMR . P(3HT-*c*-T3AA): 1H NMR (400 MHz, CDCl3) 7.00 (s, 1H), 6.76 (s, 0H), 3.95 (s, 0H), 2.84 2.74 (m, 1H), 2.56 (s, 1H), 1.73 (s, 3H), 1.40 (s, 3H), 1.33 (s, 2H), 1.25 (s, 5H), 0.88 (s, 3H).

Solubility issues notwithstanding, the work above outlines the first chemical synthesis of novel 3-hexylthiophene copolymers containing the T3T3YAA monomer - poly(3-hexylthiophene-*co*-trans-3-thiophen-3-yl-acrylic acid) as well as the methyl ester derivative M3T3YA - poly(3-hexylthiophene-*co*-methyl 3-thiophen-3-yl acrylate).

Notes

[5]In a select number of NMR spectra, sharp signals arising from contamination/impurities in the solvent are present at exactly 8.123, 4.283 and 3.525 ppm. These signals have been suppressed using available tools during analysis. An example of the unprocessed spectra can be found in Appendix B, Figure B.4.

4.3.3 Poly(3HT-*co*-N-succinimidyl 3-thiophene acetate) and Poly(3HT-*co*-N-succinimidyl 3-(thiophen-3-yl) acrylate)

Following the preparation of P3HT-*c*-M3TC, -T3AA and -T3T3YAA, it was apparent that performing the polymerisation in chloroform yields poor solubility in the final product. The polarity of the carboxylic acid side chains is likely the key factor when determining solubility as both methyl ester polymers of P(3HT-*c*-M3TA) and P(3HT-*c*-M3T3YA) - Polymers **(5)**, **(7)**, **(8)** and **(9)** were capable of dissolving in the spin-coating solvent mixture.

To address the solubility issue and improve solubility in non-polar, chlorinated solvents such as chloroform, chlorobenzene or dichloromethane, three approaches can be investigated i) reduce the polarity of enzyme-immobilising side chain, ii) produce polymers with a lower molecular weight, or naturally iii) a combination of i) and ii). Keeping chloroform as the reaction solvent, the first approach was to produce a polymer with less polar side chains. Use of polymers with N-succinimiyl esters offers a very nice approach considering that the same starting materials can be used, coupling the succinimide group to the thiophene acid protects the compound during polymerisation and finally, the N-succinidyl ester is formed

during the immobilisation step therefore removes the need for deprotection and essentially pre-activates the polymers for enzyme attachment [67]. The use of N-succinimidyl esters for the immobilisation of biomolecules has been discussed in a number of publications.

Figure 4.30: Images of A) N-succinimidyl 3-thiophene acetate (S3TA), B) P(3HT-*c*-S3TA) **(13)**, C) N-succinimidyl 3-(thiophen-3-yl)acrylate (S3T3YA), and D) P(3HT-*c*-S3T3YA) **(14)**.

Early use of succinimide-activated thiophene esters can be seen in two publications by Li et al. where an N-succinimidyl 3-thiophene acetate homopolymer and copolymer with 3-methylthiophene are prepared by electropolymerisation [289, 324]. Li develops on the idea further to produce more functional thiophene derivatives e.g. 1-(11-thiophene-3yl-undecyl)-pyrrole-2,5-dione, showcasing a broad range of bioactive functionalisation possible on a thiophene-based polymer [108]. Turning to chemically-polymerised materials, Kim et al. showcases the ability of succinimide activated thiophene esters to immobilise biomolecules. Kim produces S3TA homopolymer by $FeCl_3$ oxidative polymerisation before immobilising the anti-C-reactive protein; a bioreceptor for the useful clinical marker CRP [291]. Clayton (2011) expands on the work by Li and Kim to produce a number of

succinimide-activated thiophene ester monomers and electropolymerised copolymers with 3-methylthiophene, describing the application of these materials to immobilise glucose oxidase and detect of glucose. Additionally, Clayton establishes a procedure for synthesis of the succinimide ester derivative of T3T3YAA [67].

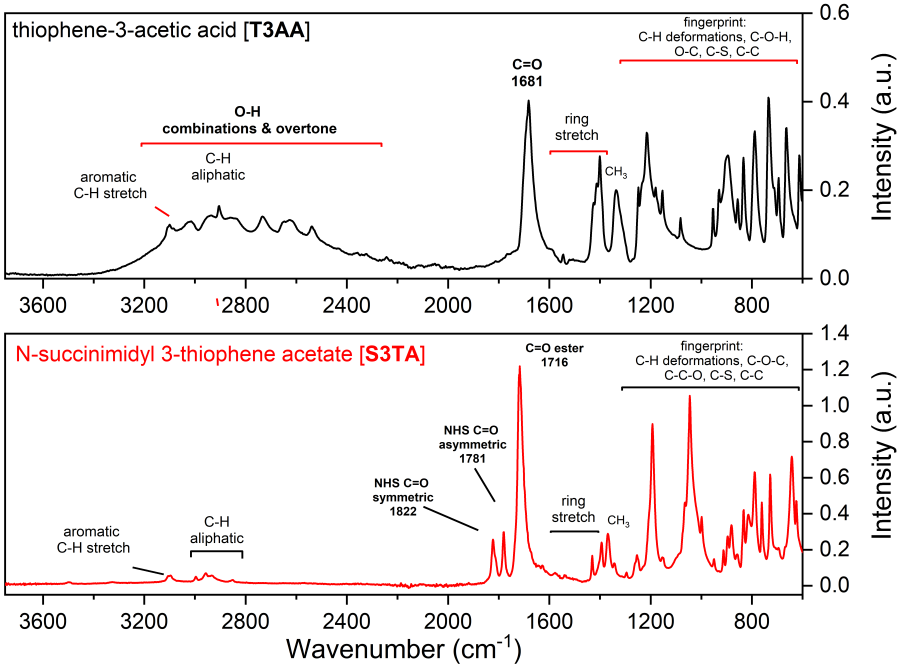

Figure 4.31: IR spectra of T3AA and synthesised N-succinimidyl 3-thiophene acetate (S3TA) monomers.

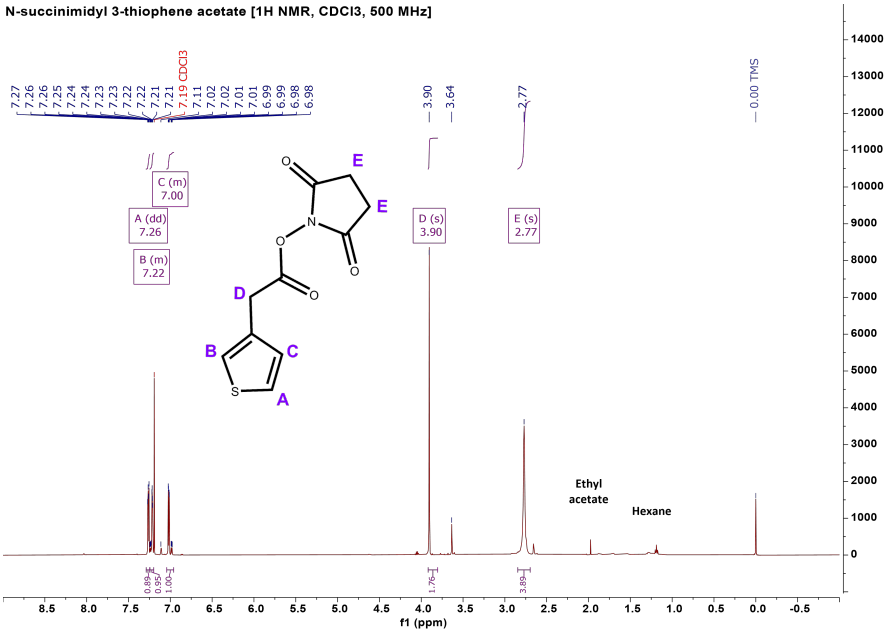

Figure 4.32: ^{1}H NMR spectrum of S3TA monomer.

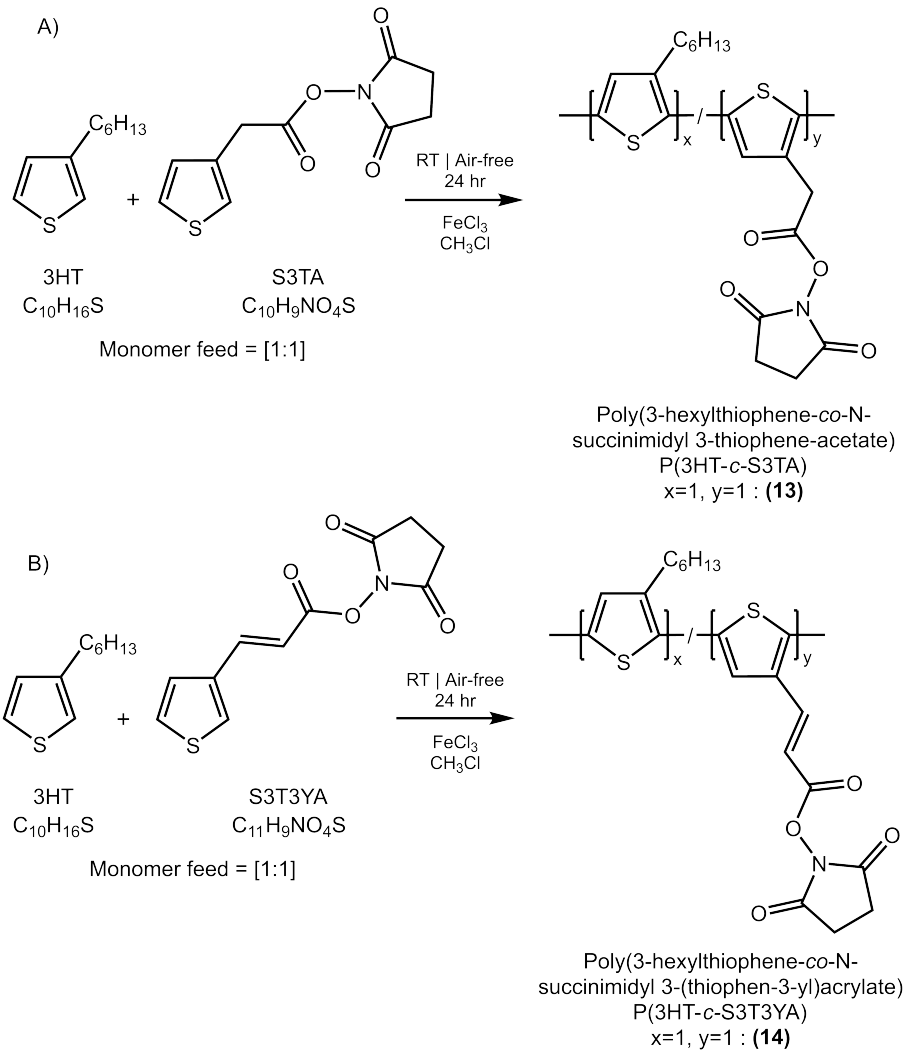

Figure 4.33: Reaction scheme for polymerisations of A) P(3HT-*c*-S3TA) [1:1] **(13)**, and B) P(3HT-c-S3T3YA) [1:1] **(14)** in $CHCl_3$.

As outlined in Section 3.2, N-succinimidyl 3-thiophene acetate was prepared from thiophene-3-acetic acid. Figure 4.31 shows comparative ATR-FTIR spectra between the as-purchased T3AA monomer and S3TA following synthesis and purification upon a silica column (eluent = ethyl acetate:hexane 9/1). In the IR spectrum for S3TA, loss of the alcohol vibration, strengthening of the ester C=O from 1681 to 1716 cm^{-1} and the appearance of asymmetric and symmetric carbonyl vibrations at 1781 and 1822 cm^{-1} indicates successful preparation. Further analysis of S3TA by proton NMR agrees with the vibrational information in the IR spectrum. The aromatic protons of the ring are located at 7.25, 7.20 and 7.02 ppm, the methylene ($-CH_2-$) is at 2.10 ppm and the signal at 2.77 ppm indicates the four protons of the succinimide ring. The peak integrals of Figure 4.32 matches the expected no. of protons,

S3TA Monomer: 1H NMR (500 MHz, CDCl3) 7.26 (dd, J = 5.0, 3.0 Hz, 1H), 7.24 7.20 (m, 1H), 7.04 6.96 (m, 1H), 3.90 (s, 2H), 2.77 (s, 4H). The presence of solvent impurities in the spectrum outlines the need for additional processing of the monomers, e.g. excessive drying under vacuum to improve purity in future projects.

The polymerisation of N-succinimidyl ester monomers with 3HT was conducted using the same method as the previous copolymers (see Figure 4.33). At a [1:1] monomer feed ratio, 3-hexylthiophene and N-succinimidyl 3-thiophene acetate were copolymerised in chloroform, yielding poly(3-hexylthiophene-*co*-N-succinimidyl 3-thiophene acetate) **(13)** as a bright red solid at a yield of 45.1% (see Figure 4.30).

Visual observations following synthesis show that polymer **(13)** possessed a stronger reddish hue when compared to the methyl esters copolymers (Figure 4.30). After purification of the polymer solids by methanol Soxhlet extraction, IR analysis was performed giving the spectrum in Figure 4.34.

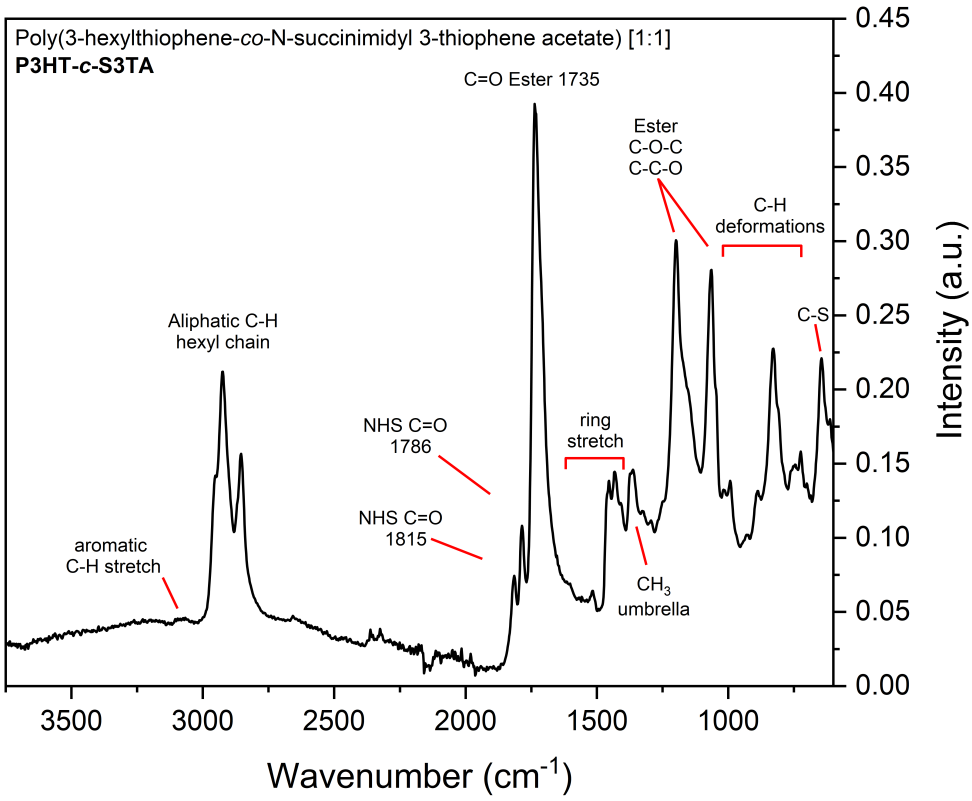

Figure 4.34: IR spectrum of P(3HT-*c*-S3TA) from $CHCl_3$ **(13)**.

The characteristic features of copolymerisation are present with the aliphatic C−H stretch at 2953, 2926 and 2855 cm^{-1} as well as the three carbonyl vibrations. In this polymer, the C=O vibrations were located at 1815 and 1784 cm^{-1} for the symmetric and asymmetric stretches

of the succinimide ring carbonyls, whereas the ester is at 1738 cm^{-1}. Further characteristic vibrations are the two intense vibrations of the ester, indicative of C-C-O and C-O-C stretching, at 1200 and 1065 cm^{-1}. Following primary structural analysis by IR, the polymer was dissolved in a range of solvents to determine solubility and potential viability in sensor application. While more soluble than the carboxylic acid copolymers, **(13)** was still only minimally soluble in the test solvents, as the polymer solutions were significantly turbid and drop cast polymer films contained large particles of undissolved solid (See Figure A.2 in Appendix A for images of polymer solution.)

0.45 and 0.2 µm PTFE syringe filters were used to remove solid particles prior to ^{1}H NMR. NMR analysis of P(3HT-*c*-S3TA) **(13)** shown in Figure 4.35 proved difficult due to the overlap between the protons of the succinimide ring at ca. 2.76 ppm and the protons of the head-tail oriented hexyl chain, also at ca. 2.76 ppm. As such, an accurate determination of the HT/HH ratio cannot be performed, and confidence in the presence of the succinimide protons is reduced. On the other hand, the small signal around 3.73 ppm is in the region that the acetate methylene ($-CH_2-$) would be present and paired with IR spectrum suggests P(3HT-*c*-S3TA) has been formed. 1H NMR (400 MHz, CDCl3) 7.13 6.75 (m, 1H), 3.95 3.40 (m, 1H), 2.79 (s, 1H), 2.55 (s, 1H), 1.70 (s, 1H), 1.51 1.39 (m, 2H), 1.33 (s, 2H), 1.25 (s, 2H), 0.90 (s, 3H).

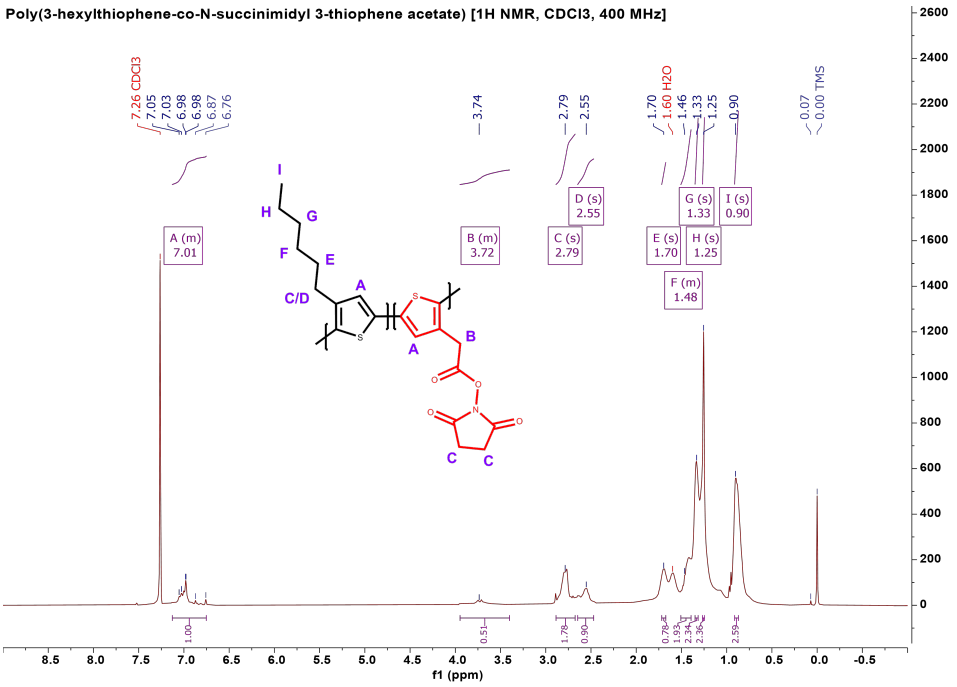

Figure 4.35: ^{1}H NMR spectrum of P(3HT-*c*-S3TA) **(13)**.

To allow for a more complete assessment of solubility, probing the idea that increasing both the length and decreasing the polarity of the pendant chain will aid in producing a soluble product, the synthesis of poly(3-hexylthiophene-co-N-succinimidyl 3-(thiophen-3-yl)acrylate) was targeted. As with the previous polymers, the initial step was to produce the N-succinimidyl ester derivative of T3T3YAA - N-succinimidyl 3-(thiophen-3-yl)acrylate (S3T3YA).

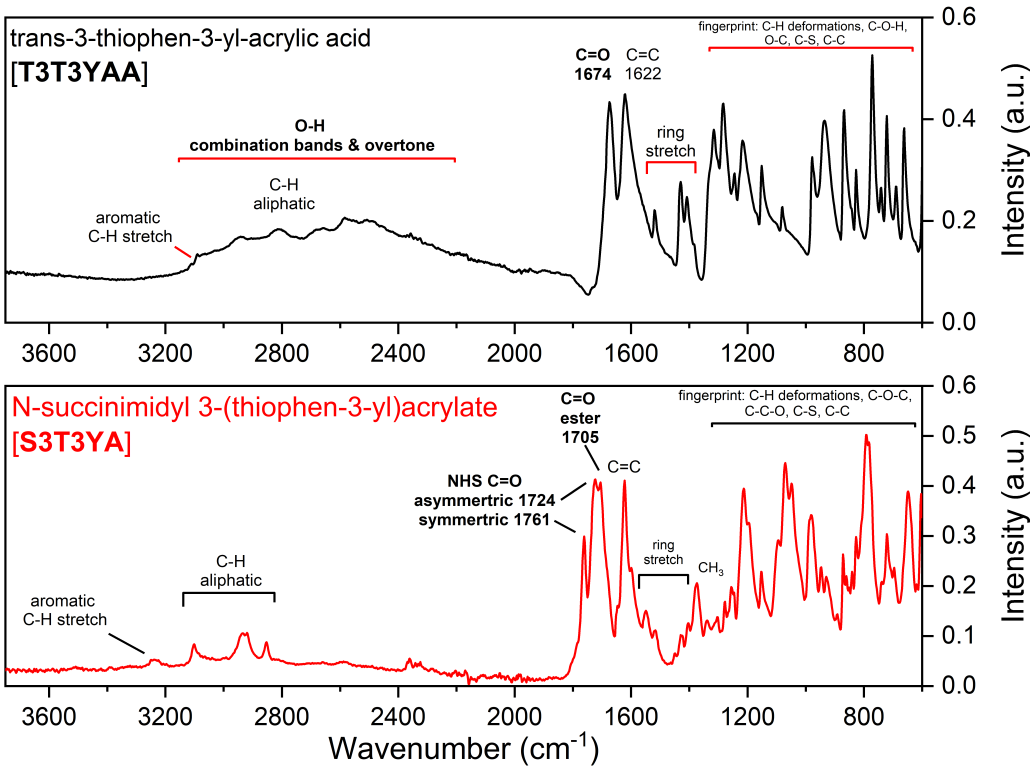

Figure 4.36: IR spectra of T3T3YAA and synthesised N-succinimidyl 3-(thiophen-3-yl)acrylate (S3T3YA) monomers.

In Figure 4.36, comparison of the IR spectra of T3T3YAA and synthesised S3T3YA shows the same changes observed in the synthesis of S3TA are present. That is, loss of the alcohol stretch, emergence of the symmetric and asymmetric NHS carbonyl peaks, at 1761 and 1724 cm^{-1} and shifting of the ester C=O from 1674 to 1705 cm^{-1}. ^{1}H NMR provides additional supporting evidence of the expected structure. Some impurities are present in Figure 4.37, again, highlighting the need for additional purification of the N-succinimidyl ester monomers. However, focusing on the dominant signals, the spectrum is as predicted. S3T3YA Monomer: 1H NMR (500 MHz, CDCl3) 7.83 (d, J = 15.9 Hz, 1H), 7.57 (d, J = 4.1 Hz, 1H), 7.31 (dd, J = 5.2, 2.9 Hz, 1H), 7.27 (d, J = 5.0 Hz, 1H), 6.33 (d, J = 15.9 Hz, 1H), 2.81 (s, 4H).

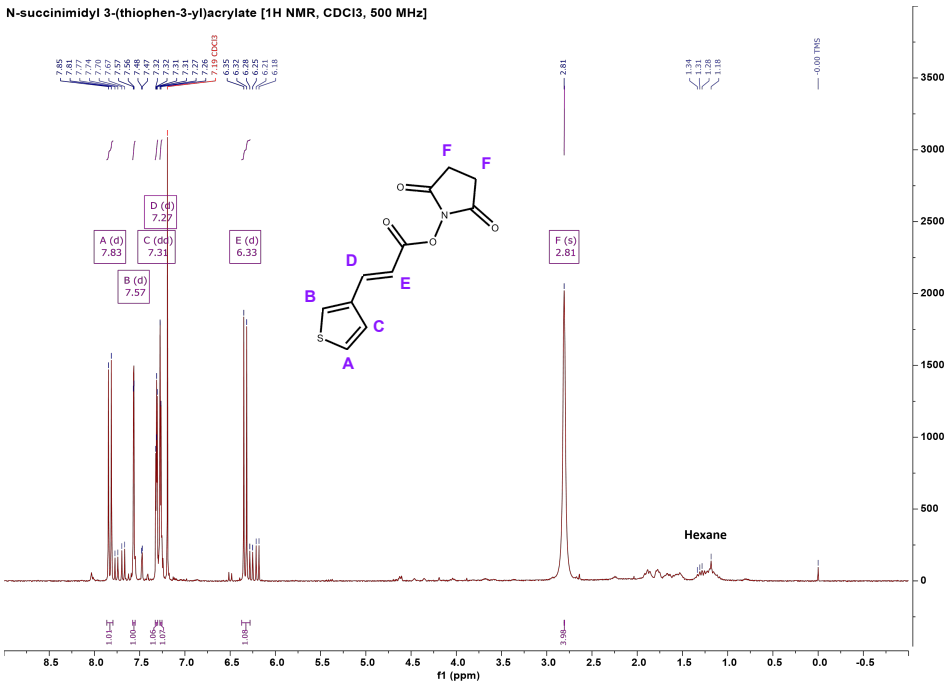

Figure 4.37: ^{1}H NMR spectrum of S3T3YA monomer.

The cluster of signals at between 7.83 - 7.31 ppm are indicative of the three aromatic ring protons (A/B/C), the highly deshielded alkene proton (D) closest to the aromatic ring but on the withdrawing environment of the ester chain can be found at 7.27 ppm while the lesser deshielded alkene proton (E) on the ester side is present at 6.33 ppm. The characteristic protons of the succinimide ring (F) yields a strong singlet peak at 2.81 ppm, giving an overall agreement between the integrals and expected no. of protons.

3-hexylthiophene and N-succinimidyl 3-(thiophen-3-yl)acrylate at a [1:1] molar ratio were polymerised in $CHCl_3$ to give poly(3-hexylthiophene-*co*-N-succinimidyl 3-(thiophen-3-yl) acrylate) **(14)** as a red-brown solid and at a yield of 50.0% (Figure 4.30.D). Although complex due to the broadening of peaks within the sub-1700 cm^{-1} region of the spectrum, IR analysis provides evidence of copolymer formation. Figure 4.38 shows the typical aliphatic C−H peaks at 2955, 2924 and 2853 cm^{-1} from the hexyl chain and the cyclic imide. Thiophene ring stretching is located between ca. 1587-1410 cm^{-1} and the C-H out-of-plane deformation and C-S is below 900 cm^{-1}. The vibrational frequencies arising from the S3T3YA comonomer, that is, a strong, broad carbonyl peak at 1712 and 1724 cm^{-1} from the ester and succinimide, respectively. The second NHS carbonyl seen at 1761 cm^{-1} in Figure 4.36 is missing from the IR spectrum of **(14)** however, as it is highly probable that the S3T3YA component is present, the C=O peak appears to be adsorbed by broadening of the peak. Also

present is the C=C alkene stretch at 1630 cm^{-1}, another characteristic vibration of T3T3YAA and its derivatives.

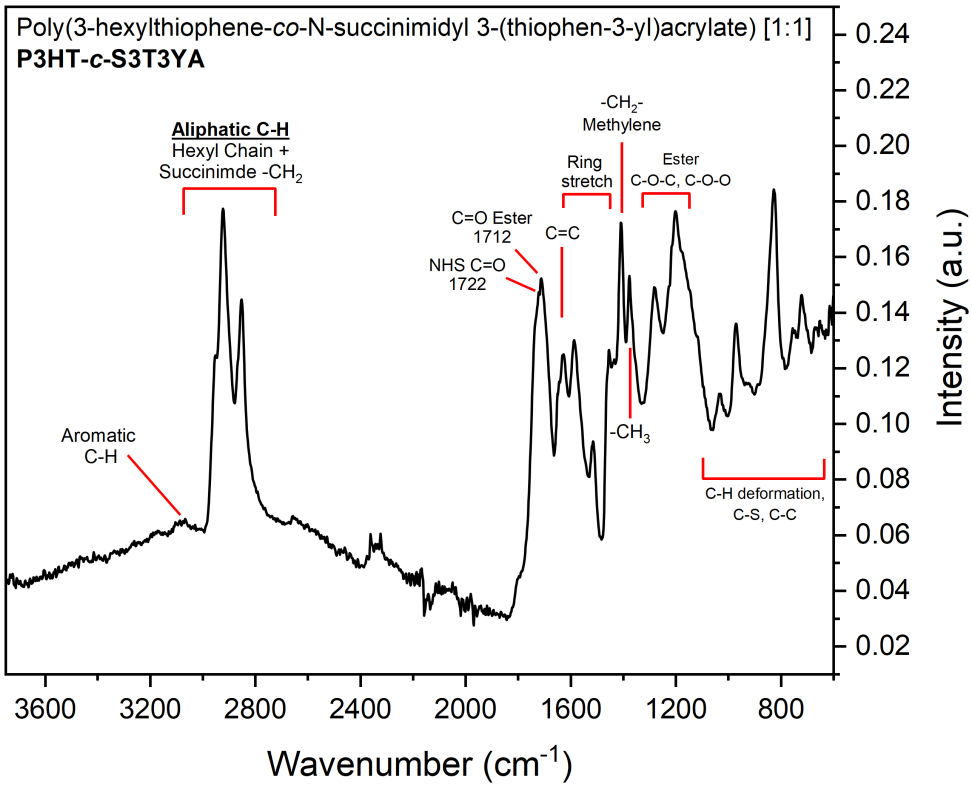

Figure 4.38: IR spectra of P(3HT-*c*-S3T3YA) from $CHCl_3$ **(14)**.

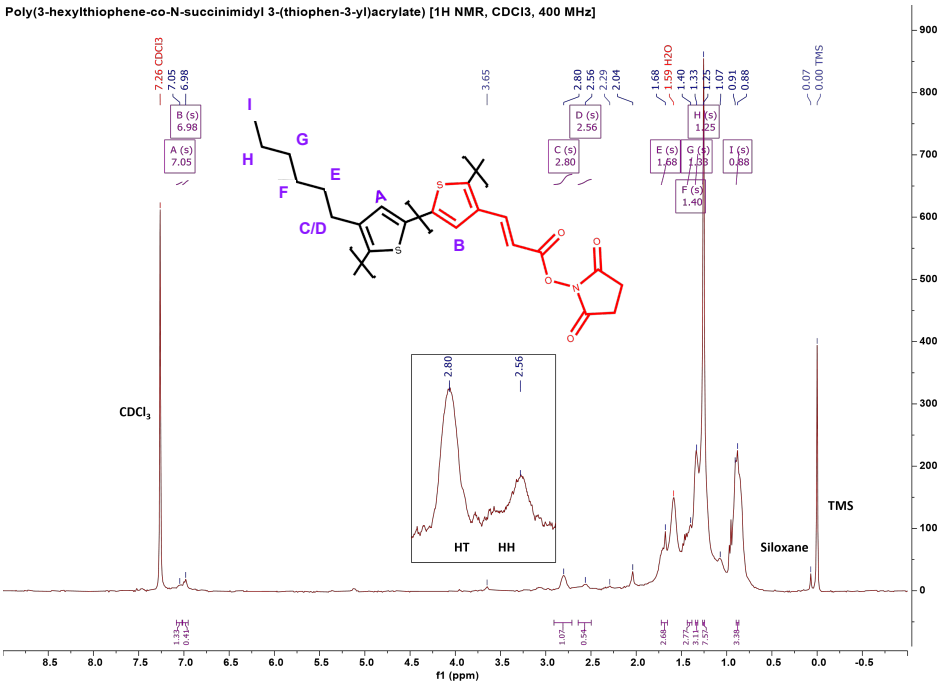

Figure 4.39: ^{1}H NMR spectrum of P(3HT-*c*-S3T3YA) **(14)**.

ATR-FTIR and proton NMR of **(14)** offer contrasting information. By analysing the spectrum in Figure 4.39, it becomes clear the compound dissolved in the $CDCl_3$ NMR solvent is

essentially P3HT homopolymer. None of the expected proton environments for the S3T3YA comonomer are present; this is similar to the solubility phenomena observed for P(3HT-*c*-T3T3YAA) **(9)**, where it is thought the copolymer is insoluble while a small portion of P3HT in the polymer solids is able to dissolve and be assessed by NMR. Figure 4.40 shows a film and solution of **(14)** where the insolubility is clear. P(3HT-*c*-S3T3YA) **(14)**: 1H NMR (400 MHz, CDCl3) 7.05 (s, 1H), 6.98 (s, 0H), 2.80 (s, 1H), 2.56 (s, 1H), 1.68 (s, 3H), 1.40 (s, 3H), 1.33 (s, 3H), 1.25 (s, 8H), 0.88 (s, 3H).

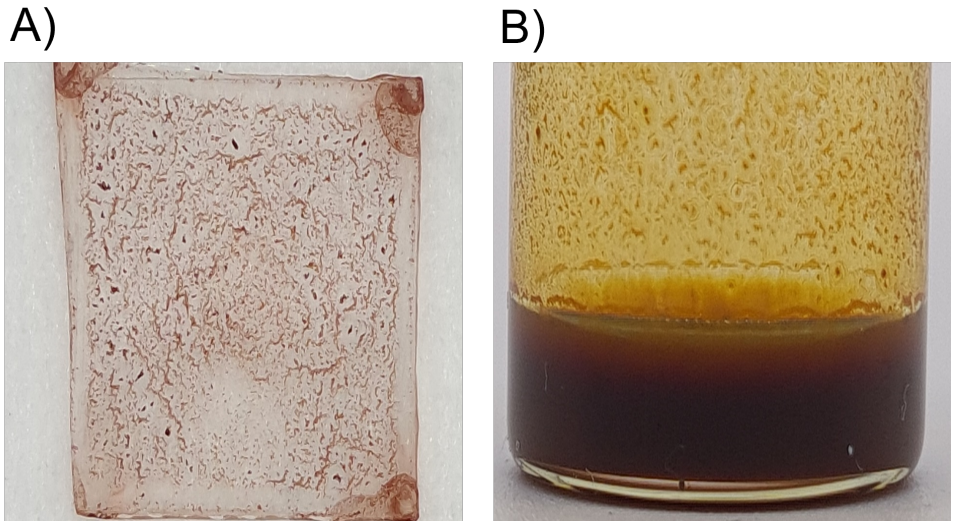

Figure 4.40: Images of A) **(14)** film on Sapphire, and B) solution of **(14)** in $CHCl_3$:C_6H_5Cl (20 mg mL^{-1}).

One of the main motivations for preparing N-succinimidyl thiophene esters was an attempt to overcome the solubility problem in P(3HT-*c*-T3AA) and P(3HT-*c*-T3T3YAA) but reducing the polarity of the pendant while retaining the required functionality for biomolecule immobilisation. As the insolubility of the synthesised polymers remains an issue, chloroform appears a less than ideal solvent in the pursuit of a processable polymer. While synthesis of the polymers using chloroform as the reaction solvent did not yield any polymer capable of solution processing. Due to a change in the $FeCl_3$ solubility and an alteration to the reaction kinetics, polymerisation performed in acetonitrile is likely to produce a lower molecular weight product at a trade-off of reaction yield. Although many factors ultimately determine solubility, as is seen in the dissolution behaviour of polymers **(7)** vs **(10)**, it is probable the chloroform polymers possess a high M_W contributing to the solubility issue.

Reproducing the same polymer using acetonitrile as the reaction should reduce the molecular weight of the materials while positively influencing the solubility, allowing for use in biosensor applications. Overall, section 4.3 outlines the first known preparations of P(3HT-*c*-M3T3YA) **(7)**, P(3HT-*c*-T3T3YAA) **(10)**, P(3HT-*c*-S3TA) **(13)**, and P(3HT-*c*-S3T3YA) **(14)** and represents extension beyond the existing body of knowledge given copolymerisation of the functional monomers with 3-hexylthiophene is not present within the literature.

4.4 Thiophene Polymerisation in Acetonitrile (CH_3CN)

The process for polymerisation between 3-hexylthiophene and the synthesised monomers remains identical for reactions in acetonitrile or chloroform. As this process is the same, the outcome of the polymerisation reactions will be addressed briefly while highlighting the key information. Any differences between polymers produced in acetonitrile and those produced in chloroform will be discussed in more detail. In broad terms, copolymerisation reactions performed in acetonitrile yielded soluble compounds. This is likely due to the reason discussed in the previous section, i.e. reduction in molecular weight of the polymers. The improved dissolution behaviour of the materials now allows for expanded analysis using UV-Vis spectrophotometry for the collection of absorption spectra and the use of GPC-SEC to determine molecular mass.

4.4.1 Carboxylic Acid Polymers - P(3HT-*c*-T3AA) and P(3HT-*c*-T3T3YAA)

Table 4.2: Summary of yields for methyl ester/carboxylic acid polymers from CH_3CN.

ID	Polymer - Target ratio	Yield
(15)/(18)	P(3HT-*c*-M3TA/T3AA) [1:1]	20.3%
(16)/(21)	P(3HT-*c*-M3TA/T3AA) [5:1]	43.8%
(17)/(20)	P(3HT-*c*-M3TA/T3AA) [10:1]	37.7%
(21)/(24)	P(3HT-*c*-M3T3YA/T3T3YAA) [1:1]	42.1%
(22)/(25)	P(3HT-*c*-M3T3YA/T3T3YAA) [5:1]	41.0%
(23)/(26)	P(3HT-*c*-M3T3YA/T3T3YAA) [10:1]	35.5%

All polymerisation reactions involving the methyl ester monomers of M3TA and M3T3YA proceeded without issue in the acetonitrile reaction solvent and oxidant mixture. The product yield for the six polymers are outlined in Table 4.2;

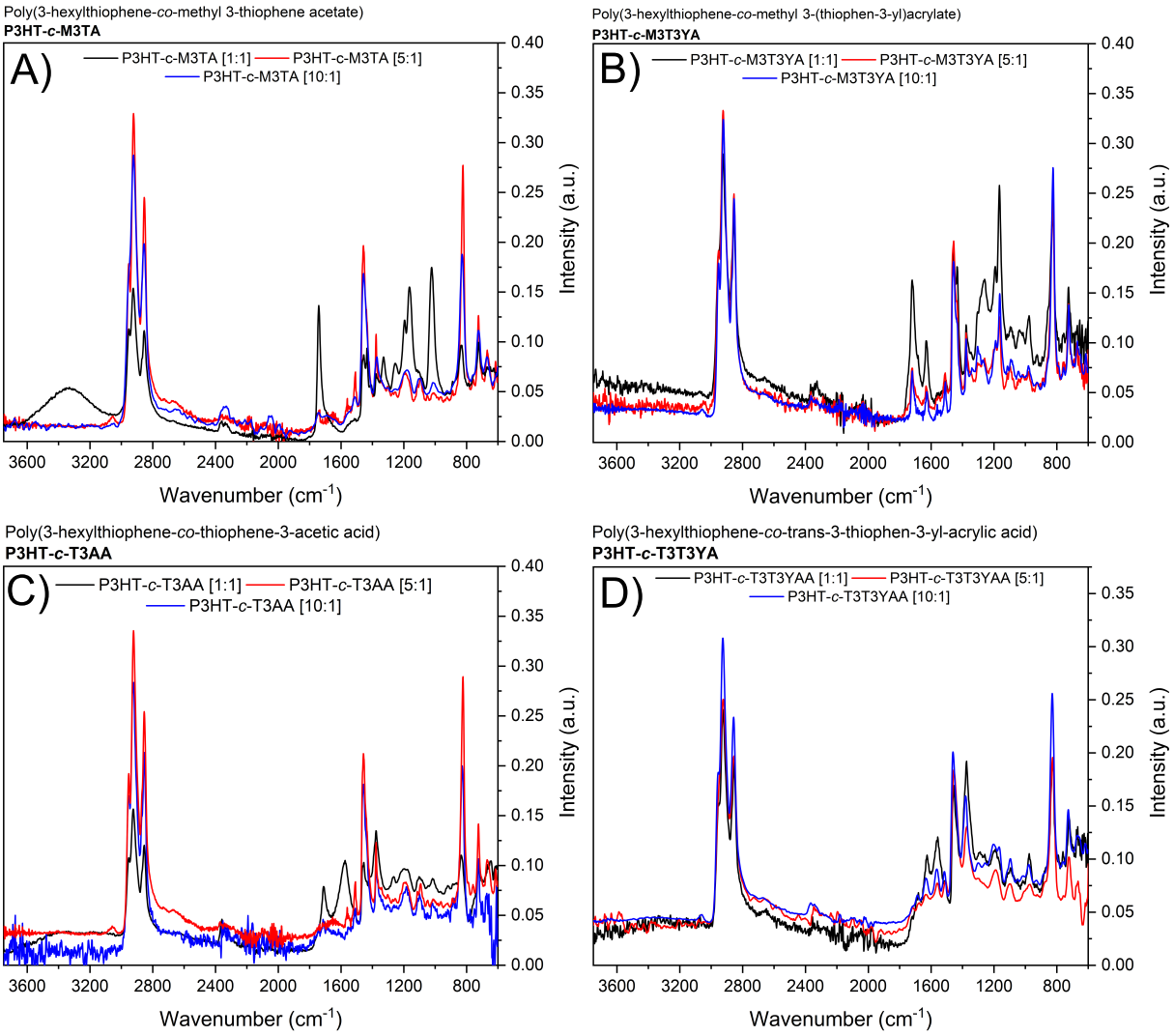

Figure 4.41: IR spectra of A) P(3HT-*c*-M3TA) **(15)**, **(16)** and **(17)**, B) P(3HT-*c*-M3T3YA) **(21)**, **(22)** and **(23)**, C) P(3HT-*c*-T3AA) **(18)**, **(21)**, **(20)** and, D) P(3HT-*c*-T3T3YAA) **(24)**, **(25)**, **(26)**.

TThe composition of the copolymer as a result of the variation in monomer feed ratio ([1:1], [5:1], [10:1]) may offer some additional reasoning for the trend in solubility. Compared to those polymers synthesised in $CHCl_3$, the CH_3CN polymers **(25)** and **(26)** were soluble in the spin-coating solvent ($CHCl_3$:C_6H_5Cl) while the insolubility of polymer **(24)** - P(3HT-*c*-T3T3YAA) remained the same. It becomes clear that an increase in 3HT content provides improvement in solubility when paired with the decrease in molecular weight due to the polymerisation in acetonitrile. This trend remained true for P(3HT-*c*-T3AA), with polymers **(16)** and **(17)** being fully soluble while polymer **(15)** is largely insoluble. Absorption spectroscopy of polymer films spin-coated onto a transparent substrate, e.g. sapphire (Al_2O_3), provides useful information. Firstly, the determination of the absorption maxima between

300 - 500 nm (λ_{max}) provides information on the characteristic $\pi - \pi^*$ transition of the conjugated polymer thiophene backbone and offers more evidence of differentiation of synthesised polymer. The $\pi - \pi^*$ absorption gives an indication of intermolecular forces and π stacking efficiency. Increases in conjugation length and a high degree of orientated π-stacking are represented by a λ_{max} shift to a longer wavelength, i.e. a bathochromic shift. Secondly, focusing on the 700 - 800 nm near-IR region of the spectra gives an indication of solubility by highlighting the presence of undissolved particles in the polymer film. At this wavelength, the bulk polymer film is transparent to the near-IR light; however, particles in the film scatter that light and produce a non-zero absorbance. The rationale for this method arises from the determination of turbidity in 'cloudy' liquid samples where the same idea of non-zero absorbance in particulate-laden samples is exploited.

Table 4.3: Table of UV-Vis Absorbance Maxima (λ_{max}) and absorbance at 800 nm - Polymers **(15)** to **(26)**.

ID-Polymer	λ_{max} (nm)	700 - 800 nm absorbance	Soluble?
(2) - P3HT	484	0	Yes
(15) - P(3HT-*c*-M3TA) [1:1]	380	0	Yes
(18) - P(3HT-*c*-T3AA) [1:1]	393	1.6	Partial
(16) - P(3HT-*c*-M3TA) [5:1]	495	0	Yes
(19) - P(3HT-*c*-T3AA) [5:1]	489	0	Yes
(17) - P(3HT-*c*-M3TA) [10:1]	453	0	Yes
(20) - P(3HT-*c*-T3AA) [10:1]	458	0	Yes
(21) - P(3HT-*c*-M3T3YA) [1:1]	449	0	Yes
(24) - P(3HT-*c*-T3T3YAA) [1:1]	482	0.1	Partial
(22) - P(3HT-*c*-M3T3YA) [5:1]	478	0.05	Yes
(25) - P(3HT-*c*-T3T3YAA) [5:1]	466	0	Yes
(23) - P(3HT-*c*-M3T3YA) [10:1]	482	0	Yes
(26) - P(3HT-*c*-T3T3YAA) [10:1]	480	0	Yes

As outlined in Table 4.3 and Figure 4.43, the [1:1] polymers **(15)** and **(21)** exhibit a hypsochromic shift relative to the P3HT reference, indicating inhibition of efficient packing due to the presence of the methyl ester and carboxylic acid side chains. However, as the relative amount of 3HT monomer increases, the absorption maximum returns to values closer to that of P3HT homopolymer and, although minimal in the higher 3HT ratio polymers, the [1:1] polymers show a clear difference between the protected methyl ester and the deprotected carboxylic acid. In this case, it is likely the bathochromic shift from 449 nm in **(21)** to 482 nm in **(24)** arises from the reformation of favourable intermolecular bonds between

the acid groups on different polymer chains, promoting better packing and increasing the conjugation length (See Figure 4.44). The same shift is observed from 380 nm in P(3HT-*c*-M3TA) - **(15)** to 395 nm in P(3HT-*c*-T3AA) - **(18)**. Across all spectra in Figures 4.43 and Figure 4.44, the discontinuity at 350 nm is the result of the spectrophotometer changing between the visible and UV-light source.

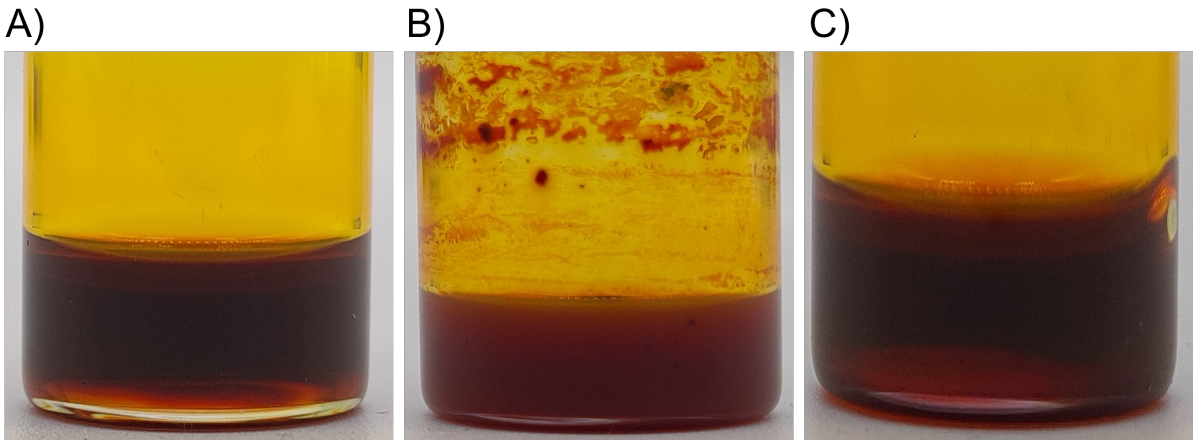

Figure 4.42: Images of polymer solutions A) P(3HT-*c*-M3TA) **(15)**, B) P(3HT-*c*-T3AA) **(18)**, and C) P3HT **(2)**.

In the near-IR region (700-800 nm), the non-zero absorbance corresponds well to the observed solubility behaviour of the polymers. In all the fully soluble polymers, the ability to deposit a continuous film of a reasonable quality allowed for the collection of a typical, strongly absorbing UV-Vis spectra with a single broad maximum. In the partial or insoluble polymers, the spectra are flat, possessing even broader absorption with scattering of near-IR light resulting in non-zero absorbance. Figure 4.42 shows the spin-coating solutions of polymers **(15)**, **(18)** and **(2)** at 15 mg mL^{-1}. This gives a representation of polymer solubility, and, as discussed, highlights how the insoluble portion of polymer **(18)** contributes to turbidity in the solution and particles in the film.

Only the polymers suitable for biosensor application, i.e. soluble and capable of enzyme immobilisation, were analysed via GPC-SEC for the determination of molecular weight and Polydispersity index. P(3HT-*c*-T3T3YAA) [5:1] - **(25)** has a M_W= 8214 g mol^{-1} and a PDI = 2.39, for P(3HT-*c*-T3T3YAA) [10:1] - **(26)** the M_W = 5007 g mol^{-1} and PDI = 1.83. In the acetic acid polymers, P(3HT-*c*-T3AA) [5:1] - **(21)** has a M_W = 13,920 g mol^{-1} and a PDI = 2.03 while P(3HT-*c*-T3AA) [10:1] - **(20)** has a M_W = 13,700 g mol^{-1} and a PDI =

2.42. The polymer weights determined here are lower than literature values for that of P3HT from a chloroform reaction solvent (>30,000 g mol^{-1}) [311, 315] but comparable to P3HT synthesised in acetonitrile [314]. This provides evidence for the hypothesis that polymerisation reactions in acetonitrile yield a lower molecular weight product.

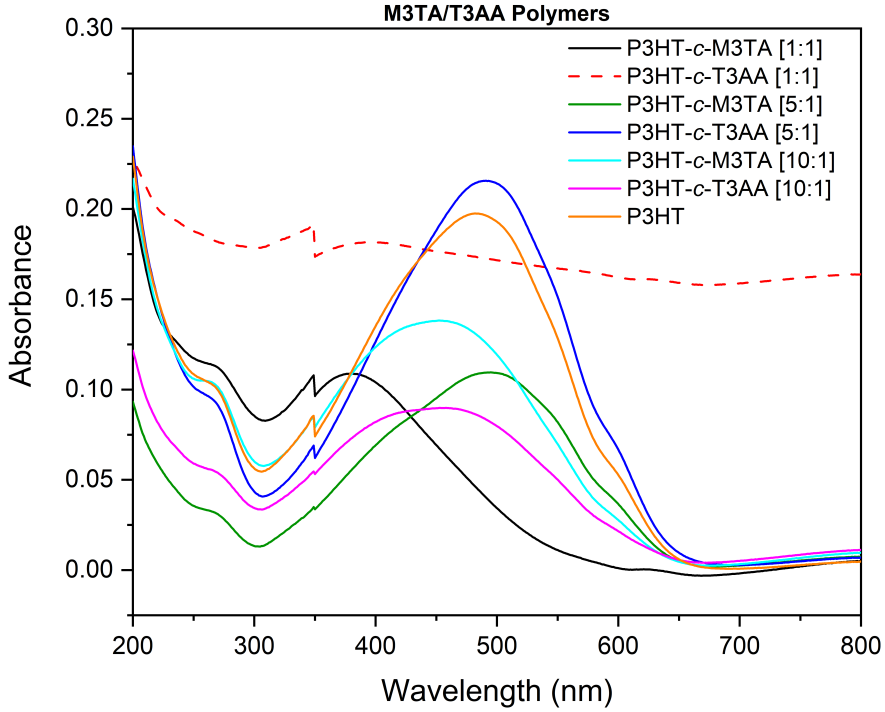

Figure 4.43: UV-Vis adsorption spectra of P(3HT-c-M3TA/T3AA) polymers **(15)** to **(20)**.

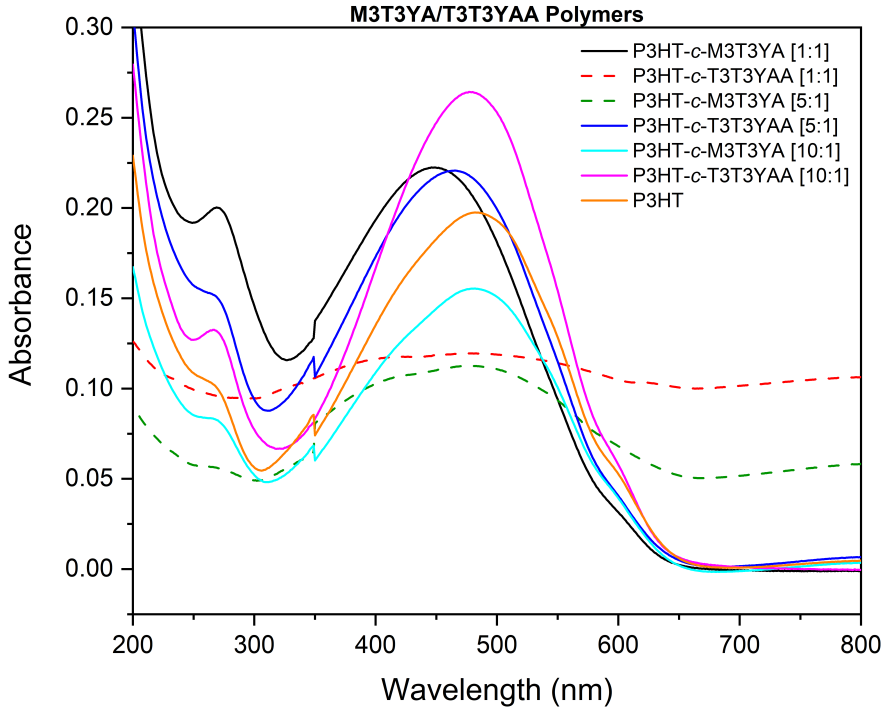

Figure 4.44: UV-Vis absorption spectra of P(3HT-c-M3T3YA/T3T3YAA) polymers **(21)** to **(26)**.

4.4.2 N-succinimidyl Ester Polymers - P(3HT-*c*-S3TA) and P(3HT-*c*-S3T3YA)

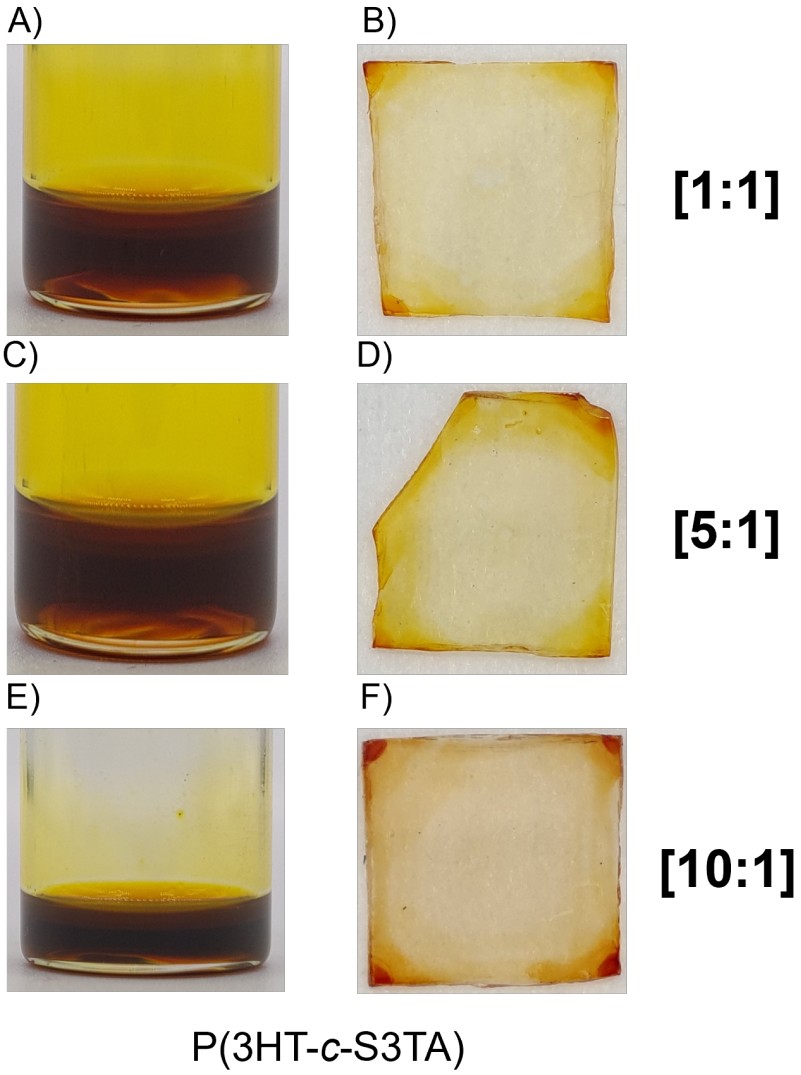

Figure 4.45: Images of P(3HT-*c*-S3TA) solutions (15 mg mL^{-1}) in $CHCl_3$:C_6H_5Cl and films on Al_2O_3 substrates. A/B) [1:1] **(27)**, C/D) [5:1] **(28)** and E/F) [10:1] **(29)**.

The final set of polymers prepared in this project were the acetonitrile variants of both N-succinimidyl esters: P(3HT-*c*-S3TA) and P(3HT-*c*-S3T3YA). As discussed above in Section 4.3.3, these monomers have been chosen to impart reactivity to the biomolecule without the need for deprotecting the polymer and the subsequent EDC/NHS coupling. The polymerisation reactions proceeded without issue, affording red/black powdered solids with monomer ratios of [1:1], [5:1] and [10:1] targeted. All six of the succinimidyl ester polymers from CH_3CN were highly soluble in the spin coating solvent mixture ($CHCl_3$:C_6H_5Cl) and was capable of producing a good quality thin film with no particulates as showcased in Figure 4.45.

The product yields in this series (Table 4.4) were lower than expected and significantly decreased when compared to the chloroform equivalents (**(13)** - 45.1% and **(14)** - 50.0%). Several factors, such as the physical conditions, e.g. reaction temperature, reaction duration, duration of monomer addition and the chemistry choices, e.g. reaction solvent, monomer/oxidant ratio, monomer choice and oxidant choice, all affect polymerisation yield. Although certain conditions, e.g. reaction temperature and oxidant choice, have a large impact on the yield, these variables can be excluded when comparing the synthesised polymers as they remain constant in all reactions, while other factors such as reaction solvent, monomer choice, and reaction-scale could offer some explanation. These factors will drastically influence the kinetics of polymerisation, affecting the product yield [304, 308, 311, 314, 325].

Table 4.4: Summary of yields for N-succinimidyl ester polymers from CH_3CN.

ID	Polymer - Target ratio	Yield
(27)	P(3HT-*c*-S3TA) [1:1]	10.9%
(28)	P(3HT-*c*-S3TA) [5:1]	7.42%
(29)	P(3HT-*c*-S3TA) [10:1]	17.0%
(30)	P(3HT-*c*-S3T3YA) [1:1]	18.1%
(31)	P(3HT-*c*-S3T3YA) [5:1]	21.6%
(32)	P(3HT-*c*-S3T3YA) [10:1]	33.2%

It was observed both the N-succinimidyl ester monomers were slightly less soluble in acetonitrile than the same monomers in chloroform and the methyl ester monomers in both solvents, therefore, as the monomer solution is fed into the oxidant, a portion of the monomer remains unreacted and is removed during polymer precipitation and purification. This may highlight the requirement for the implementation of additional purification steps during the monomer synthesis. Secondly, the reaction scale appears to have a slight impact on yield; specifically, reactions with a greater mass of starting material yielded more product, whereas less starting material gave less product. This phenomenon was not explicitly investigated, but inferred from the yield data collected throughout the duration of this project. Potential reasons could include improved mixing in larger reaction volumes, ensuring more efficient interaction between reactants leading to higher yields over the specific reaction duration. Additionally, there are practical implications to using larger reaction volumes, particularly that it is easier to handle larger quantities of material which minimises the effect of product

loss during precipitation and collection.

As with the polymer in Section 4.4.1, the solubility of polymers **(27)** to **(32)** enabled characterisation by UV-Vis and GPC-SEC. All six N-succinimidyl ester polymers possessed a hypsochromic shift relative to P3HT homopolymer, with the three variations of P(3HT-*c*-S3TA) being drastically blue-shifted. The UV-Vis spectra is presented in Figures 4.46 and 4.47 with λ_{max} values summarised in Table 4.5. The large hypsochromic shift seen in polymers **(27)**, **(28)**, and **(29)** indicates poor π-stacking and, subsequently, a lower conjugation length. The inclusion of S3TA comonomer in the polymer structure has a clear impact on the electronic structure and while a bathochromic shift is observed in all the carboxylic acid polymers, the nature of the N-succinimidyl ester groups results in no additional intermolecular forces to aid in packing efficiency. Hypsochromic shift of polymers **(30)**, **(31)**, and **(32)** is noticeably reduced compared to P(3HT-*c*-S3TA).

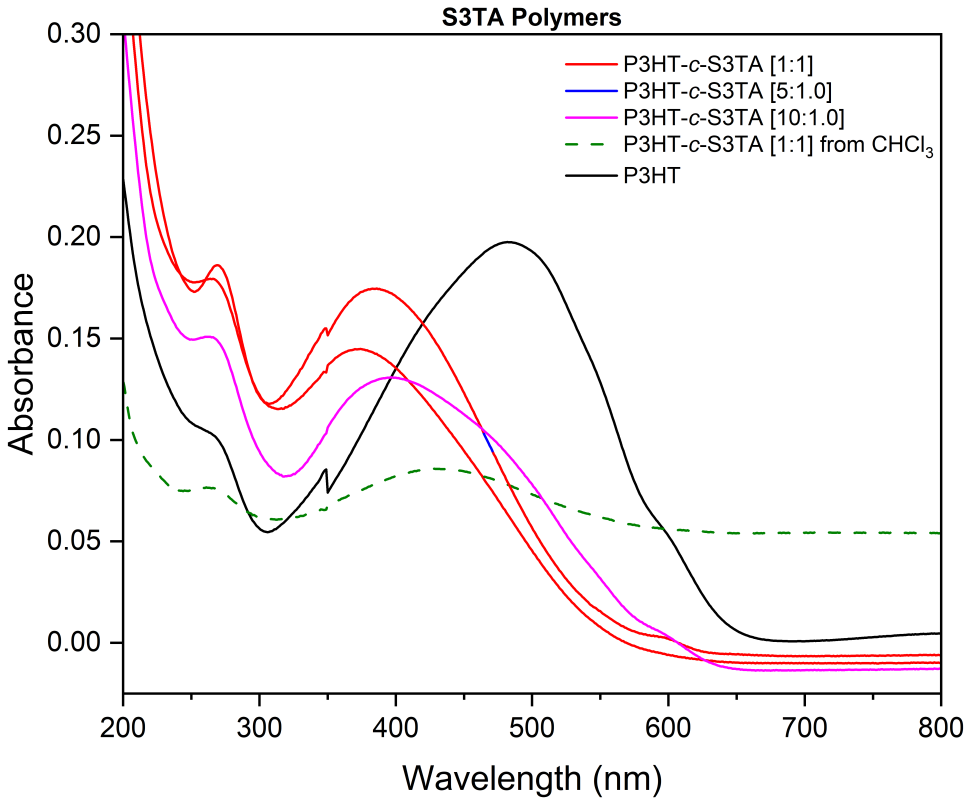

Figure 4.46: UV-Vis absorption spectra of P(3HT-*c*-S3TA) polymers **(27)** to **(29)**.

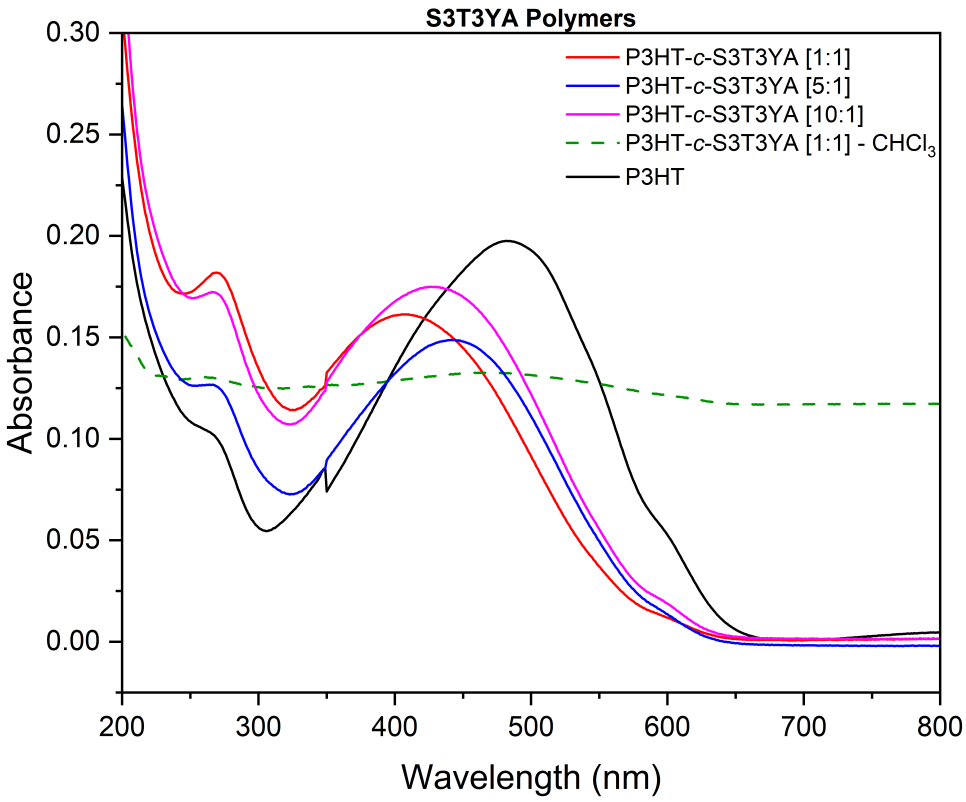

Figure 4.47: UV-Vis absorption spectra of P(3HT-*c*-S3T3YA) polymers **(30)** to **(32)**.

Table 4.5: Table of UV-Vis Absorbance Maxima (λ_{max}) and absorbance at 800 nm - Polymer **(27)** to **(32)**.

ID-Polymer	λ_{max} (nm)	700 - 800 nm absorbance	Soluble?
(2) - P3HT	484	0	Yes
(13) - P(3HT-*c*-S3TA) from $CHCl_3$	428	0.05	No
(27) - P(3HT-*c*-S3TA) [1:1]	374	0	Yes
(28) - P(3HT-*c*-S3TA) [5:1]	386	0	Yes
(29) - P(3HT-*c*-S3TA) [10:1]	397	0	Yes
(14) - P(3HT-*c*-S3T3YA) $CHCl_3$	469	0.12	No
(30) - P(3HT-*c*-S3T3YA) [1:1]	410	0	Yes
(31) - P(3HT-*c*-S3T3YA) [5:1]	441	0	Yes
(32) - P(3HT-*c*-S3T3YA) [10:1]	430	0	Yes

GPC-SEC analysis was performed on the six, soluble N-succinimidyl ester polymers as tabulated in Table 4.6. Unexpectedly, polymers **(28)** and **(29)** gave a distinct bimodal distribution of molecular weights while **(30)** does possess two peaks but are less resolved and more broad in nature. It is difficult to draw overriding conclusions from this information due to the possibility of a range of contributing factors. The bimodal distribution of polymer **(28)** may be the result of two different polymer components in the sample or two size distributions of P(3HT-*c*-S3TA) with low weight component centred on 1228 g mol^{-1} possessing a

higher concentration of S3TA monomer than the high weight component possessing more P3HT or vice versa. The data determines the low-weight component comprises ca. 25% of the eluded volume, whereas the high M_W portion makes up the other ca. 75%. The consequences of this bimodal distribution are interesting to consider.

Table 4.6: Table of molecular weights and polydispersity values for polymers **(27)** to **(32)**.

ID-Polymer	M_W (g mol^{-1})		PDI
	Peak 1	Peak 2	
(27) - P(3HT-*c*-S3TA) [1:1]	1,343	18,249	3.65
(28) - P(3HT-*c*-S3TA) [5:1]	1,228	17,678	6.21
(29) - P(3HT-*c*-S3TA) [10:1]	1,183	9,779	2.67
(30) - P(3HT-*c*-S3T3YA) [1:1]	1,280	17,840	3.29
(31) - P(3HT-*c*-S3T3YA) [5:1]	1,939		2.22
(32) - P(3HT-*c*-S3T3YA) [10:1]	2,447		1.95

The observed shifts in the UV-Vis absorption spectra may be, in part, explained by a dependence on molecular weight and polydispersity. The effect of M_W on the optoelectronic properties on thiophene-type polymers has been investigated by Hayashi et al. and by Trznadel et al. and does indicate increasing conjugation length with increasing molecular weight [312, 326].

4.5 Summary

In this chapter, the synthesis of four novel 3-hexylthiophene copolymers: P(3HT-*c*-M3T3YA), P(3HT-*c*-T3T3YAA), P(3HT-*c*-S3TA), and P(3HT-*c*-S3T3YA), has been outlined and discussed. These materials, which represent the first reported preparation of their kind, were synthesised using established methods, including methyl esterification, NHS-activation, and chemical oxidative polymerisation. The novelty of this work lies in the copolymerisation of 3-hexylthiophene, a widely studied and readily available monomer, with comonomers capable of covalently bonding biomolecules such as enzymes.

Synthesised copolymers, shown and summarised in Figure 4.48, were characterised using a range of analytical techniques. Attenuated total reflectance - fourier transform infrared spectroscopy (ATR-FTIR) was employed as the primary method owing to ease-of-access and effectiveness in identifying characteristic vibrations, such as the aliphatic C−H stretch of the

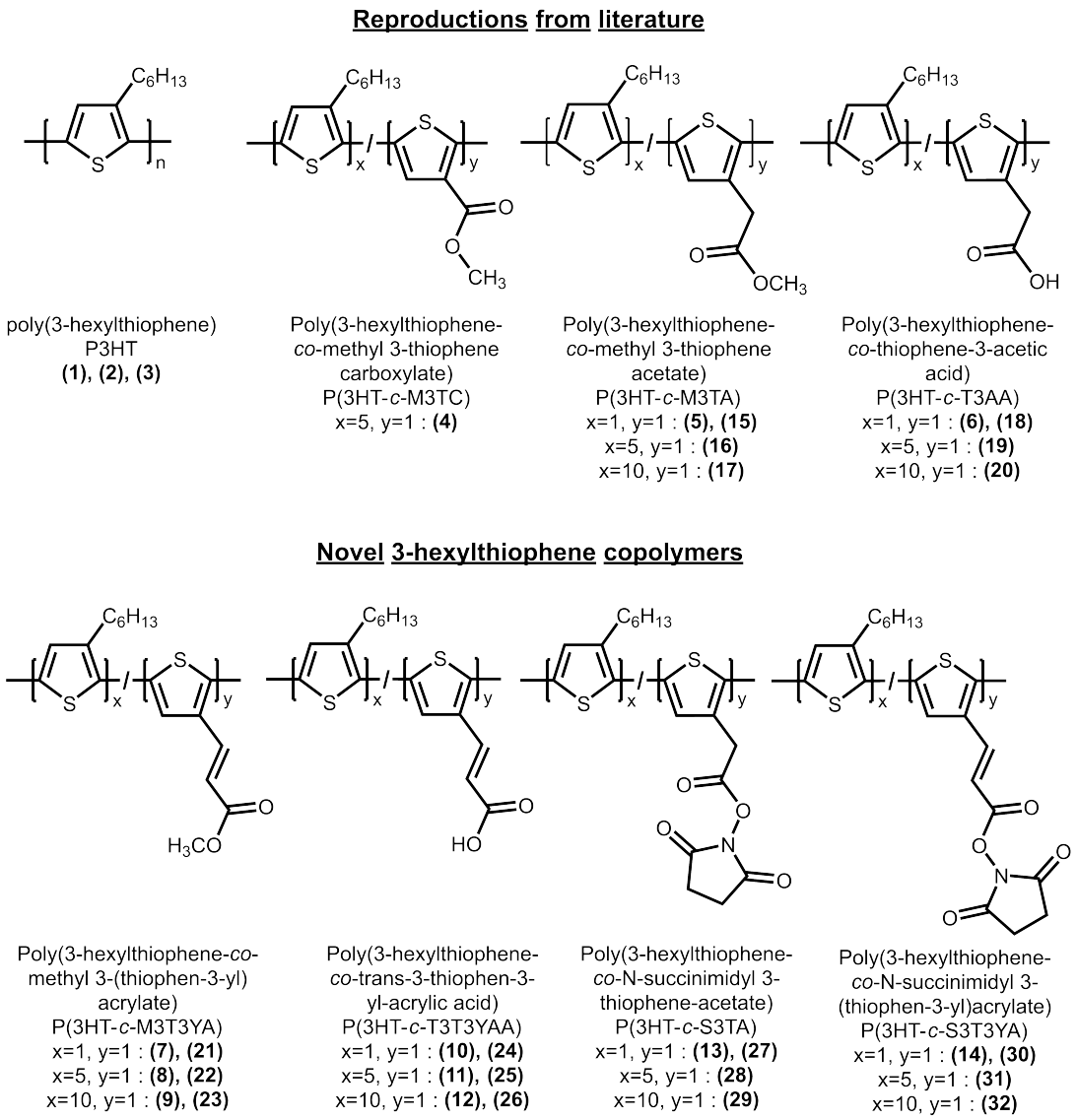

Figure 4.48: Structures of reproduced and novel 3-hexylthiophene polymers synthesised in this project.

hexyl ($-C_6H_{13}$) pendant group in 3HT and the carbonyl (C=O) vibrations in the carboxylic acid, methyl ester, or N-succinimidyl ester comonomers. Structural analysis was further supported by ^{1}H NMR when possible. For the soluble copolymers synthesised in acetonitrile, UV-Vis spectroscopy provided absorption spectra, and GPC-SEC was used to determine molecular weight distribution.

The motivations behind this work focused on the production of soluble polymers, suitable for thin film deposition by solution processing, and capable of gram-scale production through a facile and cost-effective synthesis. Although challenging, these objectives were successfully achieved. As detailed in Section 4.4, copolymers synthesised in acetonitrile, including all N-succinimidyl ester copolymers and certain T3AA and T3T3YAA polymers with high 3HT

monomer content ([5:1], [10:1]), met these criteria. Overall, the synthesis work to generate these soluble polymers enables the application of such materials in a model sensing platform as discussed and evaluated in Chapter 7.

Chapter 5
Experimental Methods - Polydimethylsiloxane (PDMS) Selective Metallisation

This chapter covers the experimental methods used in the development of a selective metallisation process that utilises surface-modified PDMS printing stamps. The processes described below includes; PDMS stamp casting, UV/O_3 surface treatment, surface regeneration methods as well as accompanying analytical techniques.

Table A.1 contains a list of reagents, chemical formulae and product purity/grades of those described in Chapters 5, 6 and 7. This can be found in Appendix A *Chemicals and Solvents*.

5.1 PDMS Stamp Preparation

The production of polydimethylsiloxane (PDMS) for use in printing is well-established [257]. Primarily used in soft lithography methods e.g. microcontact printing (μCP), the manufacturing of PDMS stamps follows a mature process to create high-quality, smooth surfaces capable of ink transfer. The PDMS used in this project (Sylgard™ 184) is supplied by the manufacturer as a two-part kit containing a silicone elastomer base and thermal cross-linking agent. The base and cross-linker were mixed in a [10:1] ratio by mass, until homogeneous. Due to the introduction of air bubbles during mixing, the liquid precursor was degassed at ~1 mbar for 30 min before casting into an aluminium plate mould (200 x 100 x 0.3 mm). The cast PDMS was cured in a convection oven (100 °C, 60 min). Once cured and solid, the PDMS blocks were left in the mould until use.

5.2 Fabrication of Photomasks

A range of masks were used in this project, from in-house fabricated geometric shapes to high-quality source-drain evaporation masks purchased from a supplier. A TS 3040 laser cutter was used to prepare basic geometric photomasks from 0.25 mm thick polyethylene naphthalene (DuPont Teijin Films™ Teonex®) or 0.5 mm thick aluminium substrates.

For complex patterns, high-density, source-drain deposition masks possessing micron-sized transistor features were purchased from Ossila.

5.3 Ultraviolet-Ozone (UV/O_3) Surface Treatment

Immediately prior to ultraviolet-ozone surface treatment, the PDMS blocks were demoulded and cut into the appropriate dimension for stamping (40 x 40 mm) or surface analysis (10 x 10 mm) before rinsing with ethanol and drying with N_2.

To achieve patterned surface modification, a mask was pressed firmly onto the PDMS surface, protecting specific areas from ozone treatment. A Novascan PSD-S digital UV/O_3 cleaner was used to irradiate samples for 240 min at a light array-to-sample height of ~5 mm. According to the manufacturer, the maximum applied power density is 28 - 32 W cm^{-2} at a wavelength of 253.7 nm.

5.4 Deposition of Krytox1506 Oil Mask

As discussed in Section 2.12, patterned metal deposition by the selective metallisation process relies on the deposition of a high-quality sacrificial oil mask onto the substrate or web. Following UV/O_3 surface treatment, 300 µL of Krytox1506 oil was coated onto modified-PDMS using a Laurell WS-650XZ-6NPPLITE spin coater. The oil is deposited onto the block statically before spinning at 5000 rpm for 180 s [136].

The oil-coated PDMS stamps were contacted to a PET substrate for 2 min to allow for the transfer of the sacrificial mask. A 200 g weight was placed on the stamp to ensure a consistent and repeatable stamping force for all PDMS stamping attempts.

5.5 Metal Deposition - Vacuum Thermal Evaporation

The use of vacuum thermal evaporation allows for the deposition of metal via a simple yet controllable process and is crucial to the success of sacrificial oil selective metallisation [270].

Oil-masked PET substrates were loaded into an Edwards E306A Vacuum Thermal Evaporator, where a thin layer of silver (Ag) or copper (Cu) was deposited. The desired metal

was evaporated from a resistive heating tungsten boat at a pressure of 9 x 10^{-5} mbar to a thickness of ~50 nm (rate of 0.5 nm s^{-1}). The film thickness was monitored by quartz crystal micro-balance (QCM).

5.6 Regeneration of PDMS Stamps

Different surface regeneration procedures were applied to UV/O_3-modified PDMS in an attempt to control PDMS's intrinsic ability to undergo hydrophobic recovery. Prior to application of a regeneration process the residual Krytox oil was removed from the surface of the PDMS by the following process: 1) rinse surface with isopropanol (C_3H_8O), 2) wipe with an isopropanol-soaked, lint-free wipe, 3) wipe with Novec™ HFE-7200 soaked clean-room wipe, 4) rinse with ethanol (C_2H_6O), and 5) dry using N_2.

During the project, two regeneration approaches were investigated.

1. **Thermal**: A sustained heat treatment was applied to the UV/O_3-PDMS blocks using a convection oven. Temperatures of 50, 100, 150 and 200 °C at treatment lengths between 15 and 90 min were investigated.

2. **Silica Dissolution**: UV/O_3-modified PDMS was submerged in a 0.01 M phosphate-buffered saline solution at 85 °C for 60 min to dissolve the 'silica-like' surface layer generated during ozone treatment. After the dissolution process, the PDMS-block was rinsed, dried using N_2.

5.7 Analytical Methods

Pristine PDMS, surface-modified PDMS, patterned metal substrates and regenerated PDMS stamps were analysed using optical and electron imaging methods, infrared spectroscopy, as well as surface analysis techniques such as XPS and drop shape analysis. The application of these methods and techniques paired with patterned metal deposition experiments allowed for the effective determination of wetting behaviour and surface regeneration efficacy.

5.7.1 Imaging

Optical micrographs were acquired using a Yenway CX40M Microscope. Scanning electron micrographs (SEM) were captured on a Zeiss EVO SEM. Operational conditions: Working distance = 8 mm, 5 kV acceleration voltage and Probe current = 250 pA. Prior to electron imaging, PDMS samples were coated with a thin layer of sputtered platinum (5 nm) to prevent with surface charging.

5.7.2 Surface Analysis

The surface chemistry of pristine, UV/O_3-modified and regenerated PDMS was determined by Attenuated total reflectance - fourier transform infrared spectroscopy (ATR-FTIR) using a Varian Excalibur FTS 3500. Measurements were taken between 3750 - 600 cm^{-1}.

Further analysis by X-ray photoelectron spectroscopy (XPS) of the surface and near-surface region of pristine and modified PDMS allowed for the characterisation of elemental composition. PDMS samples were analysed using a Thermo Scientific K-Alpha XPS instrument. Depth profile analysis was performed in order to determine changes in atomic percentages of carbon, oxygen and silicon. XPS was performed by the Oxford Materials Characterisation Service, operating at 12 KeV with a spot size of 400 μm. Depth profile survey was performed using an Argon ion source at 1000 V with a beam incident angle of 30°.

5.7.3 Roughness Characterisation

Changes in surface roughness arising from the irradiation of PDMS by UV/O_3 as well as from the application of regeneration methods, can be determined by analysis of areal roughness parameters e.g. arithmetic mean surface height (Sa). Interference microscopy for macro-scale roughness and atomic force microscope for quantification of nano-scale roughness were employed for characterisation purposes.

Macro-scale roughness was measured using a Filmetrics Profilm3D optical profiler at x50 magnification in a composite white light (WLI) and phase shifting interferometry (PSI) operation mode. Areal roughness analysis using ProfilmOnline, allowed for collection of Sa from a 100 x 100 μm selection area.

An Agilent 5400 AFM/SPM in non-contact mode was used for the collection of nano-scale roughness parameters. Operation conditions: collection area = 1 x 1 μm, scan rate = 512 lines s^{-1}. Raw AFM data was processed using Gwyddion.

5.7.4 Sessile Drop Method for Contact Angle

Determination of contact angle via drop shape analysis offered an effective method to probe the wetting behaviour of multiple liquid compounds e.g., water, Krytox1506, diiodomethane. Moreover, the determination of contact angles from a dispersive component (diiodomethane) and a polar component (water) allows for the determination of surface free energy by application of the Owens-Wendt-Rabel-Kaeble (OWRK) model. Calculating the surface energy of a solid surface allows the researcher to better understand how liquid materials will interact with the surface of interest.

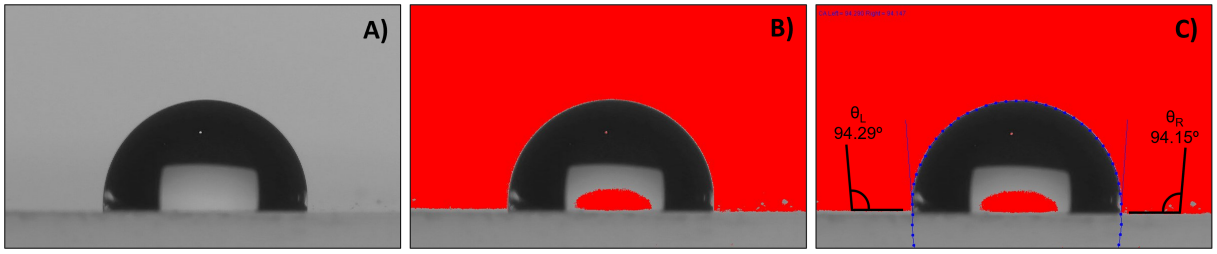

Figure 5.1: Example analysis process for determination of contact angle. A) Micrograph of water droplet on PDMS, B) Thresholding to highlight droplet edge and C) Contact angle calculation using DropSnake plug-in. $\theta_L = 94.29°$, $\theta_R = 94.14°$.

Using a 21 g hypodermic needle, droplets of Krytox1506 oil ($(C_3F_6O)_nC_5F_{12}O$), water (H_2O) and diiodomethane (CH_2I_2) are placed onto the surface of pristine or modified PDMS. Micrographs of the droplet-PDMS interface were captured using an Osilla Contact Angle Goniometer 10 s after deposition to eliminate contact angle variance caused by time-dependent spreading of the droplet. Image processing and analysis of static contact angle was performed on ImageJ using the DropSnake plug-in, an example of this process is shown in Figure 5.1 [327].

Chapter 6
UV/O_3-PDMS Selective Metallisation and Regeneration of Printing Surfaces

The chapter discusses the regeneration of UV/O_3-modified polydimethylsiloxane printing stamps by thermal and chemical enhancement of intrinsic contact angle recovery.

This work centres on the development of UV/O_3-irradiated polydimethylsiloxane (PDMS) printing plates and deposition of sacrificial Krytox1506 oil masks in a selective metallisation process. The primary motivations revolve around exploring the limitations of UV/O_3-PDMS selective metallisation by better understanding the oil-wetting behaviour and the hydrophobic/oleophobic recovery, an intrinsic property of oxidised-PDMS. Additionally, this research aims to determine a surface regeneration process to enable the re-use and repatterning of UV/O_3-PDMS print plates to reduce materials waste and plate fabrication time. Furthermore, the use of UV/O_3-PDMS in the deposition of functional electrodes will be explored with the aim of producing a simple strip electrode for application in a glucose biosensor device. This is outlined in Chapter 7 - Glucose Biosensor Electrodes: Fabrication, Immobilisation and Analysis.

6.1 Reference Data: P-PDMS and UVO240-PDMS

Oxidation of the hydrophobic pristine PDMS (P-PDMS) by 240 min UV/O_3-oxidation (UVO240-PDMS) results in modification of various material properties and characteristics. The determination of contact angles for water and Krytox1506 oil is a particularly relevant identifier for modulation of the wetting-dewetting patterning surface and, by extension, control of the hydrophobic and oleophobic recovery.

Using the sessile drop method outlined in Section 5.7.4, Figure 6.1 shows the effect of UV/O_3 surface oxidation on P-PDMS for the water (WCA), Krytox1506 (KCA) and diiodomethane contact angles (DCA) as a function of oxidation duration. The decrease to water contact angle (WCA) as a result of the sustained UV/O_3 treatment is rapid, decreasing from a hydrophobic state (95.93 ± 2.6°) on P-PDMS to a hydrophilic state (6.22 ± 1.5°) on UVO240-PDMS; however, it is the decrease in Krytox1506 contact angle (KCA) from 36.86 ± 1.9°

to 7.42 ± 1.2° that is key for oil transfer and therefore, application to deposition of the oil mask for selective metallisation.

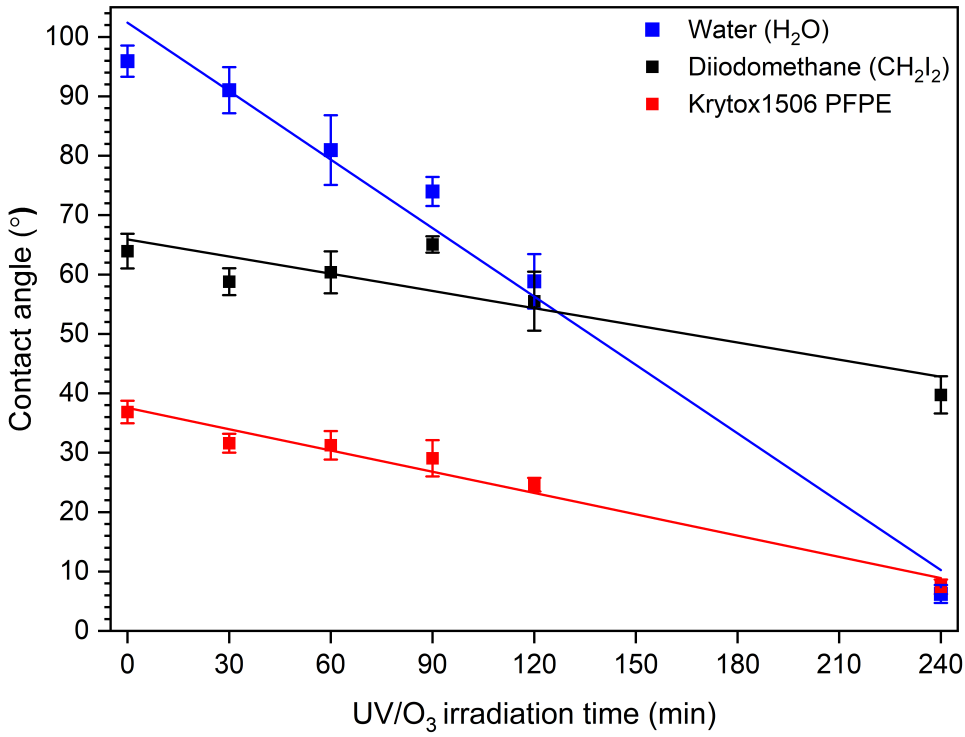

Figure 6.1: Contact angle vs UV/O_3 treatment duration (0 - 240 min) for water, Krytox1506 and diiodomethane.

The change in WCA due to the oxidation of PDMS has been investigated in the literature, with oxidation primarily achieved by methods such as O_2-plasma and coronal discharge. To a lesser extent, the oxidation of PDMS by ultraviolet-ozone (UV/O_3) has been studied in works by Efimenko et al., Fu et al., and Ma et al. and in agreement with these select studies, the contact angles in Figure 6.1 decrease linearly as a function of oxidation duration [159, 328, 329]. Similarly, as initially presented by Francis and confirmed in this work, for control of Krytox1506 wetting-dewetting, a 240 min UV/O_3-oxidation is crucial to ensure sufficiently low contact angle values for the Krytox1506 oil and, therefore, enable the deposition of patterned oil masks [136].

The observed hydrophobic-hydrophilic behaviour on P-PDMS and UVO240-PDMS is a consequence of the substitution of methyl groups (Si−CH_3) with hydrophilic silanol groups (Si−OH) on the PDMS surface. For water, wetting onto UVO240-PDMS is energetically favoured due to the formation of hydrogen bonding interactions with the surface, minimising the surface-free energy. The favourable wetting of water on oxidised-PDMS results in

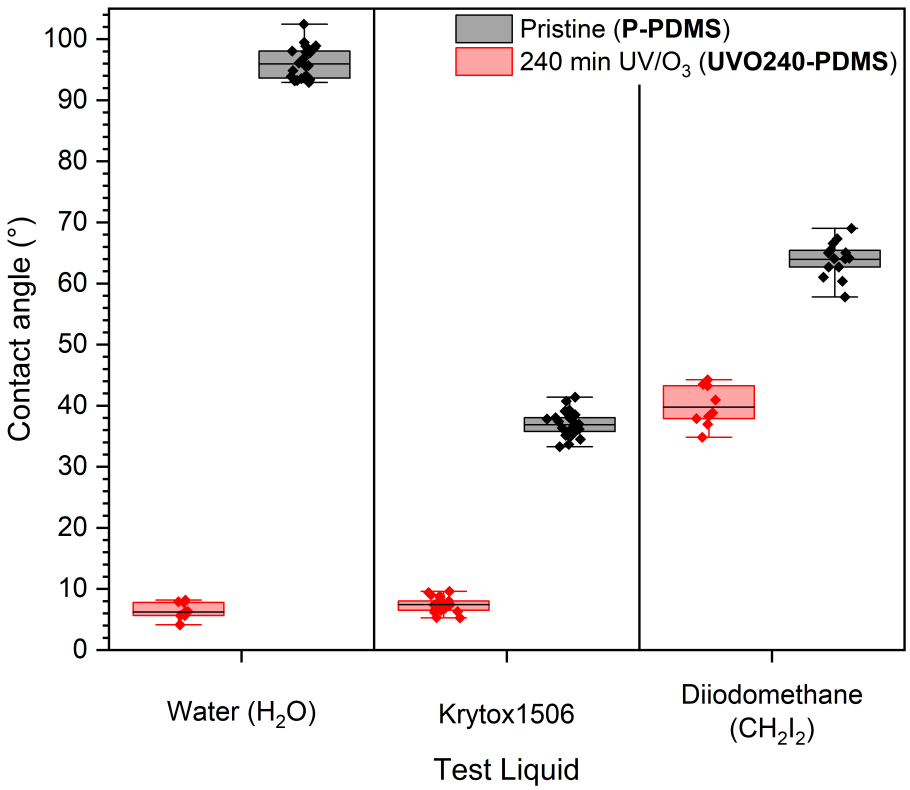

Figure 6.2: P-PDMS and UVO240-PDMS contact angle reference values for H_2O, Krytox1506, and CH_2I_2.

a strong rate of decrease for the contact angle at -0.384 degrees min^{-1} of UV/O_3 treatment. For KCA and DCA, the decrease is notably weaker, corresponding to a gradient of -0.119 and -0.096 degrees min^{-1}, respectively. The slower decrease in KCA and DCA relates to the formation of the wetting interactions for the two non-polar, halogen-containing compounds. The primary bonding interactions are weak intermolecular forces such as Van der Waals and Dipole-Dipole, resulting in wetting of Krytox1506 and CH_2I_2 being less energetically favoured as opposed to remaining in the bulk droplet. The difference in the rate of decrease between KCA and DCA is likely a result of Krytox1506 having a much larger molecular weight (~2160 g mol^{-1}) and volume compared to CH_2I_2 (267.8 g mol^{-1}). Simply put, the larger molecule can form additional interactions with the surface, favouring adhesion and wetting on the surface.

As described by Young's Equation (Equation 6.1.1), the contact angle is related to the free energy of the surface-vapour interface (SFE), free energy of the liquid-vapour interface and the solid-liquid interfacial tension,

$$\gamma_{sv} = \gamma_{sl} + \gamma_{lv} cos\theta \tag{6.1.1}$$

where γ_{sv}, γ_{sl} and γ_{lv} are the free energies of the solid-vapour, solid-liquid and liquid-vapour phases, and θ is the static contact angle at equilibrium.

Several methods for calculating the surface free energy from experimental contact angle data are described in the literature, with the extended Fowkes and Owens-Wendt-Rabel-Kaelble (OWRK) methods the most common. Both methods simplify the process to only require the contact angles of liquids with known polar and dispersive interactions [330, 331]. Table 6.1 presents the surface free energy (SFE) of UV/O_3-irradiated PDMS as a function of treatment duration. Determining SFE for the modified PDMS allows for the representation of wettability on the PDMS surface as a single value that may be applied to any coating liquid. In general, wetting of a liquid is due to the interface naturally seeking to minimise its free energy; therefore, upon adding a liquid to the surface, a high-energy surface will form bonding interactions with the liquid across its area, wetting the surface to minimise the energy. This leads to the observed inverse relationship between WCA/KCA/DCA and the SFE.

Table 6.1: Table of SFE (mJ m^{-2}) vs UV/O_3 treatment duration.

UV/O_3 Duration (min)	**Surface free energy (mJ m^{-2})**	**Reference**
0 (P-PDMS)	22.36	*This work*
30	25.24	
60	29.39	
90	32.78	
120	44.01	
240 (UVO240-PDMS)	72.80	
0	32.7	[117]
0	~19	[328]
90	~72	[328]

As well as outlining the effect of UV/O_3 treatment on PDMS, a large data set of WCA, KCA and DCA values collected throughout the project allowed for the determination of accurate contact angle reference values for P-PDMS and UVO240-PDMS as shown in Figure 6.2. Reference contact angles on P-PDMS were determined to be 95.93 ± 2.6°, 36.86 ± 1.9° and 63.95 ± 2.9° for WCA, KCA and DCA, respectively. For UVO240-PDMS, the average WCA was 6.22 ± 1.5°, the KCA was 7.42 ± 1.2° and 39.74 ± 3.1° for DCA.

In addition to contact angle and surface energy data, identifying and monitoring the sur-

face chemistry changes or lack thereof on oxidised-PDMS is also important to allow for a better understanding of the underlying interactions related to the applied surface regeneration methods and their impact on the surface's wettability. Figure 6.3 shows the ATR-FTIR spectra of P-PDMS and UVO240-PDMS with the changes as a result of UV/O_3 treatment annotated. As discussed previously, the major change associated with UV/O_3-oxidation is the substitution of silicon-bound methyl groups Si−CH_3 with silanols Si−OH. In Figure 6.3, this is represented by the appearance of an alcohol stretch (Si−OH) at 3300 cm^{-1} and an increase in the intensity of Si−O−H stretches between 900 - 820 cm^{-1}. There is also an accompanying intensity reduction associated with the loss of methyl groups Si−CH_3, including a decrease in intensity associated with the asymmetric methyl stretch at 2962 cm^{-1}, the symmetric deformation at 1257 cm^{-1}, as well as the −CH_3 rock at 788 cm^{-1}.

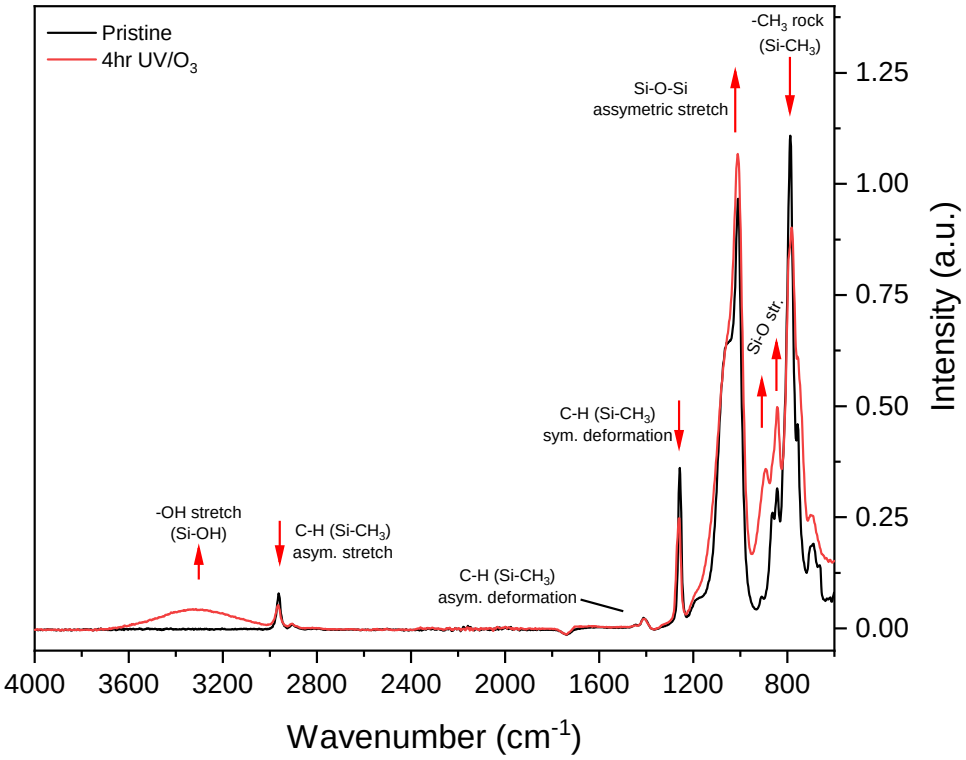

Figure 6.3: IR Spectra of pristine (P-PDMS) and UV/O_3-treated polydimethylsiloxane (UVO240-PDMS).

Oxidation of PDMS by penetrating methods, such as UV/O_3 treatment or O_2 plasma, is known to form an oxygen-rich, glassy and brittle silica-like layer with thickness of this layer, highly dependent on the method and oxidation duration used [332–335]. X-ray photoelectron spectroscopy (XPS) with depth profiling was employed on both P-PDMS and UVO240-PDMS reference samples to quantify the atom % of the surface and subsurface regions.

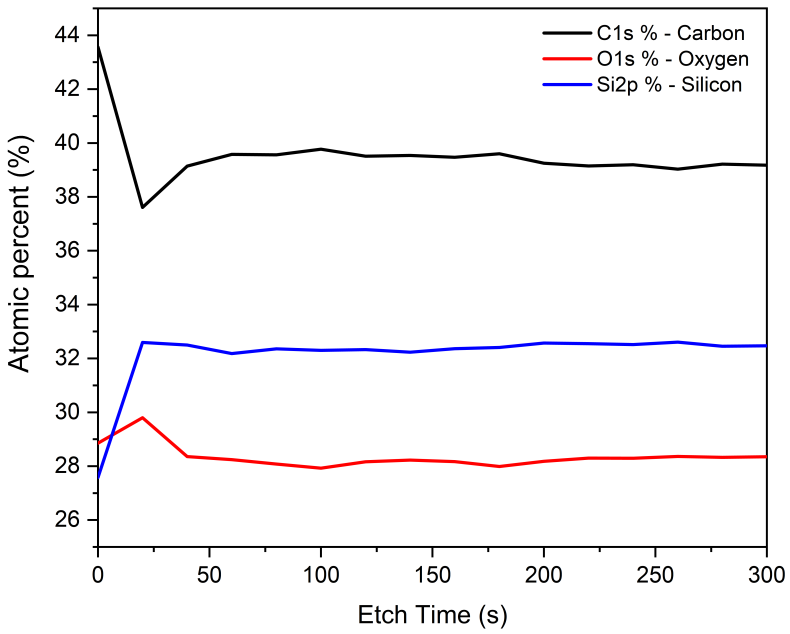

Figure 6.4: XPS depth profile as a function of etching time (s) showing the carbon, oxygen, and silicon percentages (%) for pristine PDMS (P-PDMS).

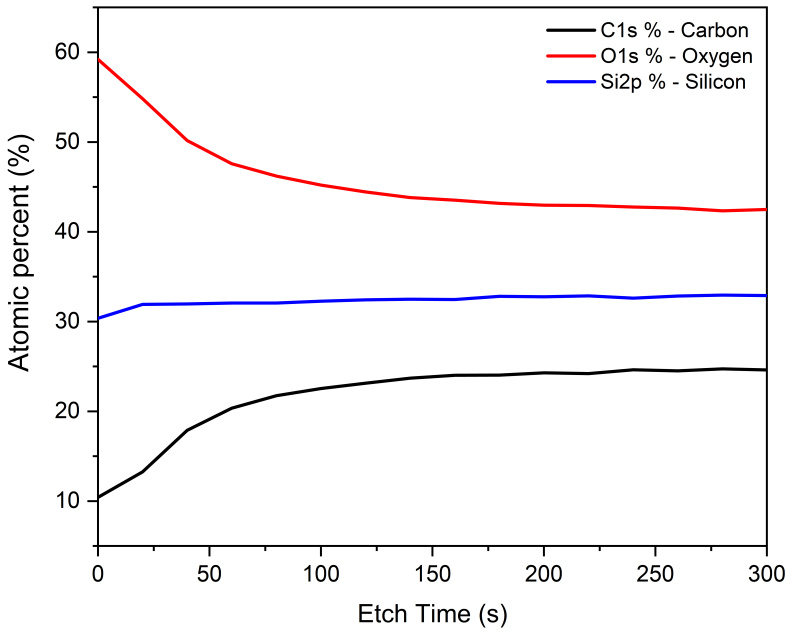

Figure 6.5: XPS atomic profile as a function of etching time (s) showing the carbon, oxygen, and silicon signals for 240 min UV/O_3 PDMS (UVO240-PDMS).

The atomic profile of P-PDMS in Figure 6.4 and the profile of UVO240-PDMS in Figure 6.5 outline the relative atomic percentages of carbon, oxygen, and silicon as assessed by detection of the C1s signal at 284 eV, the O1s signal at 532 ev and the Si2p signal at 102 eV. By measuring the atom percentages in the plateau regions in Figures 6.4 and 6.5, it is possible to determine the bulk composition for both the P-PDMS and UVO240-PDMS samples, respectively. The bulk atomic % remains relatively constant in P-PDMS with carbon at 38.98%,

silicon at 32.41% and, 28.61% for oxygen. Considering the surface region prior to depth profiling, the carbon percentage in P-PDMS is 44.12% while the oxygen and silicon percentages are 28.80% and 27.08%, respectively. The small difference between the bulk and surface percentages is likely a result of contamination from the air/environment. The bulk compositions corresponds to atomic ratios for C/O and O/Si equal to 1.362 and 0.883. These values do not match the theoretical composition of P-PDMS at $C/O = 2$ and $O/Si = 1$ i.e. 50% Carbon, 25% Oxygen and 25% Silicon. However, the atomic ratios do match the compositions frequently reported in the literature, with the deviation from the theoretical value commonly attributed to contamination and stabilising agents in the commercial elastomer kit [279, 280]. For example, the addition of silica fillers would increase atomic % of oxygen and silicon, which explains the elevated values of these atoms in the bulk P-PDMS. (See Appendix B, Figures B.5 & B.6 for XPS spectra.)

In Figure 6.5, a large change in atomic percentages is observed following UV/O_3 oxidation. The carbon content drops to 11.27% while an accompanying increase in the quantity of oxygen to 59.07% relates to the substitution of methyl groups ($Si-CH_3$) for silanol groups ($Si-OH$) on the surface, as well as the formation of the oxygen-rich silica phase. The silicon atom percentage remains stable following UV/O_3 oxidation, with the silicon content in both P-PDMS and UVO240-PDMS at a similar value (27.09% vs 29.65%). The depth profile of UVO240-PDMS in Figure 6.5 shows increased depth dependency, exhibiting a drop in oxygen percentage from 59.07% to a plateau of ca. 42% after 150s of etching. The high oxygen content before the etch suggests a significant quantity of surface bound silanol groups and other oxygen contaminations from the UV/O_3 treatment process. However, in comparison to P-PDMS, the elevated oxygen percentage remaining after the etch is further evidence of a deeply penetrating SiO_x layer that possesses a thickness greater than the sampling depth of the XPS (estimated 50 nm [336]) and is deeper than any possible surface contamination.

In addition to atom percentage, the peak binding energy provides information about the bonding and coordination of the siloxane groups; therefore, considering the Si2p peak, the difference in silicon-oxygen connectivity in the P-PDMS and UVO240-PDMS phases can be probed. On P-PDMS, the binding energy peak of Si2p in P-PDMS is centred at 101.7 eV indicating silicon with 2 oxygen atoms i.e. an ($-O-SiR_2-O-$) phase [279, 329, 333].

Following oxidation, the Si2p peak shifts to 103.38 eV, which corresponds to the formation of additional Si-O bonds (>2) and is consistent with values reported in the literature for oxidised-PDMS, for example, Özçam et al. finds unmodified, pristine-PDMS has a Si2p peak at 101.5 eV and 60 min UV/O_3-irradiated PDMS has the peak Si2p binding energy at 103.6 eV [337–339].

The final property of interest relevant to wetting-dewetting control is surface roughness. It is known that surface roughness can play a significant role in the wetting behaviour of a surface, and in general, an increase of roughness on a hydrophobic or non-wetting surface (contact angle >90°) will result in an increase in hydrophobicity, whereas the opposite is observed on a hydrophilic or wetting surface (contact angle <90°) with an increase in roughness resulting in a decrease of contact angle. This phenomenon was first presented by Wenzel, who describes the relationship between wetting and surface roughness;

$$cos\theta_w = rcos\theta \quad \text{where } r = \frac{\text{real surface}}{\text{geometric surface}} \tag{6.1.2}$$

In the Wenzel equation (Equation 6.1.2), θ_w is the apparent contact angle on a rough surface (Wenzel contact angle), r is the ratio of surface area on the real surface to the planar geometric projection of the surface and θ is the static contact angle at equilibrium on an ideal, flat surface. Given the oxidised UVO240-PDMS possesses a hydrophilic/oleophilic surface, an increase in surface roughness would result in a decrease in contact angle. A significant increase in roughness due to the applied surface regeneration method would counter the attempts to induce recovery enhancement, likely limiting the maximum recovery possible due to potential permanent topographical changes. However, to affect the wetting behaviour, a change to roughness e.g. Sa on the order of 10s - 100s of microns (μm) would be required [136, 340, 341].

The areal surface roughness (Sa) was calculated using an arithmetic mean method. The Sa data was extracted from two measurement areas - a 1^2 μm area termed the 'nano-scale' area and a 100^2 μm termed the 'microscale' area, from micrographs obtained using atomic force microscopy and optical interferometry, respectively (See Section 5.7.3 for operational details).

Figure 6.6 shows the Sa values for both areas on the same chart, grouped by sample (P-PDMS and UVO240-PDMS). The roughness data matches with similar measurements performed by Francis et al. [136] and shows there is only a minimal increase in Sa of $\sim 0.7\,\text{nm}$ over both the nano- and microscale measurement areas. This is orders of magnitude under the roughness variation needed to influence the surface's wetting behaviour, indicating the observed wetting of water and Krytox1506 is due to chemical changes to the surface and the accompanying increase in surface free energy.

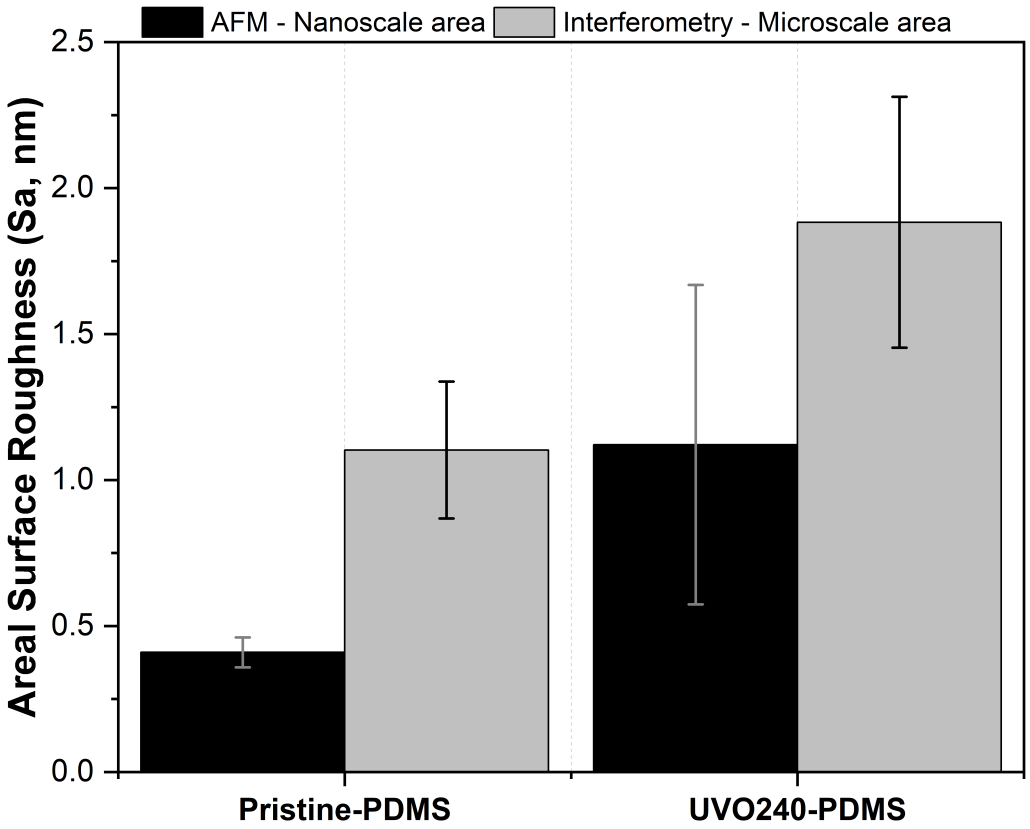

Figure 6.6: Areal Surface Roughness (Sa) of P-PDMS and UVO240-PDMS calculated by arithmetic mean. Black bar: nanoscale ($1^2\,\mu m$), grey bar: microscale ($100^2\,\mu m$).

6.2 Surface Regeneration

The deposition of a patterned metal layer by UV/O_3-PDMS selective metallisation follows a simple, multiple-step process. After PDMS plate casting and curing, fresh P-PDMS samples are covered with a patterned shadow mask before UV/O_3 irradation (240 min). Krytox1506 oil is deposited onto the UVO240-PDMS by spin-coating or pickup from an anilox roller before printing the oil onto a suitable substrate. Finally, the oiled-coated substrates are exposed to a thermally evaporated or sputtered metal source to yield the patterned metal

layer. The casting and oxidation steps are time-consuming; therefore, the reuse and the ability to clear and repattern PDMS stamps and R2R plates, would save time and money, which is highly desired for a potential industrial application of this print method.

To achieve this goal, it is proposed the PDMS printing stamps can be renewed and regenerated in a controlled manner before a second UV/O_3 patterning step, i.e. a surface rewriting process. Once oxidised by UV/O_3, the UVO240-PDMS surface undergoes a process known as hydrophobic recovery, where the hydrophilic (wetting) behaviour is slowly converted back to a hydrophobic (dewetting) state. This process can occur through a number of proposed mechanisms, for example, time-dependent reabsorption and rerechemisorption of the Si-OH group on the surface into the bulk or migration of low molecular weight (LMW) species from the bulk to the surface, however the consensus is that the latter, is the dominant process [342–345]. It has been shown that the process by which hydrophobicity recovers will happen immediately following surface treatment but in an uncontrolled, non-uniform manner across the PDMS as shown by Olah et al., Bodas et al., Eddington et al., etc. [333, 346, 347]. However, the overall recovery speed depends on several factors, such as temperature, sample thickness, local environment, etc. Unwanted hydrophobic recovery is widely regarded as an issue for the applicability of oxidised PDMS in microfluidics and is a barrier to the commercial application of UV/O_3-PDMS stamps and printheads.

Conversely, as shown by Ma et al. and discussed later by Francis, the instantaneous recovery can be significantly delayed by passivating the surface with a fluid coating [159]. The phenomenon was used to retain the hydrophilicity of patterned UVO240-PDMS and, therefore, the ability for patterned mask deposition for at least 50 days [348], meaning as long as printing stamps and plates are coated with Krytox1506 immediately after UV/O_3 oxidation, the effects of unwanted hydrophobic recovery can be negated for printing applications [348].

For the purpose of regenerating and rewriting the pattern on a UVO240-PDMS stamp, various methods for controlling hydrophobic recovery by rapidly enhancing its rate and, therefore, ensuring a complete and uniform regenerated pristine-like surface available for a second UV/O_3 patterning are discussed. The recovery enhancing or regeneration methods utilised in this project are divided into two categories: Thermal and Chemical.

- **Thermal**: The thermal approach to surface regeneration concerns the application of a sustained heat treatment to the surface of the oxidised PDMS. The thermal enhancement of hydrophobic recovery is targeted, taking advantage of the temperature dependency seen in the diffusion of low molecular weight (LMW) PDMS oligomers to the surface from the bulk. This process can be represented by an Arrhenius-type rate equation (Equation 6.2.1 as described in Hillborg et al., and Pascual et al., etc [280, 344].

$$k \propto \exp^{\left[\frac{E_a}{RT}\right]} \tag{6.2.1}$$

where k is the rate of recovery, E_a is the activation energy of LMW species in the bulk, R is the gas constant (8.314 J mol^{-1} K^{-1}) and T is the treatment temperature. In addition to the temperature dependency, the concentration of LMW PDMS species, i.e. degree of curing, influences the diffusivity of LMW and therefore, the rate of contact angle recovery. However, given the consistent preparation method, that is, [10:1] PDMS kit ratio and a 1 hr, 100°C curing temperature, this parameter is expected to be constant across all PDMS blocks used in the project [159]. There is a limit to what range of temperatures can be applied as PDMS is known to completely decompose and depolymerise at temperatures exceeding 400°C [349, 350], however in practice, it was observed during this study that at temperatures above 200°C, the PDMS stamps begin to bow, deform and become more susceptible to tearing [351]. It has been shown that thermally-enhanced hydrophobic recovery can be achieved at temperatures as low as 20°C over a long enough time frame (60 days) [344], as such, in this project, temperatures of 50, 100, 150 and 200°C were investigated.

- **Chemical**: It has been observed that oxidation of PDMS by UV/O_3 results in the formation of a 'thin, brittle silica-like layer' with a thickness ranging from 5 - 500 nm [279, 332]. Chemically-enhanced hydrophobic recovery targets the dissolution of the silica-like layer, reducing the thickness and promoting the formation of cracks and fractures to increase the rate of hydrophobic recovery. Bowen et al. present a method for dissolving the SiO_x layer, taking inspiration from the dissolution of amorphous silica by NaCl solutions in the field of geochemistry [352, 353]. In the publication, Bowen finds immersion of oxidised PDMS in a mild saline buffer, for example, 0.01

M phosphate-buffered saline at 80°C for 1 hr, results in the removal of the silica-like layer. In this project, a comparable method by immersing UVO240-PDMS in 0.01 M PBS was studied in addition to a combined chemical-thermal approach.

- **Other:** Mechnically-enhanced regeneration targets the formation of cracks and fracture via physically deforming the oxidised-PDMS to break the silica-like layer. This effect appears to have been first described by Hillborg and Gedde, showing increased rate of hydrophobic recovery by 'mild bending' on high-dose, corona discharge exposed PDMS samples [280]. Further examples within the literature are limited however, in a recent publication Mazaltarim et al. utilises mechanically induced recovery on O_2-plasma treated PDMS to produce patterned surface by controlling the wetting behaviour of water [354]. Mazaltarim shows the recovery of the surface plateaus at ∼76% of the original value (118° verses 90° WCA) on the samples in their study. In preliminary experiments investigating the effect of mechanical deformation on the recovery of krytox patterning surfaces, P-PDMS samples were blanket irradiated by UV/O_3 for 240 min to produce UVO240-PDMS blocks. Enhancement of contact angle recovery by mechanical deformation was attempted on numerous samples, this was performed by manually bending and stretching the blocks for an allotted duration of 15 min. On every attempt, the mechanical deformation of UVO240-PDMS would result in the tearing and snapping of the samples. While this contrasts the work by Mazaltarmin, there are some differences in the experimental design. Firstly, the PDMS samples used in the study by Mazaltarim are thinner than the materials used in this project (100 µm vs ca. 3 mm). A thinner PDMS film will be more flexible, allowing multiple bending actions. Secondly, the deformation performed by Mazaltarmin was conducted using a robotic, mechanical testing system for controlled stressing of the PDMS and finally, Mazalatrim employed at 10 s oxygen plasma to irradiate the PDMS which would not produce a deep oxidised layer similar to the type generated by a 240 min UV/O_3 treatment. Given the issues with tearing and brittleness of the samples relevant for stamping & R2R printing, the mechanical process is generally considered incompatible with 240 min UV/Ozone-irradiated PDMS at present.

6.3 Contact Angle and Surface Free Energy Behaviour

6.3.1 Thermal Regeneration - Sustained Heat Treatment

As per Section 5.3, sheets of cured PDMS were demoulded, cut into an appropriate dimension (10x10x3 mm), rinsed with ethanol and dried with nitrogen flow to give a debris-free, pristine surface (P-PDMS). A 240 min blanket (non-masked) UV/O_3-oxidation was performed on the P-PDMS to generate oxidised UVO240-PDMS samples. The UVO240-PDMS samples were subject to various heating regimes. To investigate the effect of thermal regeneration on UVO240-PDMS, a contact angle study was performed by measuring the static water (WCA) and Krytox1506 contact angles (KCA) as a function of heat treatment duration for the 4 temperatures of interest (50, 100, 150 and 200°C).

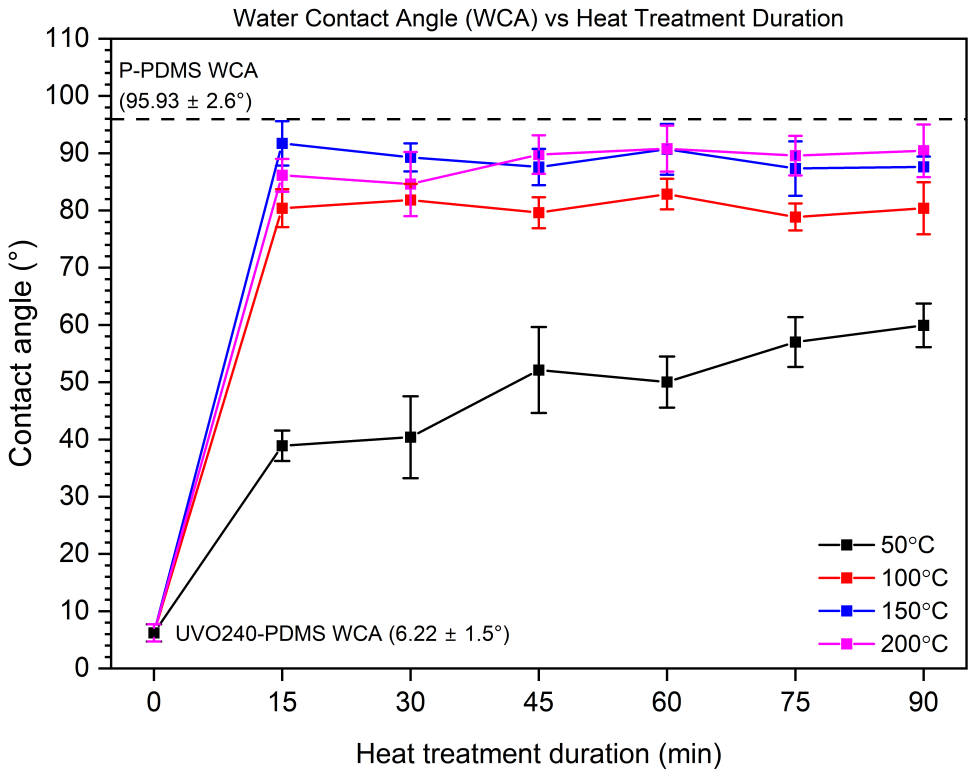

Figure 6.7: Water contact angle vs heat treatment duration following 50, 100, 150 and 200°C heat treatments on 240 min UV/O_3 oxidised-PDMS (UVO240-PDMS). Pristine PDMS P-PDMS reference value from whole project average as dashed line.

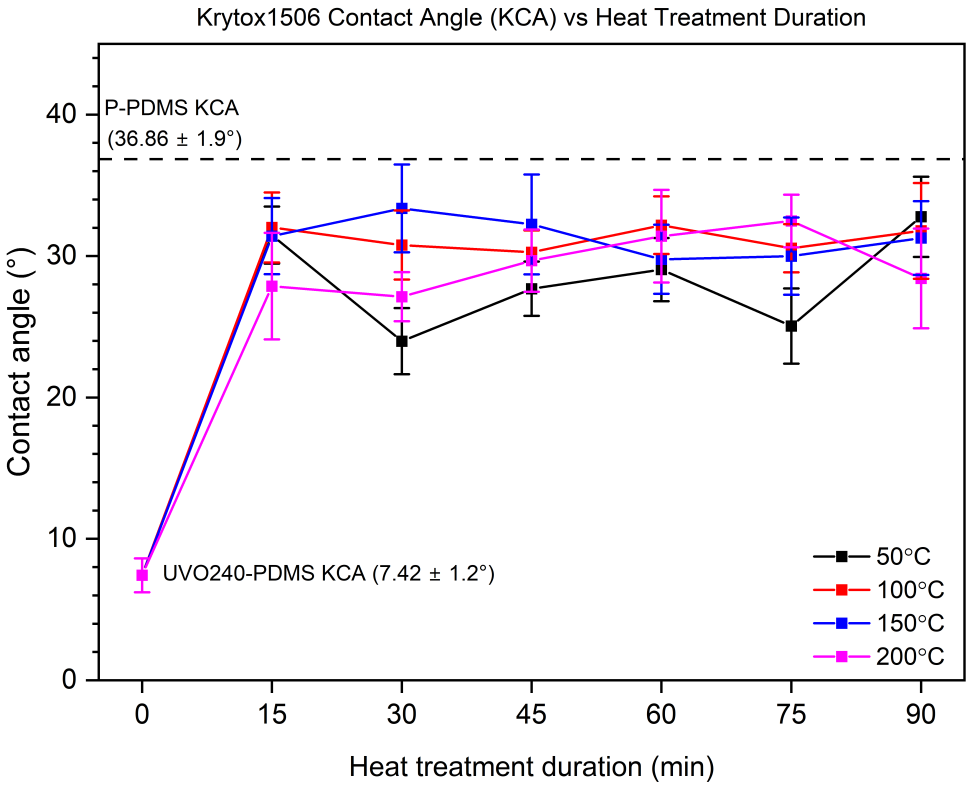

Figure 6.8: Krytox1506 contact angle vs heat treatment duration following 50, 100, 150 and 200°C heat treatments on 240 min UV/O_3 oxidised-PDMS (UVO240-PDMS). Pristine PDMS P-PDMS reference value from whole project average as dashed line.

Figure 6.7 shows the effect of heat treatment on the static water contact angle with the WCA of P-PDMS and UVO240-PDMS shown as reference lines at 95.93° and 6.2°, respectively. Recovery of hydrophobicity, i.e., the increase in WCA relative to the UVO240-PDMS reference, is observed for all applied temperatures regardless of treatment duration; however, a temperature dependency exists for the extent of recovery. Upon the onset on heating, rapid recovery occurs, and after 15 min of heat treatment for all temperatures, an appreciable increase in WCA is observed with a threshold present between 50 and 100°C. Considering the 50°C treatment at 15 min, the WCA increases to 38.9 ± 2.7° (40.5% recovery) before reaching a high of 59.9 ± 3.8° (62.5%) after 90 min of heating. At this temperature, the recovery effect increases gradually with time, following the immediate jump upon application of the heat treatment. This initial recovery from 6.22° in UVO240-PDMS to 38.9° is the result of the volatilisation of hydrophilic species bound to the surface of the oxidised PDMS as well as the onset of LMW PDMS migration to the surface [342, 345]. Summarised in Table 6.2, there is a noticeable jump in WCA recovery of 43.3% between 50 and 100°C to 80.4 ± 3.3° (83.8%) at the 15 min of heating and unlike the time dependency of the 50°C

heating, no such increase in recovery as a function of time is observed for 100°C with a WCA of 80.4 ± 4.5° (83.8%) after 90 min.

Table 6.2: WCA recovery percentages (%) for thermal regeneration regimes.

Duration (min)	Temperature (°C)			
	50	100	150	200
15	40.5%	83.8%	95.6%	89.8%
30	42.1%	85.3%	93.1%	88.2%
45	54.3%	83.0%	91.3%	93.6%
60	52.2%	86.4%	94.5%	94.7%
75	59.4%	82.2%	91.0%	93.4%
90	62.5%	83.8%	91.3%	94.3%

Increasing the temperature to 150°C results in a further ∼8% jump in the percentage recovery values, ranging between 91.0% - 95.6%. Similar results for WCA recovery are observed at 200°C between a low of 84.61 ± 2.9° (88.2%) and a high of 90.81 ± 4.0° (94.6%) with no clear time dependency for both 150 and 200°C. The data outlines that treatment temperatures ≥ 150°C induce maximum hydrophobic recovery, reaching a limit of approximately 88° or 92% in percentage terms. Overall, the general increase in recovery as a function of temperature is expected and matches similar data from the literature [344]. Contrasting the water contact angle hydrophobicity where the lower temperatures (50 & 100°C) result in less recovery than the high temperatures (150 & 200°C), oleophobic recovery of Krytox1506 contact angle (Figure 6.8) occurs in a balanced manner across all temperatures at all treatment durations, i.e. no clear temperature or time dependency. Table 6.3 presents recovery of KCA as a percentage and shows the limit is slightly lower than that of WCA for the higher temperature heat treatments (150 & 200°C); however, for 50°C, the recovery is much closer to the high temperatures. The lack of a temperature dependency for the KCA outlines a deviation from the Arrhenius-type behaviour observed for WCA hydrophobic recovery. It is likely this lack of trend for the KCA values is due to the absence of strong bonding interactions involved in the wetting and adhesion of Krytox1506 in addition to the existence of the oxygen-rich silica-like layer that causes a permanent increase in surface free energy.

The wetting behaviour of water relies overwhelmingly on the formation of hydrophilic surface species, e.g. Si−OH and hydrogen bonding interactions between the water molecules and the surface. Upon application of a thermal regeneration regime, the hydrophobic re-

Table 6.3: KCA recovery percentages (%) for thermal regeneration regimes.

Duration (min)	Temperature (°C)			
	50	100	150	200
15	85.3%	86.8%	85.1%	75.5%
30	65.0%	83.4%	90.4%	73.5%
45	75.0%	82.0%	87.4%	80.4%
60	78.7%	87.2%	80.7%	85.1%
75	67.9%	82.8%	81.3%	88.0%
90	88.8%	86.1%	84.8%	77.0%

covery relates to the loss of these bonding groups via the processes previously discussed. As water possesses a high surface tension (72 mN m^{-1}), it energetically favours remaining in the bulk droplet as opposed to wetting a surface. On a high energy surface such as UVO240-PDMS, wetting is favoured due to the minimisation of free energies however when the SFE begins to decrease due to the loss of the unstable and polar silanols, the water again prefers to remain in the droplet, increasing the WCA.

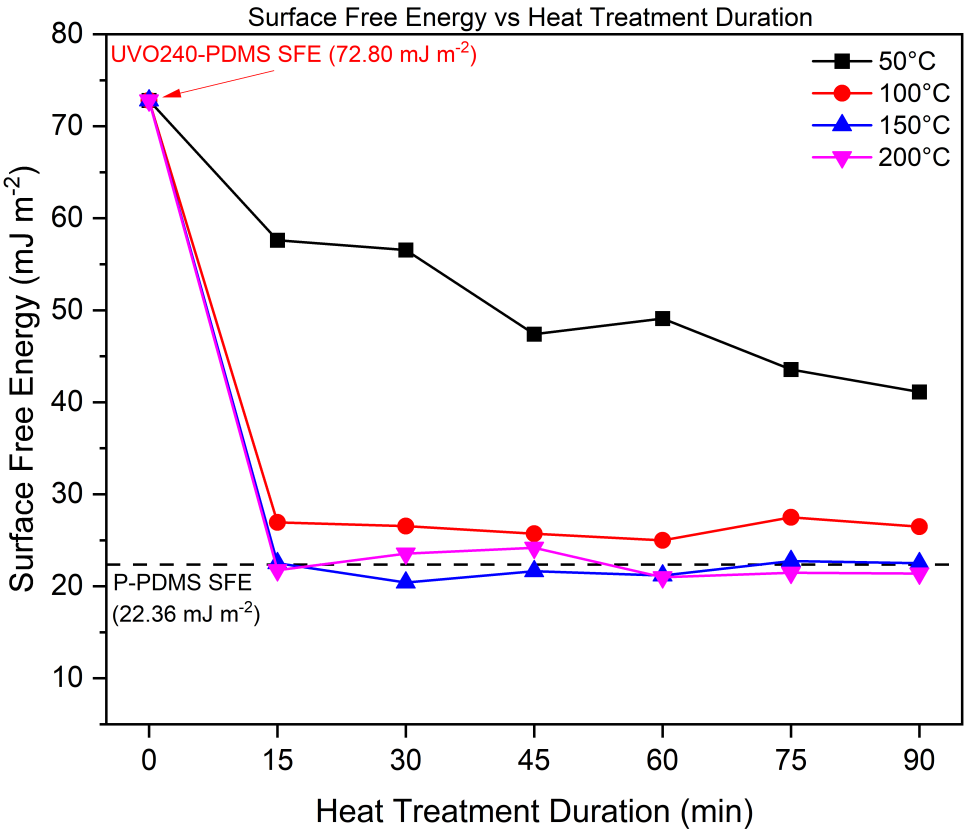

Figure 6.9: Surface Free Energy (mJ m^{-2}) of thermally regenerated, 240 min UV/O_3 oxidised-PDMS (UVO240-PDMS) as a function of treatment duration (min). Values calculated using the OWRK/Fowkes method with experimental WCA and KCA data. Pristine PDMS (P-PDMS) SFE as dashed reference line.

On the other hand, Krytox1506 adheres to the surface only by weak intermolecular forces. While the loss of the higher energy polar groups on the surface does result in the observed oleophobic recovery, the permanent changes to the surface as a result of UV/O_3-oxidation, e.g. cleavage of stable Si$-CH_3$ and formation of an oxygen-rich, silica layer, limit the total recovery possible for both hydrophobicity and oleophobicity of the surface when utilising a purely thermally-enhanced regeneration method. As Krytox1506 is a non-polar, perfluoropolyether, an estimate of the surface free energy can be calculated from KCA and WCA values by the OWRK/Fowkes method as it is assumed the bonding interactions involved for wetting of Krytox1506 are purely dispersive.

Figure 6.9 summarises the SFE data for the thermal regeneration methods collating the WCA and KCA values. The plot better represents the overall picture for both hydrophobic and oleophobic recovery, showing the higher temperatures (150 and 200°C) give a more complete recovery with no time dependency at 100°C or above. Further detail on the temperature dependency of PDMS hydrophobic recovery has been presented by Morra et al., Hillborg et al., and Pascual et al. [343, 344, 355] with the data in Figure 6.7 following a similar and expected trend irrespective of variation in PDMS composition, oxidation method and oxidation duration.

6.3.2 Chemical Regeneration - Silica Dissolution

A second approach to regenerate the patterning surface of UVO240-PDMS is through etching of the oxygen-rich, silica-like layer. Generation of the SiO_x layer during oxidation of P-PDMS by UV/O_3 contributes to the large increase in surface free energy due to the loss of stable methylsilyl (Si$-CH_3$) groups. As the primary mechanism for recovery is well understood and occurs through the diffusion-controlled migration of LMW PDMS oligomers, it is proposed that the thickness reduction or complete removal of the silica layer will increase the rate of recovery by increasing the diffusivity and, therefore, lowering time for the diffusion process [159, 356, 357]. For the application to metal deposition, the KCA is key to controlling the wetting and dewetting required to form oil mask patterns. Given that KCA on P-PDMS is already, by definition, in an oleophilic state (CA <90°), it is crucial that the regeneration method returns the KCA to the value of P-PDMS (KCA: 36.86 ± 1.9°). Thermally enhanced

regeneration is limited by the persistence of the SiO_x layer, so another approach targeting the silica layer itself was investigated. UVO240-PDMS samples were prepared following the same approach as Section 6.3.1 then subject to a chemically enhanced recovery process whereby the samples were immersed in a 1X PBS solution (0.137 M NaCl, 7.6 pH) and heated to 85°C for 60 min to dissolve or etch the SiO_x surface layer. A combined chemical and thermal approach was performed on a second set of UVO240-PDMS samples where the samples were first subject to a chemical dissolution regime followed by a heat treatment of 150°C for 60 min. For the purposes of a contact angle investigation, only the 150°C was studied as this temperature afforded the maximum recovery percentage and resulted in the complete removal of hydrophilic silanols as shown later in Figure 6.15. In essence, there was no perceived benefit to using a higher temperature.

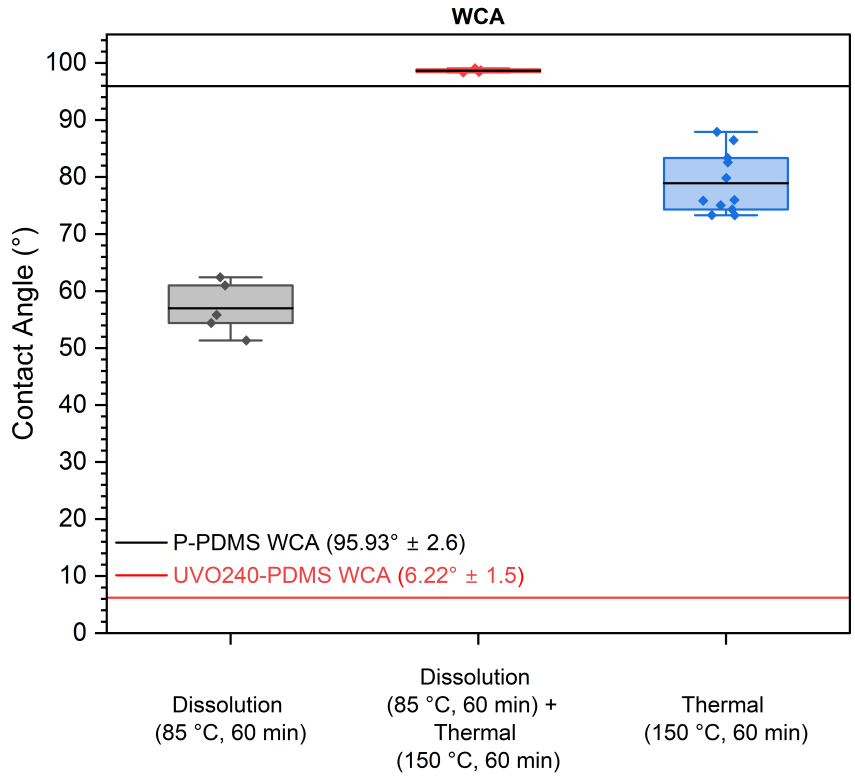

Figure 6.10: Water contact angle (°) on UVO240-PDMS samples regenerated using a chemical, thermal, and combined chemical-thermal method.

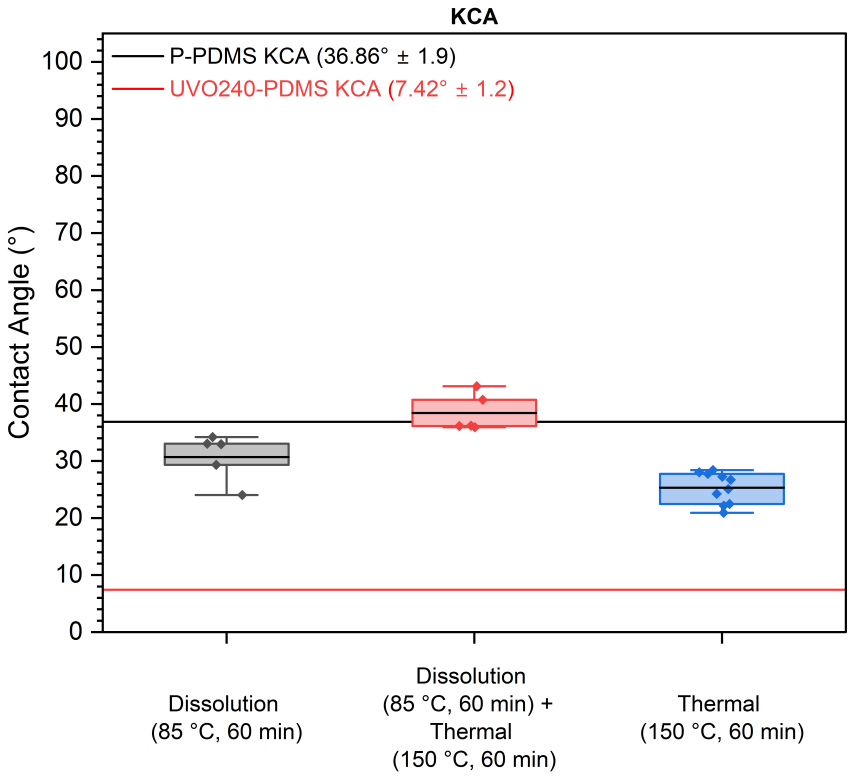

Figure 6.11: Krytox1506 contact angle (°) on UVO240-PDMS samples regenerated using a chemical, thermal, and combined chemical-thermal method.

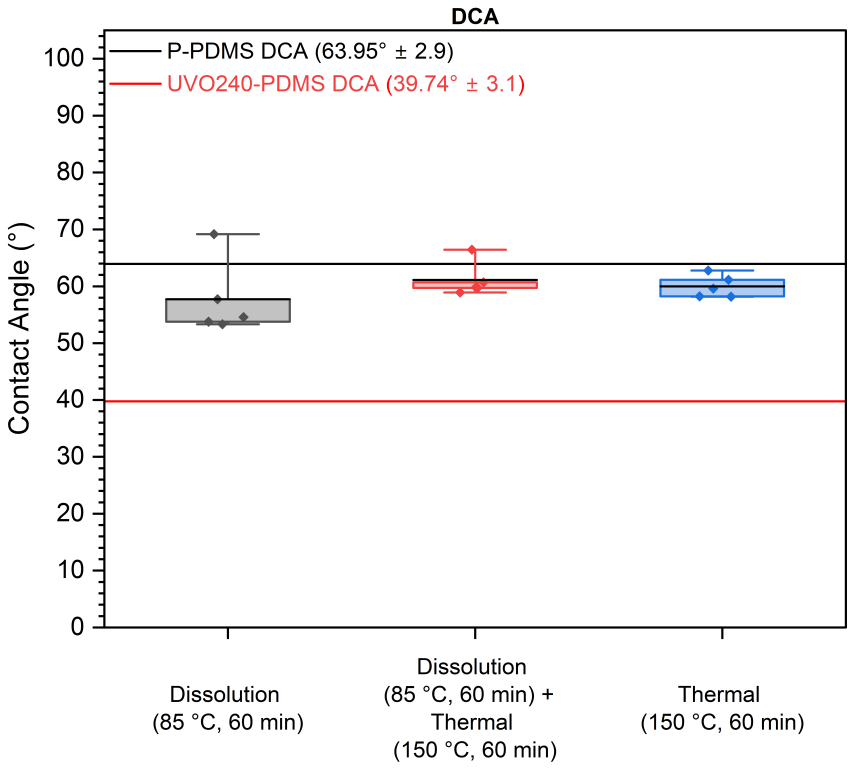

Figure 6.12: Diiodomethane contact angle (°) on UVO240-PDMS samples regenerated using a chemical, thermal, and combined chemical-thermal method.

A contact angle and surface energy investigation for the chemical, thermal and combined

chemical-thermal regeneration methods was conducted in the same manner as Section 6.3.1. Figure 6.10 shows the water contact angles (WCA) for the three regeneration methods with the chemical-only method resulting in a WCA recovery to 56.99 ± 4.63° (59.4% recovery), a repeat of the 150 °C, 60 min thermally-enhanced recovery gave a WCA of 78.90 ± 5.38° (82.2%) while the combined chemical-thermal approach exceeded expectations and resulted in the highest observed recovery for WCA up to a value of 98.64 ± 0.3° (102.8%). The oleophobic recovery of Krytox1506 contact angle for the chemical-only regeneration (Figure 6.11) was 83.3% to a contact angle of 30.71 ± 4.16°. The thermal method was 70.0% (25.79 ± 2.39°) and the combined approach again resulted in a higher than P-PDMS contact angle 38.42 ± 3.3° or 104.2% recovery. Lastly for the contact angle of CH_2I_2 on this set of regenerated UVO240-PDMS samples in Figure 6.12 were 57.72 ± 6.64° (90.3%), 59.99 ± 2.0° (93.8%) and 61.12 ± 3.0° (95.6%) for the chemical-only, thermal and combined chemical-thermal regeneration methods, respectively. Table 6.4 represents this data in terms of percentage recovery, and in Table 6.5, the calculated surface free energy values are shown. By taking into account the standard error in the measurement, the combined method offers a repeatable approach to achieving complete recovery of the hydrophobicity (WCA) and oleophobicity (KCA), even exceeding the values of WCA and KCA on P-PDMS.

Table 6.4: Table of Percentage recovery values for water, Krytox1506 and diiodomethane contact angles.

Sample	**Recovery**		
	WCA	**KCA**	**DCA**
Chemical-only (PBS 85°C, 60 min)	59.4%	83.3%	90.3%
Thermal (150°C, 60 min)	82.2%	70.0%	93.8%
Combined Chemical + Thermal	102.8%	104.2%	95.6%

Table 6.5: Table of Calculated Surface Free Energy (SFE) for chemically-enhanced regeneration methods. **Reference values in bold**.

Sample	**Surface Free Energy (mJ m^{-2})**
Combined Chemical + Thermal	20.04
P-PDMS	**22.36**
Thermal (150°C, 60 min)	30.78
Chemical-only (PBS 85°C, 60 min)	44.99
UVO240-PDMS	**72.80**

For the chemical-only approach, hydro- and oleophobic recovery is on par with the 50°C heat

treatment, yielding comparable percentage values and surface energy when considering the same treatment timescale (60 min). It was expected that the recovery for the chemical-only process would be much higher, exceeding the low temperature thermal regeneration, given the elevated temperature and potential for increased diffusivity of LMW PDMS due to the thickness reduction in the silica-like layer. As this was not the case, it is clear that the mechanism for hydrophobic and oleophobic recovery induced by the chemical approach is more complex and a balance between positive and negative influences that increase the rate of recovery and impede or delay it. Given what is already known about the primary mechanisms involved with recovery of hydrophobicity and oleophobicity, the positive influences aim to increase rate of diffusion-controlled migration of LMW PDMS from the bulk to the surface, as well as promote the reorientation and/or the volatilisation of polar, hydrophilic surface groups. It is also proposed that the elevated temperatures required during the dissolution step, would further increase the rate of LMW PDMS migration which is known to follow an Arrhenius-type rate behaviour and as such, has a strong temperature dependency as seen previous in Section 6.3.1.

As the recovery values are lower than expected given the elevated temperature and dissolution of the silica-like layer, there must be some process that will likely negatively impact the rate significantly. In publications by Chen et al. and Ma et al., the stability of oxidised-PDMS surfaces and delay of intrinsic hydrophobic recovery are discussed [159, 358]. The retardation of intrinsic hydrophobic recovery is a common topic of the literature as many researchers want to stop or delay the WCA increase of oxidised-PDMS for application in microfluidics, and in both studies, immersion in water is presented as an effective method of preventing recovery. As shown by Chen, the rate of recovery is likely influenced by the difference in relative permittivity between the oxidised-PDMS surface ($\epsilon_{PDMS} = 2.65$) and the environment ($\epsilon_{H_2O} = 80$, $\epsilon_{PBS} = 80$, $\epsilon_{air} = 1$), with the relative permittivity a measure of the polarity, i.e. the higher the relative permittivity, the more polar the compound. Water and therefore an aqueous buffer such as PBS, will impede the reorientation of hydrophilic groups towards the bulk due to the prevalence of h-bonding between the water molecules and the polar groups on the surface in addition to slowing the migration of LMW species towards the surface. A similar effect of preventing or delaying the intrinsic recovery has been

shown by Francis et al. and was achieved by coating the oxidised UVO240-PDMS sample in Krytox1506 [348]. This is a relevant consideration as the Krytox1506 oil mask used in the printing and metal deposit must be removed from the PDMS so that the surface is free and clear of residual liquids, as this may impact the effectiveness of the applied regeneration method.

Comparatively, the combined chemical-thermal treatment shows a much-increased hydro- and oleophobic recovery to a value marginally higher than P-PDMS and is therefore indicative of total recovery ($\geq$100%). It is apparent that the post-etching bake is key to driving the recovery to the values shown in Table 6.4. Application of the 150°C, 60 min heat treatment allows the PDMS to return to a purely temperature-dependent process where partial yet rapid recovery was previously observed. Assuming the majority of the recovery is a result of the heat treatment, the chemical dissolution reduces or potentially eliminates the SiO_x layer's barrier effect. The barrier effect to the migration of LMW PDMS by the oxygen-rich silica layer can be similarly reduced by inducing cracks and fractures through the layer. The formation of cracks in the SiO_x facilitates the rapid diffusion of LMW species, leading to a similarly increased rate of recovery. This mechanically-induced recovery has been described in numerous publications, for example, Hillborg et al. [280, 343], including an in-depth study by Mazaltarim et al. [354].

6.4 Surface Characterisation

6.4.1 Surface Chemistry Analysis

Characterisation of the surface chemistry and topographic properties will allow for improved correlation between the contact angle data and regeneration method. IR spectroscopy was performed to probe the underlying chemical changes to oxidised UVO240-PDMS as a result of thermal, chemical and combined regeneration. Samples of pristine, oxidised and heat-treated UVO240-PDMS are shown in Figure 6.13. Focus was placed on the edge conditions of the thermal treatments as the most significant differences in WCA and KCA were observed at these conditions, therefore, the four thermally enhanced recovery regimes analysed were 50°C for 15 min and 90 min as well as 200°C for 15 min and 90 min.

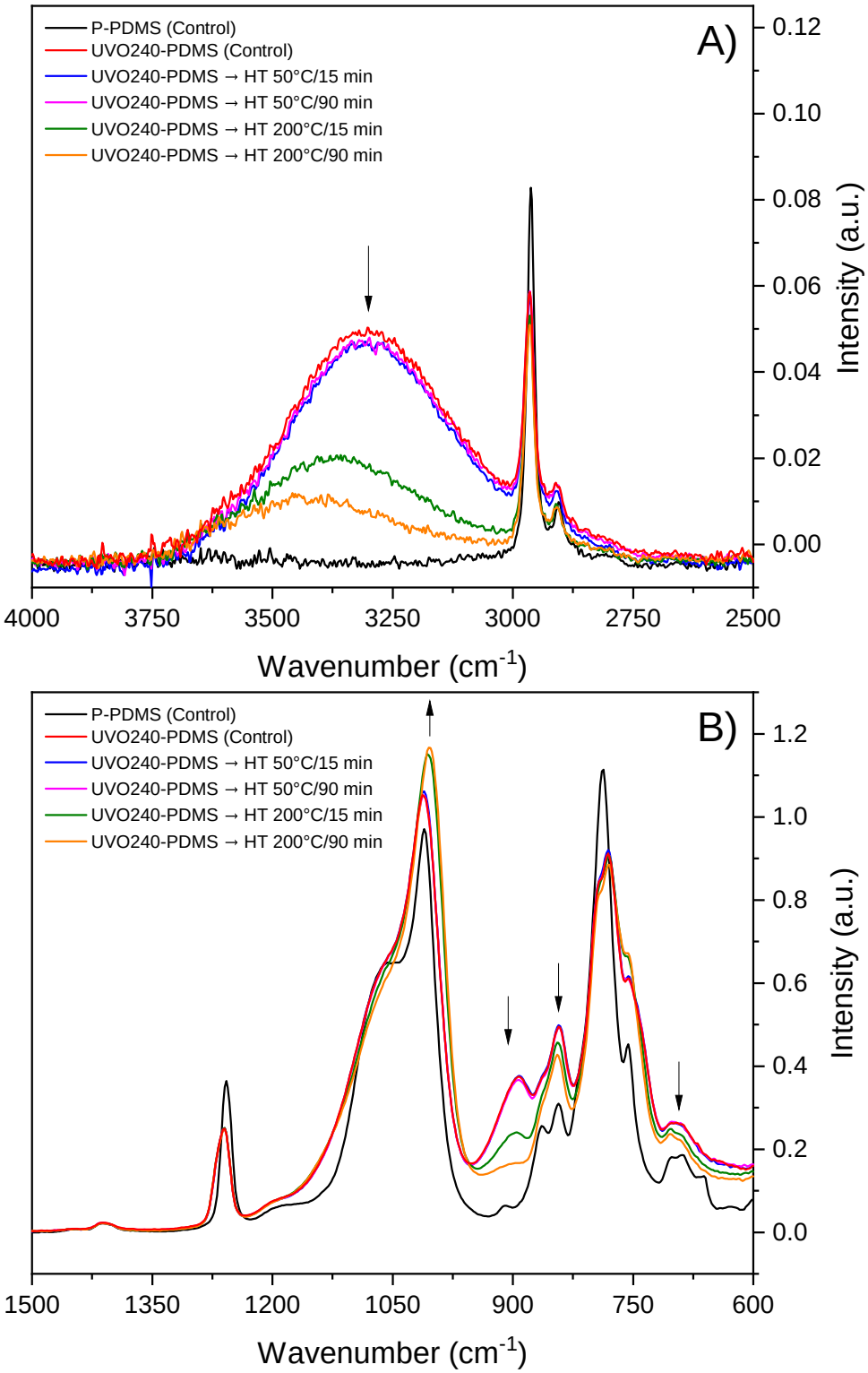

Figure 6.13: IR Spectra of P-PDMS, UVO240-PDMS and UVO240-PDMS subject to heat treatment regeneration process. Focusing on regions of interest at A) 4000 - 2500 cm^{-1} and B) 1500 - 600 cm^{-1}.

In Figure 6.13.A, the spectrum is centred on the −OH silanol stretch at 3300 cm^{-1}. As previously mentioned, oxidation by UV/O_3 results in the formation of silanol groups (Si−OH) following cleavage of the methylsilyl groups Si−CH_3 in P-PDMS. Upon application of the

200°C heat treatment to UVO240-PDMS, the intensity of the alcohol vibration begins to reduce with a longer duration, producing a greater reduction in the peak height. This reduction represents the loss of silanol groups from the oxidised surface. The hydroxyl loss appears to occur via silanol condensation, resulting in the formation of new Si−O−Si bridges [279, 338, 355].

Evidence of the condensation process is seen in Figure 6.13.B by the increase of the Si−O−Si stretch at 1010 cm^{-1} for both 200°C samples, which are accompanied by a reduction of both the Si−O stretches of the silanol group (Si−OH) at 893 and 840 cm^{-1}. As proposed by Fritz et al. and Senzai et al., loss of hydrophilic species bound to the surface of the UVO240-PDMS, e.g. Si−O, carbonyls, etc., to the environment may occur due to heat-induced volatilisation. [342, 345]. Relative to the intensity of the peaks in the UVO240-PDMS reference, the characteristic vibrations of PDMS methyl groups ($Si-CH_3$) at 2962, 1257 and 786 cm^{-1} do not change upon application of heat treatment, i.e. the trimethylsilyl group are neither reformed nor further eliminated from the surface. The intensity of the methyl vibrations remains at the level of UVO240-PDMS, indicating that oxidation of PDMS by UV/O_3 results in the permanent loss of $-CH_3$ content from the surface. The spectra for both 50°C samples in Figure 6.13 are almost identical to that of UVO240-PDMS reference with only a minor reduction in the −OH stretch observed, which is likely the loss of silanols to the atmosphere or by reorientation of the polymer chains away from the surface. The IR data corresponds well to the WCA and KCA data in Section 6.3, providing further reasoning for the large difference between 50°C and the higher temperature regenerated samples. Additionally, this data lends credence to the theory by Hillborg that the brittle, glass-like silica layer on UVO240-PDMS acts as an effective barrier at a lower temperature before undergoing a transition to a pristine-like rubbery state where increased LMW PDMS diffusivity is observed [343].

Figure 6.14 shows the IR spectra of UVO240-PDMS samples subject to chemical and combined chemical-thermal regeneration processes alongside comparative 60 min heat treatments. The thermally-enhanced recovery regimes (50, 100 & 150°C for 60 min) in Figure 6.15 show the same changes in vibration intensities as in Figure 6.13, that is, a reduction in the alcohol peak of the silanol at ∼3000 cm^{-1}, an increase in the Si−O−Si peak at ∼1010cm^{-1} and decreases in the other Si−O intensities below 900cm^{-1}. Similarly, the higher

the temperature, the greater the reduction in intensity of the oxidised species.

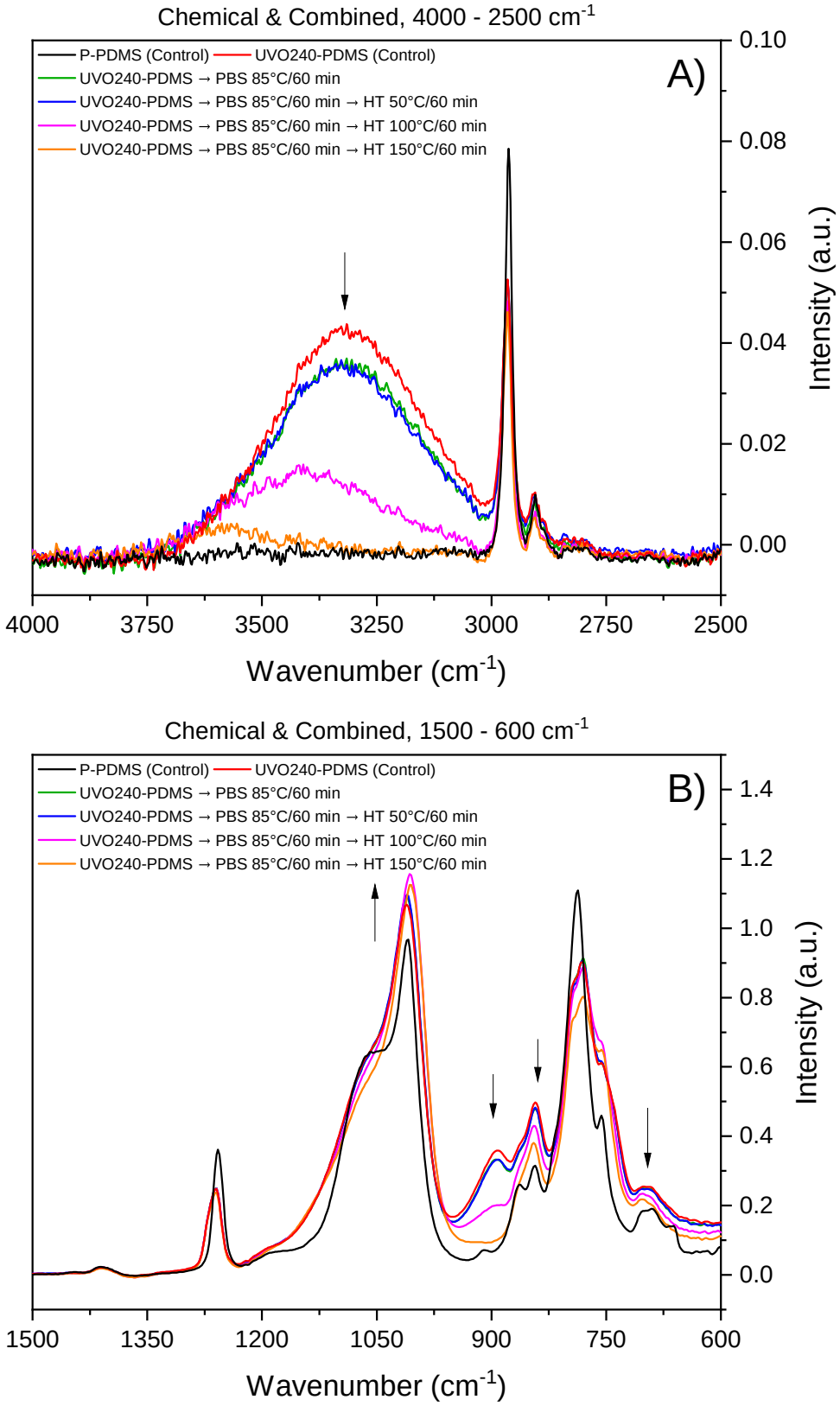

Figure 6.14: IR Spectra of P-PDMS, UVO240-PDMS and UVO240-PDMS subject to chemical-only and combined chemical-thermal processes at 50, 100 and 150°C. A) 4000 - 2500 cm^{-1} and B) 1500 - 600 cm^{-1}.

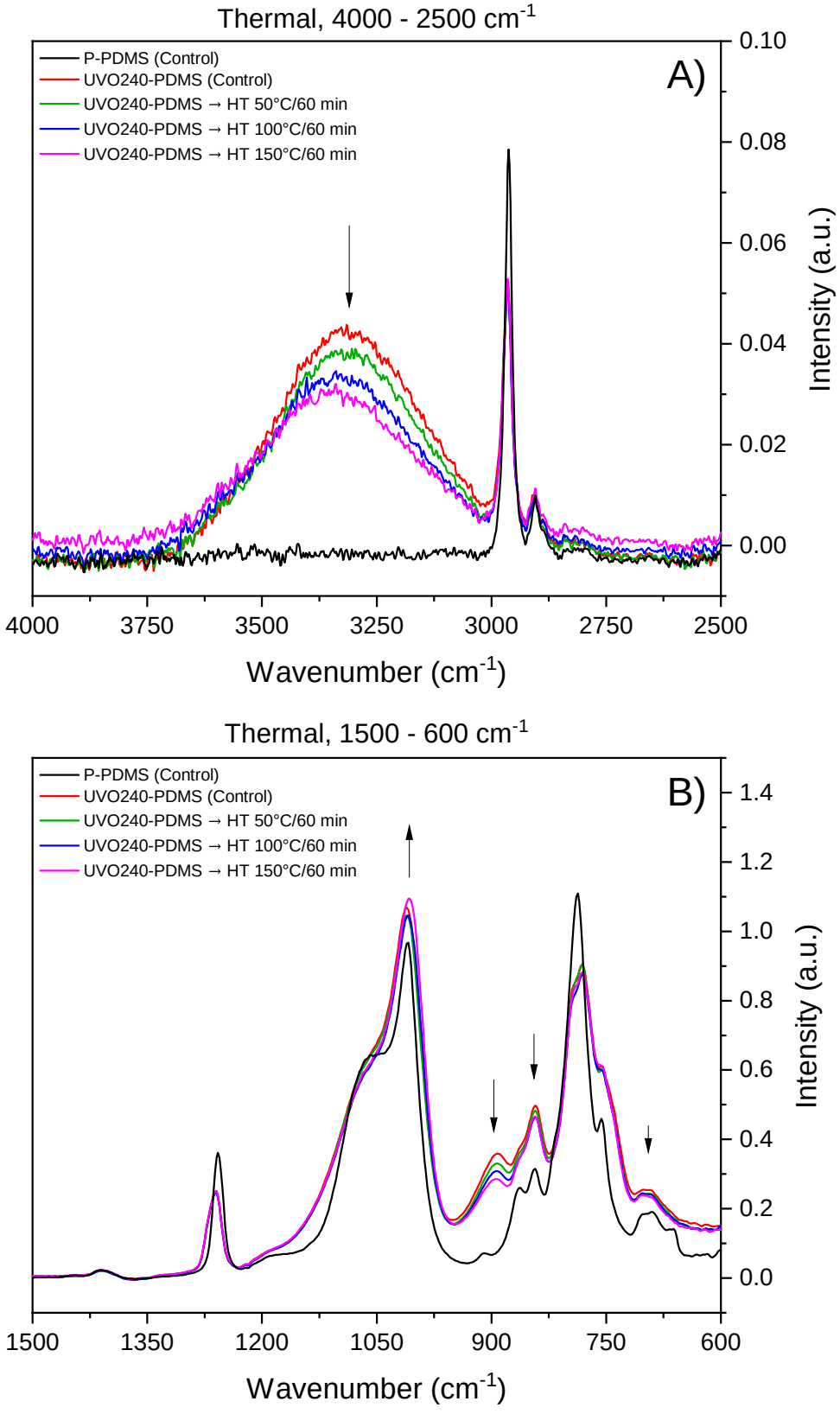

Figure 6.15: IR Spectra of P-PDMS, UVO240-PDMS and UVO240-PDMS subject to 60 min thermal regeneration at 50, 100 and 150°C. A) 4000 - 2500 cm^{-1} and B) 1500 - 600 cm^{-1}.

In comparison, focusing around the alcohol stretch in Figure 6.14.A, there is a significant decrease in the Si−OH vibration for the preferred combined regeneration of PBS dissolution

(85°C, 60 min) + 150°C, 60 min heat treatment.

The spectrum in Figure 6.14.B suggests the hydrophilic species are removed due to the significant loss in intensities of the Si−O vibration close to the level in P-PDMS, however comparable to the thermal data, the methyl content, i.e. Si−CH_3 does not recover. Interestingly, both the chemical-only spectrum and the chemical-thermal (50°C) sample show an identical but minimal reduction in vibrations. It is possible the reduction of the chemical and chemical-thermal (50°C) sample corresponds solely to the loss of weakly-bound surface groups to the environment or reorientation, whereas the higher temperature combined spectra show a greater loss of silanols by migration of LMW PDMS.

The similarity between the chemical/combined process and the thermal methods in Figures 6.14 and 6.15, respectively, shows that ATR-FTIR is not capable of characterising the oxygen-rich, silica-layer. However, the IR data does provide strong evidence that the combined regime removes the majority of the hydrophilic species, e.g. Si−OH, from the surface, which is a contributing factor to the observed recovery of WCA and KCA.

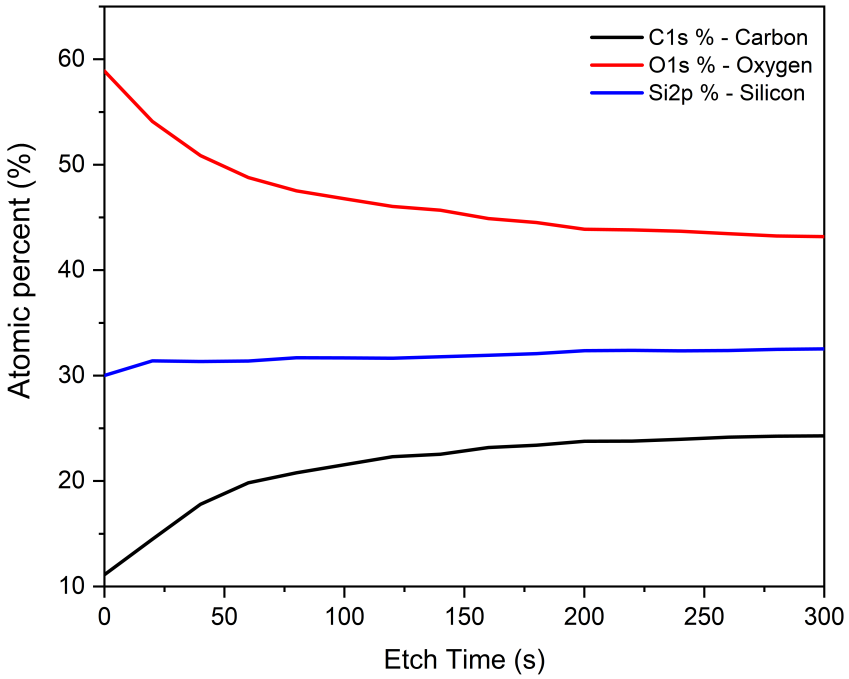

Figure 6.16: XPS depth profile of heat treated UVO240-PDMS - 50°C, 15 min.

Depth profiling XPS enabled the characterisation of the near-surface region, which is predominately comprised of the oxygen-rich silica-like phase. By determining the atomic percentages of oxygen, carbon, and silicon as well as the peak binding energies, the effective-

ness of modifying or removing the silica can be determined. Firstly, Figures 6.16 and 6.17 shows the XPS atomic profiles for two heat-treated sample (50°C for 15 min and 200°C for 15 min), respectively. (See Appendix B, Figures B.7 & B.8 for spectra.)

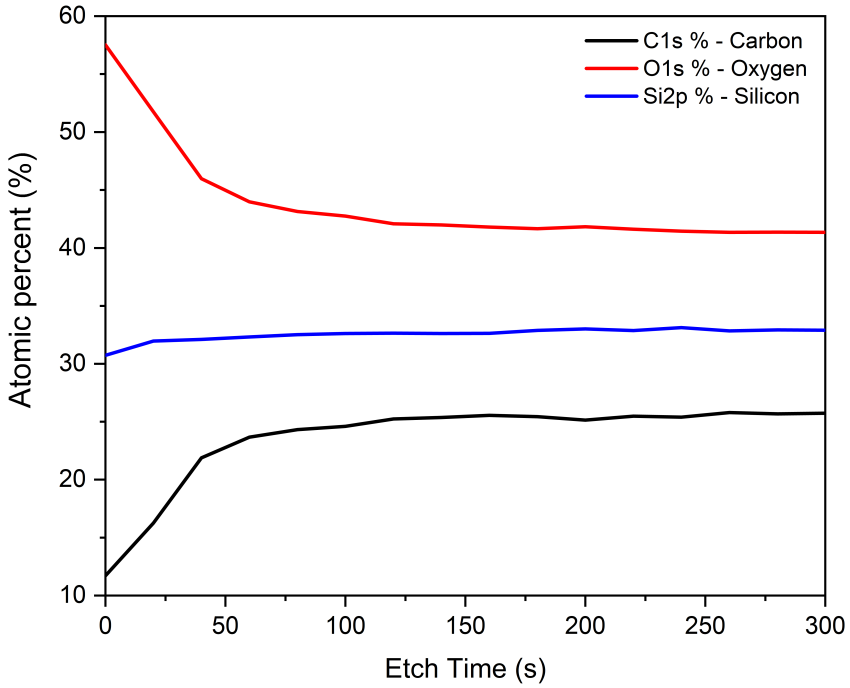

Figure 6.17: XPS depth profile of heat treated UVO240-PDMS - 200°C, 15 min

Both profiles in the above as well as the accompanying percentage data in Tables 6.6 and 6.7 match closely with the reference UVO240-PDMS in Figure 6.5. The measurement before depth profiling summarises the composition of the oxidised surface, while the etched measurement (after 300 s) outlines the composition of the oxygen-rich silica layer in the near-surface region.

Table 6.6: XPS atomic composition of surface Layer (0 s etch).

Sample	**Atomic Composition** (%)			**C/O ratio**
	Carbon	**Oxygen**	**Silicon**	
P-PDMS	44.12	28.8	27.09	1.532
UVO240-PDMS	11.27	59.07	29.65	0.191
UVO240→50°C, 15 min	11.6	59.11	29.29	0.196
UVO240→200°C, 15 min	11.7	58.52	29.78	0.200

There is minimal differentiation between Figures 6.5, 6.16 and 6.17 as the silica-like layer possesses an identical composition irrespective of applied heat treatment. As the chemical composition of this silica layer remains the same, it will not contribute to recovery through

Table 6.7: XPS atomic composition of subsurface and oxidised silica layer (300 s etch).

Sample	Atomic Composition (%)			C/O ratio
	Carbon	Oxygen	Silicon	
P-PDMS	38.98	28.61	32.41	1.362
UVO240-PDMS	24.70	42.50	32.80	0.581
UVO240→50°C, 15 min	24.42	42.99	32.59	0.568
UVO240→200°C, 15 min	25.73	41.73	32.54	0.617

alteration of bonding interactions. The silica-like layer is persistent and unperturbed by heat treatment. As discussed, Hillborg proposed that the glassy silica-like layer formed during oxidation is an effective barrier to the diffusion of LMW species to the hydrophilic surface at room temperature. As the temperature increases to ca. 60°C, the silica-like layer may undergo a transition from a glassy state, to a more rubbery state that allows for an increased LMW PDMS diffusivity [343]. Therefore, despite the silica layer remaining after heat treatment, the conversion into a state with an increased rate of migration occurring between 50 and 100°C would offer some explanation for the difference in WCA recovery.

Turning to the chemical-only and combined chemical-thermal (150°C, 60 min) methods, further XPS corroborates the mixture of theories explaining the observed recovery. Considering Figures 6.18 and 6.19, the atomic profile and percentages appear similar to the pristine surface (Figure 6.4) and therefore indicates the silica-layer formed during UV/O_3 oxidation is no longer present, that is, has been dissolved. However, there is a small disconnect between the IR spectra in Figure 6.14 and the atomic percentages in Figure 6.19. Specifically, the intensity of the carbon containing vibrations e.g. 2982 cm^{-1} does not recover to the intensity of that in P-PDMS while the carbon element concentration in the XPS does recover. It is possible this is the result of differences in sampling depth of both techniques or sensitivities to different functional groups of the individual techniques, and differences in sample preparation and oxidation. It is worth noting that the samples used in the ATR-FTIR and XPS were different such that they were prepared, oxidised and analysed over 1 year apart.

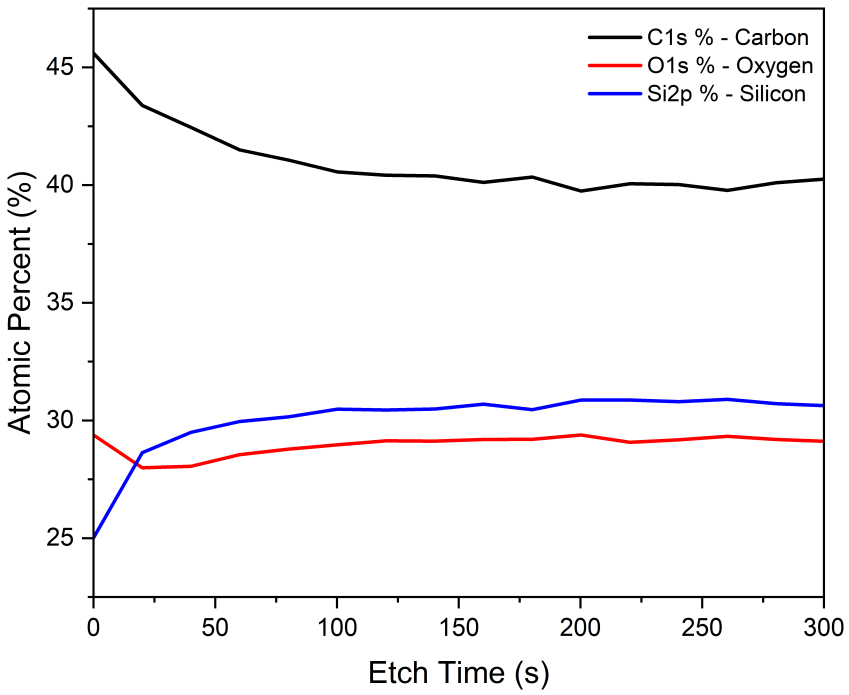

Figure 6.18: XPS depth profile of UVO240-PDMS subject to chemically-enhanced recovery - Silica Dissolution (PBS 85°C, 60 min). See Appendix B, Figure B.9 for spectra.

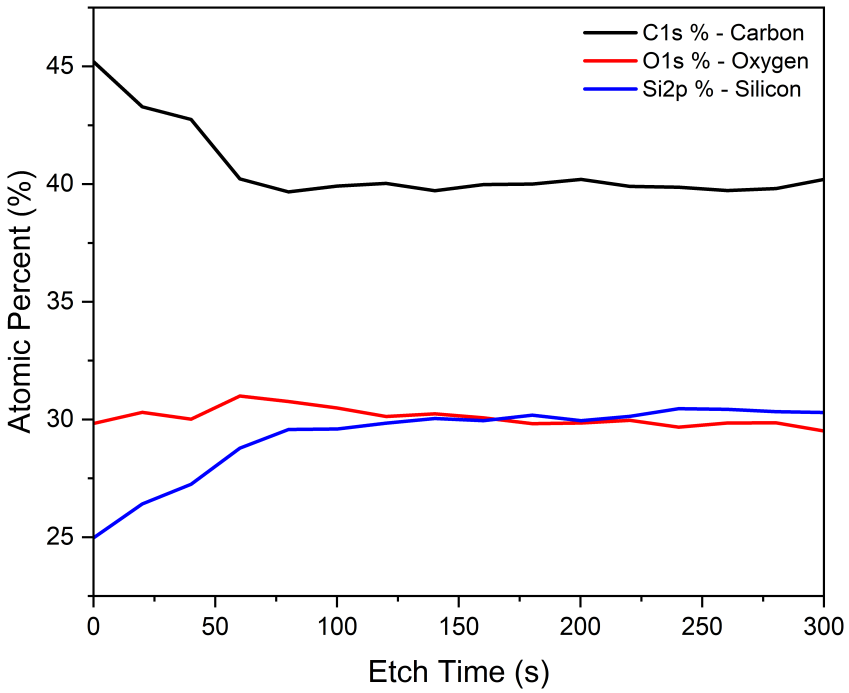

Figure 6.19: XPS depth profile of UVO240-PDMS subject to combined thermal & chemically-enhanced recovery - Silica Dissolution (PBS 85°C, 60 min) → heating (150°C, 60 min). See Appendix B, Figure B.10 for spectra.

The dissolution of the silica layer is further evidenced by the shift in Si2p peak binding energy. In Figure 6.20, the peak binding energies of various regeneration processes are presented. The shift of the Si2p peak for both the chemical-only and combined processes

back to the approximate value of P-PDMS, e.g. 101.3 eV, is indicative of the siloxane phase due to the removal of the SiO_x-like layer which has a higher peak binding energy around 103.3 eV.

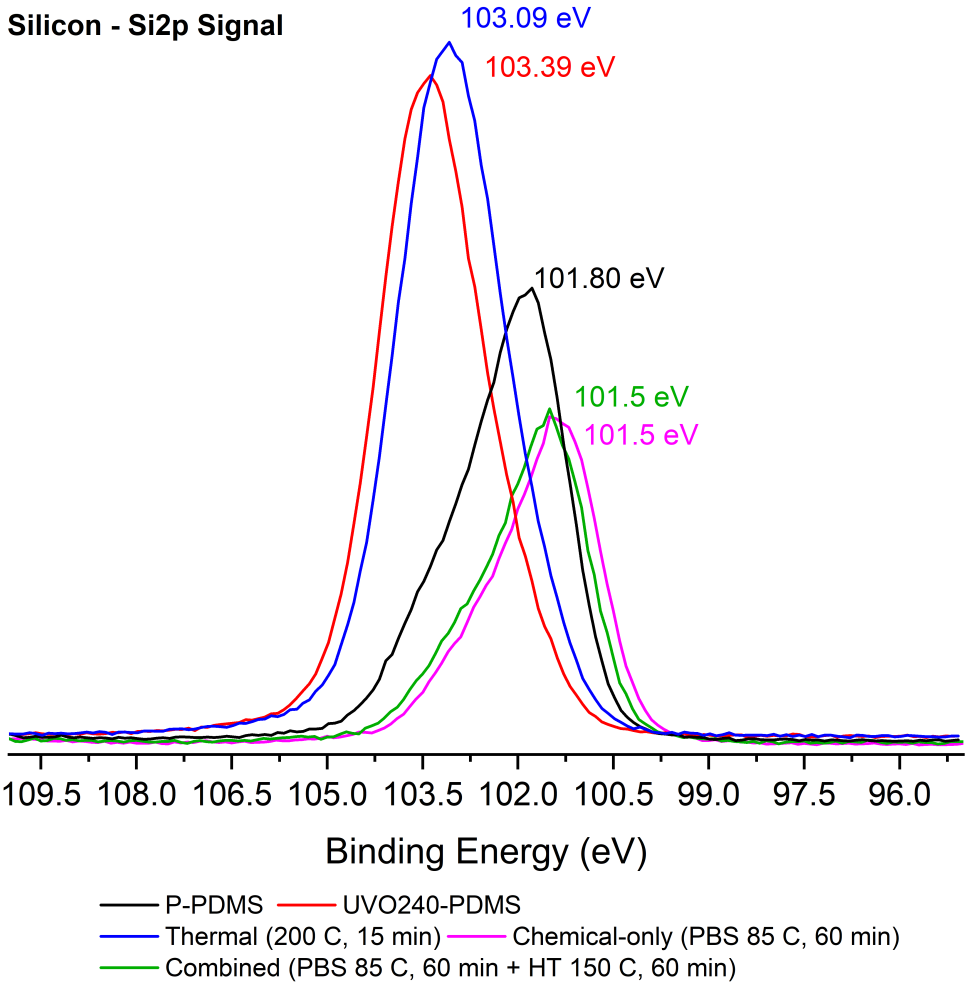

Figure 6.20: XPS Si2p peak binding energy.

6.4.2 Roughness Analysis

As outlined in Section 5.7.3, Sa values over two areas of 100^2 µm and 1^2 µm were determined using optical interferometry and AFM, respectively. Figure 6.23 shows the microscale and Figure 6.24 shows the nanoscale roughness for the thermal extremes, chemical-only and combined regeneration methods. Considering the microscale area, there is a general increase in Sa as a result of higher treatment temperature and duration from 1.883 ± 0.43 nm on UVO240-PDMS to 5.088 ± 1.89 nm for the 200°C, 90 min sample. As outlined in Figure 6.23, the chemical-only approach has a microscale roughness comparable with the 200°C/90 min thermal regeneration, while a relatively large increase in Sa is found on the

combined chemical-thermal treatment up to 13.925 ± 3.27 nm. Over a nanoscale area as measured by atomic force microscopy (Figure 6.24), the changes in areal surface roughness relative to the reference are minimal, with all the applied regeneration methods resulting in negligible change of ± ∼ 1 nm. While the applied surface regeneration methods result in a small nanometre-scale increase in areal surface roughness, the magnitude of this increase on the scale of nanometres will have no impact on the wetting behaviour of the surface.

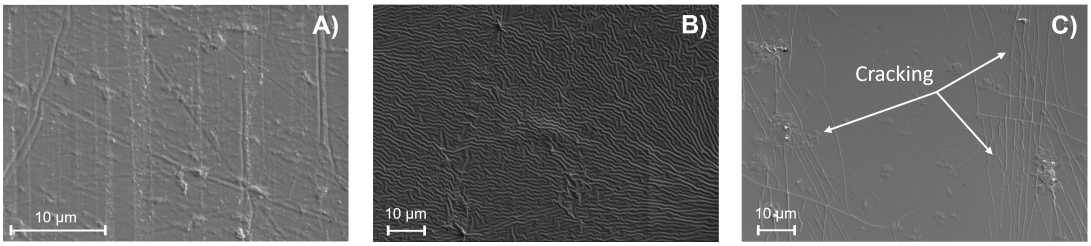

Figure 6.21: Micrographs of thermally-regenerated PDMS samples showing the formation of cracks following an application of a high-temperature regeneration regime. A) UVO240-PDMS Reference Sample, B) 50°C, 15 min thermally-regenerated sample, and C) 200°C, 15 min sample with surface cracking annotated.

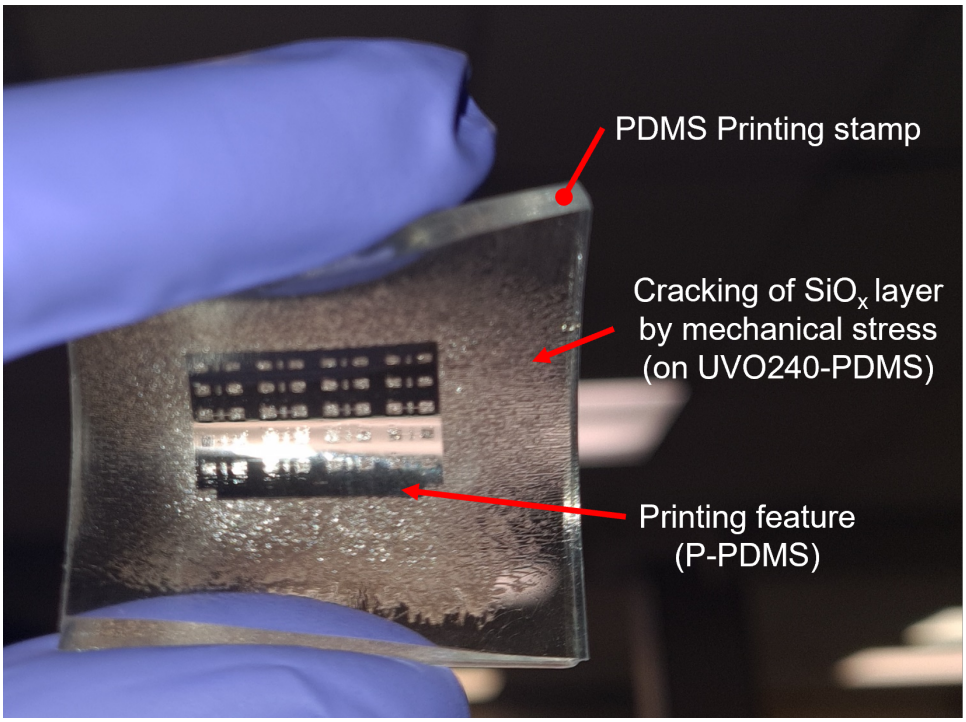

Figure 6.22: Photograph of UVO240-PDMS with cracking due to mechanical deformation (bending and stretching).

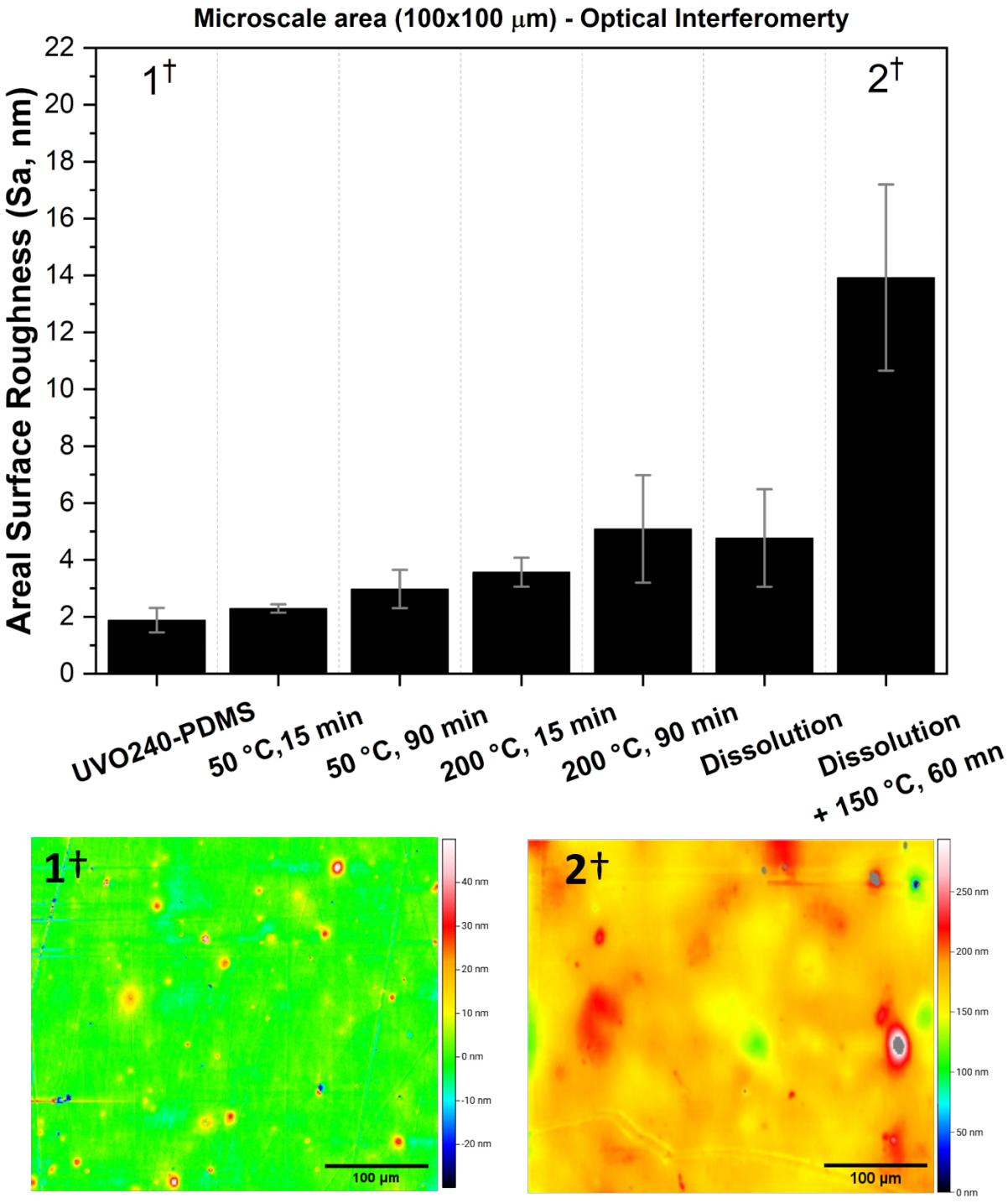

Figure 6.23: Areal arithmetic mean microscale surface roughness (Sa, nm) vs Regeneration Process from interferometry over an area of 100^2 μm. 1†/2† : Select 2-D optical profilometry images of PDMS surfaces.

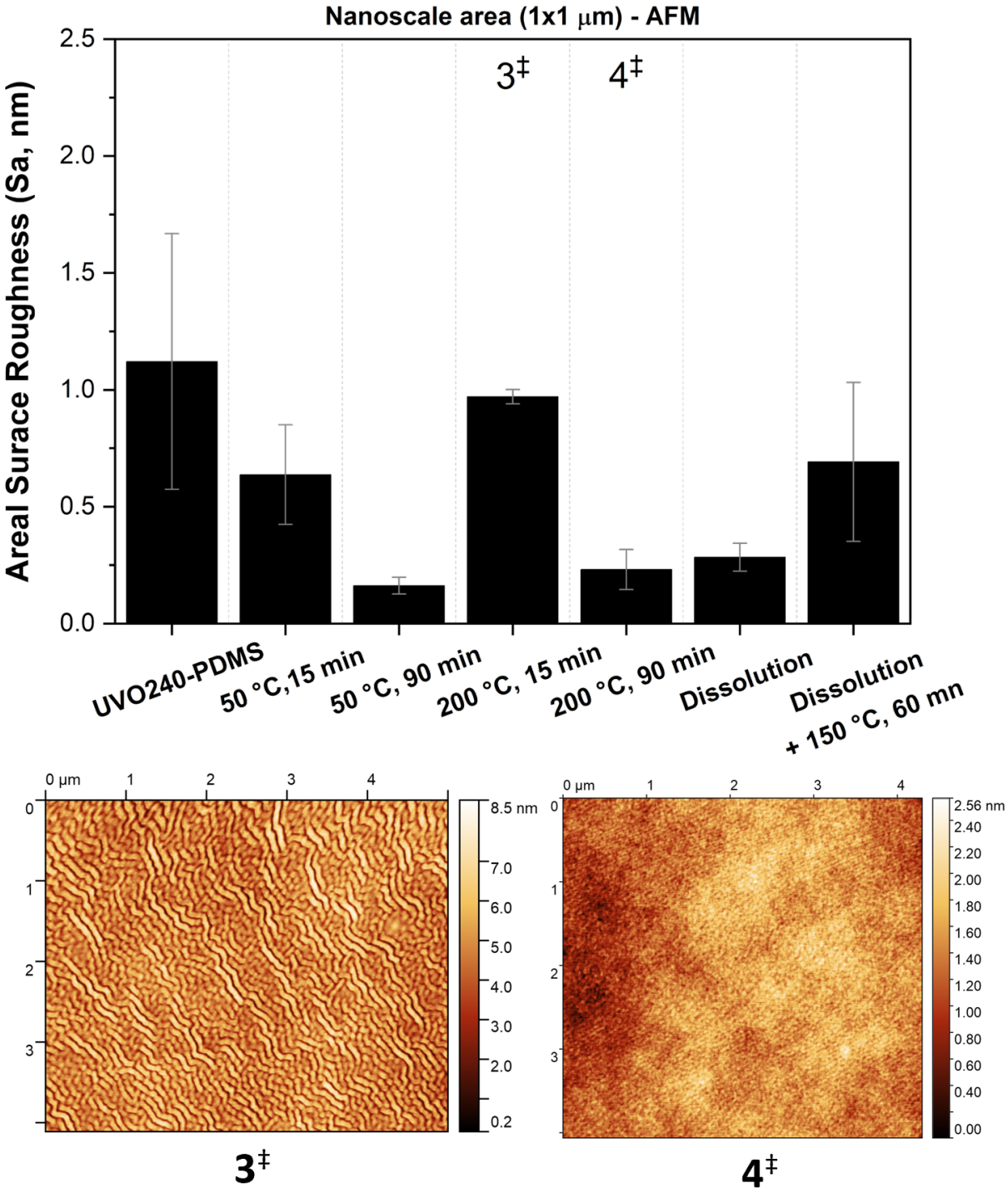

Figure 6.24: Areal arithmetic mean microscale surface roughness (Sa, nm) vs Regeneration Process Nanoscale roughness from AFM over an area of 1^2 μm. 3‡/4‡: Select 2-D AFM micrographs of PDMS surfaces.

The difference between the increase in microscale roughness and the unchanged surface on the nano-scale may be the result of cracks forming throughout the brittle silica layer. It has previously been shown that the induced stresses of a thermal bake to oxidised-PDMS samples can result in cracking [280]. Figure 6.21 shows micrographs of a UVO240-PDMS reference verse the 50 and 200°C (15 min) thermally regenerated surfaces. Images A and B show the surfaces are void of cracks and relates to low surface roughness values. In Figure 6.21.C, the formation of cracks on the surface also corresponds to a ∼3 nm increase in Sa for the 200°C heated sample.

The cracks in the silica-like layer are on the order of 10s of microns in length, as such, the formation of the cracking network can be observed by the human eye if it is extensive enough, for example, visualisation of the cracks was achieved by repeated mechanical deformation (bending and stretching) of a UVO240-PDMS sample. The image in Figure 6.22 shows this cracking on the surface of a UVO240-PDMS block that has been purposefully deformed to induce crack formation. This highlights the need for careful handling of the PDMS blocks throughout the whole process.

6.5 Patterning and Images Analysis

6.5.1 Direct Metal Deposition on PDMS Substrates

Several promising surface regeneration methods, informed by contact angle data and compelling evidence of surface/near-surface chemistry changes, have been outlined in the previous sections. Both the high-temperature thermal treatments (150 & 200°C) and the chemically-enhanced processes have demonstrated significant recovery for the water and Krytox1506 contact angles. The data underscores the theoretical viability of regenerating the surface of oxidised UVO240-PDMS for repatterning applications. Chemical analysis by surface-sensitive ATR-FTIR and XPS has shown that the combined chemical-thermal method appears to result in the complete reversion of the oxidised surface to a pristine-like state. While the regeneration methods have been shown to result in improved recovery evidently, translation to real patterned metal deposition by UV/O_3-PDMS selective metallisation proved challenging. In the following section, select attempts of utilising the regeneration methods to achieve

pattern rewriting and the reuse of oxidised-PDMS printing stamps are presented.

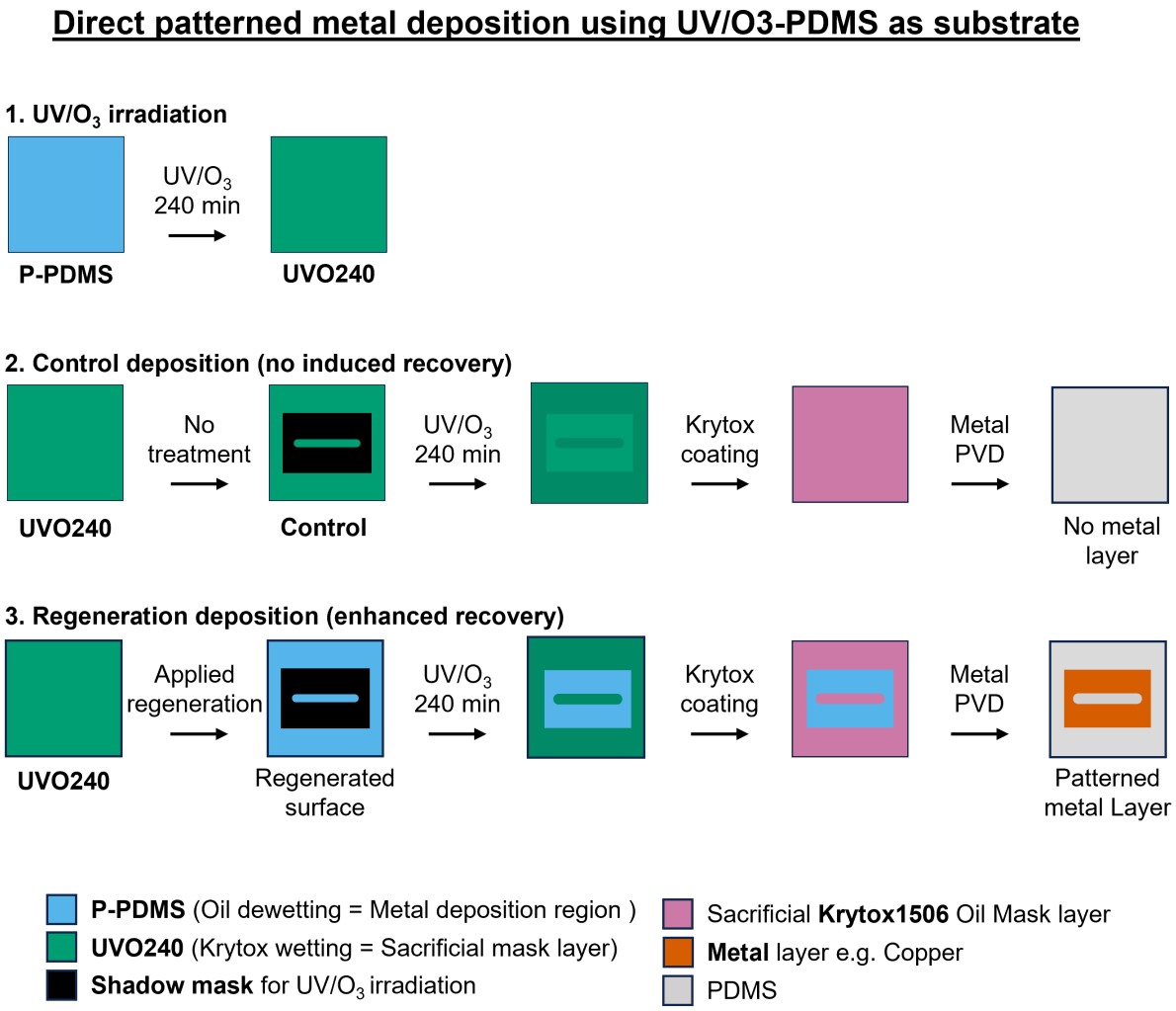

Figure 6.25: Schematic representation of theoretical outcome for patterned metal deposition using UV/O_3-PDMS as the substrate. 1) UV/O3 irradation of P-PDMS, 2) Control sample with no applied regeneration method (Intrinsic recovery), and 3) Deposition process with regenerated PDMS samples.

Typically, the normal process for deposition of a patterned metal layer by UV/O_3-PDMS selective metallisation is as follows;

1. **Oxidise**: Prepare and oxidise a PDMS block (stamp) using a 240 min UV/Ozone treatment. This is performed through a patterned mask in the design of the final metal pattern, similar to the use of a positive resist in photolithograhpy.
2. **Coat:** Deposit a thin-layer of Krytox1506 PFPE vaccum oil onto the UVO240-PDMS stamp. Oil coats the stamp over areas of the PDMS irradiated by UV/Ozone i.e. the oxidised PDMS.
3. **Stamp:** Transfer oil pattern from the Krytox-coated UVO240-PDMS to a suitable sub-

strate (e.g. a PET sheet) via stamping or R2R printing. The substrate will now be coated by oil on the negative spaces of the pattern.

4. **Metallisation**: Deposition of metal via a PVD process such as vacuum thermal evaporation will, in essence, develop the substrate leaving a pattern metal layer. As mentioned, the oil prevents metal deposition, yielding a patterned metal layer in the parts of the substrate that were not coated with Krytox1506.

An initial of experiments eliminated the oil mask transfer stage (3. Stamp), simplifying the regeneration and metal deposition processes. However, by using PDMS as the substrate for both oil and metal deposition, it is only possible to perform a single metallisation step. This contrasts a full process where the oil coated PDMS can be used for repeat deposition of an oil mask onto a secondary substrate.

As outlined in Figure 6.25, a complete process for the 'direct' metal deposition begins with oxidation of PDMS blocks by a blanket UV/O_3-irradiation (240 min). The blanket oxidised PDMS blocks are in a fully wetting / oleophilic state where the Krytox1506 oil would coat its entire area, i.e. preventing metal deposition. A sample is left without regeneration to undergo an intrinsic and uncontrolled hydrophobic recovery process, this will act as a control. The remaining fully oxidised UVO240-PDMS surfaces are regenerated by a thermal (150°C, 60 min), chemical (PBS immersion @ 85°C, 60 min) or combined (PBS immersion then 150°C heat treatment) processes.

Following regeneration, a second UV/O_3-oxidation is performed through a shadow mask to yield a patterned oxidised layer to which Krytox1506 was deposited by spin coating. Finally, the oil masked PDMS substrates were developed by exposure to a thermally evaporated metal source to yield the final patterned metal layer. As oxidising the whole pristine-PDMS surface, results in a UVO240-PDMS surface with a Krytox1506 wetting state that is, no metal deposition should be possible, successful regeneration of the UVO240-PDMS should yield a patterned metal layer at the end of the process.

The images in Figure 6.26 show the result of direct metal deposition onto repatterned UV/O_3-PDMS substrates. Expectedly, the control sample that was not subject to a regeneration process, showed minimal or partial formation of the patterned metal layer. As

oxidised PDMS does naturally recover contact angle, a partial metal layer resembling the shadow mask pattern was likely to form, highlighting the need for application of a controlled and uniform surface regeneration process which is one of the primary motivations for this work. The quality and completeness of the metal layer as a result of the surface regeneration process on blanket oxidised UVO240-PDMS, matches the trend in KCA outlined in Figures 6.11, that is, thermal<chemical≪combined, in terms of percentage recovery. There is a large difference in the final metal layer for the thermally-regenerated (150°C, 60 min) and chemically-regenerated (PBS 85°C, 60 min) samples despite similar levels of recovery, strongly suggesting removal of the oxygen-rich silica-layer is crucial to achieving repatternability of the oxidised UVO240-PDMS surface. The result from metal deposition on PDMS substrates are promising and show that the applied regeneration method, particularly chemical methods, can effectively induce recovery of the UVO240-PDMS to enable a secondary patterning by UV/O_3, deposition of patterned oil mask due to control of wetting-dewtting on the regenerated surface and the final patterned metal deposition.

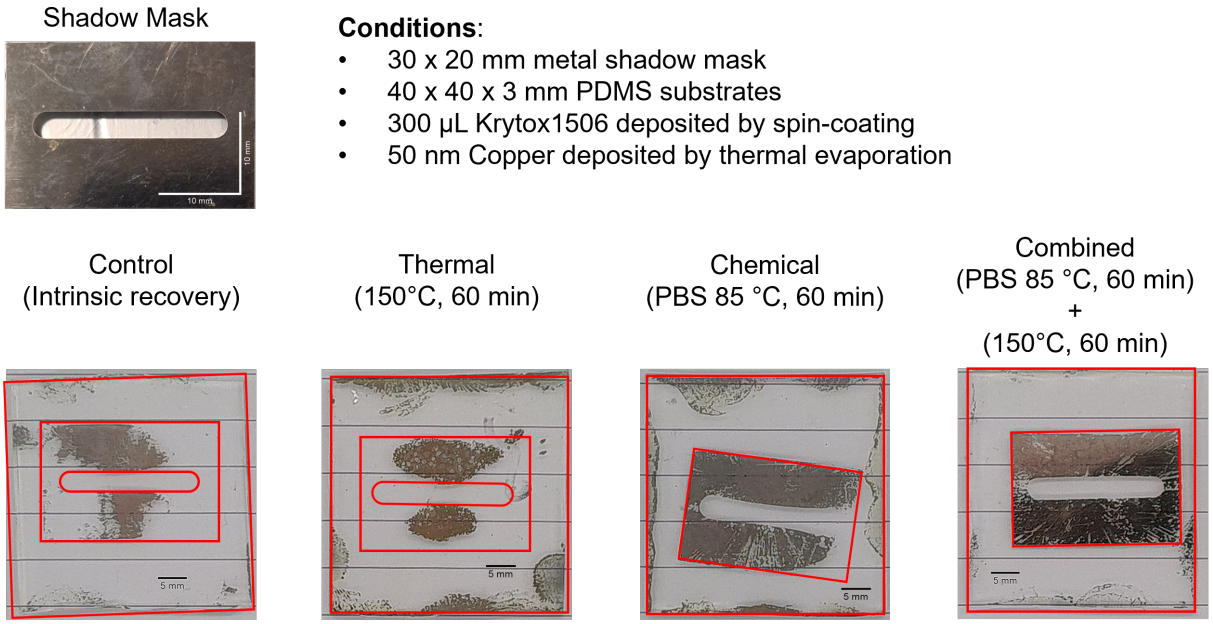

Figure 6.26: UV/O_3-PDMS metal deposition utilising PDMS as the substrate. Images of 4 samples include a control and 3 regenerated samples - thermal, chemical and combined chemical-thermal. The expected patterned metal feature is outlined in red.

The direct metal deposition onto regenerated, repatterned PDMS offers little in terms of real application to the deposition of electrodes onto flexible, plastic substrates and acts purely as a proof-of-concept that the UVO240-PDMS can be regenerated to allow for a patterned

metal deposition. Direct deposition avoids potential issues arising from oil mask printing, the removal of residual Krytox1506 from used printheads and the problematic wetting-dewetting behaviour of Krytox1506. In the second part of this section, a double-patterning process with oil transfer by stamping will be presented.

6.5.2 Stamped Oil Transfer and Rewriting

UV/O_3-PDMS was utilised as a stamp to enable the transfer of a patterned Krytox1506 oil mask onto flexible plastic (PET) substrates. Following a similar process as outlined in Figure 6.25, the complete double-pattern, or rewriting process is shown in Figure 6.27. The main difference between the direct deposition and the double patterning process is that both the oxidation steps are performed through a shadow mask as opposed to an initial blanket UV/O_3 oxidation to the entire P-PDMS surface. Additionally, following completion of oil mask transfer onto PET, the remaining and residual Krytox1506 needs to be removed from the surface of the PDMS before application of a regeneration treatment.

Throughout the rewriting process, the initial deposition for all samples will exhibit a single feature on the patterned metal layer. In the case of the control sample, the second deposition is expected to present elements of both the first and second patterns, reflecting the surface's negligible regeneration in the absence of enhancement of the recovery process. Conversely, with stamps subjected to a regeneration process, it is expected that the second deposition will show only the secondary patterned feature given that the original pattern has been successfully removed during the regeneration process. This is described in steps 2, 4 and 5 of Figure 6.27.

Figures 6.28 and 6.29 showcase images of resultant patterned metal layers from the complete metal deposition process. For each PDMS stamp, two separate stampings were performed to create two metallised samples. The expected metal pattern for the 1st pattern is highlighted in red with the expected feature from the 2nd shadow mask pattern in blue. The patterned metal features in Figure 6.28 serve as reference markers as the deposition of metal layers by UV/O_3-PDMS is already understood and relatively consistent process.

To summarise as outlined in Figure 6.28, all four of the initial patterned PDMS stamps,

prior to regeneration and repatterning, produced metal layers with sharp features and importantly, clear differentiation between the metallised and non-metallised areas.

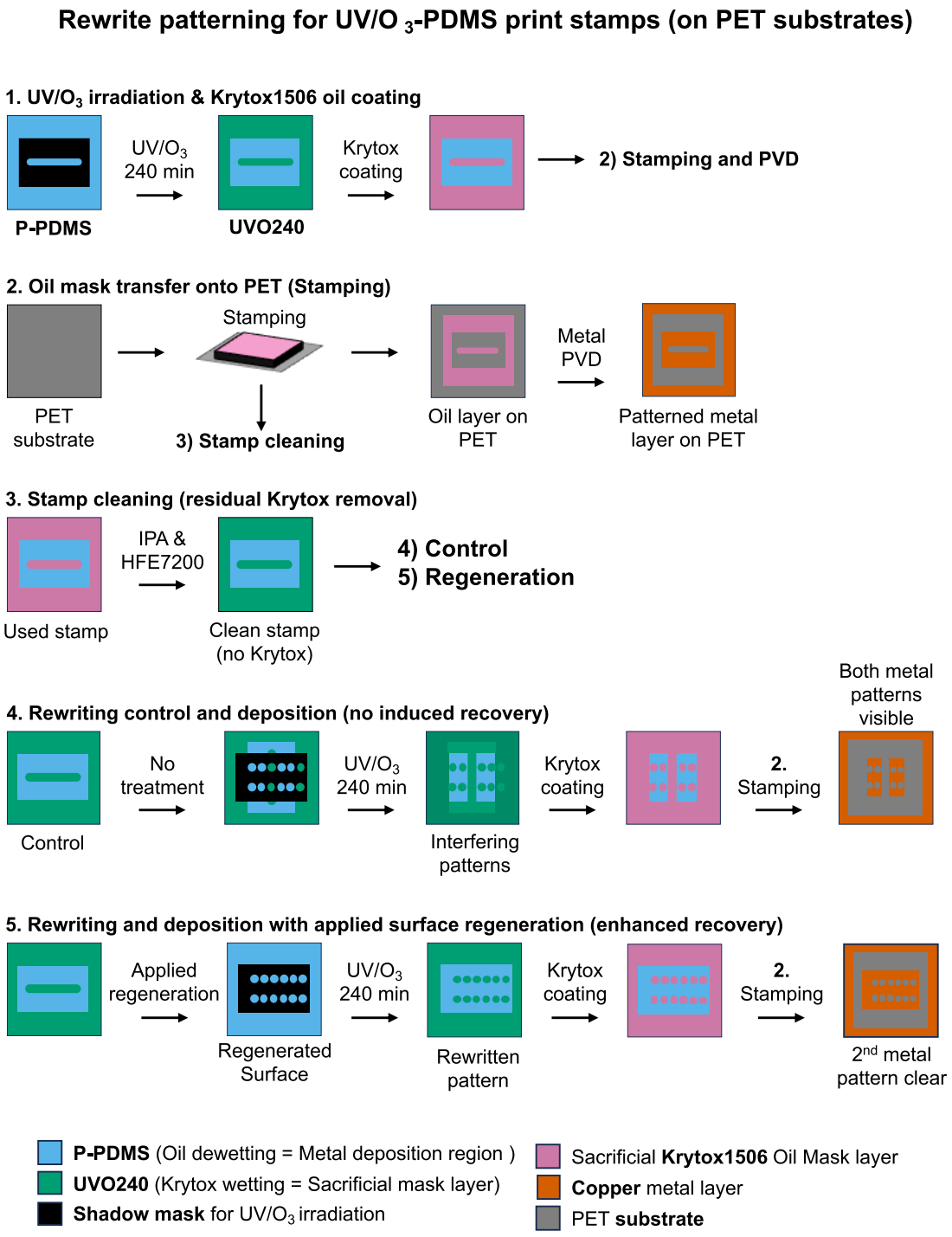

Figure 6.27: Schematic representation of theoretical outcome for patterned metal deposition using UV/O_3-PDMS as a print stamp for oil mask deposition onto PET substrates 1) Patterned UV/oxidation of P-PDMS through a shadow mask and coating of patterned Krytox1506 layer, 2) Deposition of Krytox1506 oil mask onto PET and development on metal layers by PVD onto oil-masked PET substrates, 3) Cleaning of used PDMS stamps by IPA rinse and HFE-7200 wiping and, rewriting (2nd patterned UV/O_3 oxidation) onto 4) control (no regeneration) or 5) regenerated PDMS samples.

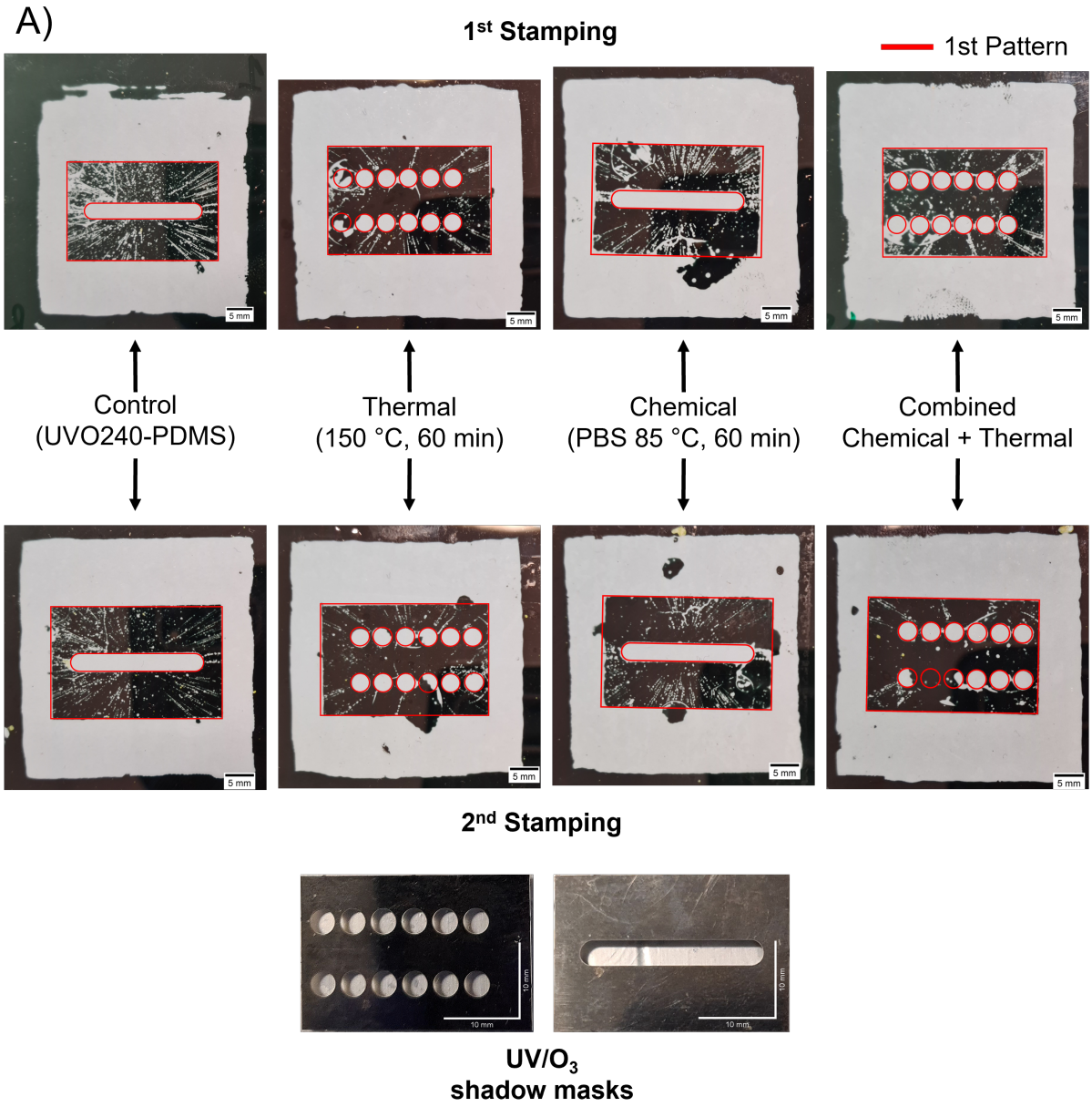

Figure 6.28: UV/O_3-PDMS metal deposition using PDMS stamps for patterned oil mask transfer onto PET. Images of patterned metal layers **before** application of regeneration processes (1st pattern).

To remove the residual Krytox1506, the used PDMS stamps were cleaned by rinsing with IPA before wiping with an ethoxynonafluorobutane ($C_6H_5F_9O$) soaked, lint-free cleanroom tissue. The hydrofluoroether solvent (HFE-7200) was chosen as it one of the limited compounds that is thought to be miscible with Krytox1506 [359]. Once visually clean and no longer oily to the touch, the PDMS stamps were subject to surface regeneration processes before a second hydrophilisation by UV/O_3 in which a shadow mask a different feature was used to produce a contrasting patterned surface. After a fresh coating of Krytox1506 oil onto the PDMS stamp, a final set of oil mask transfer onto PET substrates and the sub-

sequent metal evaporation was performed to produce metal layers from the regenerated surfaces. The images in Figure 6.29 show the final metallised substrates after regeneration, repatterning and metal deposition.

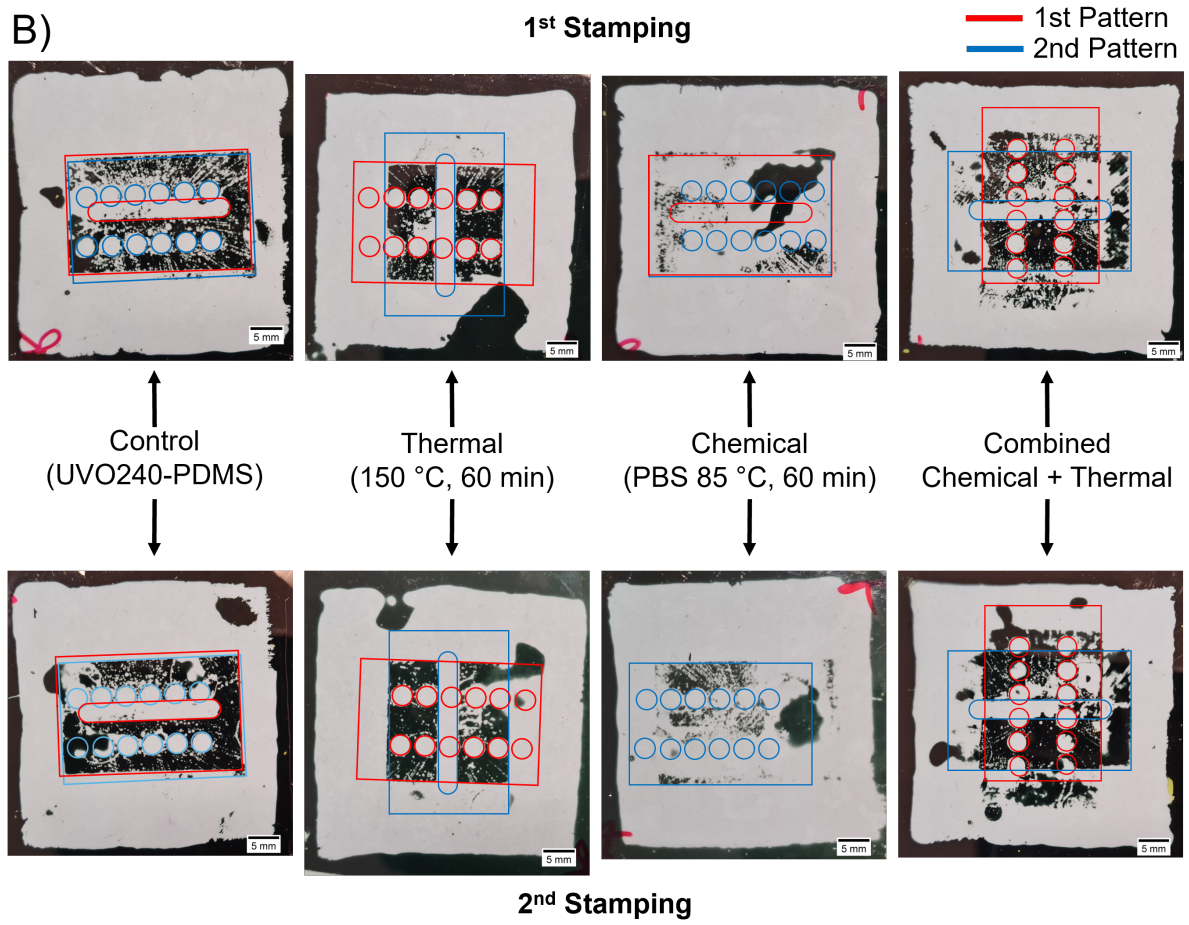

Figure 6.29: UV/O_3-PDMS metal deposition using regenerated PDMS stamps for patterned oil mask transfer onto PET - Example 2. Images of patterned metal layers **after** to application of regeneration processes (1st pattern and 2nd pattern).

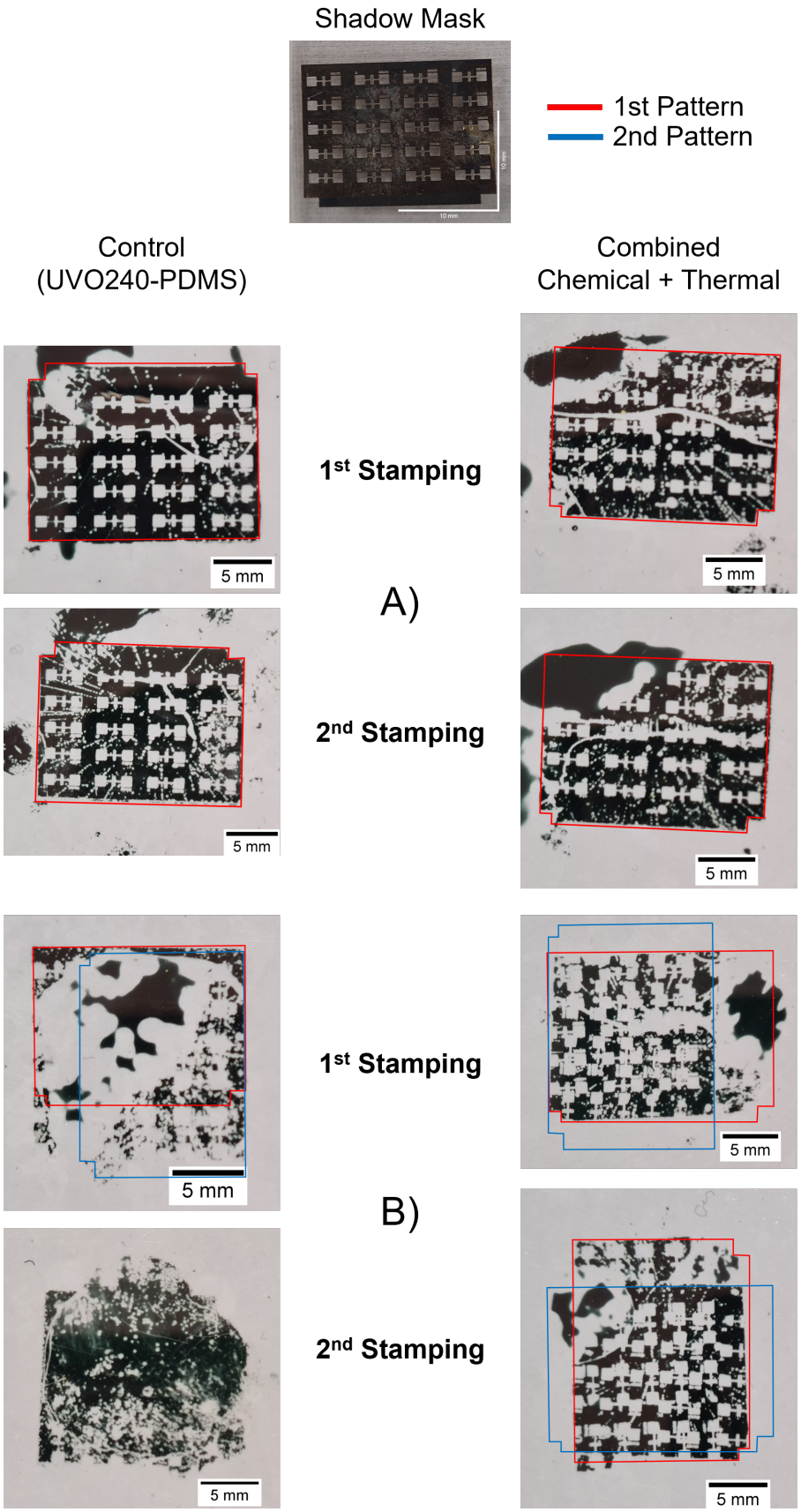

Figure 6.30: UV/O_3-PDMS metal deposition using regenerated PDMS stamps - High resolution Source-Drain mask (1st pattern and 2nd pattern). A) 1st patterning and deposition and B) 2nd patterning and deposition with mask placed perpendicular to 1st pattern.

It is immediately clear that features from both the 1st and 2nd shadow mask patterns are present in the final metal layers directly opposing what was expected on account of the experimental data and previous direct deposition example. The identifying features of both the basic geometric shadow masks, that is, the small circles and rounded bar, are visible. The presence of both the key features indicates that despite performing the regeneration process, Krytox1506 oil is wetting the regions of the block that were originally oxidised during the 1st UV/O_3-oxidation. This is the opposite result from the direct depositions shown in outlined in the example Figure 6.26. Multiple repeats of the rewrite, double-patterning deposition process with a variety of different shadow mask shapes, including a high-resolution source-drain shadow mask with 30 μm features, gave in the same outcome. Furthermore, in the chemical-only samples of Figure 6.29, the quality of the metal layer and overall expected coverage of the pattern is very poor. This emphasises the inconsistency in the rewritten UV/O_3-PDMS deposition process to produce a quality and repeatable metal pattern each attempt. In additional examples, the chemical-only regeneration process has produced patterned metal layers of comparable quality to the others with both feature present, i.e., the final metal layers are indistinguishable irrespective of applied surface regeneration process.

Images of developed metal layers from a pattern rewriting example using a high-resolution shadow mask are shown in Figure 6.30 alongside micrographs of select features in Figure 6.31.

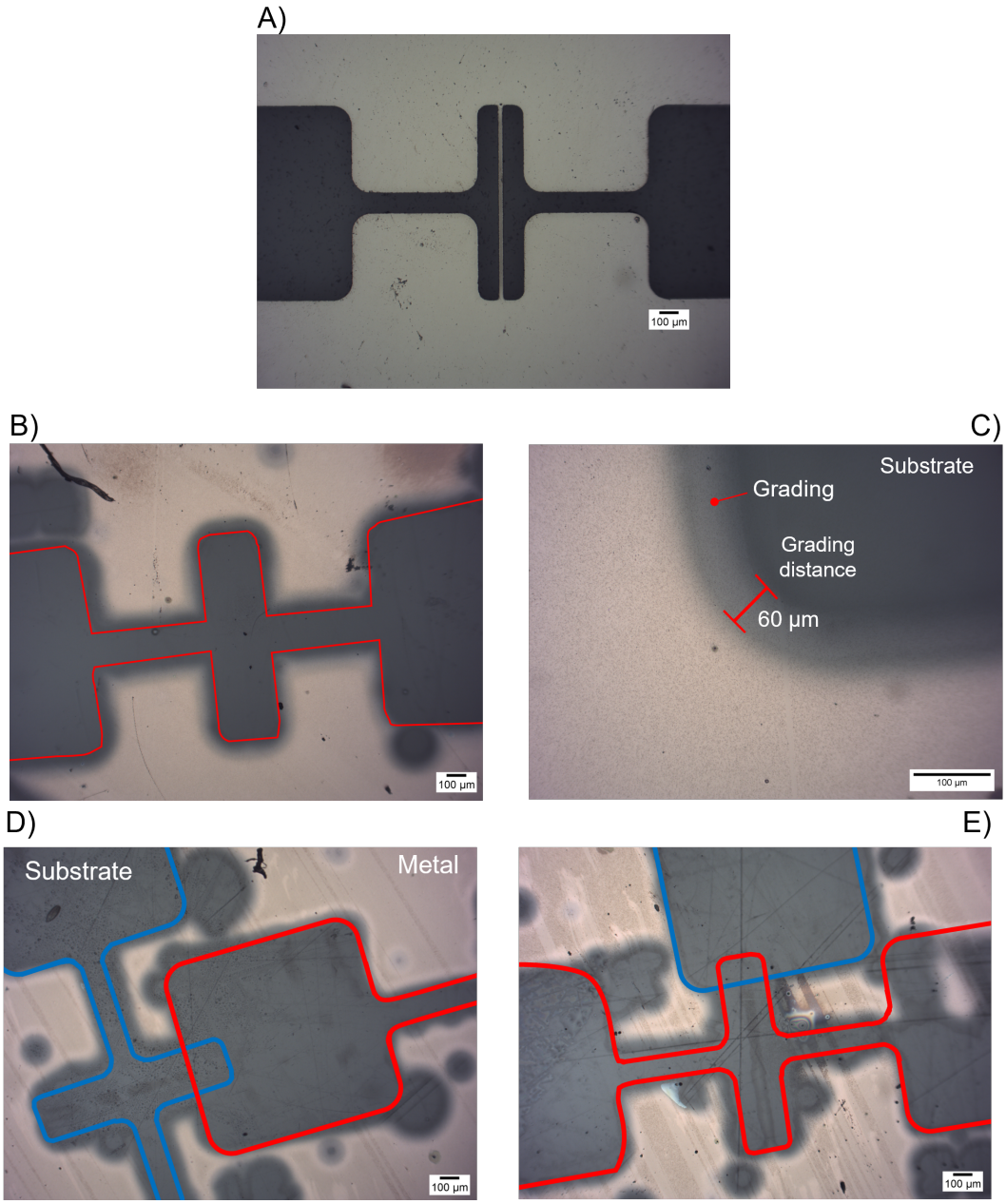

Figure 6.31: Micrographs of high-resolution UV/O_3-PDMS pattern rewriting examples. A) Shadow mask with 30 µm linewidth feature. B) Channel feature from 1st stamping of 1st pattern (before regeneration). C) Quality of metal layer showing a region of grading. D) & E) Overlapping features of both 1st pattern and 2nd pattern.

In the high-resolution example, the same outcome as the geometric shape patterns was observed, that is, clear patterned metal features from the 1st and 2nd stamping in the initial patterning step, followed by the presences of both the patterns in the 2nd set of patterned metal layers after regeneration. Although the control sample in this case gave a very poor layer with no discernible features, the double patterned stamp, which underwent a combined chemical-thermal regeneration, showed overlap. The pattern overlap is easier to vi-

sualise in the micrographs of Figures 6.31.D & E as outlined by the blue and red highlights.

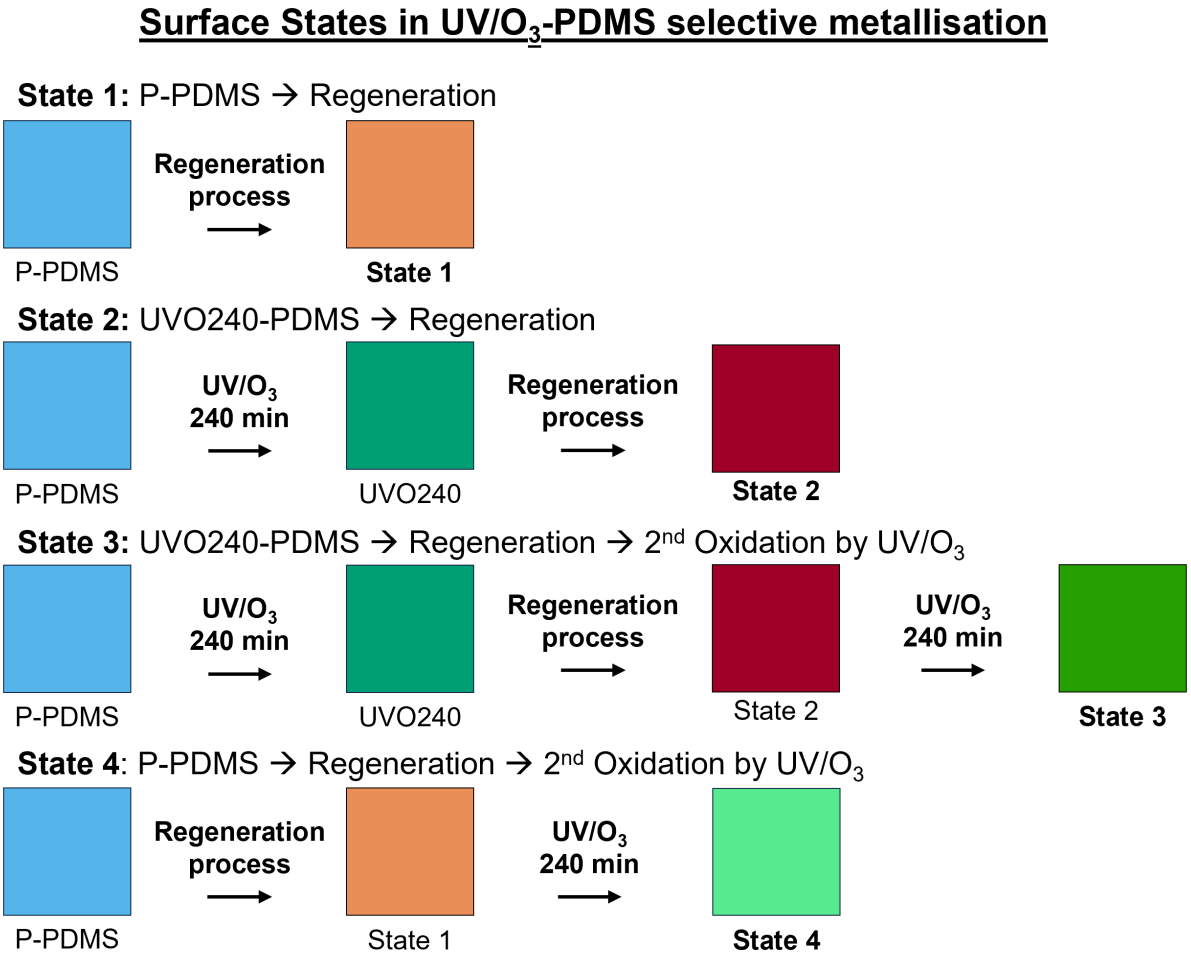

Figure 6.32: Graphical representation of the surface states in UV/O_3-PDMS oxidation-regeneration.

The disconnect between the experimental contact angle data (Figure 6.11) that shows a recovery of Krytox1506 contact angle for the combined regeneration process, and the outcome of the double patterning process raises a complex issue that would ultimately require additional investigation given the current understanding. It is possible the failure to translate the experimental data and direct deposition examples to double patterned stamps is a result of a combination of factors i) the wetting of Krytox1506 on the different surface states of oxidised and regenerated PDMS, ii) non-complete dissolution and interaction of oxygen-rich silica layer and iii) Krytox1506 residue remains on the surface of PDMS stamps, preventing regeneration. In the analytical samples e.g. those used to determine WCA as well as the direct depositions, wetting of Krytox1506 takes places on two states of the oxidised PDMS. The proposed states are outlined graphically in Figure 6.32 with all states starting from a

pristine (P-PDMS) surface. In the case of direct deposition and experimental data collection, the blanket UV/O_3-oxidation followed by regeneration then a secondary oxidation through a shadow mask leads to states **2** and **3**. For the pattern rewriting examples, as a blanket oxidation is not performed, some surface remains in a pristine state before regeneration (state **1**) while other regions of the regenerated P-PDMS surface is oxidised (state **4**). A contact angle study was performed to investigate the possibility that the regenerated surface states resulted in changes to the WCA and KCA.

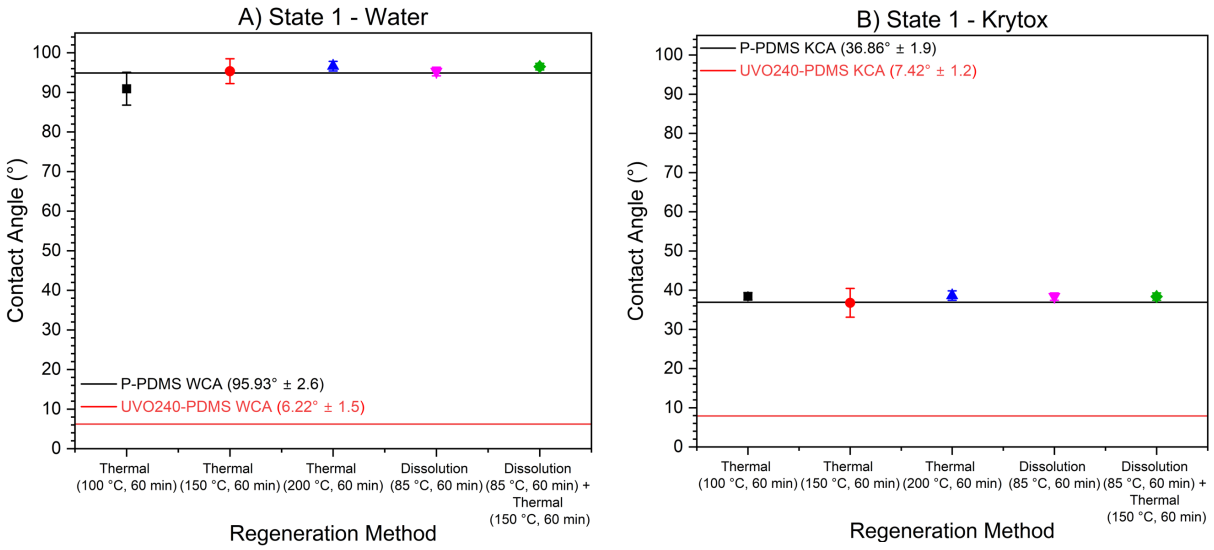

Figure 6.33: Contact angle of A) Water and B) Krytox1506 oil on surface state 1 (P-PDMS → Regeneration).

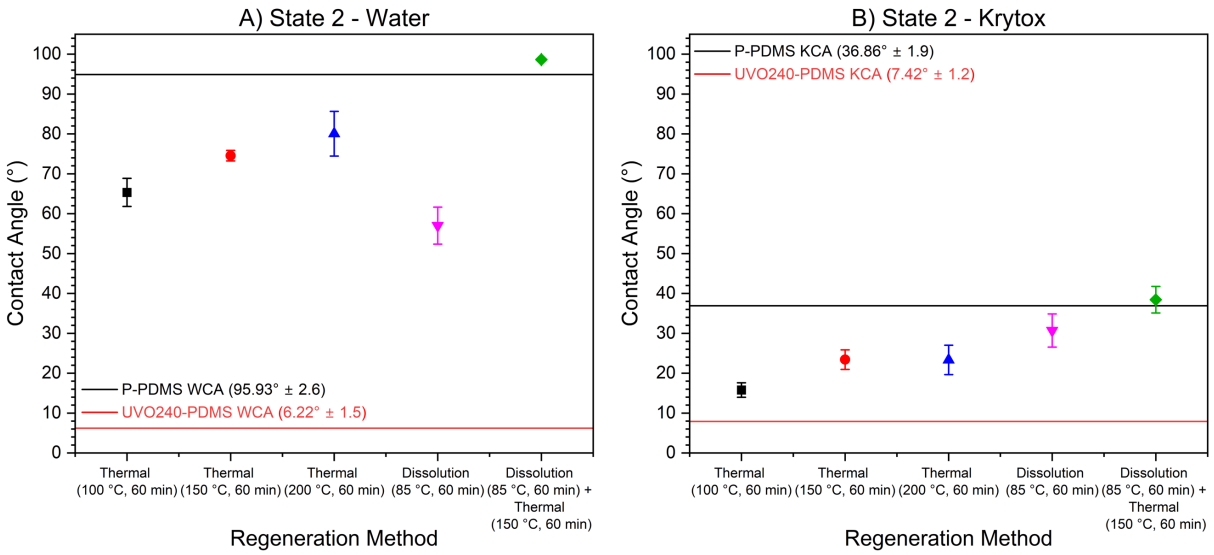

Figure 6.34: Contact angle of A) Water and B) Krytox1506 oil on surface state 2 (UVO240-PDMS → Regeneration).

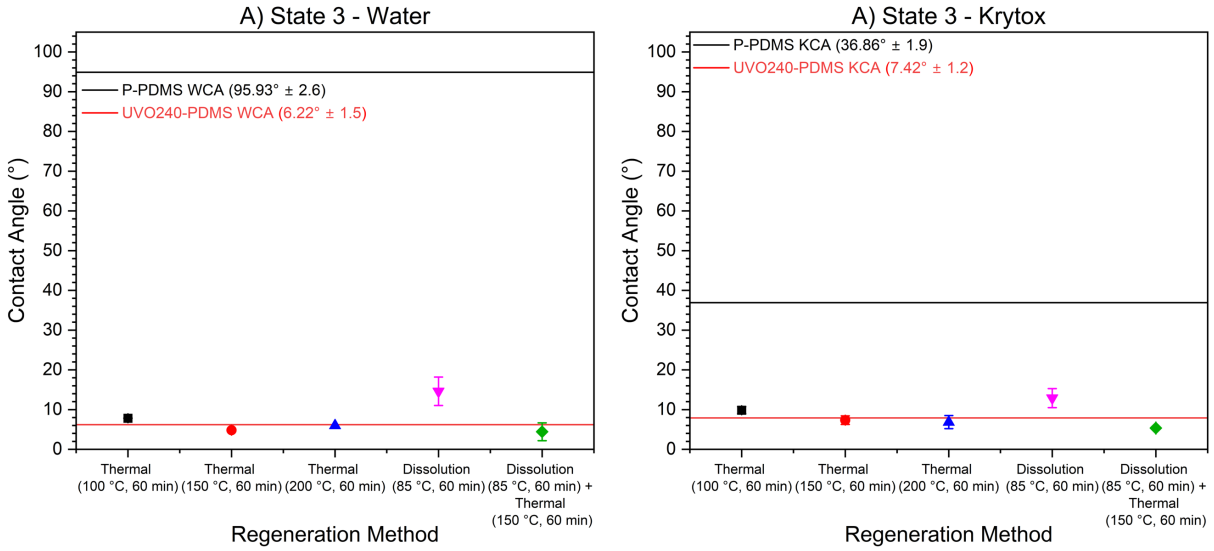

Figure 6.35: Contact angle of A) Water and B) Krytox1506 oil on surface state 3 (UVO240-PDMS → Regeneration → UV/O_3, 240 min).

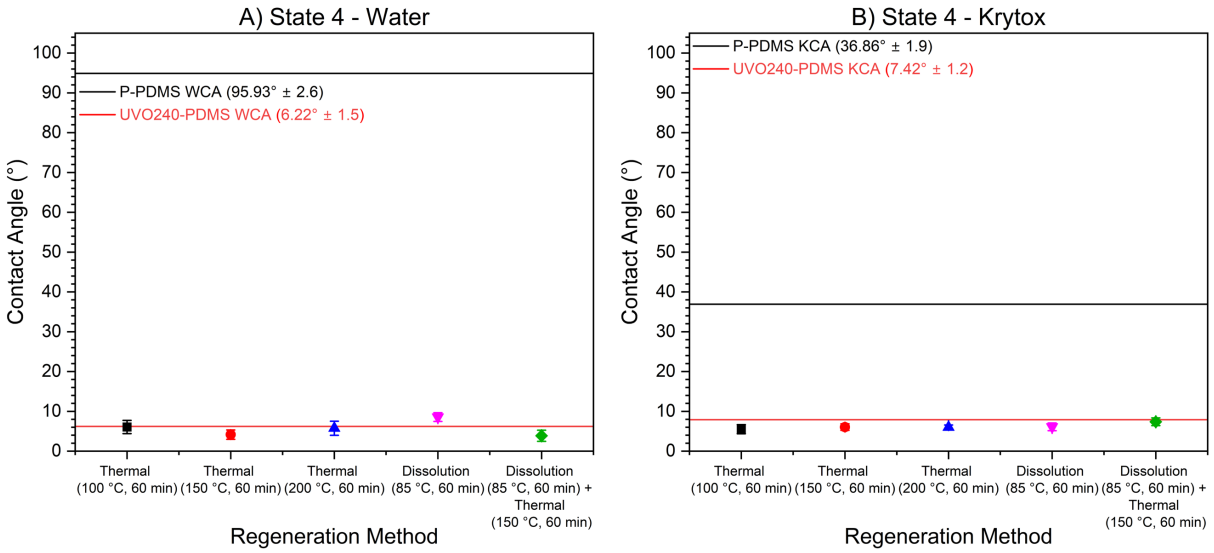

Figure 6.36: Contact angle of A) Water and B) Krytox1506 oil on surface state 4 (Pristine → Regeneration → UV/O_3, 240 min).

The pristine surface following application of a thermal, chemical or combined regeneration process (state **1**) in Figure 6.33 showed no change in WCA and KCA values, reletive to the comparable P-PDMS reference values. State **2** in Figure 6.35 represents the oxidised-PDMS surface following regeneration, as previously outlined in Section 6.3 and shows the contact angle is heavily dependent on the effectiveness of the regeneration with the combined chemical-thermal process exhibiting total hydrophobic and oleophobic recovery. State **3** in Figure 6.35 describes the double oxidised surface with its expected wetting surface highlighted by the low WCA and KCA values and finally, Figure 6.36 outlines the contact angle

values for surface state **4** which is the regenerated P-PDMS surface after oxidisation. Comparison of WCA and KCA values on the surface states against the references in Figure 6.2 shows that regeneration has no significant impact on the expected values, and as such, will likely not result in observed failure to repattern the surface. Another possible cause for the failed rewrite patterning may be due to an inability to effectively removal residue Krytox1506 from the surface of the PDMS stamps during the cleaning process. This may drastically reduce the enhancement of recovery and therefore the contact angle of Krytox1506 on the regenerated PDMS, leading to a mismatch between the expected and real wetting behaviour. Ultimately, this disconnect between the contact angle data and information such as ATR-FTIR and XPS of the Si2P signal, outline the regeneration to a pristine PDMS state and the results from the real double patterning application remains a complex issue that warrants further investigation.

6.6 Summary

In this chapter, the general understanding of novel UV/O_3-PDMS selective metallisation has been developed through investigations of contact angle, surface chemistry and topological changes as a result of applied thermal and chemical surface regeneration processes. Focusing primarily on the hydro- and oleophobic recovery of 240 min UV/O_3 oxidised PDMS, new contact angle and surface energy data for both the thermally-enhanced approaches in Figures 6.7 and 6.8 as well as the chemically-enhanced regimes in Figure 6.12 describe a method for complete and rapid regeneration. The novel combined chemical-thermal method (Submerge in ionic buffer at 85°C, 60 min followed by a 150°C, 60 min bake) exhibited >100% recovery of WCA and KCA, near total loss of hydrophilic surface groups as assessed by ATR-FTIR (Figure 6.14) and dissolution of the oxygen-rich, silica-like layer as evidenced by XPS (Figures 6.19 & 6.20). Furthermore, the contact angle and IR data presented in this in the chapter, provides evidence and support to the proposed mechanisms which hydrophobic recovery is known to proceed by, that is, temperature-dependent, diffusion-control migration of low-molecular weight PDMS oligomers from the bulk to the surface, reorientation of hydrophilic surface groups and the condensation of surface silanols (Si−OH). Furthermore, it has been shown that oleophobic recovery occurs largely as a re-

sult of the same mechanisms but does not exhibit the same temperature-dependency owing to the inter-molecular interactions involved in the wetting of Krytox1506. Finally, a number of rewrite deposition examples; a first of their kind, have been presented in the later part of the chapter and while the successful repatterning of oxidised PDMS was observed when using PDMS as a substrate, the regeneration process in a a double-pattern rewriting PDMS stamp process did not exhibit an ability to overwrite the original pattern.

Chapter 7
Glucose Biosensor Electrodes: Fabrication, Immobilisation and Analysis

This chapter describes the use of solution-processable P3HT copolymers described in Chapter 4. A glucose biosensor based on a gold/polymer/glucose oxidase strip electrode is presented. The successful covalent immobilisation and retention of enzyme activity will be outlined by a colorimetric assay and electrochemical analysis.

7.1 Sensor Fabrication and Enzyme Immobilisation

A set of soluble P3HT copolymers have been utilised in the fabrication of glucose biosensing electrodes. The synthesis and characterisation of the polymers outlined in Table 7.1 has been discussed in Chapter 4, Section 4.4 - Thiophene Polymerisation in Acetonitrile (CH_3CN).

Table 7.1: Table of P3HT copolymers used in the fabrication of glucose biosensor electrodes. 3HT=3-hexylthiophene, T3AA=Thiophene-3-acetic acid, T3T3YAA=Trans-3-thiophen-3-yl-acrylic acid, S3TA=N-succinimidyl 3-thiophene acetate, and S3T3YA=N-succinimidyl 3-(thiophen-3-yl)acrylate.

Polymer ID	Composition	Ratio
(19)	P(3HT-*c*-T3AA)	[5:1]
(20)	P(3HT-*c*-T3AA)	[10:1]
(25)	P(3HT-*c*-T3T3YAA)	[5:1]
(26)	P(3HT-*c*-T3T3YAA)	[10:1]
(27)	P(3HT-*c*-S3TA)	[1:1]
(28)	P(3HT-*c*-S3TA)	[5:1]
(29)	P(3HT-*c*-S3TA)	[10:1]
(30)	P(3HT-*c*-S3T3YA)	[1:1]
(31)	P(3HT-*c*-S3T3YA)	[5:1]
(32)	P(3HT-*c*-S3T3YA)	[10:1]

The fabrication of biosensor electrodes used in this project relies on two main principles; i) the solution-processability of synthesised polymers for the deposition of thin films and, ii) the covalent immobilisation of enzymes to the carboxylic acid or N-succinimdyl ester group on the polymer chain via a carbodiimide cross-linking type reaction. As outlined in Chapter 3, solutions of soluble polymers (see Table 7.1) at a concentration of 15 mg mL^{-1} in a $CHCl_3/C_6H_5Cl$ solvent mixture [8:2 v/v] were deposited by spin-coating. The quality,

uniformity, and continuity of the coating was assessed by visual and microscopic inspection as presented in Figures 7.1 and 7.2. All polymers, irrespective of monomer composition, yielded a good-quality, pin-hole free thin film on ITO-glass, while on the Au strip electrode, the film was not as uniform with effects of the spin-coating process such as comet streaks. However, the polymer films on Au were continuous over the complete electrode area. A 15 min UV/O_3 treatment of the substrate prior to spin-coating, as the increase in surface free energy aided wettability of the polymer solution during depostion. All polymer films were prepared immediately prior to enzyme immobilisation in an attempt to minimise photodegradation [360], the polymer film thicknesses were measured to range between 103 - 140 nm using optical profilometry (See Figure B.11 in Appendix B).

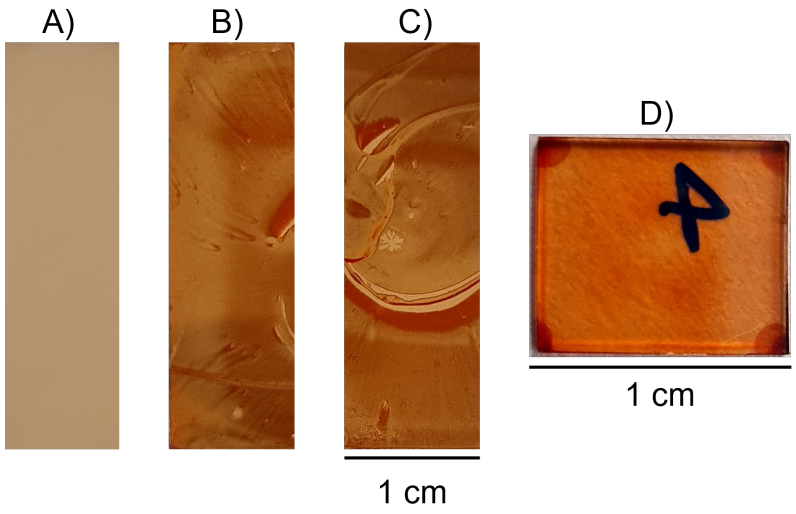

Figure 7.1: Photographs of A) Bare Au Strip electrode, B & C) Polymer thin films on Au Strip electrode and D) Polymer thin film on ITO-glass electrode. All polymer films were deposited by spin-coating.

Figure 7.2 presents micrographs of A) an uncoated gold electrode, and polymer **(19)** thin films on B) Au/PET and C) ITO, respectively. The images show the presence of debris on the electrode and under/in the polymer film. It is possible the debris may affect the electrical performance of the device, and preparation of the devices in a cleanroom may be beneficial, however, as the goal of this project is to show a prototype sensor, optimisation was considered to be secondary in importance to producing a working device on a restricted time frame.

The enzyme is conjugated to the polymer backbone through the carboxylic acid and N-succinimidyl ester functionalities. Polymers containing the carboxylic acid groups require

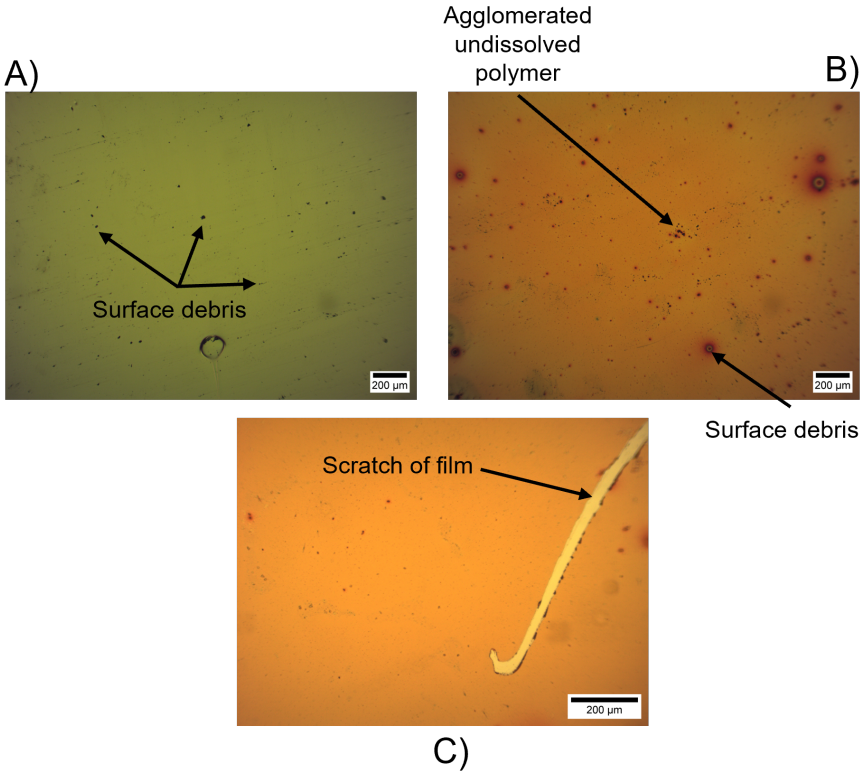

Figure 7.2: Optical micrographs of A) Bare Au strip electrode, B) Polymer thin film on Au Strip electrode and C) Polymer thin film on ITO-glass electrode.

activation using EDC/NHS before enzyme exposure while the N-succinimidyl ester groups are pre-activated allowing for immobilisation immediately after polymer film deposition. In accordance with the method in Section 3.7, films of polymers **(19)**, **(20)**, **(25)**, **(26)** were immersed in a solution containing 1-ethyl-3-(3-dimethylaminopropyl) carbodiimide (EDC) and N-hydroxysuccinimide (NHS) for 3 hr. To immobilise the enzyme, each of the polymer films were immersed in a 5 mg mL^{-1} solution of Glucose Oxidase for 6 hr. Following the immobilisation, all electrodes were repeatedly rinsed with PBS to remove weakly and unbound enzyme before storage in PBS at 4°C until use.

Successful enzyme binding was confirmed by a colorimetric binding assay utilising a horseradish peroxidase (HRP) and o-dianisidine chromogen system. As outlined in Section 3.8.2, the presence of active Glucose oxidase (GOx) enzyme, results in a strong orange-brown colour change upon the addition of an appropriate substrate, i.e. β-D-glucose. The GOx enzyme reacts with glucose to form glucono-1,5-lactone and hydrogen peroxide H_2O_2. The generated H_2O_2 reacts with the HRP, catalysing the oxidation of the colourless o-dianisidine into the brown/orange quinoneimine chromophore [52]. As H_2O_2 is produced due to the glu-

cose oxidase/glucose reaction, the development of a strong colour change is indicative of active GOx.

This type of assay is optimised for determining the activity of free enzymes in solution as opposed to the polymer-fixated enzyme in this study, therefore, the purpose of this test was to confirm covalent-bonding of active enzyme to the film. The polymer-enzyme films were immersed in an assay solution containing o-dianisidine, peroxidase and glucose for 10 min before the absorbance of the solution at 460 nm was measured. Figure 7.3 shows the absorbance values for each polymer-GOx film alongside insoluble polymers; P3HT-*c*-T3T3YAAs **(10)** and **(25)** exposed to GOx following NHS-EDC activation, as well as control samples of P3HT-GOx and ITO glass-GOx for comparison. In summary, all soluble polymers with an enzyme binding functionality gave a non-zero absorbance, indicating the presence of active glucose oxidase. Prior to performing the assays, all films were repeatedly rinsed to remove any unbound or weak, non-covalently bound enzyme as such, any colour change during the assay can be assumed to arise from active enzyme immobilised to the polymer film.

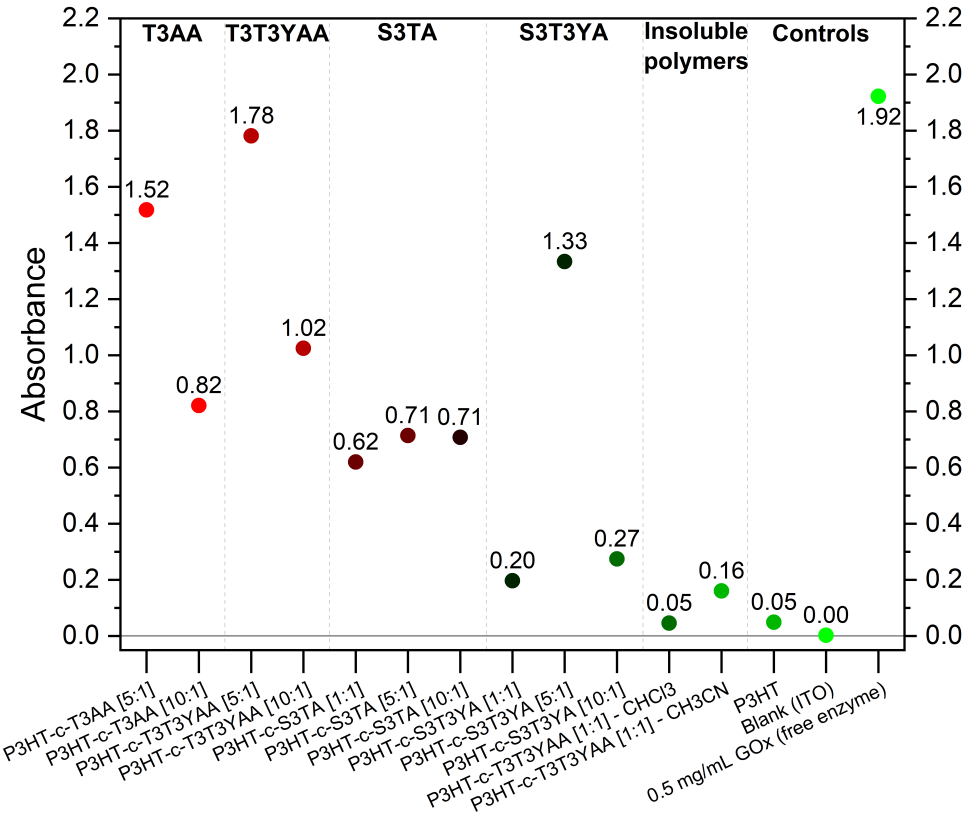

Figure 7.3: Absorbance values for polymer-immobilised glucose oxidase for the determination of binding by a HRP/o-dianisidine colorimetric assay.

The N-succinimidyl ester monomers S3TA and S3T3YA were pre-activated for reaction with enzyme bound amine residues e.g. Lysine, therefore, during immobilisation both polymer types do not require activation of the carboxylic acid via EDC/NHS. Both carboxylic acid polymers gave a higher absorbance, indicating a higher quantity or a more active enzyme was present in these films.

7.2 Cyclic Voltammetry

Electrochemical analysis of the enzyme-polymer sensing electrodes by cyclic voltammetry and chronoamperometry allowed for the determination of electrochemical redox properties and quantification of the sensors by calculating figures of merit i.e. linear range, limit of detection (LoD), sensitivity, selectivity, and reusability.

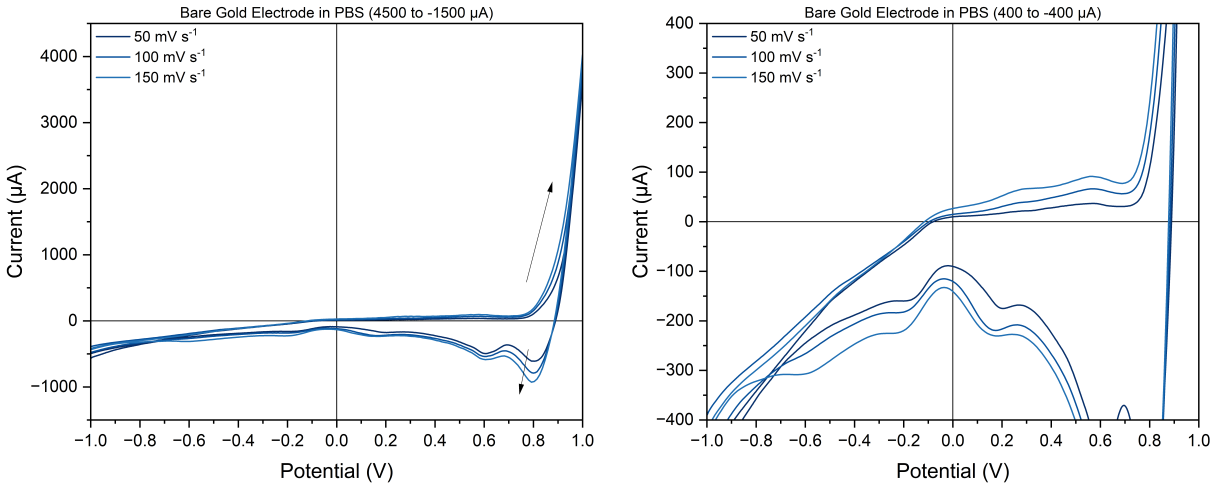

Figure 7.4: Cyclic voltammogram of a bare, uncoated gold strip electrode in PBS. Left) Y-axis scale = -1500 to 4500 and Right) Y-axis scale = -400 to 400 µA.

The Au/polymer/GOx electrodes were probed using cyclic voltammetry to assess electroactivity and quantify the redox behaviour. All measurements were performed in PBS with an additional 50 mM of KCl as a supporting electrolyte in order to minimise ohmic drop within the electrochemical system. Figure 7.4 presents the electrochemical response for a bare gold strip electrode (30x10x0.250 mm) in a PBS electrolyte solution. The increase in current at ~0.8 V corresponds to oxidation of the gold surface and the onset of electrode degradation, while at potentials exceeding 1 V electrolysis of the PBS solution results in the evolution of gas from the surface of the electrode [361, 362]. During the reverse (cathodic) sweep, the

appearance of the peak at 0.8 V likely relates to the electrochemical reduction of gold oxides in phosphate buffers [363, 364].

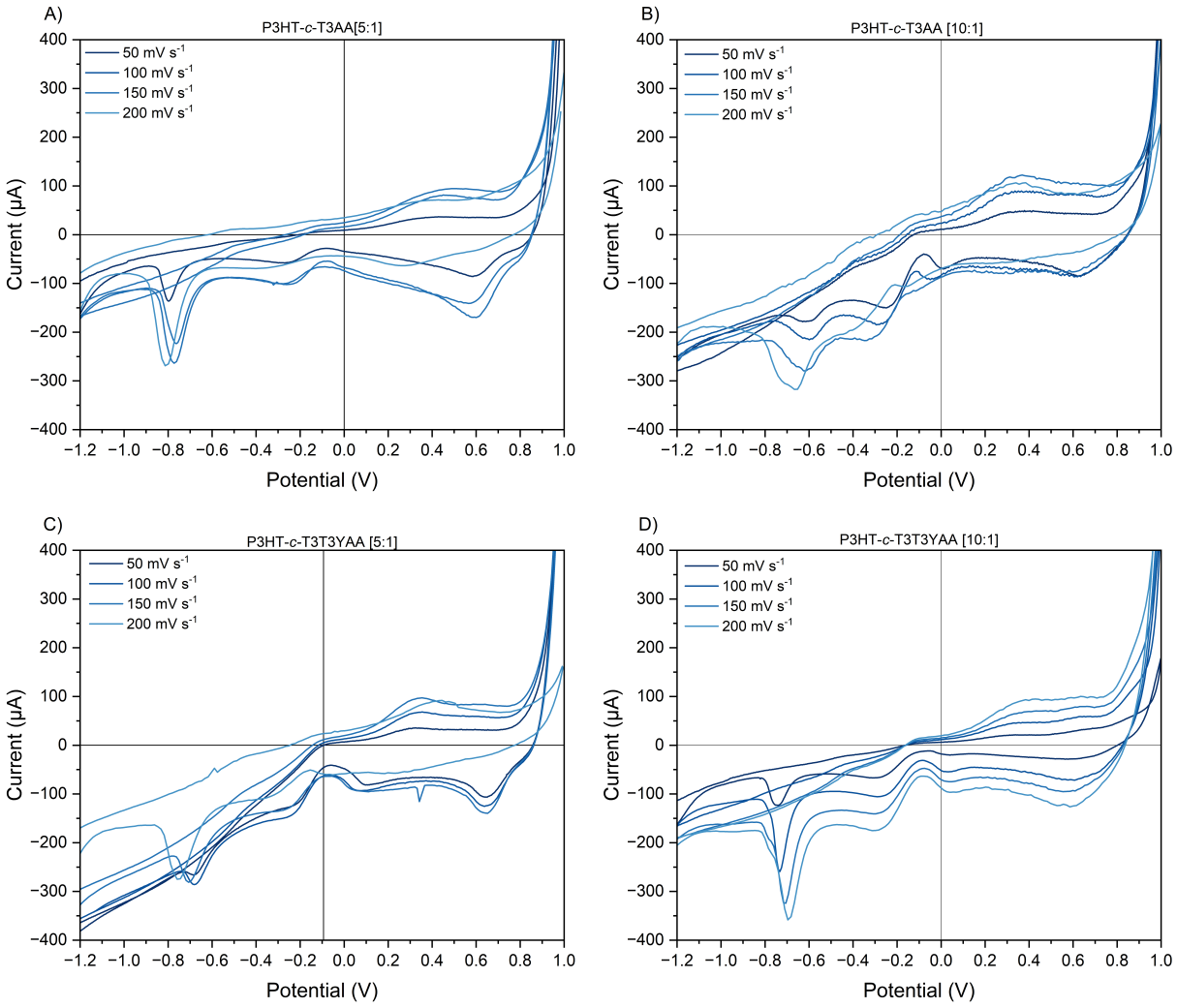

Figure 7.5: Cyclic voltammograms of enzyme electrode with a polymer binding matrix of A) P(3HT-*c*-T3AA)[5:1] **(19)**, B) P(3HT-*c*-T3AA)[10:1] **(20)**, C) P(3HT-*c*-T3T3YAA)[5:1] **(25)**, and D) P(3HT-*c*-T3T3YAA)[10:1] **(26)**.

As shown in Figures 7.5 and 7.6, all polymer-GOx coated electrodes show complex voltammograms with multiple electron transfers. The similar peaks observed across all electrodes are expected given 3-hexylthiophene is the majority component in each polymer. Excluding P(3HT-*c*-T3T3YAA) **(26)** which showed minimal redox behaviour with no clear oxidation peak, the polymer-enzyme composites possessed a single anodic peak (E_{pa}) located between 0.39 - 0.53 V with onset voltages (E_{onset}) ranging between 0.09 - 0.22 V. The presence of three cathodic peaks (E_{pc}) indicate multiple reduction processes occur during the voltage sweep, with prominent processes occurring between 0.59 and 0.71 V, -0.11 and -0.28 V and -0.58 and -0.97 V vs Ag/AgCl. Reversibility of the redox processes is observed over sequential

scans for a range of scan rates, that is, between 50 - 200 mV s^{-1}. The observed oxidation and reduction processes between 0.5 and 1 V can be attributed to the redox process of the P3HT-based polymer [26, 66, 110, 365, 366] while the cathodic peaks between -0.2 and -1 V relate to reduction processes within the glucose oxidase (GOx) and its redox-active co-factor Flavinadenine dinucleotide (FAD) [367–370]. The result suggests that the FAD centre, which is deep within the GOx protein shell, is capable of direct electron transfer with the polymer-coated electrode.

Table 7.2: Summary of Cyclic Voltammetry data. E_{pa}: Anodic peak potential, I_{pa}: Anodic peak current, E_{onset}: Anodic onset potential, E_{pc}: Cathodic Peak potential, I_{pc}: Cathodic peak current.

Polymer	E_{pa} **(V)**	I_{pa} **(μA)**	E_{onset} **(V)**	E_{pc} **(V)**			I_{pc} **(μA)**		
				1	**2**	**3**	**1**	**2**	**3**
P(3HT-*c*-T3AA) [5:1]	0.47	79.27	0.11	0.59	-0.27	-0.79	-192.9	-77.8	-210.3
P(3HT-*c*-T3AA) [10:1]	0.38	121.93	0.10	0.62	-0.28	-0.60	-121.9	-114.3	-118.9
P(3HT-*c*-T3T3YAA) [5:1]	0.39	81.21	0.12	0.34	-0.11	-0.69	-121.9	-69.3	-128.3
P(3HT-*c*-T3T3YAA) [10:1]	-	-	-	-	-0.28	-0.73	-	-65.3	-146.6
P(3HT-*c*-S3TA) [1:1]	0.40	83.72	0.09	0.71	-0.25	-0.58	-138.6	-156.3	-164.7
P(3HT-*c*-S3TA) [5:1]	0.42	173.35	0.17	0.03	-0.28	-0.58	-160.97	-90.33	-69.86
P(3HT-*c*-S3TA)[10:1]	0.32	68.87	0.13	0.67	-0.68	-0.96	-129.2	-181.1	-190.5
P(3HT-*c*-S3T3YA) [1:1]	0.42	165.90	0.19	0.04	-0.27	-0.57	-197.0	-129.6	-106.1
P(3HT-*c*-S3T3YA) [5:1]	0.41	99.59	0.20	0.66	-0.28	-0.97	-159.0	-121.2	-37.5
P(3HT-*c*-S3T3YA) [10:1]	0.41	60.97	0.15	0.67	-0.29	-0.96	-151.0	-65.1	-30.7

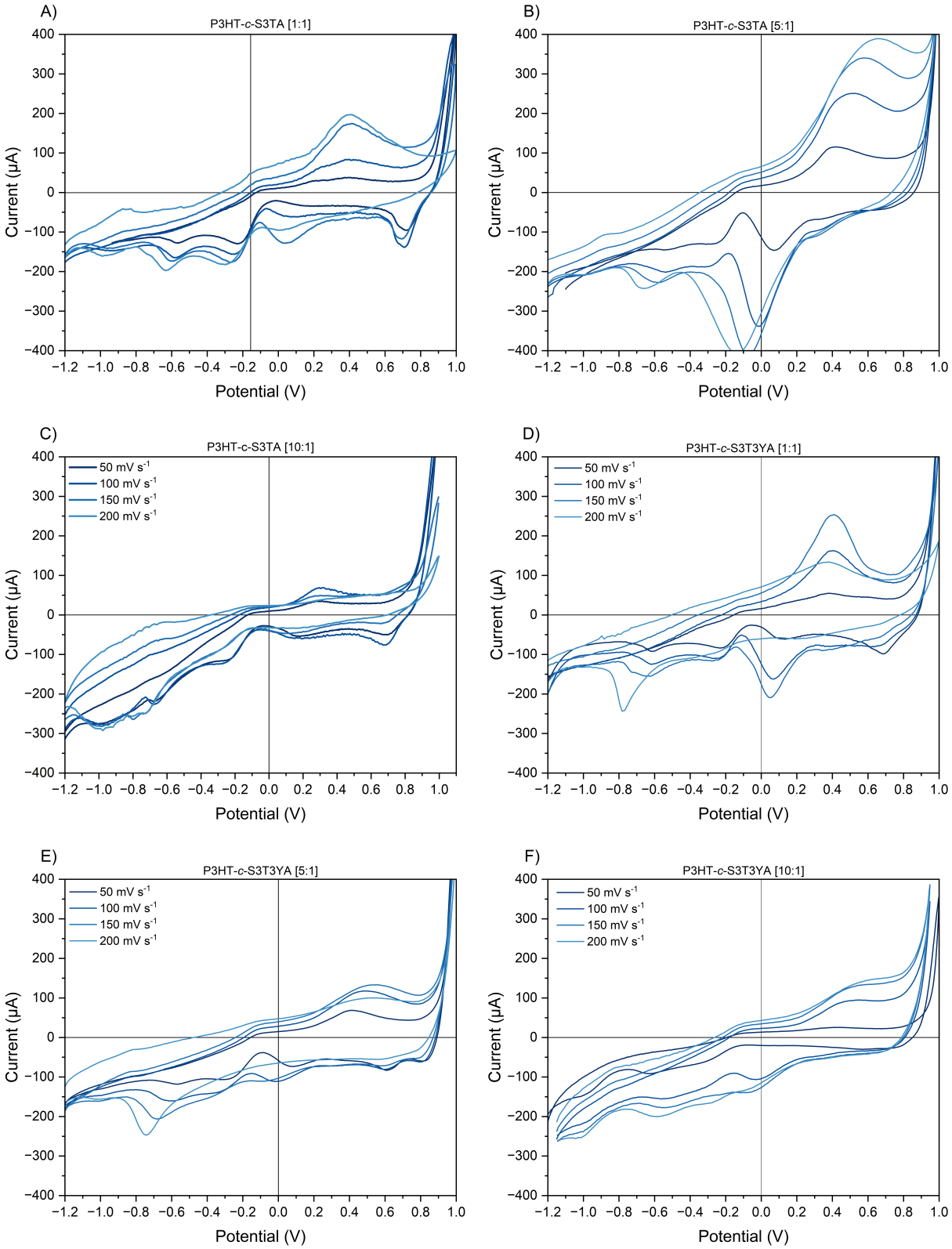

Figure 7.6: Cyclic voltammograms of enzyme electrode with a polymer binding matrix of A) P(3HT-*c*-S3TA)[1:1] **(27)**, B) P(3HT-*c*-S3TA)[5:1] **(28)**, C) P(3HT-*c*-S3TA)[10:1] **(29)**, D) P(3HT-*c*-S3T3YA)[1:1] **(30)**, E) P(3HT-*c*-S3T3YA)[5:1] **(31)**, and F) P(3HT-*c*-S3T3YA)[10:1] **(32)**.

7.3 Chronoamperometry - Response to Glucose

The ability of each sensing electrode to detect glucose was evaluated using chronoamperometry. This method allows for real-time monitoring of the current response when the sensor is exposed to increasing concentrations of glucose. Under application of a constant voltage above the oxidation potential of the copolymer (0.7 V), the resultant current response is directly related to the catalytic redox activity of GOx at the biosensor's surface. The peak current for each concentration can be extracted from the current vs time data to yield a calibration curve (peak current vs substrate concentration e.g. Figure 7.7), allowing for determination of sensor performance metrics such as, limit of detection (LoD), linear range and sensitivity. The normal fasting glucose concentration in a non-diabetic human typically ranges between ∼4 - 6 mM in whole blood [77, 371] whereas a person with diabetes may experience postprandial glucose levels ranging between ∼4 - 10 mM [66, 372]. Any concentration above the normal range is considered hyperglycemia, or high blood sugar whereas hypoglycemia, or low blood sugar, is defined as a concentration below approx. 3.5 mM [373].

The amperometric measurements in this project were taken between concentration range 1 - 24 mM. As outlined in Section 3.11.2, phosphate-buffered saline (PBS) was used as the electrolyte in a three-electrode electrochemical setup to maintain suitable pH and isotonicity for the enzyme in use - Glucose Oxidase from *Aspergillus niger* (GOx). For each polymer, a triplicate of electrodes were fabricated and used to measure the response to different concentrations of glucose, focusing on electrode-to-electrode reliability and measurement stability, as assessed by short-term (48 hr) and long-term (21 days) testing regimes. Following data acquisition, peak current values were extracted from the current-time scans then plotted again glucose concentration to obtain the calibration curves. Example current-time scans collected during the chronoamperometry measurements can be found in Appendix B, Figure B.13.

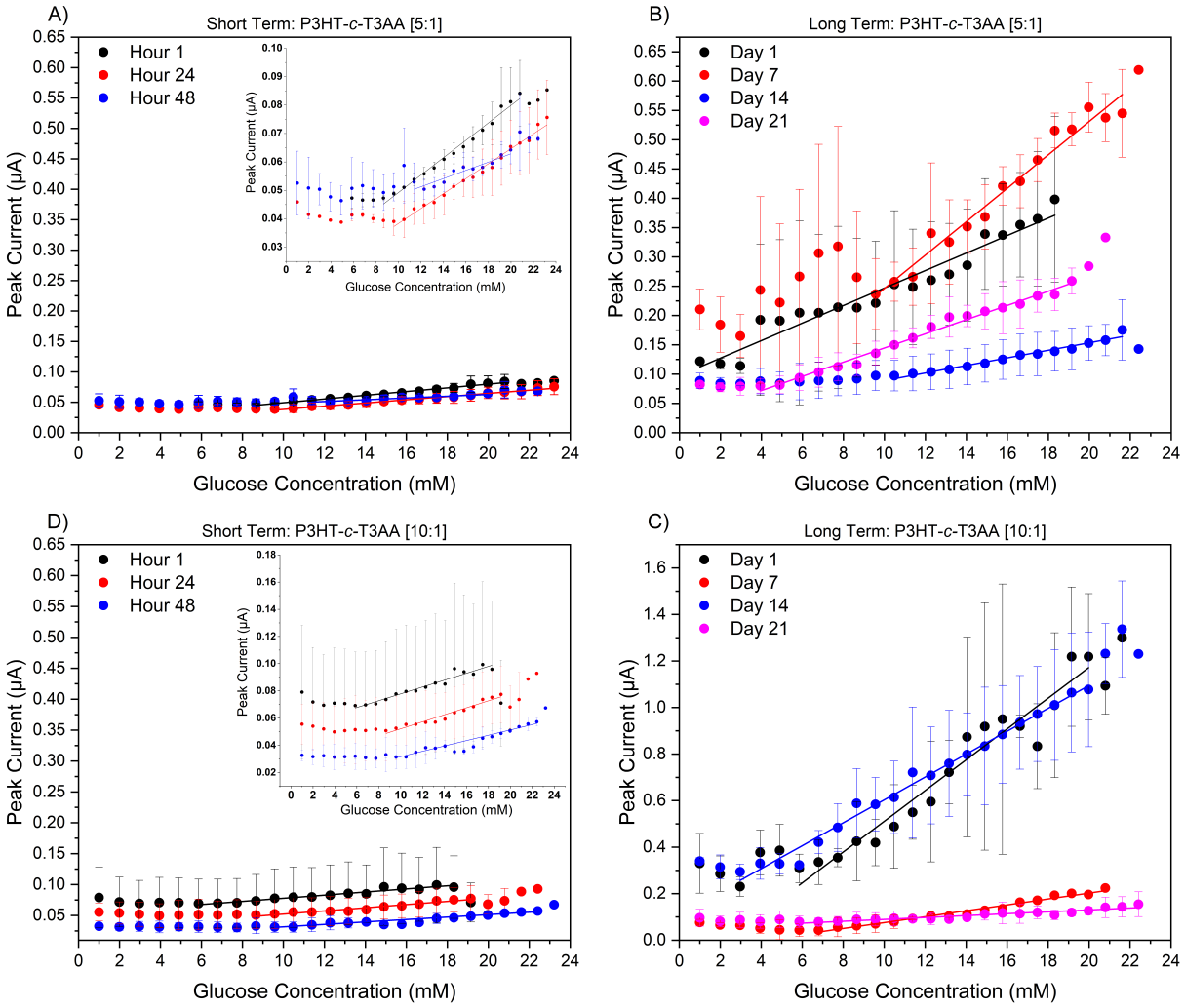

Figure 7.7: Calibration curves from amperometric response to glucose by Au/P(3HT-*c*-T3AA)/GOx electrodes. A) T3AA[1:1] **(19)** - Short Term (48 hr), B) T3AA[1:1] **(19)** - Long Term (21 days), C) T3AA[10:1] **(20)** - ST, and D) T3AA[1:1] **(20)** - LT. Insets show the corresponding plot with a reduced Y-axis scale.

7.3.1 P(3HT-*c*-T3AA)

Chemically synthesised enzyme binding copolymers combining 3-hexylthiophene (3HT) and Thiophene-3-acetic acid (T3AA) have been seen in the literature, for example, Lai et al. prepared a P(3HT-*c*-T3AA)[1:1]/Urease electrode for the potentiometric detection of urea [38]. Although Lai's work is not directly comparable due to the difference in electrochemical transduction, Lai's work shows mediator-free, enzymatic sensing of a small molecule is possible using a P(3HT-*c*-T3AA)/enzyme biosensor. The work in this DPhil project provides further evidence for the suitability of polythiophenes in sensing applications.

The calibration curves for the two soluble T3AA polymers **(19)** and **(20)** are presented in Figure 7.7 with short term testing (3 measurements over 48 hours) and long term testing

Table 7.3: Biosensor performance properties for T3AA containing polymers **(19)** and **(20)**.

Time	Linear Range (mM)	LoD (mM)	Sensitivity ($\mu A\,mM^{-1}$)	Stability (%)	Repeatability (%)
P(3HT-*c*-T3AA) [5:1]					
Hour 1	9 to 23	1.64	0.0031	87.9	88.3
Hour 24	10 to 26	1.79	0.0026		
Hour 48	12 to 22	6.96	0.0015		
Day 1	1 to 20	2.03	0.0149	48.9	42.9
Day 7	10 to 25	2.56	0.0285		
Day 14	11 to 24	2.88	0.0065		
Day 21	4 to 21	1.18	0.0120		
P(3HT-*c*-T3AA) [10:1]					
Hour 1	6 to 20	2.79	0.0025	63.2	52.3
Hour 24	9 to 21	3.30	0.0026		
Hour 48	10 to 25	2.14	0.0020		
Day 1	6 to 22	2.91	0.0662	17.7	27.5
Day 7	7 to 23	1.95	0.0127		
Day 14	3 to 23	1.07	0.0490		
Day 21	6 to 25	4.11	0.0041		

(4 measurements over 21 days) performed for each batch of polymer-GOx sensing electrodes. This polymer, that is, P3HT-*c*-T3AA has been investigated as a reference material given its use in the literature for the exact purpose of a conductive binding agent in electrochemical biosensors [38]. The sensor properties extracted from the curves are given in Table 7.3. In summary, P(3HT-*c*-T3AA) [5:1] - **(19)** produced a higher quality sensor performance when compared to **(20)** with greater electrode-to-electrode repeatability and greater measurement stability. Over the 48 hr short term testing, **(19)**-GOx had a repeatability of 88.3%, outlining good consistency in current response across the three electrodes, while the measurement stability of 87.9% shows sensor response is maintained over the 48 hours. Over three weeks (21 days), stability and repeatability of **(19)**-GOx reduced, dropping to 48.9% and 42.9%, respectively.

The drop in stability could be attributed to many factors. For instance, as each batch of electrodes was produced over the course of a month, minor variations in the fabrication process may have resulted in differences in the quality of the gold thin film or polymer coating i.e. polymer film thickness and uniformity. Moreover, enzyme biosensors are known to suffer from stability issues due to biomolecule leaching, strong pH and temperature depen-

dence, and the susceptibility to oxidative damage. In the case of glucose oxidase, H_2O_2 can denature the enzyme by oxidising certain residues while the spontaneous hydrolysis of the catalytic byproduct gluconolactone to gluconic acid, reduces the pH of the medium [374, 375]. Both mechanisms degrade the enzyme's stability over time, reducing the performance of the sensors.

The **(20)**-GOx sensor electrodes had worse stability and showed poorer repeatability when compared to **(19)**. In short term testing, the sensors possessed a stability and repeatability 62.5% and 52.3%, respectively while over 21 days, these metrics worsened further to 17.7% and 27.5%. Referring to the calibration curves in Figure 7.7, the measurement stability is related to the spread of the whole data set with less stable devices possessing large spread. The repeatability is the relative average of all the error bars for each measurement, with both metrics calculated from the coefficient of variation.

The sensor performance metrics for **(19)** and **(20)** are also outlined in Table 7.3. Both **(19)** and **(20)**-GOx electrodes possess similar linearity and sensitivity over 48 hr with **(19)** having a slightly lower limit of detection at 1.64 mM for the 1st measurement (Hour 1). At each additional measurement (24 & 48 hr), there is a reduction in sensitivity as well as a restriction of the linear range which is likely the result of loss of enzyme activity as a result of denaturing. The long term testing showed no clear trend with day 1 & day 21 for **(19)**, exhibiting similar sensitivity and linearity (1 - 20 mM and 4 - 21 mM) while for polymer **(20)** the day 1 & day 14 measurements showed comparable sensitivity over an equally high current range ($\sim$0.30 to 1.3 μA).

7.3.2 P(3HT-*c*-T3T3YAA)

Trans-3-thiophen-3-yl-acrylic acid (T3T3YAA) differs from T3AA due to the acrylic acid functionality. The added C=C alkene linkage is thought to improve biosensor performance by increasing the amperometric response due to the additional conjugation length and by introducing more space for the enzyme. The extra carbon spacer reduces the steric interactions between the polymer and enzyme, facilitating easier enzyme binding and allowing for binding of an enzyme with high activity [67, 376, 377].

The calibration curves for T3T3YAA containing polymers and the extracted sensor performance data are shown in Figure 7.8 and Table 7.4. P(3HT-*c*-T3T3YAA) **(25)** and **(26)** exhibit slightly reduced stability and repeatability when compared the P(3HT-*c*-T3AA) [5:1] **(19)** but was on par with P(3HT-*c*-T3AA) [10:1] **(20)** over the short term.

Table 7.4: Biosensor performance properties for P(3HT-*c*-T3T3YAA) **(25)** and **(26)**.

Time	Linear Range (mM)	LoD (mM)	Sensitivity ($\mu A\,mM^{-1}$)	Stability (%)	Repeatability (%)
P(3HT-*c*-T3T3YAA) [5:1]					
Hour 1	9 to 25	1.43	0.0031	74.9	78.5
Hour 24	13 to 24	3.13	0.0013		
Hour 48	10 to 26	1.83	0.0037		
Day 1	1 to 23	3.39	0.0348	0	5.4
Day 7	4 to 23	2.23	0.0058		
Day 14	8 to 24	3.17	0.1017		
Day 21	6 to 20	3.47	0.0051		
P(3HT-*c*-T3T3YAA) [10:1]					
Hour 1	10 to 23	4.33	0.0039	67.2	62.5
Hour 24	12 to 25	3.57	0.0020		
Hour 48	6 to 23	1.44	0.0052		
Day 1	8 to 21	1.82	0.0207	65.5	43.3
Day 7	7 to 24	2.22	0.0342		
Day 14	6 to 24	1.24	0.0052		
Day 21	4 to 21	1.32	0.0129		

Across 21 days, the difference was significant with large fluctuations in current output observed in the **(25)**-GOx electrodes leading to a stability of 0%. **(26)**-GOx performed better with the electrode exhibiting a repeatability of 43.3% and a stability of 62.5%. Both polymers **(25)** and **(26)** exhibited very comparable sensing properties to the T3AA materials with the batch of electrodes for the short term tests possessing a linear range between ∼9 to 26 mM and low LoDs <5 mM. Interestingly, the lack of oxidation by P(3HT-*c*-T3T3YAA)[10:1] **(26)**, as outlined in Table 7.2, did not hinder the sensor performance giving the comparable properties to polymers **(19)**, **(20)** and **(26)** which all possessed strong oxidation peaks. As all acid polymers possess the reduction peak below -0.50 V and exhibit sensor response, it strengthens the probability that this reduction peak is related to the redox activity of the glucose oxidase enzyme.

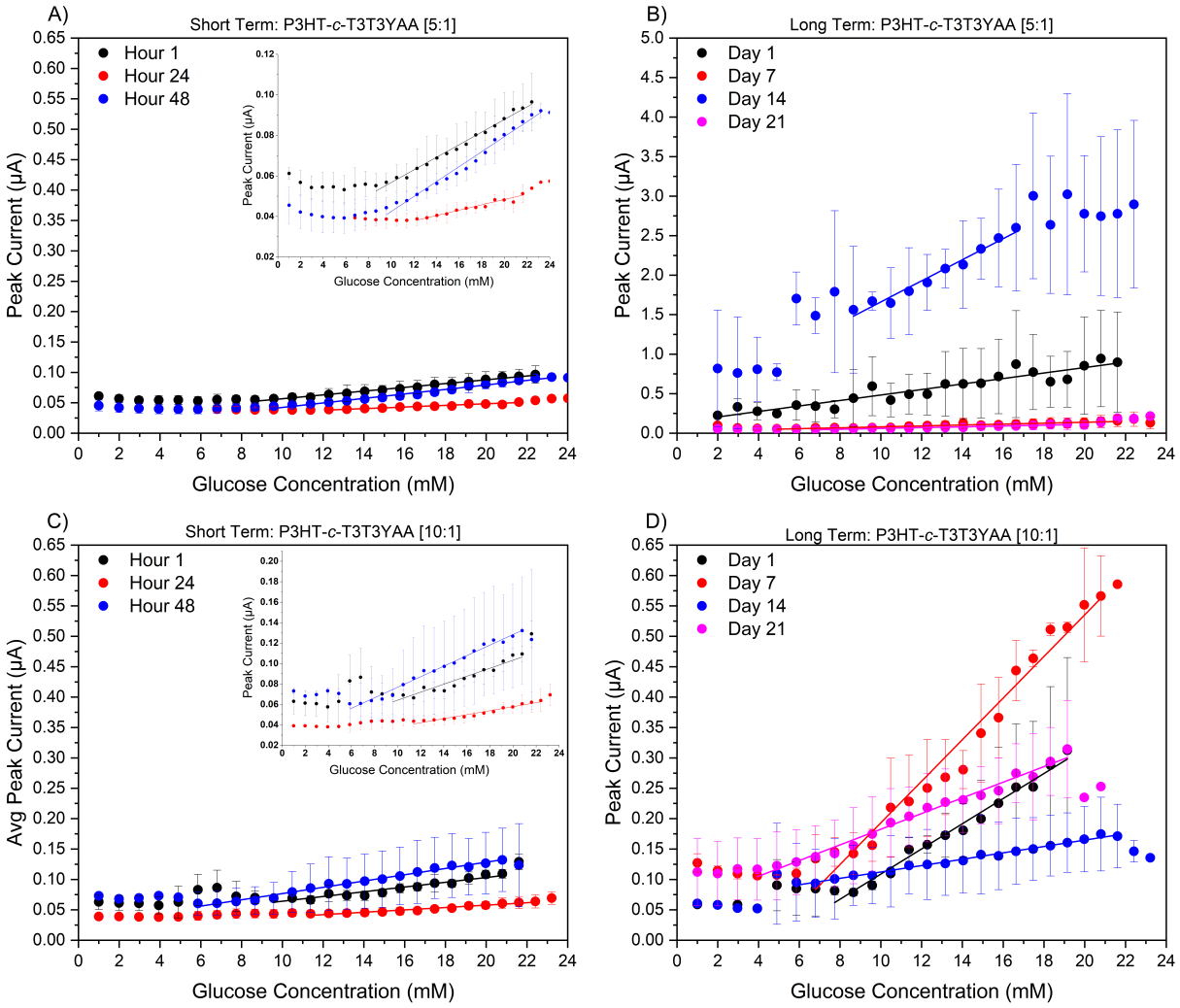

Figure 7.8: Calibration curve from amperometric response to glucose of Au/P(3HT-*c*-T3T3YAA)/GOx electrodes. A) P(3HT-*c*-T3T3YAA) [5:1] **(25)** - ST (48 hr), B) P(3HT-*c*-T3T3YAA) [5:1] **(25)** - LT (21 days). C) T3T3YAA [10:1] **(26)** - ST, and D) T3T3YAA [10:1] **(26)** - LT. Insets show the corresponding plot with a reduced Y-axis scale.

7.3.3 P(3HT-*c*-S3TA)

The three polymers containing a pre-activated, N-succinimidyl ester co-monomer P(3HT-*c*-S3TA) [1:1] - **(27)**, [5:1] - **(28)** and [10:1] - **(29)** were conjugated to glucose oxidase without the use of NHS/EDC carbodiimide. Determination of the amperometric response for the Au/P(3HT-*c*-S3TA)/GOx electrodes to glucose is shown in Figure 7.9 and Table 7.5. The S3TA polymers exhibited a range of results, balancing stability, repeatability and sensing performance. P(3HT-*c*-S3TA) [1:1] **(27)** possessed strong linearity over long term testing detecting a clear increase in glucose concentration across the largest range (1 to ~20 mM) for all polymers analysed in this project. The electrodes were unstable and offered no repeatability across the whole measurement period however if each measurement day

Table 7.5: Biosensor performance properties for S3TA containing polymers **(27)**, **(28)** and **(29)**.

Time	Linear Range (mM)	LoD (mM)	Sensitivity ($\mu A\,mM^{-1}$)	Stability (%)	Repeatability (%)
P(3HT-*c*-S3TA) [1:1]					
Hour 1	9 to 24	4.29	0.0174	47.0	47.0
Hour 24	8 to 25	2.26	0.0183		
Hour 48	8 to 25	3.16	0.0062		
Day 1	1 to 19	1.13	0.1750	0	0
Day 7	1 to 23	0.96	0.0015		
Day 14	1 to 20	0.88	0.0023		
Day 21	7 to 18	1.73	0.0063		
P(3HT-*c*-S3TA) [5:1]					
Hour 1	1 to 25	2.40	0.0091	54.5	53.7
Hour 24	5 to 25	2.74	0.0081		
Hour 48	3 to 23	1.25	0.0215		
Day 1	3 to 18	4.71	0.0035	70.8	68.9
Day 7	6 to 20	2.63	0.0059		
Day 14	9 to 23	1.66	0.0136		
Day 21	6 to 18	3.06	0.0139		
P(3HT-*c*-S3TA) [10:1]					
Hour 1	1 to 26	1.36	0.0156	50.4	42.0
Hour 24	2 to 21	3.14	0.0298		
Hour 48	5 to 22	2.28	0.0264		
Day 1	4 to 27	3.25	0.0083	66.3	51.4
Day 7	5 to 20	2.14	0.0087		
Day 14	9 to 26	1.44	0.0152		
Day 21	3 to 25	2.42	0.0025		

is considered separately, the current response to glucose was very consistent for the three electrodes (Day 1 = 82%, Day 7 = 47%, Day 14 = 94% & Day 21 = 82%). This day to day variation may raise concerns in how the electrochemical system was prepared for that specific day of analysis, for example, a lower than ideal volume of saturated KCl in the Ag/AgCl reference electrode, may cause changes in the cell potential which would by extension, effect the current measured. The day-to-day current variation should be addressed in any further work to ensure improved accuracy when quantifying the stability and repeatability of the polymer-enzyme biosensor. The polymers with a higher 3HT monomer content **(28)** and **(29)** exhibited slightly weaker sensor performance but greatly improved stability/repeatability.

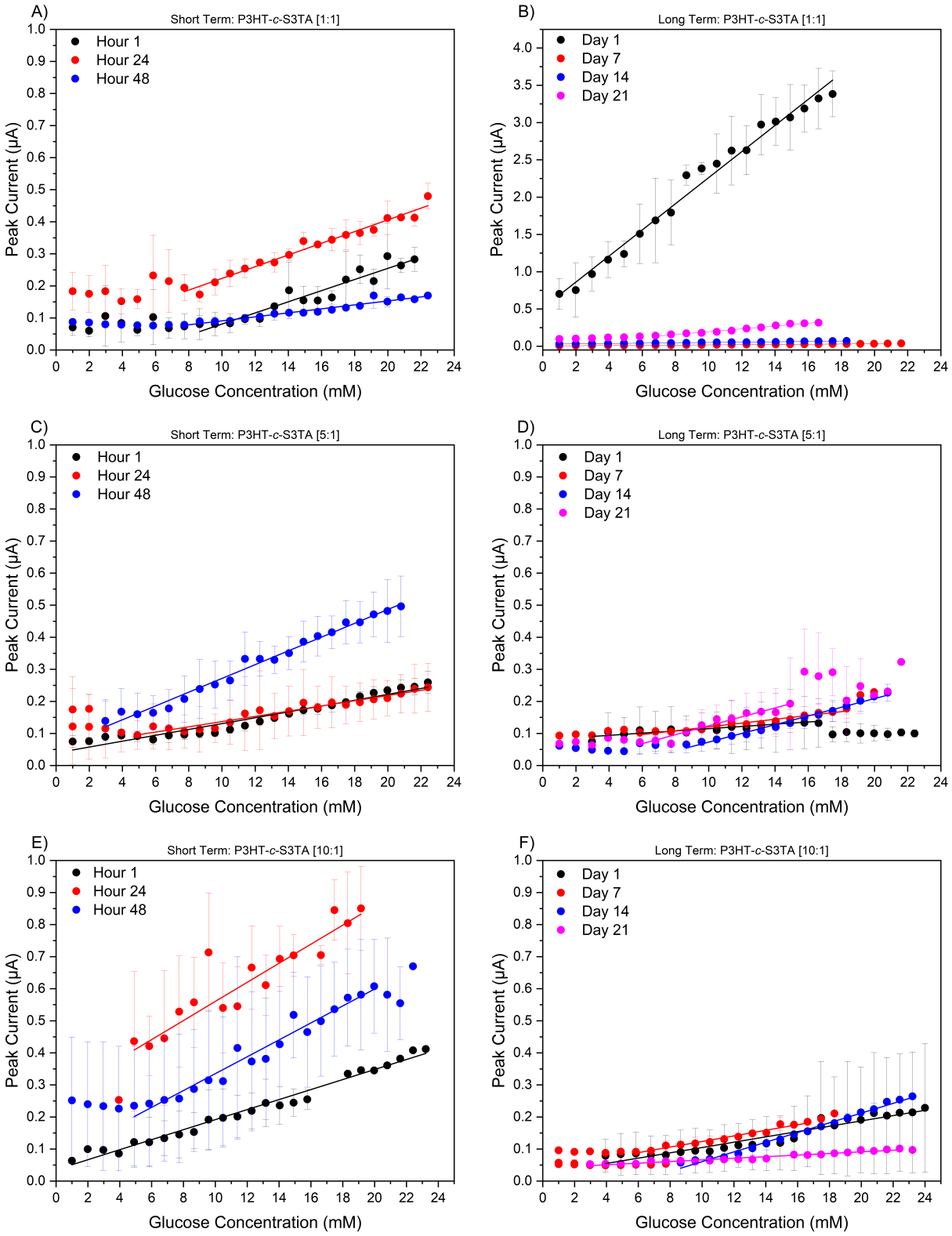

Figure 7.9: Calibration curve from amperometric response to glucose of Au/P(3HT-*c*-S3TA)/GOx electrodes. A) P(3HT-*c*-S3TA) [1:1] **(27)** - Short Term (48 hr) and B) P(3HT-*c*-S3TA) [1:1] **(27)** - Long Term (21 days), C) P(3HT-*c*-S3TA) [5:1] **(28)** - ST, D) P(3HT-*c*-S3TA) [5:1] **(28)** - LT, E) P(3HT-*c*-S3TA) [10:1] **(29)** - ST, and F) P(3HT-*c*-S3TA) [10:1] **(29)** - LT.

Additionally, collating the data from both the acid (T3AA & T3T3YAA) variants and the P(3HT-*c*-S3TA), it appears the polymers closest to 10% functional monomer component possess the greatest stability, a wide range of linearity and low limit of detection. This has also been observed by Clayton and Kuwahara et al. for electropolymerised 3-methylthiophene-based glucose biosensors [67, 68, 316], it is proposed that 10% functional monomer content is optimal for biosensor performance as balance between the diffusion limitation of the substrate and products caused by excessive enzyme and immobilising enough enzyme to generate a transducible signal is important. For short term testing, the stability, and repeatability for each of the three polymer were comparable between a range of 47 - 54.5% and 42 - 53.7%, respectively. The sensor performance for **(28)** and **(29)** was better when compared to **(27)** with a wide linear range, lower LoD and high maximum sensitivity observed.

7.3.4 P(3HT-*c*-S3T3YA)

The last set of polymers-GOx electrodes assessed for their amperometric response to glucose was P(3HT-*c*-S3T3YA) [1:1] - **(30)**, [5:1] - **(31)** and [10:1] - **(32)**. As discussed previously, S3T3YA refers to the N-succinimidyl ester derived from T3T3YAA, therefore, comparison between P(3HT-*c*-T3T3YAA) **(26)** & **(27)** is appropriate. In summary, as presented in Figure 7.10 and Table 7.6, the stability and repeatability of the three S3T3YA polymers was less varied in comparison to both S3TA and T3T3YAA variants ranging between 65.5% - 39.4% and 62.4% - 31% in short term testing and between 27.4% - 68.0% and 30.9% - 59.1% over the longer term measurements.

Overall, the sensor performance was similar to each of the other polymer-GOx compositions tested in this project, with linearity present after ∼5 mM and limit of detection values approximately between 1 and 4 mM. Similarly, there was no clear trend in performance across both the short and long term testing periods with the majority of sensing electrodes producing μA scale currents between 0 - 1 μA at sensitives of between 0.003 and 0.03 $\mu A\,mM^{-1}$.

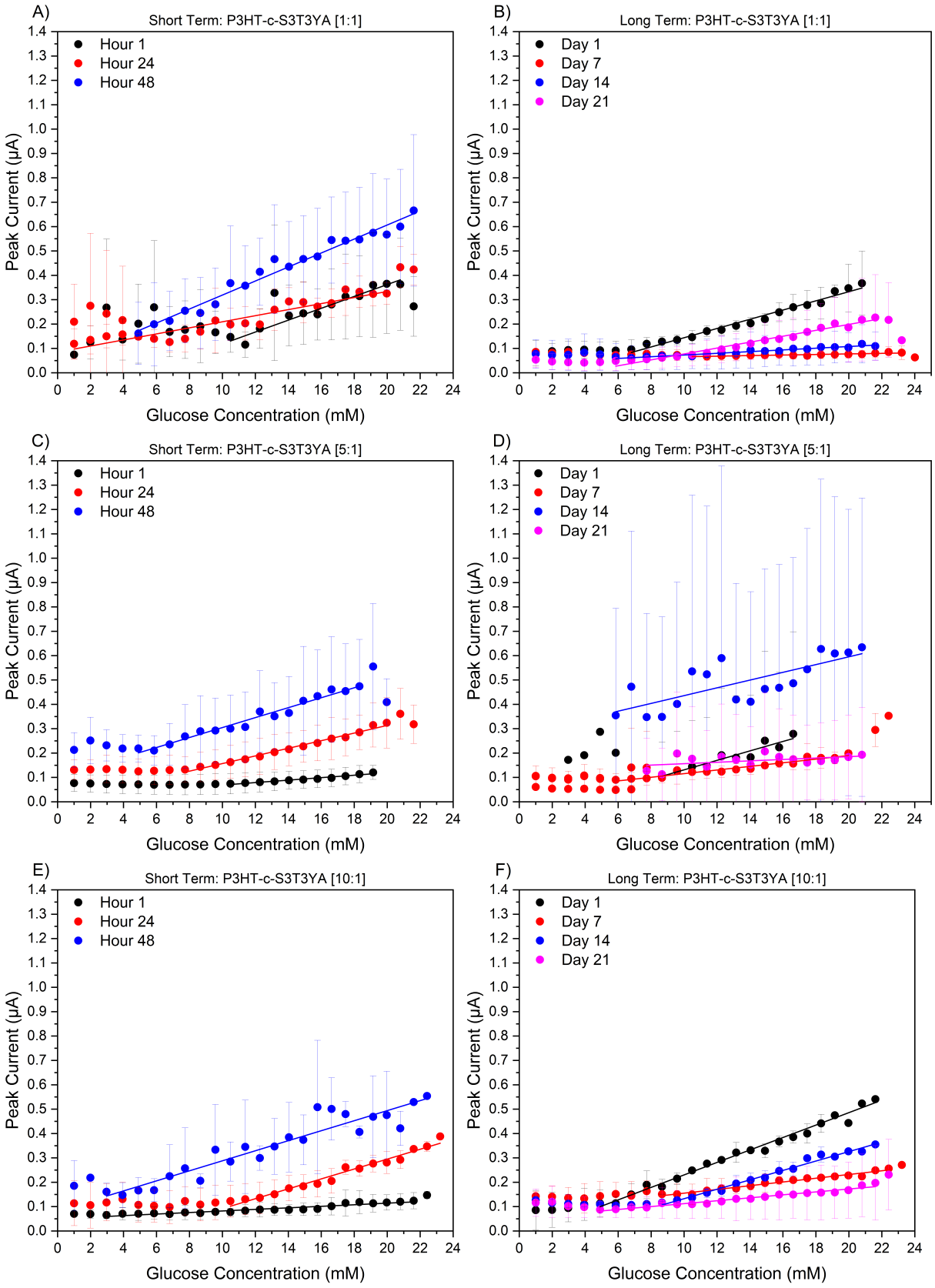

Figure 7.10: Calibration curve from amperometric response to glucose of Au/P(3HT-*c*-S3T3YA)/GOx electrodes. A) P(3HT-*c*-S3T3YA) [1:1] **(30)** - Short Term (48 hr) and B) P(3HT-*c*-S3T3YA) [1:1] **(30)** - Long Term (21 days), C) P(3HT-*c*-S3T3YA) [5:1] **(31)** - ST, D) P(3HT-*c*-S3T3YA) [5:1] **(31)** - LT, E) P(3HT-*c*-S3T3YA) [10:1] **(32)** - ST and F) P(3HT-*c*-S3T3YA) [10:1] **(32)** - LT.

Table 7.6: Biosensor Performance Properties for S3T3YA containing polymers **(30)**, **(31)** and **(32)**.

Time	Linear Range (mM)	LoD (mM)	Sensitivity ($\mu A\,mM^{-1}$)	Stability (%)	Repeatability (%)
P(3HT-*c*-S3T3YA) [1:1]					
Hour 1	11 to 23	3.54	0.0244	65.5	62.4
Hour 24	1 to 22	3.10	0.0124		
Hour 48	5 to 24	1.86	0.0287		
Day 1	7 to 23	1.92	0.0189	54.1	45.3
Day 7	11 to 26	7.78	0.0012		
Day 14	6 to 24	2.81	0.0035		
Day 21	6 to 24	2.08	0.0121		
P(3HT-*c*-S3T3YA) [5:1]					
Hour 1	11 to 21	3.46	0.0051	40.9	53.1
Hour 24	5 to 24	1.61	0.0156		
Hour 48	5 to 20	1.92	0.0204		
Day 1	9 to 18	4.93	0.0194	27.4	30.9
Day 7	6 to 22	2.76	0.0074		
Day 14	6 to 23	10.03	0.0159		
Day 21	8 to 23	24.61	0.1278		
P(3HT-*c*-S3T3YA) [10:1]					
Hour 1	3 to 23	3.22	0.0032	39.4	31
Hour 24	11 to 26	2.68	0.0203		
Hour 48	3 to 25	3.54	0.0206		
Day 1	5 to 24	1.15	0.0256	68.0	59.1
Day 7	9 to 25	2.35	0.0077		
Day 14	9 to 24	1.76	0.0193		
Day 21	5 to 24	2.32	0.0060		

7.4 Selectivity

In addition to assessing the response to glucose for each of the biosensor electrodes, the selectivity of select polymers was investigated. In this test, polymers-GOx electrodes of P(3HT-*c*-T3AA) [10:1] **(20)**, P(3HT-*c*-T3T3YAA) [10:1] **(26)**, P(3HT-*c*-S3TA) [10:1] **(29)** and P(3HT-*c*-S3T3YA) [10:1] **(32)** were assessed for their response to urea, a major metabolic waste compound found in urine. For each electrode, the amperometric response to urea between 0 to 24 mM over 400 s was measured using the same method as described in Section 3.11.2. Continuing after 400 s, the response to glucose was then recorded using the same electrochemical cell. In Figure 7.11, the outcome of the selectivity experiments are summarised.

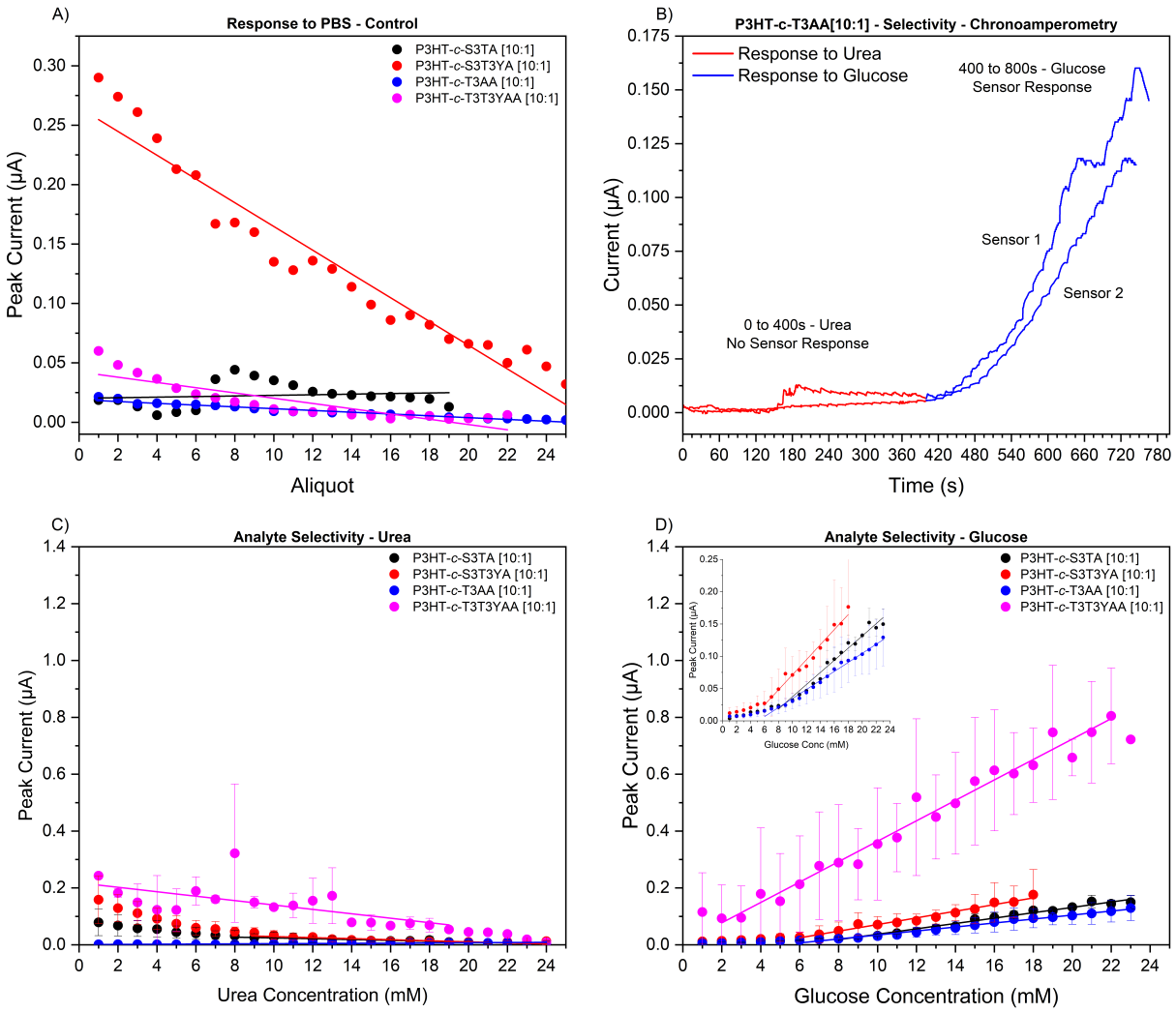

Figure 7.11: Amperometry plots of selectivity measurements for polymer **(20)**, **(26)**, **(29)** and **(32)**. A) Response to PBS only (Control), B) Polymer **(20)** Chronoamperogram for response to urea (0-400 s) and glucose (400-800 s), C) Calibration curve (Urea) for **(20)**, **(26)**, **(29)** and **(32)** and, D) Calibration curve (Glucose) for **(20)**, **(26)**, **(29)** and **(32)**. Inset show the corresponding plot with a reduced Y-axis scale for polymers **(20)**, **(26)** and **(32)**.

For each of the selected polymer-GOx electrodes, the response to phosphate-buffered saline blank solution is outlined in the calibration curve of 7.11.A. None of the tested devices show a current gain as a result of addition of the ionic solution outlining baseline stability in the absence of the target substrate, an important characteristic for accurate detection of analyte. Moreover, the sensors exhibit low background noise owing to the flat nature of the response, which essential for achieving high sensitivity.

An example chronoamperogram for the urea-glucose selective measurements is shown in 7.11.B. The current gain/response between 0-400 s owing to the addition of 1 mM urea aliquots is minimal however following the addition of glucose to the electrochemical cell,

the current response is rapid, increasing with each aliquot of substrate. The insensitivity to urea and detection of glucose shows the polymer-GOx electrodes are highly selective and do not impact on the inherent specificity of the enzyme bioreceptor. This data also confirms that the polymer provides a stable and inert platform for enzyme immobilisation, ensuring that only the specific interaction between the enzyme and target substrate will produce a measurable response and that non-specific adsorption of molecules onto the polymer itself does not generate a signal.

Table 7.7: Performance properties for selectivity measurements against urea and glucose using polymers **(20)**, **(26)**, **(29)** and **(32)**

Analyte	Linear Range (mM)	LoD (mM)	Sensitivity ($\mu A\,mM^{-1}$)
P(3HT-*c*-T3AA) [10:1]			
Urea	-	-	0.0003
Glucose	6 to 24	1.43	0.0070
P(3HT-*c*-T3T3YAA) [10:1]			
Urea	-	-	-0.0078
Glucose	2 to 22	1.58	0.0359
P(3HT-*c*-S3TA) [10:1]			
Urea	-	-	-0.0014
Glucose	8 to 24	2.19	0.0094
P(3HT-*c*-S3T3YA) [10:1]			
Urea	-	-	-0.0019
Glucose	6 to 18	2.00	0.0115

The extracted sensor performance data from the calibration curves in Figures 7.11.C to E is presented in Table 7.7. As discussed, all polymer-GOx sensors exhibit negative or negligible sensitivity to the addition of urea while detecting glucose with a wide linear range, low LoD and a sensitivity and, order of magnitude greater than urea. In any future work, an expanded selectivity test against other physiological interferents and competing analytes e.g. uric acid, ascorbic acid (vitamic C), para-acetylaminophenol, sucrose, etc. would provide greater evidence for the suitability of the P3HT-based enzyme binding agents in glucose sensing applications. Additionally, further analysis of glucose concentration could be performed in bodily fluid e.g. serum, dermal ISF as well as non-animal samples such as fruit juices and waste waters to highlight the potential versatility of the system.

7.5 Electrodes by UV/O_3-PDMS Selective Metallisation

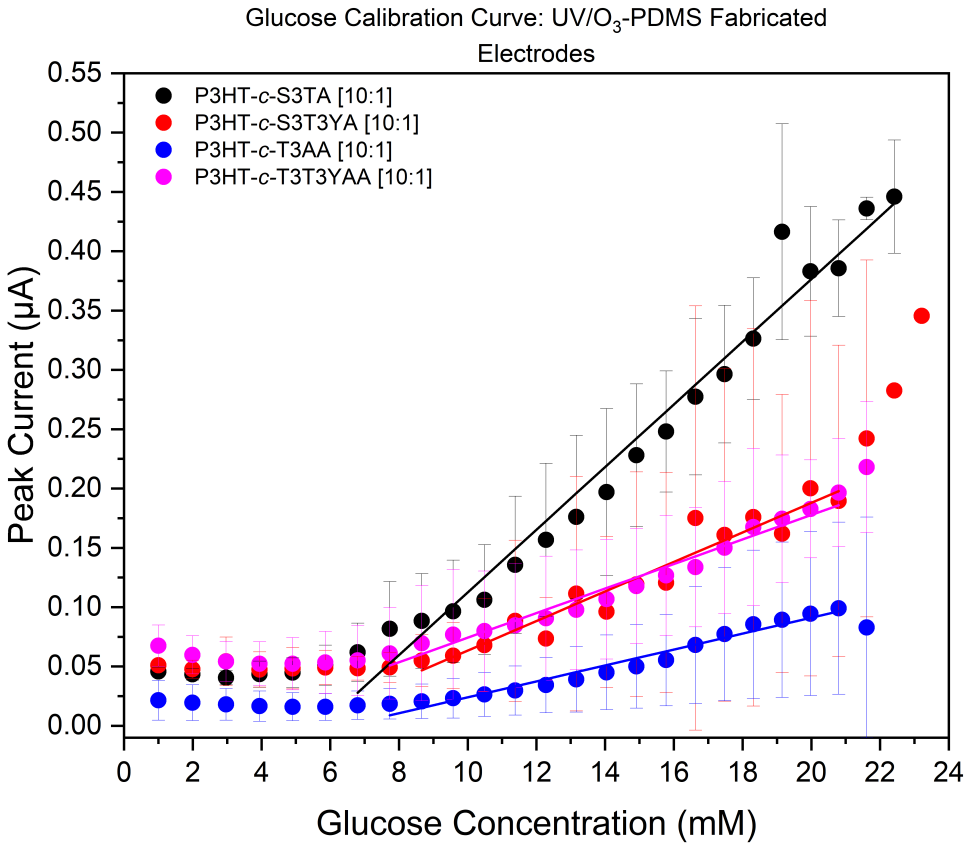

Figure 7.12: Calibration curve for polymers **(20)**, **(26)**, **(29)** and **(32)**-GOx glucose response on UV/O_3-PDMS deposited gold thin film electrodes.

Finally, the combination of electrodes fabricated using UV/O_3-PDMS selective metallisation and select polymer-GOx for glucose sensing is showcased below. The two key aspects of this test were to show that the UV/O_3PDMS method is capable of depositing an electrically conductive metal film that is functional, unaffected by residual Krytox1506 oil and able to withstand an aqueous environment. Following on from the selectivity measurements, the same polymers were chosen for this test, i.e. **(20)**, **(26)**, **(29)** and **(32)**. Figure 7.12 and Table 7.8 present the plot and extracted performance data. The different polymers (**(20)**, **(26)**, **(29)** and **(32)**) deposited onto electrodes fabricated using UV/O_3 selective metallisation all exhibit a strong linear response to glucose, with comparable performance to their traditional shadow-mask fabricated counterparts shown in the preceding figures and data. Looking at the UV/O_3-PDMS deposited gold electrodes, it can be seen that the film is not entirely continuous; a result of Krytox1506 oil comet streaks remaining in ideally, oil-free dewetting portion of the stamp. This is a by-product of using spin-coating to coat

each stamp with the oil. The images in Figure 7.13 shows the non-continuous UV/O_3-PDMS deposited film as well as a high quality electrode deposited through a shadow-mask. It can be suggested that the polymer-GOx film is able to overcome the poor quality gold layer due to the intrinsic conductivity of the P3HT-based polymer and that the high conductivity of the gold allows for the current to travel around the defects as evidenced by the negligible performance change, irrespective of the patchy electrode.

Table 7.8: Performance properties for the response to glucose using polymers **(20)**, **(26)**, **(29)** and **(32)** on UV/O_3-PDMS deposited gold thin film electrodes.

Polymer	Linear Range (mM)	LoD (mM)	Sensitivity ($\mu A\,mM^{-1}$)
P(3HT-*c*-T3AA) [10:1]	8 to 16	2.52	0.0067
P(3HT-*c*-T3T3YAA) [10:1]	8 to 23	2.36	0.0103
P(3HT-*c*-S3TA) [10:1]	7 to 25	2.16	0.0264
P(3HT-*c*-S3T3YA) [10:1]	9 to 23	3.88	0.0125

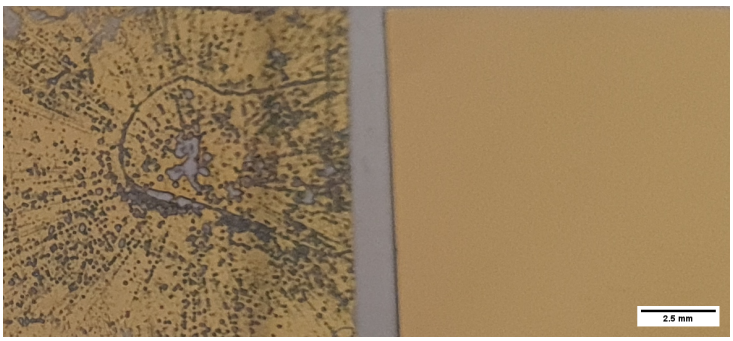

Figure 7.13: Images of gold thin film electrodes on PET substrates. Left) Prepared by UV/O_3-PDMS stamped deposition, Right) Prepared by thermal evaporation through a shadow mask.

7.6 Summary

In this section, an application for the soluble, as synthesised, P3HT-based copolymers has been outlined. Numerous sensing electrodes based on an enzymatic biosensor principle have been fabricated for the detection of glucose. These biosensors have been analysed using a range of methods, namely; colorimetric assay, cyclic voltammetry and chronoamperometry. A summary of the fabrication of the sensing electrodes and the conjugation of the enzyme - Glucose Oxidase (GOx), to the functional co-monomer has been outlined. The bioreceptor was bound to carboxylic acid containing polymers **(19)**, **(20)**, **(25)** and **(26)** via a simple EDC/NHS cross-linking reaction. For polymers **(27)** - **(32)**, enzyme conjugation was

achieved without additional reagents due to the presence of preactivated N-succinimidyl ester-type groups. The covalent attachment of the enzyme to the polymer structure has been confirmed by i) an o-dianisidine/peroxidase assay (Figure 7.3), and ii) retention of glucose sensing capability over 21 days, during which the electrodes were stored in a 0.1 M PBS solution at 4°C (Section 7.3). Cyclic voltammetry and constant potential chronoamperometry were utilised to assess the electrochemical properties and sensing performance of each polymer-glucose oxidase composite. Cyclic voltammetry allowed for determination of electrochemical redox reactions within the film, with the majority of polymers possessing a complex voltammograms with multiple electron transfers. The response to the enzyme's target substrate - β-D-glucose and an interferent - urea, was measured amperometrically using a three-electrode electrochemical cell consisting of the Au/Polymer/GOx working electrode, a platinum wire counter electrode and a Ag/AgCl reference. In general, the polymer-enzyme electrodes exhibit selective recognition of glucose, detecting the substrate linearly over a wide concentration range (1 to 25 mM), with low Limit of Detection (LoD) and at range of sensitivities. The measurement stability and electrode-to-electrode repeatability over short term (48 hr) and long term (21 days) was calculated using the coefficient of variation to assess repeatability in sensing glucose and how repeatable different batches of sensors are.

Table 7.9: Performance metrics for various conductive polymer based biosensors.

Glucose Oxidase Electrode	Technique	Limit of Detection (LoD)	Sensitivity (uA mM_{-1})	Linear Range (mM)	Stability (Days)	Ref
Au/P3HT-*c*-S3TA [1:1]	Amperometry	1.13	0.180	1 to 19	< 21	This Work
Au/P(3HT-*c*-S3TA) [5:1]		4.71	0.004	3 to 18	> 21	
Au/P(3HT-*c*-S3TA) [10:1]		3.25	0.008	4 to 27	> 21	
Au/P(3HT-*c*-S3T3YA) [1:1]		1.92	0.019	7 to 23	> 21	
Au/P(3HT-*c*-S3T3YA) [5:1]		4.93	0.019	9 to 18	> 21	
Au/P(3HT-*c*-S3T3YA) [10:1]		1.15	0.026	5 to 24	> 21	
Au/P(3HT-*c*-T3AA) [5:1]		2.03	0.015	1 to 20	> 21	
Au/P(3HT-*c*-T3AA) [10:1]		2.91	0.066	6 to 22	< 21	
Au/P(3HT-*c*-T3T3YAA) [5:1]		3.39	0.035	1 to 23	< 21	
Au/P(3HT-*c*-T3T3YAA) [10:1]		1.82	0.021	8 to 21	> 21	
Si-SiO2/PEDOT-PSS	OTFT	n/a	1.65	1.1 to 16.5	n/a	[106]
Pt/Poly(2,2'-BT)	Amperometry	0.03	n/a	0.09 to 5.2	<15	[27]
Pt/Poly(4,4'-bBT)	Amperometry	0.05	n/a	0.15 to 5.2	<30	[27]
Pt/Al2O3/PPy	Amperometry	0.03	7.4	0.5 to 10.4	<14	[378]
Au/Poly(dTT-bT)	Amperometry	0.12	35	0.2 to 2	>30	[379]
Pt/Poly(3MT-T3AA)	Amperometry	0.5	n/a	1 to 7	>28	[67]
Pt/Poly(3MT-S3TA)	Amperometry	0.5	n/a	1 to 7	>28	[67]
C/Cs/poly(TP)	Amperometry	$9.7x10^{-5}$	0.322	0.001 to 0.01	>60	[380]

Abbreviations: 3-hexylthiophene (3HT), N-succinimidyl 3-thiophene acetate (S3TA), N-succinimidyl 3-(thiophen-3-yl)acrylate (S3T3YA),Thiophene-3-acetic acid (T3AA), Trans-3-thiophen-3-yl-acrylic acid (T3T3YAA), Poly(3,4-ethylenedioxythiophene):poly(styrene sulfonate) (PEDOT:PSS), 2,2'-bithiophene (2,2'-BT), 4,4'-bis(2-methyl-3-butyn-2-ol)-2,2'-bithiophene (4,4'-bBT), Polypyrrole (PPy), 2,5-di(2-thienyl)thieno[3,2-b]thiophene (dTT-bT), 3-methylthiophene (3MT), Chitosan (Cs), [N1, N4-bis(2,5-di(thiophene-2-yl)-1H-pyrrol-1-yl) terephthalamide] (TP).

Comparison of the glucose oxidase sensing electrodes presented in this project to relevant conductive polymer-based biosensors from the literature can be viewed in Table 7.9. A difference between this project's sensors and the sensors in the literature revolves around the configuration of the electrochemical cell as well as the electrode itself, specifically, all the similar devices found in the literature utilise platinum, carbon or gold wire/disk electrode while the electrodes presented here are thin-film gold on PET i.e. a one-sided electrode. Such a difference may explain the clear variation between the larger current responses in the literature articles and the low microamp scale currents outlined above in Section 3.11.2.

Ultimately, analysis of the chronoamperometry data brings to light the need for further refinement of various system components, for example, the in-house amperometry system (Section 3.11.2) due to the possible susceptibility to outside interference as well as optimisation of the sensor electrode device stack (film thickness, enzyme immobilisation time, optimal functional monomer content, etc). Four polymer-GOx electrodes **(20)**, **(27)**, **(29)** and **(32)** were assessed for selectivity. The results show the polymer-GOx electrodes are highly specific to glucose and insensitive to urea. Finally, the preparation of sensing electrodes fabricated using UV/O_3-PDMS deposited gold thin films paired with polymers **(20)**, **(27)**, **(29)** and **(32)** were presented.

Chapter 8
Conclusion and Future Works

In this final chapter, the principle conclusions of this project are summarised and the possibility of future work is considered and discussed.

By leaning on the properties and versatility of polymers, the work in this thesis aims to present new processes, developments and, materials related to the preparation of flexible and printable biosensor devices. Specifically, for the purpose of covalently immobilising enzyme bioreceptors for use in a sensing electrode, soluble copolymers based on a 3-hexylthiophene (3HT) majority monomer and thiophene carboxylic acid derived comonomer have been synthesised and characterised as outlined in Chapter 4. Moreover, Chapter 5 presents the development of a method for the deposition of patterned metal layers, with a focus on the regeneration of UV/O_3-PDMS printing stamps. Finally, the application of the synthesised materials described in Chapter 4 and UVO_3-PDMS selective metallisation outlined in Chapter 6 for the fabrication of glucose sensor is shown in Chapter 7.

8.1 Synthesis of Thiophene Copolymers for the Immobilisation of Biomolecules

This works presents the first synthesis of four novel 3-hexylthiophene copolymers (See Figure 8.1;

i) poly(3-hexylthiophene-*co*-methyl 3-(thiophen-3-yl)acrylate)
ii) poly(3-hexylthiophene-*co*-trans-3-thiophen-3-yl acrylic acid)
iii) poly(3-hexylthiophene-*co*-N-succinimidyl 3-thiophene acetate)
iv) poly(3-hexylthiophene-*co*-N-succinimidyl 3-(thiophen-3-yl)acrylate)

Low-cost, carboxylic acid functionalised thiophene monomers (T3CA, T3AA, T3T3YAA) were converted into a set of polymerisable monomers via known synthetic pathways. As described in Chapter 3, acid-catalysed methyl esterification and N-hydroxysuccinimide (NHS) activation were successfully applied to yield 3-thiophene methyl esters and 3-thiophene N-succinimidyl esters, respectively [67, 290, 301]. A common polymerisation method found

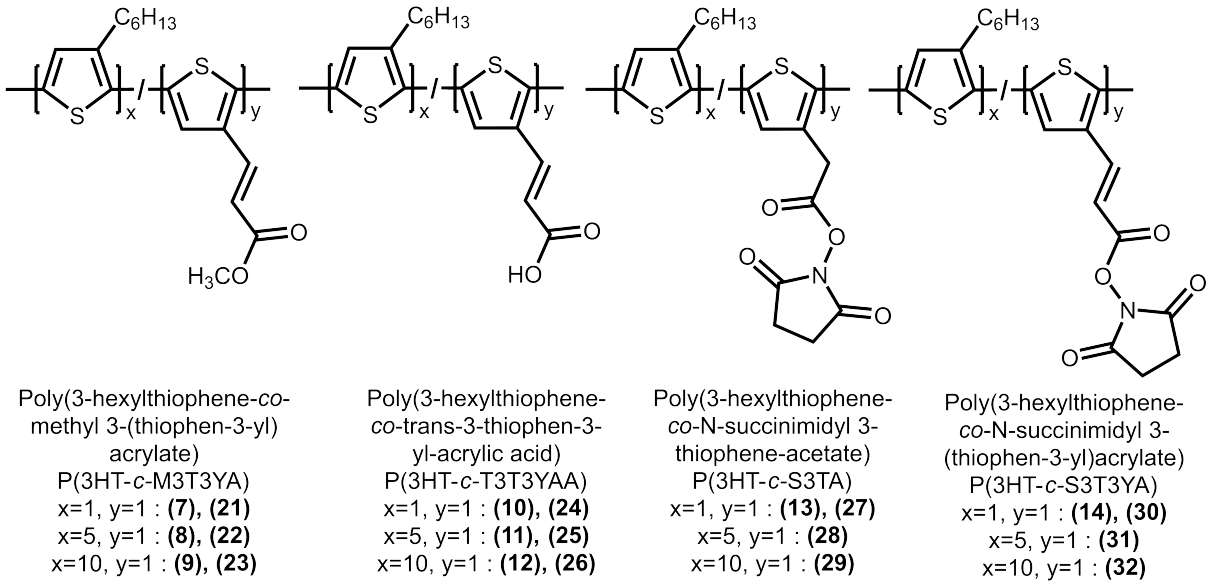

Figure 8.1: Chemical structures of novel 3-hexylthiophene copolymer synthesised during project.

extensively in the literature was utilised for the preparation of copolymer materials [149, 200, 226]. As detailed in Section 3.3, the polymerisation was carried out using either a chloroform ($CHCl_3$) or acetonitrile (CH_3CN) reaction solvent with a fourfold molar equivalent of the oxidant; iron(III) chloride ($FeCl_3$). The monomer mixture consisted of 3HT and one of the following: M3TC, M3TA, M3T3YA, S3TA, or S3T3YA which were combined in molar ratios of [1:1], [5:1], or [10:1]. All synthesised monomers and polymers have been characterised using a range of molecular spectroscopy techniques, e.g. ATR-FTIR, ^{1}H NMR and UV-Vis. The use of ATR-FTIR was crucial to the effective identification of characteristic vibrations found in the polymer. For example, Figure 4.3 present the three sharp peaks of a 3HT aliphatic C−H stretch between 2950-2850 cm^{-1} while the environment-dependent shifting of the carbonyl C=O vibration in the functional co-monomer can be observed in Figure 4.12. Furthermore, Figures 4.8 and 4.10 highlight that appropriate protection of the starting R−COOH monomer is indeed necessary due to an inability to undergo oxidative polymerisation as a result of decomposition [283]. Nuclear magnetic resonance (NMR) was utilised for further structural analysis when possible, thus allowing for determination of the polymer regioregularity (RR). UV-Vis spectroscopy was performed on a select number of polymer products following reaction in acetonitrile to determine both peak absorbance (λ_{max}) and solubility by measuring the solution turbidity. Finally, when permitted by polymer solubility in tetrahydrofuran (C_4H_8O), GPC was employed to determine molecular weight (M_W).

As discussed in Section 4.3, copolymers prepared using chloroform as a reaction solvent possessed limited solubility. it has been elucidated by the literature, this is likely caused by two factors i) chloroform often results in a higher molecular weight product with a broader polydispersity and ii) the reintroduction of the COOH moiety following ester deprotection reduces solubility due to the formation of intermolecular bonding between the solvent and polymer chain. After changing an acetonitrile reaction solvent, the proposed reduction in molecular weight resulted in all N-succinimidyl ester copolymers variations prepared as well as some of the T3AA and T3T3YAA polymers containing a high 3HT monomer % to meet the material requirements set in Chapter 1 i.e. solubility and solution-processability.

A number of avenues for further work can be proposed based on the outcomes of this chapter. Firstly, further optimisation of the synthetic procedures; specifically the polymerisation and deprotection reactions, would be beneficial to refining the material properties. For example, typical refinements found in the literature include i) adjusting the monomer feed ratio to generate copolymers with an optimal percentage of the functional monomer while balancing the electronic performance with bioreceptor binding capability [68, 289, 316] ii) fine-tuning the molecular weight of the polymer to achieve suitable performance while maintaining solubility [310, 312]. Greater investigation into the processability of these material by producing films using print deposition methods may showcase the potential in the mass production of flexible electronics. Furthermore, the use of alternative processing method such as electrospinning into polymeric nanofibres may allow for improved immobilisation capability through the optimisation of film properties e.g. porosity, surface area. A proof of concept example for the electrospinning of polymers **(26)** and **(29)** is shown in Appendix B, Figure B.15.

8.2 UV/O_3-PDMS Selective Metallisation and Regeneration of Printing Surfaces

In this chapter, investigations into the contact angle, surface chemistry and topological changes as a result of applied thermal and chemical surface regeneration processes has allowed for better understanding of the underlying mechanisms of UV/O_3-PDMS selective metallisation, hydrophobic recovery on oxidised-PDMS and the suitability of UV/O_3-

PDMS as a possible roll-to-roll printing plate material. For both thermally-enhanced and chemically-enhanced regeneration processes, a focus on measuring the recovery of contact angle (WCA & KCA) and surface free energy SFE on 240 min UV/O_3 oxidised PDMS relative to pristine PDMS. As presented in Figures 6.7, 6.8, 6.10 and 6.11, a new chemical-thermal method (Submerge in ionic buffer at 85°C, 60 min followed by a 150°C, 60 min bake) was found to exhibit complete recovery of WCA and KCA, near total loss of hydrophilic surface groups as assessed by ATR-FTIR (Figure 6.14) and dissolution of the oxygen-rich, silica-like layer as evidenced by XPS (Figures 6.19 & 6.20). Water, Krytox1506 and diiodomethane contact angle data presented in Section 6.3 as well as the aforementioned IR characterisation provides further evidence to that in the literature, supporting the proposed mechanisms which hydrophobic recovery is known to proceed by, i.e. temperature-dependent, diffusion-control migration of low-molecular weight PDMS oligomers from the bulk to the surface, reorientation of hydrophilic surface groups and the condensation of surface-bound silanol groups Si−OH. However, for recovery of Krytox1506 contact angle, it is proposed that this occurs largely as a result of the same mechanisms but does not exhibit the same temperature-dependency owing to the inter-molecular interactions involved in the wetting of perfluoropolyether PFPE. In Section 6.5, a number of rewrite deposition examples have been presented and outlined mixed success. While the successful repatterning of oxidised PDMS was observed when using PDMS as a substrate, the regeneration process in a double-pattern rewriting PDMS stamp process did not exhibit an ability to overwrite the original pattern. Although a complex issue that will require further investigation, it is hypothesised the inability to utilise the UV/O_3-PDMS as a rewritable stamp material is the result of i) unexpected wetting of Krytox1506 on the different surface states of oxidised and regenerated PDMS, ii) non-complete dissolution and interaction between Krytox1506 and the oxygen-rich silica-like layer and, iii) residual Krytox1506 remaining on the surface of PDMS stamps, preventing complete regeneration. As such, proposed future works revolve around resolving the disconnect between the theoretical evidence for regeneration and the limited success during application to metal deposition. For example, investigating the use of different oils which are easier to clean off the oxidised PDMS or oils of a different chemistry that has a weaker interaction to the hydrophilic surface. Moreover, the theoretical basis of

thermally-enhanced contact angle recovery on UV/O_3-PDMS can be further understood by collecting many more data points over a temperature range with smaller increments. As observed in Figure 6.7 and 6.8 between 50 and 100°C, there is a large jump in contact angle that obfuscates possible information on the idea that the silica-like layer acts as a barrier to recovery at low temperatures but undergoes a transition at higher temperatures where recovery due to the low-molecular weight PDMS migration is observed [343]. Additionally, as discussed first by Francis et al. [348], an expansion into the maskless patterning of PDMS printing plates and the ability to deposit high-resolution oil features warrants a specific investigation. A preliminary study performed by the author (not included in this thesis) has shown the capability for PDMS to undergo patterning by electron beam lithograph, yielding recessed features with single-μm lateral resolution (see Appendix B, Figure B.14).

8.3 Glucose Biosensor Electrodes: Fabrication, Immobilisation and Analysis

In Chapter 7, the soluble P3HT copolymers (ID: **(19)**, **(20)**, **(25)** to **(32)**) described in Chapter 4 have been utilised in the fabrication of flexible, glucose biosensing electrodes. Additionally, the UV/O_3-PDMS selective metallisation process outlined in Chapter 6 has been used to produce a set of gold electrodes upon which, the polymer-enzyme conjugate can be deposited. As such, Chapter 7 aims to showcase both the biomolecule immobilisation capability of the polymer and the ability for UV/O_3-PDMS selective metallisation to produce functional electrodes. Following the fabrication processes outlined in Chapter 3, the biosensors were analysed using a spectrophotometric (colorimetric) assay, cyclic voltammetry and various chronoamperometry tests. Owing to the difference in functional monomer chemistries within the polymers, e.g. carboxylic acid or N-succinimidyl esters, enzyme immobilisation was performed using simple EDC/NHS cross-linker reaction for the COOH-containing polymers or without additional reagents due to the presence of preactivated N-succinimidyl ester groups. The covalent attachment of the enzyme, glucose oxidase (GOx) to the polymer was confirmed using two methods i) an o-dianisidine/horseradish peroxidase assay as described in Section 3.8.2 with results in Figure 7.3, and ii) retention of glucose sensing capability an extended test duration (21 days), during which the electrodes

were stored in a 0.1 M PBS solution at 4°C so as to not denature the enzyme. Electrochemical analysis (cyclic voltammetry & constant potential chronoamperometry) was performed to assess both the sensing performance of each polymer-glucose oxidase composite and their respective electrochemical properties e.g. oxidation/reduction potential. In summary, the majority of polymers-enzyme electrode possessed complex voltammograms with multiple electron transfers. As presented in Table 7.2, the oxidation and reduction processes seen between 0.5 - 1 V were assigned to the redox process of the P3HT-based polymer while the cathodic peaks between -0.2 and -1 V relate to reduction processes within the glucose oxidase (GOx) and its redox-active co-factor Flavinadenine dinucleotide (FAD).

Chronoamperometry was employed to measure the response to (GOx)'s target substrate, β-D-glucose, while the specificity and selectivity was probed by measuring the response to urea. In general, biosensor electrodes exhibited selective recognition of β-D-glucose, detecting the monosaccharide linearly over a wide concentration range (1 to 25 mM). During short term (48 hr) and long term (21 day) testing, the measurement stability and electrode-to-electrode variation was determined to assess the reliability of glucose sensing measurement and the repeatability of different sensor batches, for example, as presented in Table 7.3, polymer **(19)** (P3HT-*c*-T3AA) possessed a stability of 87.9% and repeatability of 88.3% (CV%) over 48 hours. In section 7.4, biosensor electrodes using polymers **(20)**, **(27)**, **(29)** and **(32)** were assessed for selectivity against urea. In this testing, the four polymer-GOx sensing electrodes were shown to be insensitive to urea and selective to glucose. Polymer-GOx biosensor electrodes fabricated using uv/acro−PDMS-PDMS deposited gold thin films were also presented and shows comparable sensor performance to electrode that were produced using a shadow mask.

Further refinement of the test equipment, e.g. the in-house amperometry system, may allow for more accurate data collect by reducing the susceptibility of the electrochemical cell to outside interference i.e. noise from vibrations. This may be achieved by using a commercial potentiostat with amperometry capability. Moreover, optimisation of the device stack, specifically, the polymer layer would likely provide the greatest sensor performance boost, studying the effect of polymer film thickness, enzyme immobilisation time, functional monomer content may improve the response to the biomarker and the reusability of device.

Finally, alongside development of the existing platform, additional work related to the sensor as a whole, will further showcase the ability of the polymers for use in biosensor devices. For example, due to binding capability of the functional monomer, investigating the use of other bioreceptors e.g. antibodies or different enzymes, would outline the capability of the polymers to be a generalised linker agent.

Appendix A
Chemicals and Solvents

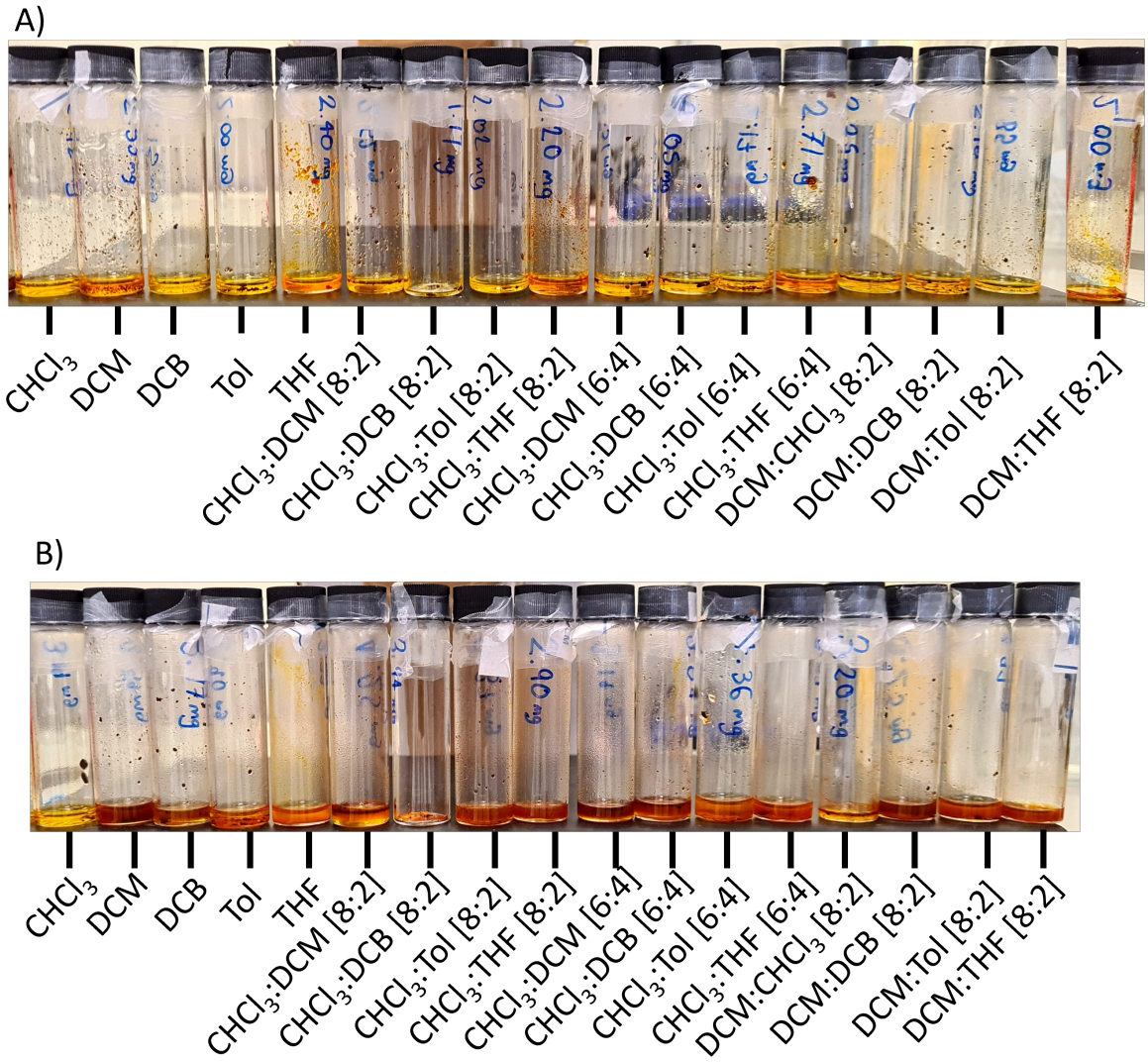

Figure A.1: Images of polymer solutions from solubility testing A) P3HT-*c*-T3AA **(6)** and B) P3HT-*c*-T3T3YAA **(12)**. Polymer concentration = 5 mg mL^{-1}. Solvents: Chloroform, dichloromethane (DCM), dichlorobezene (DCB), toluene (Tol) and tetrahydrofuran (THF) used neat, as [8:2] or [6:4] solvent mixtures. Solutions were heated at 70°C for 24 hr.

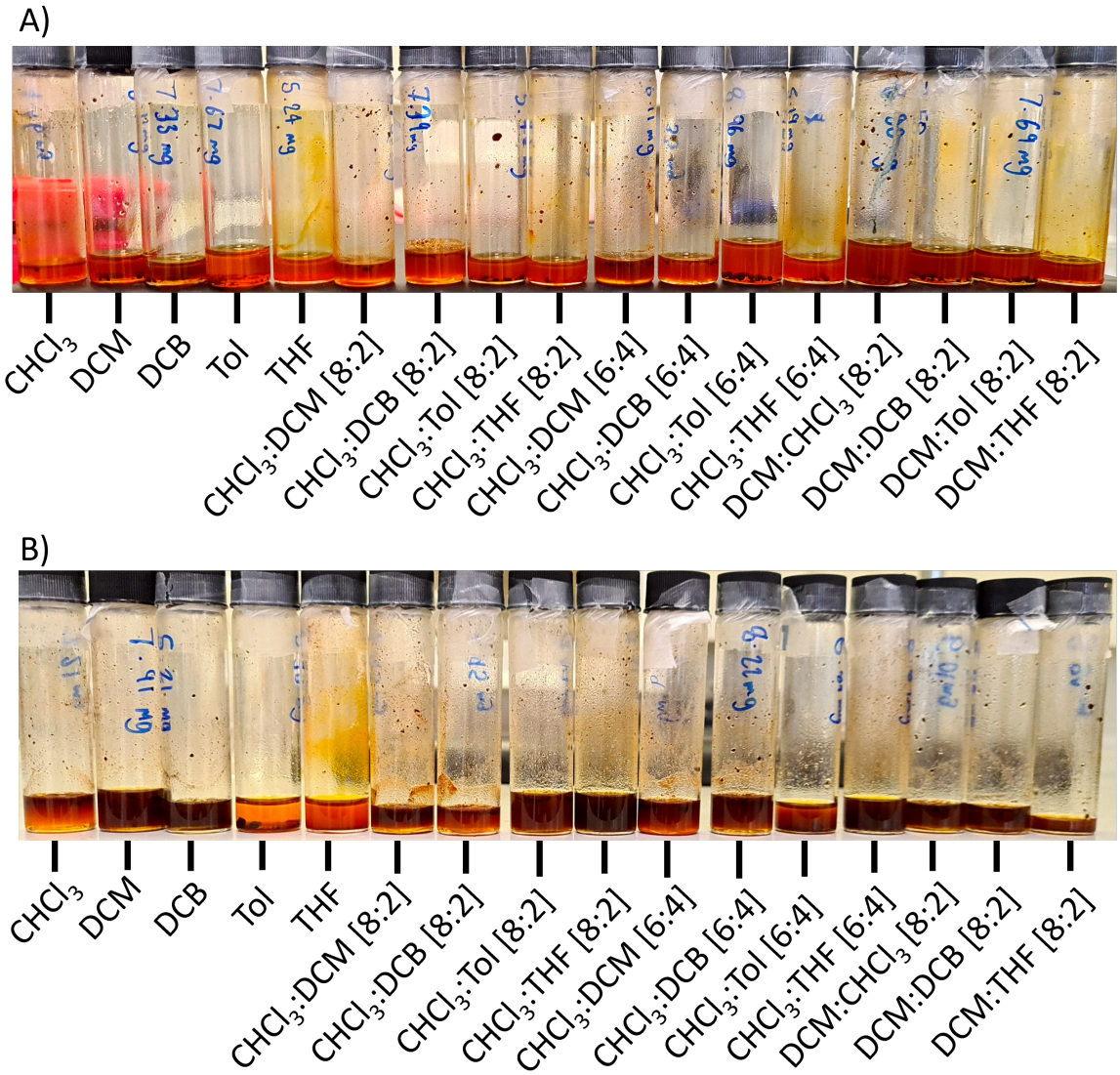

Figure A.2: Images of polymer solutions from solubility testing A) P3HT-*c*-S3TA **(15)** and B) P3HT-*c*-S3T3YA **(16)**. Polymer concentration = 5 mg mL^{-1}. Solvents: Chloroform, dichloromethane (DCM), dichlorobezene (DCB), toluene (Tol) and tetrahydrofuran (THF) used neat, as [8:2] or [6:4] solvent mixtures. Solutions were heated at 70°C for 24 hr.

Table A.1: Table of chemicals, formula, and grade/purity used in PDMS experiments.

Compound	Formula	Grade/Purity
Dow Sylgard™ 184 Polydimethylsiloxane	$(Si(CH_3)_2O)_n$	≥99.0%
3M Novec™ 7200 (ethoxy-nonafluorobutane)	$C_4F_9OC_2H_4$	99.0%
Chemours Krytox™ 1506	$(C_3F_6O)_nC_5F_{12}O$	N/A
Diiodomethane	CH_2I_2	99.0%
Ethanol, puriss. p.a., absolute	CH_3OH	≥99.8%

Table A.2: Table of chemicals, formula, and grade/purity.

Compound	Formula	Grade/Purity
Thiophenes		
Thiophene	C_4H_4S	≥ 99.0 %
3-hexylthiophene	$C_{10}H_{16}S$	99.0 %
Thiophene-3-carboxylic acid	$C_5H_4O_2S$	> 98.0 %
methyl 3-thiophene-carboxylate	$C_6H_6O_2S$	Synthesised in-house
Thiophene-3-acetic acid	$C_6H_6O_2S$	98.0 %
Methyl 3-thiophene acetate	$C_7H_8O_2S$	Synthesised in-house
N-succinimidyl 3-thiophene acetate	$C_{10}H_9NO_4S$	Syntheised in-house
Trans-3-thiophen-3-yl-acrylic acid	$C_7H_6O_2S$	98.0 %
Methyl 3-(thiophen-3-yl)acrylate	$C_8H_8O_2S$	Synthesised in-house
N-succinimidyl 3-(thiophen-3-yl)acrylate	$C_{11}H_9NO_4S$	Synthesised in-house
Synthesis Ragents		
Iron(III) chloride, anhydrous	$FeCl_3$	≥ 97.0 %
N-hydroxysuccinimide	C4H5NO3	> 98.0 %
N,N'-dicyclohexylcarbodiimide	$C_{13}H_{22}N_2$	99.0 %
Sodium Hydroxide, reagent grade	NaOH	≥ 98.0 %
Magnesium Sulfate, anhydrous	$MgSO_4$	≥ 99.5 %
Biosensors Preparation and Testing		
EDC.hydrochloride	$C_8H_{17}N_3 \cdot HCl$	99.0 %
1x Phosphate-Buffered Saline, tablets	N/A	N/A
Glucose Oxidase from *Aspergilus Niger*	EC 1.1.3.4	Type X-S, 100 - 250 KU g^{-1}
Glucose Oxidase from *Aspergilus Niger*	EC 1.1.3.4	Type IV, > 100 KU g^{-1}
Horseradish peroxidase	EC 1.11.1.7	Type II, 100 - 250 KU g^{-1}
Urea, BioReagent	CH_4N_2O	≥ 98.0 %
o-dianisidine dihydrochloride	$C_{14}H_{16}N_2O_2 \cdot {}_2HCl$	98.0 %
D-(+)-Glucose, anhydrous	$C_6H_{12}O_6$	99.0 %
Potassium Chloride, puriss.p.a	KCl	99 - 100.5 %
Solvents and Acids		
Chlorobenzene	C_6H_5Cl	≥ 99.0 %
Chloroform, for HPLC, amylene stabilised	$CHCl_3$	≥ 99.8 %
Acetonitrile, for HPLC, gradient grade	CH_3CN	≥ 99.9 %
Methanol, for HPLC	CH_3OH	≥ 99.9 %
Hexane	C_6H_{14}	95.0 %
Acetone, puriss. p.a.,	C_3H_6O	≥ 99.8 %
Ethanol, puriss. p.a., absolute	CH_3OH	≥ 99.8 %
Isopropanol, puriss. p.a.,	C_3H_7OH	≥ 99.8 %
Tetrahydrofuran, anhydrous, inhibitor-free	C_4H_8O	≥ 99.9 %
Chloroform, deuterated	$CDCl_3$	99.8 %
Chloroform, deuterated, 0.03% v/v TMS	$CDCl_3$	99.8 %
Ethyl acetate, ACS reagent	$C_4H_8O_2$	≥ 99.5 %
Hydrochloric acid, ACS reagent	HCl	37.0 %
Sulfuric acid, for analysis	H_2SO_4	98.0 %

Appendix B
Analysis and Spectra

B.1 Infrared Spectroscopy (ATR-FTIR)

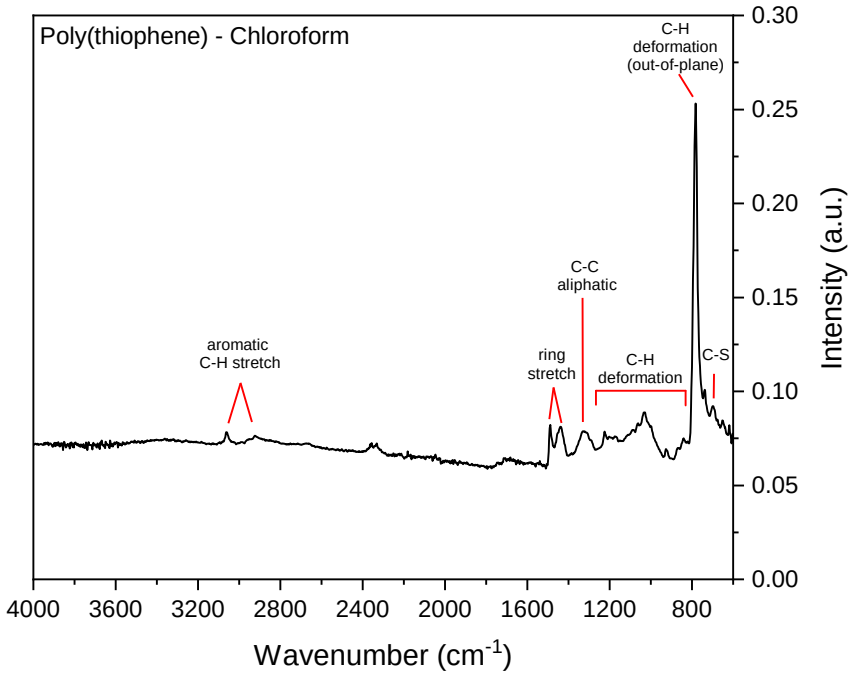

Figure B.1: IR spectrum of polythiophene from $CHCl_3$ - PTh.

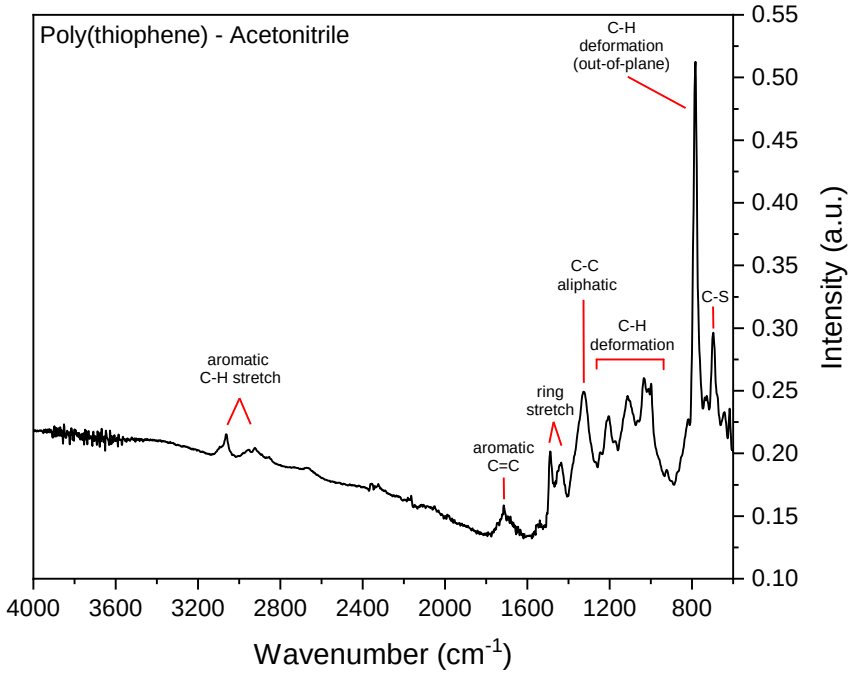

Figure B.2: IR spectrum of polythiophene from CH_3CN - PTh.

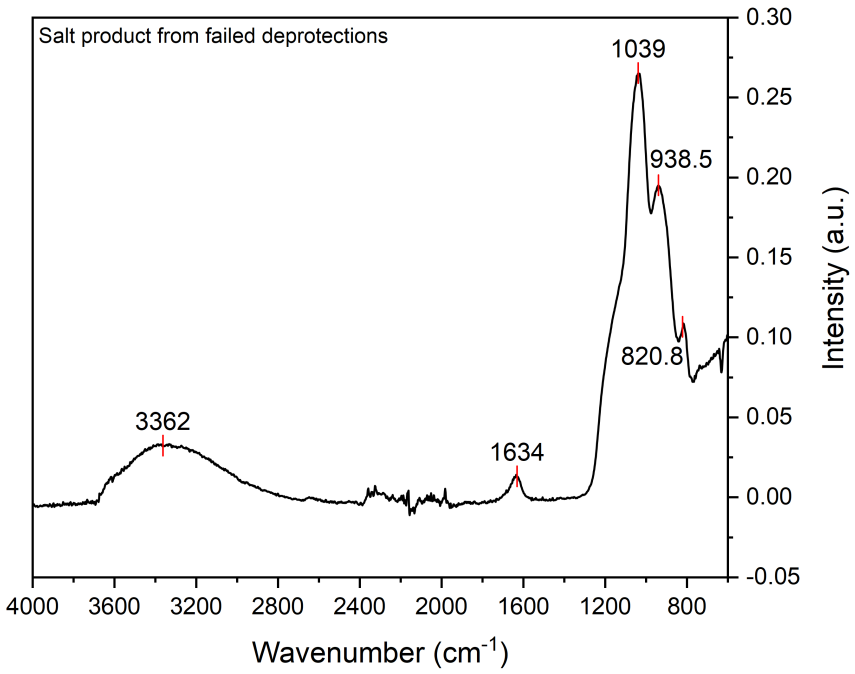

Figure B.3: IR spectrum of salt-like compound from alkaline hydrolysis of P(3HT-*c*-M3TA) **(7)**.

B.2 Nuclear Magnetic Resonance Spectroscopy (NMR)

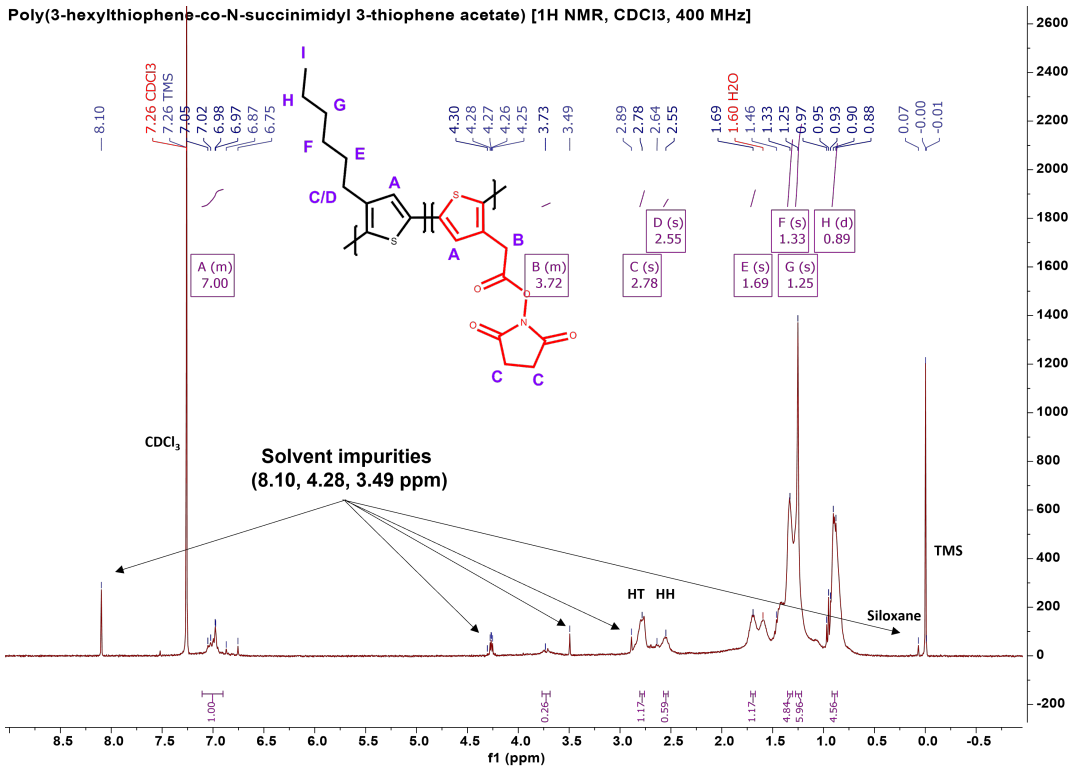

Figure B.4: ^{1}H NMR spectrum of poly(3-hexylthiophene-*co*-N-succinimidyl 3-thiophene acetate) with solvent impurities highlighted. Specifically, common impurities at 8.10, 4.28 and 3.5 ppm that appear in some spectra included in this thesis.

B.3 X-ray Photoelectron Spectroscopy (XPS)

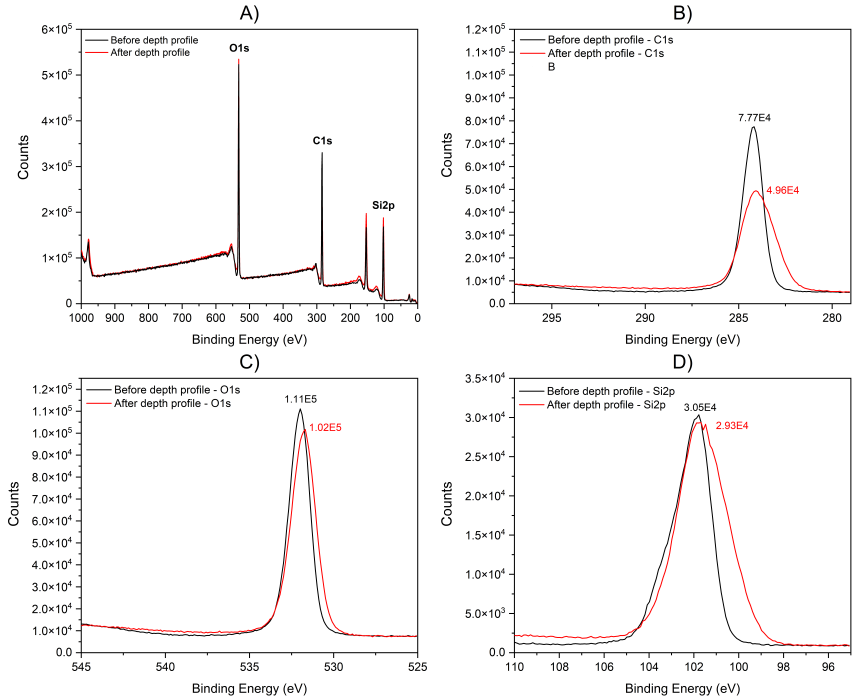

Figure B.5: XPS Spectra for pristine polydimethylsiloxane (P-PDMS).) A) Survey Scan, B) C1s (297-282 eV), C) O1s (545 - 525 ev), and D) Si2p (110-95 eV).

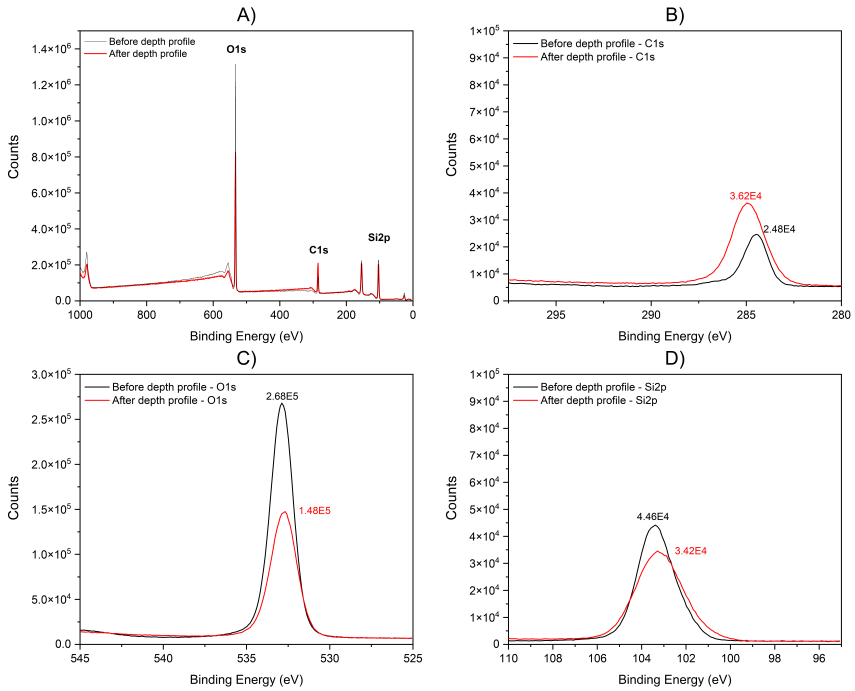

Figure B.6: XPS Spectra for 240 min UV/O_3 treated polydimethylsiloxane (UVO240-PDMS) A) Survey Scan, B) C1s (297-282 eV), C) O1s (545 - 525 ev), and D) Si2p (110-95 eV).

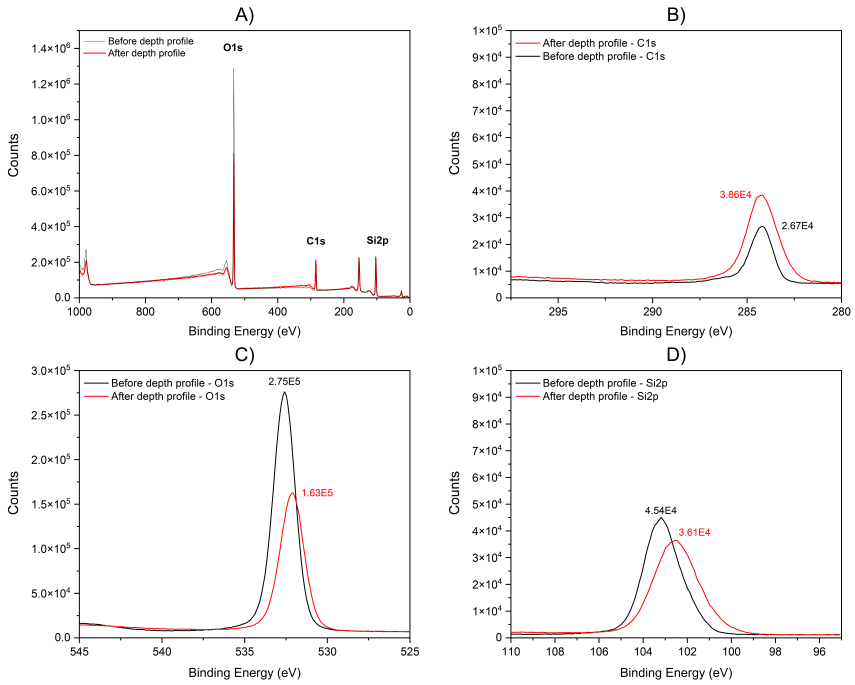

Figure B.7: XPS Spectra for thermally regenerated UVO240-PDMS - 50°C, 15 min A) Survey Scan, B) C1s (297-282 eV), C) O1s (545 - 525 ev), and D) Si2p (110-95 eV).

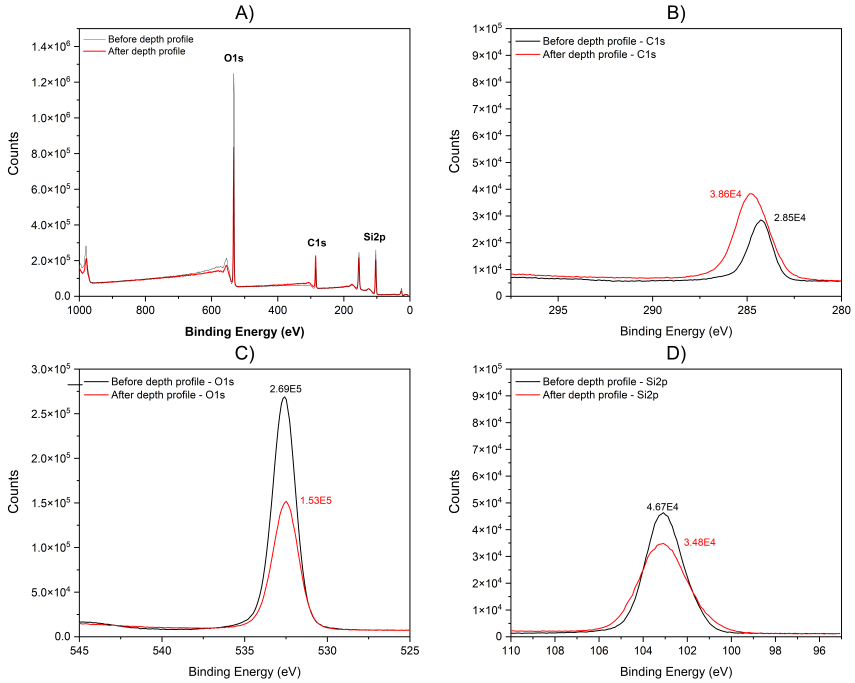

Figure B.8: XPS Spectra of thermally regenerated UVO240-PDMS - 200°C, 15 min A) Survey Scan, B) C1s (297-282 eV), C) O1s (545 - 525 ev), and D) Si2p (110-95 eV).

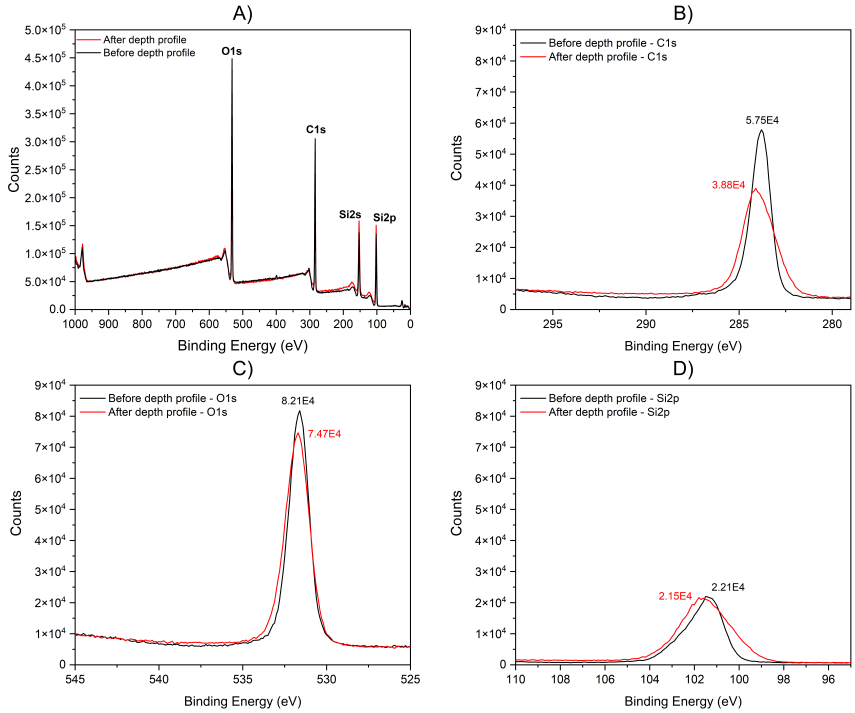

Figure B.9: XPS Spectra of chemically regenerated UVO240-PDMS - PBS immersion (85°C, 60 min) A) Survey Scan, B) C1s (297-282 eV), C) O1s (545 - 525 ev), and D) Si2p (110-95 eV).

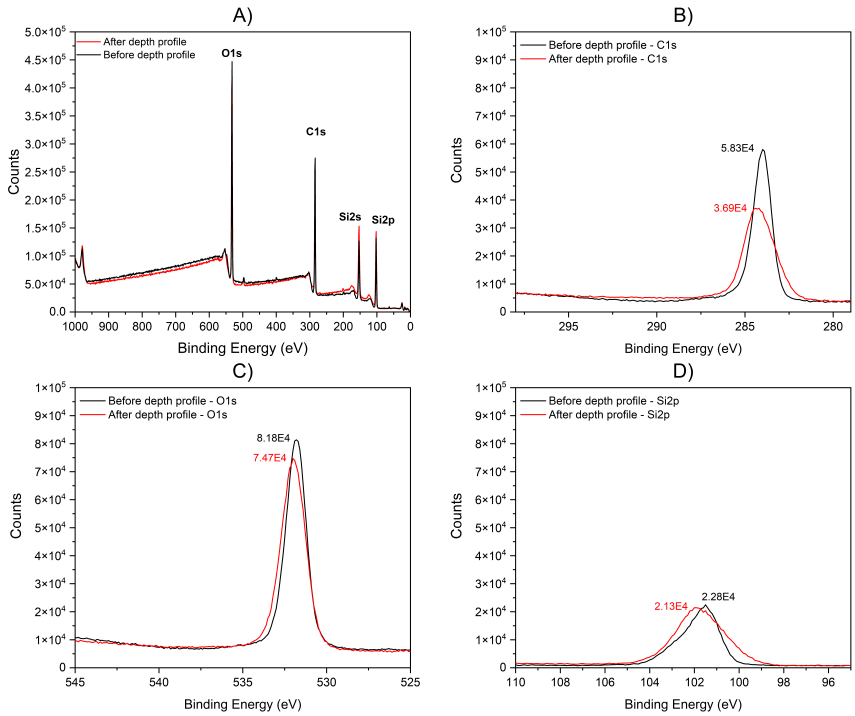

Figure B.10: XPS Spectra of combination chemical-thermal regenerated UVO240-PDMS - PBS immersion (85°C, 60 min) → HT (150°C, 60 min) A) Survey Scan, B) C1s (297-282 eV), C) O1s (545 - 525 ev), and D) Si2p (110-95 eV).

B.4 Profilometry

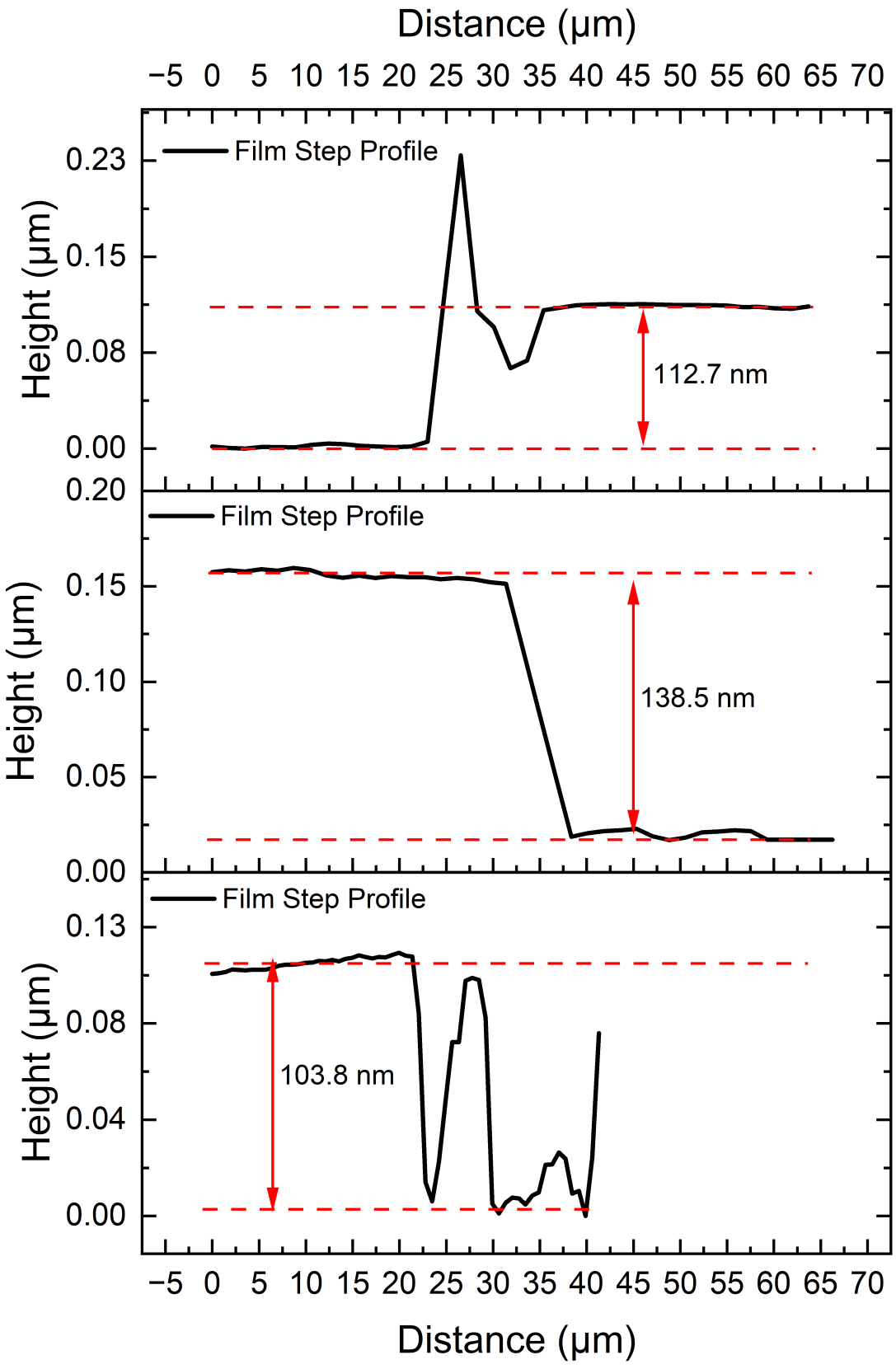

Figure B.11: Step height analysis of polymer thin-films for determination of film thickness. Data collected using profilometry.

B.5 Other/Future Works

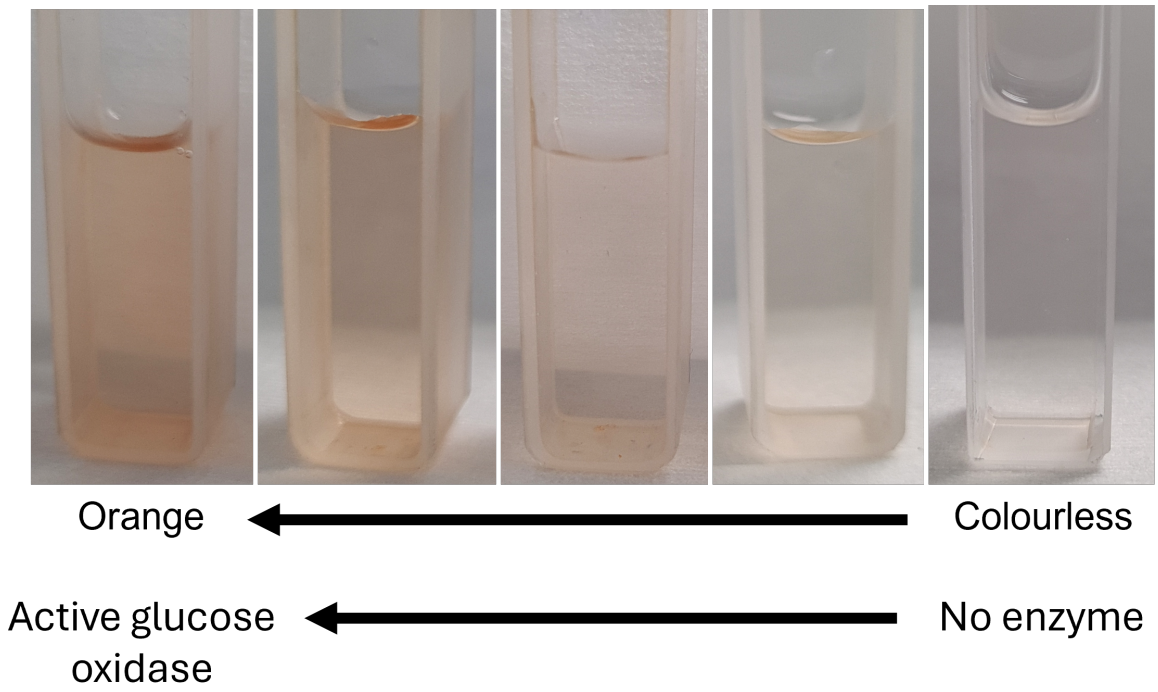

Figure B.12: Images of colour change from o-dianisidine colorimetric assay.

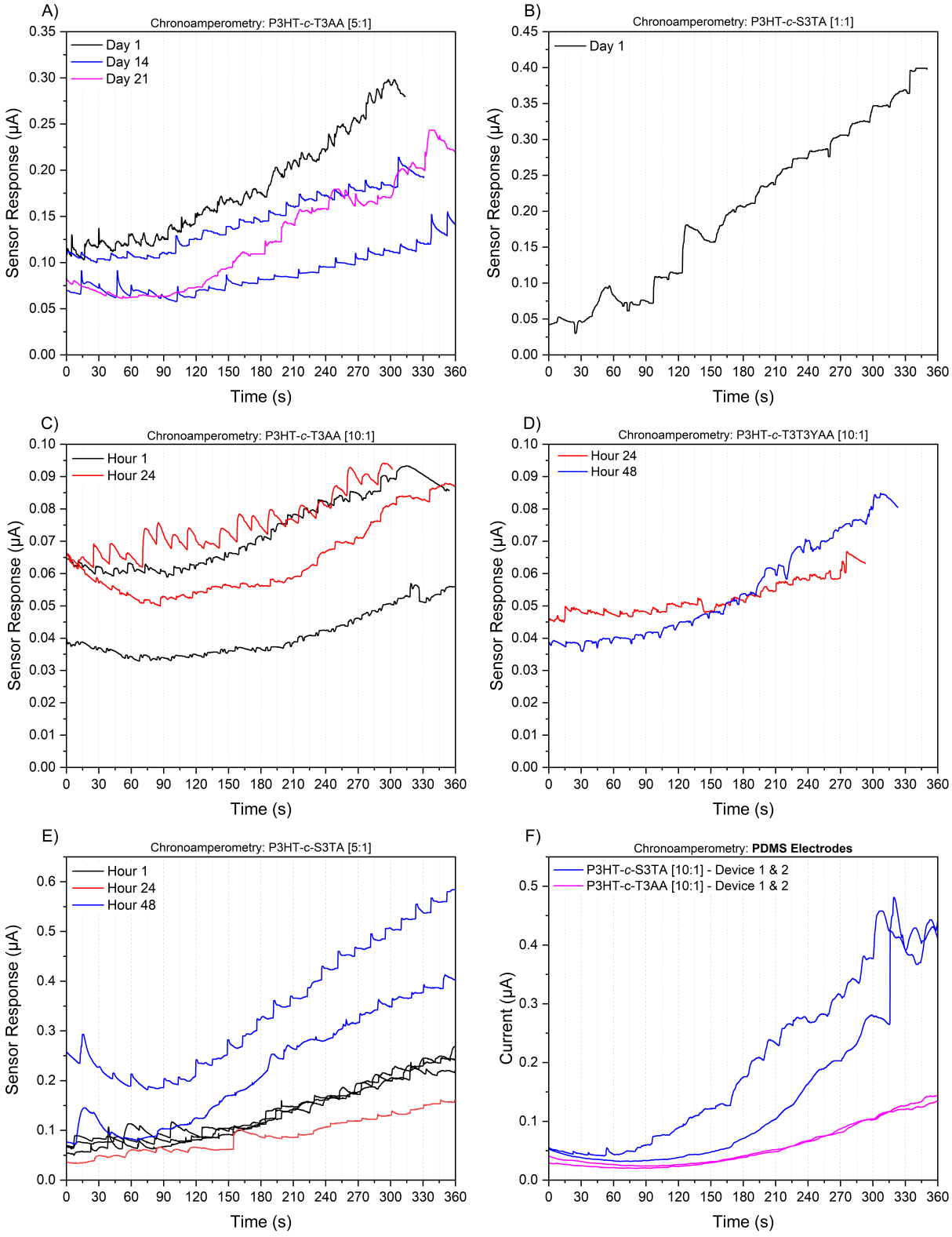

Figure B.13: Example Chronoamperography scans (current vs time) for select polymer-GOx, glucose sensing electrodes. A) P3HT-c-T3AA [5:1], B) P3HT-c-S3TA [1:1], C) P3HT-c-T3AA [10:1], D) P3HT-c-T3T3YAA [10:1], E) P3HT-c-S3TA [5:1] and F) Sensor electrodes fabricated using UV/O_3-PDMS metallisation.

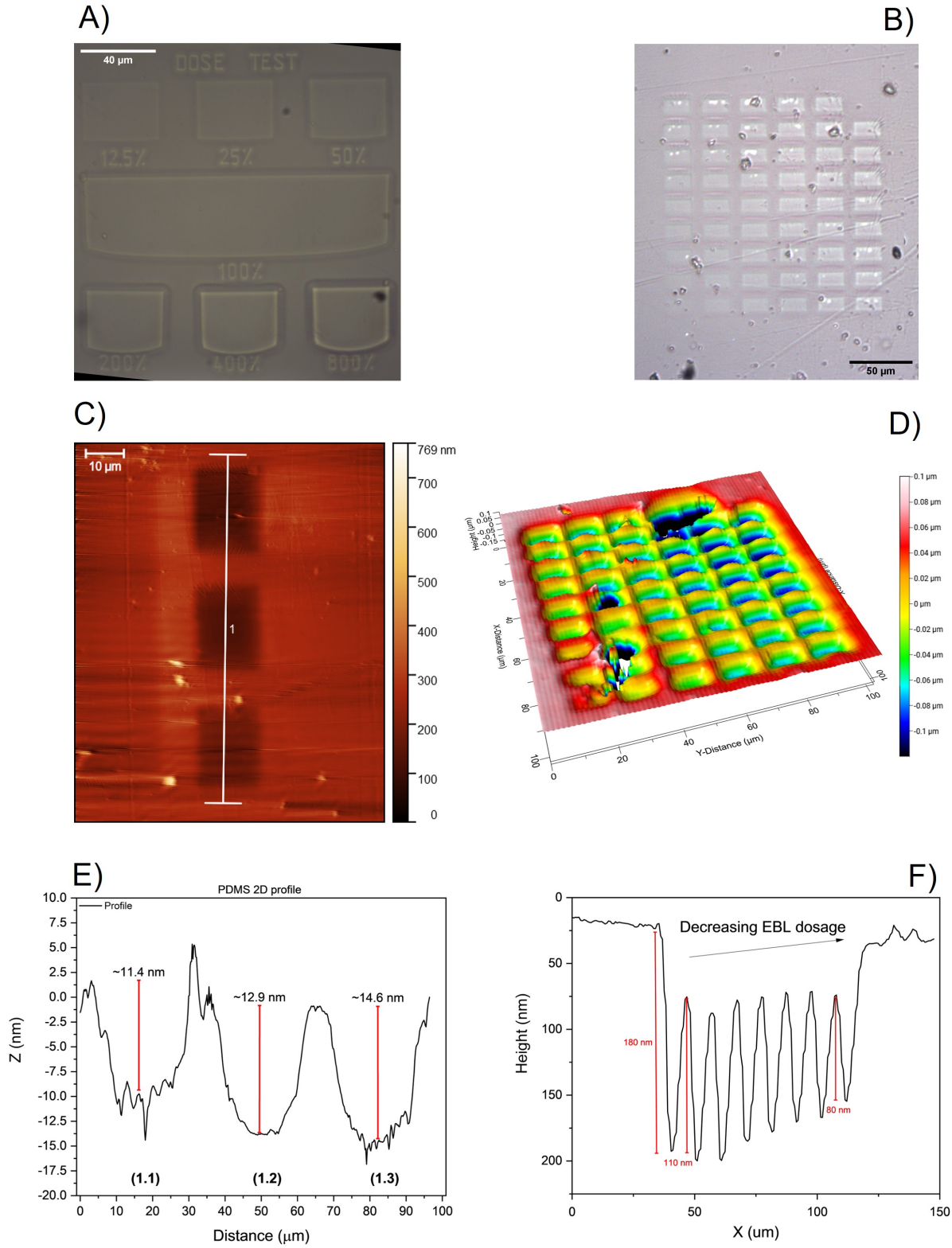

Figure B.14: Future work: Electron beam patterning of polydimethylsiloxane.

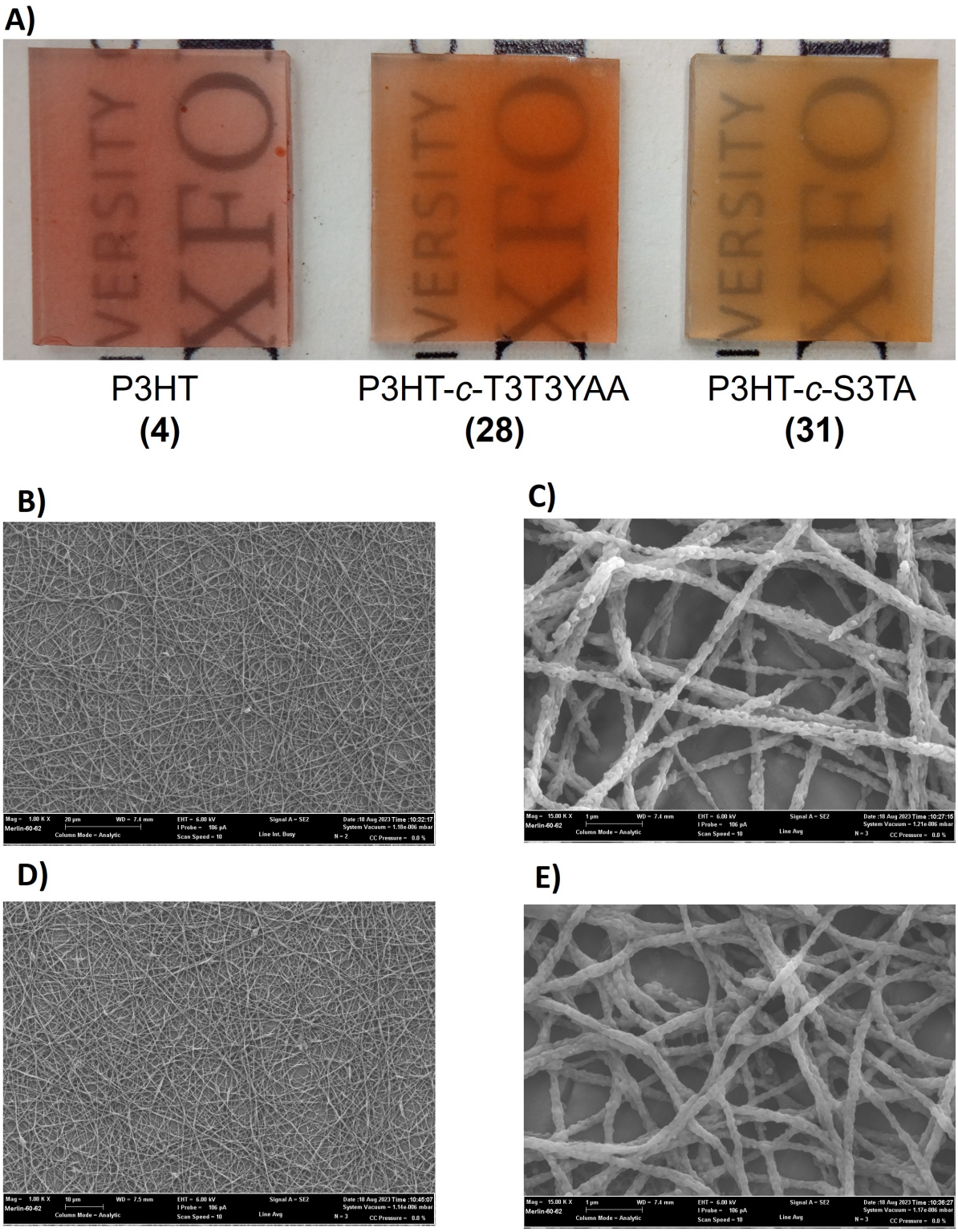

Figure B.15: Future work: Electrospun deposition of polymers. A) Images of P3HT **(4)**, P3HT-*c*-T3T3YAA **(28)** and P3HT-*c*-S3TA **(31)** fibre network on ITO substrate. B) Electron micrograph of P3HT **(4)** fibre network (x1k magnification), C) Micrograph of **(4)** at x15k mag, D) Micrograph of P3HT-*c*-T3T3YAA **(28)** fibre network at x1k mag and, E) Polymer **(28)** micrograph at x15k magnification. Electrospinning performed by R Schofield.

Bibliography

(1) *Organic Electronics Market Size, Share & Growth Analysis Report 2020-2027*, tech. rep., Precedence Research, 2020.

(2) *Printed and Flexible Sensors Market 2020-2027*, tech. rep., Precedence Research, 2020.

(3) M. Dyson, *Flexible & Printed Electronics 2023-2033: Forecasts, Technologies, Markets*, tech. rep., IDTechEx, Cambridge, UK, 2023.

(4) L. C. Clark et al., *Journal of Applied Physiology*, 1953, **6**, 189–193.

(5) L. C. Clark and C. Lyons, *Annals of the New York Academy of Sciences*, 1962, **102**, 29–45.

(6) S. J. Updike and G. P. Hicks, *Nature*, 1967, **214**, 986–988.

(7) G. G. Guilbault and J. G. Montalvo, *Journal of the American Chemical Society*, 1969, **91**, 2164–2165.

(8) D. P. Newman, *Membrane for Enzyme Electrode*, 1976.

(9) R. Dixon, *Yellow Springs Instruments - Model 23A's revolutionary legacy*, 2021.

(10) A. McNaught and A. Wilkinson, *The IUPAC Compendium of Chemical Terminology*, ed. V. Gold, International Union of Pure and Applied Chemistry (IUPAC), Research Triangle Park, NC, 2nd edn., 2019, p. 464.

(11) F. Arduini and A. Amine, in *Biosensors Based on Aptamers and Enzymes*, ed. M. B. Gu and H.-S. Kim, Springer Berlin Heidelberg, Berlin, Heidelberg, 2014, pp. 299–326.

(12) P. Damborský, J. vitel and J. Katrlík, *Essays in Biochemistry*, 2016, **60**, 91–100.

(13) J. Kaur and P. K. Singh, *Physical Chemistry Chemical Physics*, 2020, **22**, 15105–15119.

(14) G. Sauerbrey, *Zeitschrift für Physik*, 1959, **155**, 206–222.

(15) M. Pohanka, *Materials*, 2018, **11**, 448.

(16) A. Janshoff, H.-J. Galla and C. Steinem, *Angewandte Chemie*, 2000, **39**, 4004–4032.

(17) B. Danielsson, *Journal of Biotechnology*, 1990, **15**, 187–200.

(18) M. Yakovleva, S. Bhand and B. Danielsson, *Analytica Chimica Acta*, 2013, **766**, 1–12.

(19) B. Bjarnason, P. Johansson and G. Johansson, *Analytica Chimica Acta*, 1998, **372**, 341–348.

(20) J. Adlerberth et al., *Journal of Thermal Analysis and Calorimetry*, 2020, **140**, 763–771.

(21) P. Kumar et al., *Biomaterials-Based Sensors*, ed. P. Kumar et al., Springer Nature Singapore, Singapore, 2023, pp. 1–411.

(22) L. C. Lopes, A. Santos and P. R. Bueno, *Sensors and Actuators Reports*, 2022, **4**, 100087.

(23) K. G. Coronado-Apodaca et al., *Topics in Catalysis*, 2023, **66**, 606–624.

(24) A. Mulchandani and K. Rogers, *Enzyme and Microbial Biosensors*, ed. A. Mulchandanim and K. Rogers, Humana Press, New Jersey, 1st edn., 1998, vol. 6, p. 269.

(25) B. Hill, *Accu-Chek Advantage: Electrochemistry for Diabetes Management*, tech. rep. 2, 2005, pp. 45–48.

(26) Inamuddin, Beenish and M. Naushad, *Korean Journal of Chemical Engineering*, 2016, **33**, 120–125.

(27) M. Pilo et al., *Journal of Analytical Methods in Chemistry*, 2018, **2018**, 1–7.

(28) M. A. Morales and J. M. Halpern, *Bioconjugate Chemistry*, 2018, **29**, 3231–3239.

(29) E. Martínez-Periñán et al., *Electrochimica Acta*, 2018, **292**, 887–894.

(30) W. Li et al., *Talanta*, 2020, **219**, 121322.

(31) X. Zhao et al., *Food Control*, 2023, **154**, 110012.

(32) S. K. Kang et al., *Polymer Journal*, 2004, **36**, 937–942.

(33) A. K. Cheng, D. Sen and H.-Z. Yu, *Bioelectrochemistry*, 2009, **77**, 1–12.

(34) H. R. Jamei, B. Rezaei and A. A. Ensafi, *Bioelectrochemistry*, 2021, **138**, 107701.

(35) Y. V. Plekhanova and A. N. Reshetilov, *Journal of Analytical Chemistry*, 2019, **74**, 1159–1173.

(36) Y. Wu et al., *ACS Synthetic Biology*, 2021, **10**, 333–344.

(37) M. Moraskie et al., *Biosensors and Bioelectronics*, 2021, **191**, 113359.

(38) C.-Y. Lai et al., *Biosensors*, 2017, **7**, 13.

(39) J. Das and P. Sarkar, *RSC Advances*, 2016, **6**, 92520–92533.

(40) A. R. de Brito et al., *Surfaces and Interfaces*, 2021, **22**, 100839.

(41) E. Watanabe et al., *Journal of Food Science*, 1983, **48**, 496–500.

(42) A. Mulchandani, J. Luong and K. Male, *Analytica Chimica Acta*, 1989, **221**, 215–222.

(43) A. R. Shalaby, *Food Research International*, 1996, **29**, 675–690.

(44) Z. Toul and L. Macholán, *Collection of Czechoslovak Chemical Communications*, 1975, **40**, 2208–2217.

(45) R. Draisci et al., *Food Chemistry*, 1998, **62**, 225–232.

(46) B. Bóka et al., *Electroanalysis*, 2012, **24**, 181–186.

(47) J. Castillo et al., *Biosensors and Bioelectronics*, 2003, **18**, 705–714.

(48) J. H. T. Luong, S. Hrapovic and D. Wang, *Electroanalysis*, 2005, **17**, 47–53.

(49) S. Leonardo and M. Campàs, *Microchimica Acta*, 2016, **183**, 1881–1890.

(50) M. Amin et al., *Nanomaterials*, 2022, **13**, 36.

(51) J. A. Bauer et al., *Biomolecules*, 2022, **12**, 472.

(52) S. B. Bankar et al., *Biotechnology Advances*, 2009, **27**, 489–501.

(53) H. Hecht et al., *Journal of Molecular Biology*, 1993, **229**, 153–172.

(54) U. Hanefeld, L. Gardossi and E. Magner, *Chem. Soc. Rev.*, 2009, **38**, 453–468.

(55) J. M. Guisan, *Immobilization of Enzymes and Cells*, Humana Press, Totowa, New Jersey, 3rd, 2013, vol. 1051, pp. 1–375.

(56) B. Somchob et al., *Talanta*, 2024, **270**, 125510.

(57) K. Promsuwan et al., *Talanta*, 2023, **256**, 124266.

(58) K. Zhang, Ph.D. Thesis, University of Oxford, 2020, p. 201.

(59) C.-M. Chen et al., *IEEE Journal of Biomedical and Health Informatics*, 2020, **24**, 2208–2215.

(60) Y. Zhang and G. S. Wilson, *Analytica Chimica Acta*, 1993, **281**, 513–520.

(61) J. Wang and F. Lu, *Journal of the American Chemical Society*, 1998, **120**, 1048–1050.

(62) L. Zhu et al., *Biosensors and Bioelectronics*, 2007, **23**, 528–535.

(63) S. Xu et al., *Microchimica Acta*, 2014, **181**, 535–541.

(64) D. Mackey et al., *Sensors and Actuators B: Chemical*, 2007, **122**, 395–402.

(65) N. Martens, *Biosensors and Bioelectronics*, 1995, **10**, 393–403.

(66) J. Wang, in *Electrochemical Sensors, Biosensors and their Biomedical Applications*, Elsevier, 2008, pp. 57–69.

(67) K. Clayton, Ph.D. Thesis, University of Huddersfield, 2011, p. 256.

(68) T. Kuwahara et al., *Synthetic Metals*, 2005, **152**, 29–32.

(69) W. Schuhmann, *Biosensors and Bioelectronics*, 1995, **10**, 181–193.

(70) S. Dzyadevych et al., *IRBM*, 2008, **29**, 171–180.

(71) W. Zhang and G. Li, *Analytical Sciences*, 2004, **20**, 603–609.

(72) U. Gupta et al., *Biotechnology and Bioengineering*, 2022, **119**, 3393–3407.

(73) Y. Ito et al., *Biosensors and Bioelectronics*, 2019, **129**, 189–197.

(74) Y. Tian et al., *Biosensors and Bioelectronics*, 2005, **21**, 557–564.

(75) M. Gerard, *Biosensors and Bioelectronics*, 2002, **17**, 345–359.

(76) G. A. Naikoo et al., *Bioengineering & Translational Medicine*, 2022, **7**, 1–17.

(77) M. Wei et al., *Chemical Communications*, 2020, **56**, 14553–14569.

(78) A. Sassolas, L. J. Blum and B. D. Leca-Bouvier, *Biotechnology Advances*, 2012, **30**, 489–511.

(79) A. Rodriguez-Abetxuko et al., *Frontiers in Bioengineering and Biotechnology*, 2020, **8**, 1–27.

(80) U. Nestor, H. Frodouard and M. Theoneste, *Advances in Nanoparticles*, 2021, **10**, 1–25.

(81) N. R. Mohamad et al., *Biotechnology and Biotechnological Equipment*, 2015, **29**, 205–220.

(82) M. Kamble, H. Salvi and G. D. Yadav, *Journal of Porous Materials*, 2020, **27**, 1559–1567.

(83) N. Carlsson et al., *Advances in Colloid and Interface Science*, 2014, **205**, 339–360.

(84) R. Reshmi, G. Sanjay and S. Sugunan, *Catalysis Communications*, 2006, **7**, 460–465.

(85) M. Ates, *Materials Science and Engineering: C*, 2013, **33**, 1853–1859.

(86) T. M. S. K. Pathiranage et al., *Journal of Polymer Science Part A: Polymer Chemistry*, 2017, **55**, 3327–3346.

(87) J. Scotto et al., *Applied Surface Science*, 2020, **525**, 146440.

(88) S. Sharmeen et al., in *Functional Polysaccharides for Biomedical Applications*, Elsevier, 2019, ch. 11, pp. 357–395.

(89) S. Zhang et al., *Sensors and Actuators, B: Chemical*, 2005, **109**, 367–374.

(90) H. Meskher et al., *Nanoscale Advances*, 2022, **5**, 992–1010.

(91) V. Nagal et al., *New Journal of Chemistry*, 2021, **45**, 18863–18870.

(92) Z. Ashkan et al., *International Journal of Biological Macromolecules*, 2021, **168**, 708–721.

(93) T. Jesionowski, J. Zdarta and B. Krajewska, *Adsorption*, 2014, **20**, 801–821.

(94) T. Sarkar, N. Mukherjee and J. Das, *Applied Physics A*, 2022, **128**, 336.

(95) M. J. Jara Fornerod et al., *Chemistry of Materials*, 2023, **35**, 7577–7587.

(96) J. M. Guisan, *Immobilization of Enzymes and Cells*, Humana Press, Totowa, New Jersey, 2nd, 2008, pp. 1–447.

(97) D. Keller et al., *Biomacromolecules*, 2017, **18**, 2777–2788.

(98) M. Amounas et al., *Journal of Membrane Science*, 2000, **176**, 169–176.

(99) M. Sardar and K. Mirza, in *Biocatalyst Immobilization*, Elsevier, 2023, ch. 12, pp. 269–290.

(100) P. Henke et al., *ACS Applied Materials and Interfaces*, 2020, **12**, 18792–18802.

(101) R. C. Rodrigues et al., *Biotechnology Advances*, 2021, **52**, DOI: 10.1016/j.biotechadv.2021.107821.

(102) A. H. Rather et al., *Biotechnology and Bioengineering*, 2022, **119**, 9–33.

(103) S. Li et al., *Applied Biochemistry and Biotechnology*, 2020, **190**, 982–996.

(104) C.-W. Wu, J.-G. Lee and W.-C. Lee, *Biotechnology and Applied Biochemistry*, 1998, **27**, 225–230.

(105) C. Mateo et al., *Enzyme and Microbial Technology*, 2006, **39**, 274–280.

(106) J. Liu, M. Agarwal and K. Varahramyan, *Sensors and Actuators B: Chemical*, 2008, **135**, 195–199.

(107) B. Philip et al., *Smart Materials and Structures*, 2004, **13**, 295–298.

(108) G. Li et al., *Journal of Polymer Science Part A: Polymer Chemistry*, 2005, **43**, 4547–4558.

(109) D. A. Thadathil et al., *Molecular Catalysis*, 2022, **524**, 112314.

(110) F. Teodorescu et al., *Revista de Chimie*, 2013, **64**, 15–21.

(111) F. Gholami et al., *Scientific Reports*, 2018, **8**, 1–14.

(112) A. Kros et al., *Advanced Materials*, 2001, **13**, 1555–1557.

(113) S. Madakba et al., *Starch/Staerke*, 2013, **65**, 146–150.

(114) C. Dhand et al., *Thin Solid Films*, 2010, **519**, 1145–1150.

(115) A. Kreider et al., *Applied Surface Science*, 2013, **273**, 562–569.

(116) L. Yu, *Frontiers in Bioscience*, 2005, **10**, 2848.

(117) J. Li et al., *ACS Applied Materials & Interfaces*, 2023, DOI: 10.1021/acsami.3c08013.

(118) D. Ucan et al., *Sensors and Actuators, B: Chemical*, 2014, **201**, 545–554.

(119) A. Cuetos et al., *Journal of Molecular Catalysis B: Enzymatic*, 2012, **74**, 178–183.

(120) H. R. Allcock and S. Kwon, *Macromolecules*, 1986, **19**, 1502–1508.

(121) S. Jose et al., *Electrochimica Acta*, 2023, **460**, 142591.

(122) S. D. Minteer, *Enzyme Stabilization and Immobilization: Methods and Protocols*, Humana Press, New Jersey, 1st edn., 2011, pp. 1–229.

(123) Y. R. Maghraby et al., *ACS Omega*, 2023, **8**, 5184–5196.

(124) Q. Lei et al., *Advanced Functional Materials*, 2020, **30**, 1–28.

(125) A. Rex and J. H. Z. dos Santos, *Journal of Sol-Gel Science and Technology*, 2023, **105**, 30–49.

(126) N. Ganonyan et al., *Materials Today*, 2020, **33**, 24–35.

(127) S. Cosnier and M. Holzinger, *Chemical Society Reviews*, 2011, **40**, 2146–2156.

(128) E. J. Choi et al., *Materials Today*, 2023, **62**, 129–150.

(129) I. S. Kucherenko et al., *Applied Nanoscience*, 2023, **13**, 7037–7045.

(130) J. Park et al., *ACS Sensors*, 2020, **5**, 1363–1373.

(131) A. N. Sokolov, M. E. Roberts and Z. Bao, *Materials Today*, 2009, **12**, 12–20.

(132) S. Khan, L. Lorenzelli and R. S. Dahiya, *IEEE Sensors Journal*, 2015, **15**, 3164–3185.

(133) S. Fruncillo et al., *ACS Sensors*, 2021, **6**, 2002–2024.

(134) C. M. Didier et al., *Microsystems & Nanoengineering*, 2023, **9**, 22.

(135) L. Gonzalez-Macia et al., *The Analyst*, 2010, **135**, 845.

(136) G. Francis, B. W. Stuart and H. E. Assender, *Journal of Colloid and Interface Science*, 2020, **568**, 273–281.

(137) S. B. Dulay et al., *Biosensors and Bioelectronics*, 2014, **59**, 342–349.

(138) S. Zhu et al., *Analytica Chimica Acta*, 2021, **1175**, 338759.

(139) M. A. Buttkewitz, C. Heuer and J. Bahnemann, *Current Opinion in Biotechnology*, 2023, **83**, 102978.

(140) Y. Liu et al., *Biosensors and Bioelectronics*, 2018, **100**, 374–381.

(141) Y. Yoshimi et al., *Journal of Artificial Organs*, 2009, **12**, 264–270.

(142) M. Caldara et al., *ACS Sensors*, 2021, **6**, 4515–4525.

(143) Y. Li et al., *Biosensors and Bioelectronics*, 2024, **249**, 116018.

(144) H. Uehara et al., *ACS Nano*, 2009, **3**, 924–932.

(145) A. Ambrózy, L. Hlavatá and J. Labuda, *Acta Chimica Slovaca*, 2013, **6**, 35–41.

(146) Y. Tobimatsu and M. Schuetz, *Current Opinion in Biotechnology*, 2019, **56**, 75–81.

(147) N. C. Paxton et al., *European Polymer Journal*, 2019, **118**, 412–428.

(148) D. Fichou, *Handbook of Oligo- and Polythiophenes*, Wiley-VCH Verlag, Weinheim, Germany, 1st edn., 1998, p. 558.

(149) R. D. McCullough, *Advanced Materials*, 1998, **10**, 93–116.

(150) I. F. Perepichka and D. F. Perepichka, *Handbook of Thiophene-based Materials: Applications in Organic Electronics and Photonics*, Wiley-VCH Verlag, Weinheim, Germany, 1st edn., 2009, p. 833.

(151) C. Zanardi, F. Terzi and R. Seeber, *Analytical and Bioanalytical Chemistry*, 2013, **405**, 509–531.

(152) T. P. Kaloni et al., *Chemistry of Materials*, 2017, **29**, 10248–10283.

(153) B. Adhikari and S. Majumdar, *Progress in Polymer Science*, 2004, **29**, 699–766.

(154) I. Wong and C.-M. Ho, *Microfluidics and Nanofluidics*, 2009, **7**, 291.

(155) Y.-T. Chen et al., *Sensors*, 2017, **17**, 2300.

(156) M. P. Wolf, G. B. Salieb-Beugelaar and P. Hunziker, *Progress in Polymer Science*, 2018, **83**, 97–134.

(157) K. Raj M and S. Chakraborty, *Journal of Applied Polymer Science*, 2020, **137**, 1–14.

(158) D. Qi et al., *Advanced Materials*, 2021, **33**, 1–25.

(159) K. Ma et al., *Journal of Colloid and Interface Science*, 2011, **363**, 371–378.

(160) K. Zalewski, Z. Chyek and W. A. Trzciski, *Polymers*, 2021, **13**, 1080.

(161) M. Mariello et al., *Advanced Materials*, 2022, **34**, DOI: 10.1002/adma.202201129.

(162) A. Zengin and T. Caykara, *Thin Solid Films*, 2011, **519**, 3135–3140.

(163) W. Brutting, W. Brütting and C. Adachi, *Physics of organic semiconductors*, Wiley-VCH, Weinheim, 2nd comple, 2012.

(164) M. Hatano, S. Kambara and S. Okamoto, *Journal of Polymer Science*, 1961, **51**, 26–29.

(165) H. Shirakawa et al., *Journal of the Chemical Society, Chemical Communications*, 1977, 578.

(166) C. K. Chiang et al., *Physical Review Letters*, 1977, **39**, 1098–1101.

(167) C. K. Chiang et al., *Applied Physics Letters*, 1978, **33**, 18–20.

(168) T. Clarke et al., *Synthetic Metals*, 1979, **1**, 21–28.

(169) A. G. MacDiarmid et al., *Philosophical Transactions of the Royal Society of London. Series A, Mathematical and Physical Sciences*, 1985, **314**, 3–15.

(170) R. S. Potember et al., *Polymer Journal*, 1987, **19**, 147–156.

(171) S. N. Chen et al., *Applied Physics Letters*, 1980, **36**, 96–98.

(172) A. Tsumura, H. Koezuka and T. Ando, *Applied Physics Letters*, 1986, **49**, 1210–1212.

(173) G. Bidan, B. Ehui and M. Lapkowski, *Journal of Physics D: Applied Physics*, 1988, **21**, 1043–1054.

(174) J. H. Burroughes et al., *Nature*, 1990, **347**, 539–541.

(175) G. Yu et al., *Science*, 1995, **270**, 1789–1791.

(176) X. Zhou et al., *Journal of Applied Polymer Science*, 2019, **136**, 6–11.

(177) K.-J. Baeg et al., *Advanced Materials*, 2013, **25**, 4267–4295.

(178) Y. Wang et al., *Science Advances*, 2017, **3**, 1–10.

(179) S. Subramaniyan et al., *Advanced Energy Materials*, 2011, **1**, 854–860.

(180) A. R. Bin Mohd Yusoff et al., *Advanced Functional Materials*, 2014, **24**, 2240–2247.

(181) R. McNeill et al., *Australian Journal of Chemistry*, 1963, **16**, 1056–1075.

(182) B. A. Bolto, R. McNeill and D. E. Weiss, *Australian Journal of Chemistry*, 1963, **16**, 1090–1103.

(183) S. L. Meisel, G. C. Johnson and H. D. Hartough, *Journal of the American Chemical Society*, 1950, **72**, 1910–1912.

(184) M. Armour et al., *Journal of Polymer Science Part A-1: Polymer Chemistry*, 1967, **5**, 1527–1538.

(185) T. Yamamoto, K. Sanechika and A. Yamamoto, *Journal of Polymer Science: Polymer Letters Edition*, 1980, **18**, 9–12.

(186) J. W.-P. Lin and L. P. Dudek, *Journal of Polymer Science: Polymer Chemistry Edition*, 1980, **18**, 2869–2873.

(187) K. Namsheer and C. S. Rout, *RSC Advances*, 2021, **11**, 5659–5697.

(188) M. A. Ansari et al., *RSC Advances*, 2018, **8**, 8319–8328.

(189) M. C. Scharber and N. S. Sariciftci, *Advanced Materials Technologies*, 2021, **6**, DOI: 10.1002/admt.202000857.

(190) S. Fratini et al., *Nature Materials*, 2020, **19**, 491–502.

(191) S. Dongmin Kang and G. Jeffrey Snyder, *Nature Materials*, 2017, **16**, 252–257.

(192) C. Wang et al., *Chemical Society Reviews*, 2018, **47**, 422–500.

(193) C. Liu et al., *Materials Horizons*, 2017, **4**, 608–618.

(194) *Large Area and Flexible Electronics*, ed. M. Caironi and Y.-Y. Noh, Wiley-VCH Verlag GmbH & Co. KGaA, Weinheim, Germany, 2015, p. 592.

(195) A. Zen et al., *Advanced Functional Materials*, 2004, **14**, 757–764.

(196) H. Sirringhaus et al., *Nature*, 1999, **401**, 685–688.

(197) A. Marrocchi et al., *Energy and Environmental Science*, 2012, **5**, 8457–8474.

(198) M. H. Choi et al., *Journal of Industrial and Engineering Chemistry*, 2015, **29**, 120–128.

(199) R. L. Elsenbaumer, K. Y. Jen and R. Oboodi, *Synthetic Metals*, 1986, **15**, 169–174.

(200) R. I. Sugimoto et al., *Chemistry Express*, 1986, **1**, 635–638.

(201) K. Kawabata et al., *Polymer Journal*, 2017, **49**, 169–176.

(202) B. A. Miller-Chou and J. L. Koenig, *Progress in Polymer Science*, 2003, **28**, 1223–1270.

(203) Y. M. Chang, Y. T. Hsiao and K. W. Tsai, *Advanced Energy Materials*, 2024, **14**, 1–18.

(204) S. Holliday et al., *Nature Communications*, 2016, **7**, 1–11.

(205) D. Xu et al., *Nature Communications*, 2022, **13**, 1–8.

(206) R. P. Ortiz, A. Facchetti and T. J. Marks, *Chemical Reviews*, 2010, **110**, 205–239.

(207) P. Lin and F. Yan, *Advanced Materials*, 2012, **24**, 34–51.

(208) A. C. Arias et al., *Chemical Reviews*, 2010, **110**, 3–24.

(209) P. Martins et al., *Advanced Functional Materials*, 2023, **33**, DOI: 10.1002/adfm.202213744.

(210) P. Kovacik et al., *Organic Electronics*, 2012, **13**, 687–696.

(211) U. Kraft et al., *Organic Electronics*, 2016, **35**, 33–40.

(212) I. Osaka and R. D. Mccullough, *Accounts of Chemical Research*, 2008, **41**, 1202–1214.

(213) L. Ding et al., *Chemical Reviews*, 2023, **123**, 7421–7497.

(214) H. Chan, *Progress in Polymer Science*, 1998, **23**, 1167–1231.

(215) K. Tamao et al., *Tetrahedron*, 1982, **38**, 3347–3354.

(216) J. Clayden, N. Greeves and S. Warren, *Organic Chemistry*, Oxford University Press, Oxford, 2nd, 2012, vol. 7, pp. 408–426.

(217) K. Yoshino, S. Hayashi and R.-i. Sugimoto, *Japanese Journal of Applied Physics*, 1984, **23**, L899.

(218) S. Hotta, M. Soga and N. Sonoda, *Synthetic Metals*, 1988, **26**, 267–279.

(219) A. Noro et al., *Polymer Preprints, Japan*, 2005, **54**, 3506–3507.

(220) Y. Kametani and M. Ouchi, *ACS Polymers Au*, 2021, **1**, 10–15.

(221) S. Jadoun et al., *European Polymer Journal*, 2021, **155**, 110561.

(222) F. R. Mayo and F. M. Lewis, *Journal of the American Chemical Society*, 1944, **66**, 1594–1601.

(223) J. Huang and S. R. Turner, *Polymer*, 2017, **116**, 572–586.

(224) Y. Qiu et al., *ACS Macro Letters*, 2016, **5**, 332–336.

(225) M. M. Alam et al., *Journal of Polymer Science, Part A: Polymer Chemistry*, 2017, **55**, 919–927.

(226) A. Shit, P. Chal and A. K. Nandi, *Physical Chemistry Chemical Physics*, 2018, **20**, 15890–15900.

(227) P. F. Moonen, I. Yakimets and J. Huskens, *Advanced Materials*, 2012, **24**, 5526–5541.

(228) J. Zikulnig et al., *Advanced Sensor Research*, 2023, **2**, 1–39.

(229) H. Yang, W. R. Leow and X. Chen, *Small Methods*, 2018, **2**, 1–7.

(230) S. S. Dhanabalan and A. Thirumurugan, *Advances in Flexible and Printed Electronics*, IOP Publishing, 2023, pp. 1–298.

(231) S. Kirchmeyer, *Translational Materials Research*, 2016, **3**, 010301.

(232) S. Chung, K. Cho and T. Lee, *Advanced Science*, 2019, **6**, 1801445.

(233) Y. Yang et al., *Journal of Materials Science: Materials in Electronics*, 2000, **11**, 89–96.

(234) P. M. Grubb et al., *Scientific Reports*, 2017, **7**, 1202.

(235) X. Qiu et al., *Coatings*, 2022, **12**, DOI: 10.3390/coatings12121893.

(236) K. S. Kwon et al., *Flexible and Printed Electronics*, 2021, **6**, DOI: 10.1088/2058-8585/abd29e.

(237) C. Fisher et al., *Advanced Materials Technologies*, 2023, **8**, 1–37.

(238) R. Søndergaard et al., *Materials Today*, 2012, **15**, 36–49.

(239) W. J. Hyun et al., *Advanced Materials*, 2015, **27**, 109–115.

(240) S. M. F. Cruz, L. A. Rocha and J. C. Viana, in *Flexible Electronics*, ed. S. Rackauskas, InTech, 2018, ch. 3, p. 25.

(241) P. Rosa, A. Câmara and C. Gouveia, *Open Journal of Internet Of Things*, 2015, **1**, 16–36.

(242) G. Grau et al., *Flexible and Printed Electronics*, 2016, **1**, 023002.

(243) J. Noh et al., *IEEE Transactions on Electronics Packaging Manufacturing*, 2010, **33**, 275–283.

(244) T. Cosnahan, A. A. Watt and H. E. Assender, Materials Today: Proceedings, 2018, vol. 5, pp. 16051–16057.

(245) M. K. Kwak et al., *Journal of Colloid and Interface Science*, 2010, **343**, 301–305.

(246) X. Liu and J. T. Guthrie, *Surface Coatings International Part B: Coatings Transactions*, 2003, **86**, 91–99.

(247) F. T. Association, *Flexography: Principles And Practices*, Foundation of Flexographic Technical Association, 5th edn., 1999.

(248) A. Bastola et al., *Materials Today Electronics*, 2023, **6**, 100058.

(249) D. Shukla, Y. Liu and Y. Zhu, *Nanoscale*, 2022, **15**, 2767–2778.

(250) E. Carlos et al., *Flexible and Printed Electronics*, 2022, **7**, DOI: 10.1088/2058-8585/ac4bb1.

(251) K. Fukuda, *16th International Conference on Nanotechnology - IEEE NANO 2016*, 2016, 838–841.

(252) R. Po et al., *Energy and Environmental Science*, 2014, **7**, 925–943.

(253) Y. Luo et al., *ACS Nano*, 2023, **17**, 5211–5295.

(254) J. R. Sheats, *Journal of Materials Research*, 2004, **19**, 1974–1989.

(255) R. Kukla, R. Ludwig and J. Meinel, *Surface and Coatings Technology*, 1996, **86-87**, 753–761.

(256) W. A. MacDonald et al., *Journal of the Society for Information Display*, 2007, **15**, 1075.

(257) A. Perl, D. N. Reinhoudt and J. Huskens, *Advanced Materials*, 2009, **21**, 2257–2268.

(258) M. I. Maksud, M. S. Yusof and M. M. A. Jamil, *Advanced Materials Research*, 2014, **844**, 158–161.

(259) S. Hassan et al., *IOP Conference Series: Materials Science and Engineering*, 2017, **203**, DOI: 10.1088/1757-899X/203/1/012017.

(260) S. M. Rossnagel, *Journal of Vacuum Science & Technology A: Vacuum, Surfaces, and Films*, 2003, **21**, S74–S87.

(261) D. M. Mattox, *Handbook of Physical Vapor Deposition (PVD) Processing*, Elsevier, 2nd, 2010, p. 793.

(262) D. M. Taylor, *Semiconductor Science and Technology*, 2015, **30**, 054002.

(263) S. H. Kim et al., *International Journal of Precision Engineering and Manufacturing*, 2017, **18**, 1111–1117.

(264) I. Manunza and A. Bonfiglio, *Biosensors and Bioelectronics*, 2007, **22**, 2775–2779.

(265) C. Bishop, *Vacuum Deposition onto Webs, Films and Foils*, Elsevier, Oxford, 3rd, 2015, p. 603.

(266) G. A. Abbas et al., *Organic Electronics*, 2014, **15**, 1998–2006.

(267) B. Kumar, B. K. Kaushik and Y. S. Negi, *Journal of Materials Science: Materials in Electronics*, 2014, **25**, 1–30.

(268) K. A. Morgan et al., *Scientific Reports*, 2019, **9**, 4393.

(269) W. Decker et al., 2019, DOI: http://dx.doi.org/10.14332/svc16.proc.0036.

(270) T. Cosnahan, A. A. Watt and H. E. Assender, *Surface and Coatings Technology*, 2018, **336**, 128–132.

(271) B. W. Stuart et al., *Applied Surface Science*, 2020, **505**, 144294.

(272) J. Zhang et al., *ACS Applied Materials and Interfaces*, 2016, **8**, 33999–34007.

(273) P. C. Hidber et al., *Langmuir*, 1996, **12**, 1375–1380.

(274) N. Copeland, *In-register in-vacuum pattern printing -from wish to reality*, tech. rep., General Vacuum Equipment Ltd, Lancashire, 2008.

(275) B. Piwcyzk, *US Patent: Vacuum deposition methods and masking structure*, 1977.

(276) K. Nagatomi et al., *US Patent: Process for producing metallised plastic film*, 1989.

(277) M. Zare et al., *Journal of Applied Polymer Science*, 2021, **138**, 1–18.

(278) I. Miranda et al., *Journal of Functional Biomaterials*, 2022, **13**, DOI: 10.3390/jfb13010002.

(279) M. J. Owen and P. J. Smith, *Journal of Adhesion Science and Technology*, 1994, **8**, 1063–1075.

(280) H. Hillborg and U. Gedde, *Polymer*, 1998, **39**, 1991–1998.

(281) G. Sui et al., *Analytical Chemistry*, 2006, **78**, 5543–5551.

(282) S. Yanagida et al., *Journal of Photochemistry and Photobiology A: Chemistry*, 2004, **166**, 75–80.

(283) Kim et al., *Macromolecules*, 1999, **32**, 3964–3969.

(284) O. Bertran et al., *Polymer*, 2007, **48**, 6955–6964.

(285) I. Migneault et al., *BioTechniques*, 2004, **37**, 790–802.

(286) X. Wang et al., *Biochemical Engineering Journal*, 2016, **112**, 20–31.

(287) L. Liu et al., *Electrochimica Acta*, 2013, **89**, 616–622.

(288) M. Béra-Abérem, H.-A. Ho and M. Leclerc, *Tetrahedron*, 2004, **60**, 11169–11173.

(289) G. Li et al., *Macromolecular Chemistry and Physics*, 1998, **199**, 2255–2266.

(290) P. Baüerle et al., *Advanced Materials*, 1996, **8**, 214–218.

(291) H.-C. Kim et al., *Polymers for Advanced Technologies*, 2009, **20**, 298–302.

(292) N. Aydemir, J. Malmström and J. Travas-Sejdic, *Physical Chemistry Chemical Physics*, 2016, **18**, 8264–8277.

(293) S. Chen, W. Chen and G. Xue, *Macromolecular Bioscience*, 2008, **8**, 478–483.

(294) S. Soylemez et al., *Journal of Materials Chemistry B*, 2014, **2**, 511–521.

(295) H. U. Bergmeyer, in *Methods of Enzymatic Analysis*, ed. H. U. Bergmeyer and K. Gawehn, Elsevier, Weinheim, 2nd edn., 1974, vol. 1, ch. 2, pp. 456–458.

(296) S. Hotta et al., *Macromolecules*, 1987, **20**, 212–215.

(297) R. Liu and Z. Liu, *Chinese Science Bulletin*, 2009, **54**, 2028–2032.

(298) M. R. Karim, *Journal of Nanomaterials*, 2012, **2012**, DOI: 10.1155/2012/174353.

(299) R. S. Futane, V. M. Raut and S. D. Dhande, *Rasayan Journal of Chemistry*, 2016, **9**, 842–848.

(300) L. F. Cházaro-Ruiz, A. Kellenberger and L. Dunsch, *The Journal of Physical Chemistry B*, 2009, **113**, 2310–2316.

(301) O. Bertran et al., *Polymer*, 2008, **49**, 1972–1980.

(302) A. Pron et al., *Macromolecules*, 1995, **28**, 4644–4649.

(303) A. Husain, S. Ahmad and F. Mohammad, *Materialia*, 2020, **14**, 100868.

(304) D. Thanasamy et al., *Polymer*, 2019, **175**, 32–40.

(305) J. M. R. C. Fernando and G. K. R. Senadeera, *Current Science*, 2008, **95**, 743–750.

(306) K. Majid et al., *Journal of Materials Science: Materials in Electronics*, 2009, **20**, 958–966.

(307) J. Roncali, *Chemical Reviews*, 1992, **92**, 711–738.

(308) T. Olinga and B. François, *Synthetic Metals*, 1995, **69**, 297–298.

(309) M. Roesing, J. Howell and D. Boucher, *Journal of Polymer Science Part B: Polymer Physics*, 2017, **55**, 1075–1087.

(310) R. Spann and D. Boucher, *Journal of Polymer Science*, 2023, **61**, 503–514.

(311) T. A. P. Hai and R. Sugimoto, *Journal of Molecular Structure*, 2017, **1146**, 660–668.

(312) M. Trznadel et al., *Macromolecules*, 1998, **31**, 5051–5058.

(313) S. Amou et al., *Journal of Polymer Science Part A: Polymer Chemistry*, 1999, **37**, 1943–1948.

(314) J. Gadient, R. Groch and C. Lind, *Polymer*, 2017, **115**, 21–27.

(315) J. He et al., *Journal of Applied Polymer Science*, 2007, **105**, 3543–3550.

(316) T. Kuwahara et al., *Polymer*, 2005, **46**, 8091–8097.

(317) P. Englebienne and M. Weiland, *Chemical Communications*, 1996, **1200**, 1651.

(318) O. Bertran et al., *Journal of Physical Chemistry B*, 2010, **114**, 6281–6290.

(319) M. Giglioti et al., *Solar Energy Materials and Solar Cells*, 2004, **82**, 413–420.

(320) A. L. Gomes et al., *Journal of Polymer Research*, 2011, **18**, 1509–1517.

(321) C. Delia Casa et al., *Makromolekulare Chemie. Macromolecular Symposia*, 1992, **59**, 233–246.

(322) C. Della Casa et al., *Acta Polymerica*, 1997, **48**, 251–255.

(323) A. d. F. Mescoloto et al., *Polímeros Ciência e Tecnologia*, 2014, **24**, 31–35.

(324) G. Li et al., *Macromolecular Chemistry and Physics*, 1998, **199**, 525–533.

(325) Y. Liu et al., *Polymer Bulletin*, 2015, **72**, 1817–1826.

(326) S. Hayashi, S.-i. Yamamoto and T. Koizumi, *Scientific Reports*, 2017, **7**, 1078.

(327) A. Stalder et al., *Colloids and Surfaces A: Physicochemical and Engineering Aspects*, 2006, **286**, 92–103.

(328) K. Efimenko, W. E. Wallace and J. Genzer, *Journal of Colloid and Interface Science*, 2002, **254**, 306–315.

(329) Y. J. Fu et al., *Langmuir*, 2010, **26**, 4392–4399.

(330) F. M. Fowkes, *The Journal of Physical Chemistry*, 1963, **67**, 2538–2541.

(331) D. K. Owens and R. C. Wendt, *Journal of Applied Polymer Science*, 1969, **13**, 1741–1747.

(332) S. Béfahy et al., *Langmuir*, 2010, **26**, 3372–3375.

(333) A. Oláh, H. Hillborg and G. Vancso, *Applied Surface Science*, 2005, **239**, 410–423.

(334) H. R. Cho, D. Choi and M. Byun, *Thin Solid Films*, 2020, **697**, 137812.

(335) Y. Berdichevsky et al., *Sensors and Actuators B: Chemical*, 2004, **97**, 402–408.

(336) A. Santoso et al., *Chemical Communications*, 2022, **58**, 10805–10808.

(337) A. E. Özçam, K. Efimenko and J. Genzer, *Polymer*, 2014, **55**, 3107–3119.

(338) J. Kim, M. K. Chaudhury and M. J. Owen, *Journal of Colloid and Interface Science*, 2000, **226**, 231–236.

(339) D. W. Fakes et al., *Surface and Interface Analysis*, 1987, **10**, 416–423.

(340) H. Nakae et al., *Acta Materialia*, 1998, **46**, 2313–2318.

(341) M. Kanungo et al., *Langmuir*, 2014, **30**, 7358–7368.

(342) J. L. Fritz and M. J. Owen, *The Journal of Adhesion*, 1995, **54**, 33–45.

(343) H. Hillborg, M. Sandelin and U. W. Gedde, *Polymer*, 2001, **42**, 7349–7362.

(344) M. Pascual et al., *Soft Matter*, 2019, **15**, 9253–9260.

(345) T. Senzai and S. Fujikawa, *Langmuir*, 2019, **35**, 9747–9752.

(346) D. Bodas and C. Khan-Malek, *Sensors and Actuators, B: Chemical*, 2007, **123**, 368–373.

(347) D. T. Eddington, J. P. Puccinelli and D. J. Beebe, *Sensors and Actuators B: Chemical*, 2006, **114**, 170–172.

(348) G. Francis, Ph.D. Thesis, University of Oxford, 2019, p. 108.

(349) G. Camino, S. Lomakin and M. Lazzari, *Polymer*, 2001, **42**, 2395–2402.

(350) G. Camino, S. Lomakin and M. Lageard, *Polymer*, 2002, **43**, 2011–2015.

(351) M. Liu, J. Sun and Q. Chen, *Sensors and Actuators A: Physical*, 2009, **151**, 42–45.

(352) J. J. Bowen et al., *Advanced Functional Materials*, 2015, **25**, 5520–5528.

(353) J. P. Icenhower and P. M. Dove, *Geochimica et Cosmochimica Acta*, 2000, **64**, 4193–4203.

(354) A. J. Mazaltarim et al., *ACS Applied Materials and Interfaces*, 2019, **11**, 33452–33457.

(355) M. Morra et al., *Journal of Colloid And Interface Science*, 1990, **137**, 11–24.

(356) H.-C. Kim et al., *Macromolecular Research*, 2006, **14**, 173–178.

(357) M. Mortazavi and M. Nosonovsky, *Applied Surface Science*, 2012, **258**, 6876–6883.

(358) I. J. Chen and E. Lindner, *Langmuir*, 2007, **23**, 3118–3122.

(359) M. Murata and K. Higashi, *US Patent: Anti-Reflective Materials*, 2003.

(360) H. Hintz et al., *Chemistry of Materials*, 2011, **23**, 145–154.

(361) J. Rodríguez-López, M. A. Alpuche-Avilés and A. J. Bard, *Journal of the American Chemical Society*, 2008, **130**, 16985–16995.

(362) R. Santos de Amorim et al., *Results in Chemistry*, 2024, **7**, 101488.

(363) C. Barus et al., *Electrochimica Acta*, 2007, **52**, 7978–7985.

(364) N. P. Shetti, S. J. Malode and S. T. Nandibewoor, *Analytical Methods*, 2015, **7**, 8673–8682.

(365) M. Skompska and A. Szkurat, *Electrochimica Acta*, 2001, **46**, 4007–4015.

(366) R. Gonçalves, E. C. Pereira and L. F. Marchesi, *International Journal of Electrochemical Science*, 2017, **12**, 1983–1991.

(367) A. Guiseppi-Elie, C. Lei and R. H. Baughman, *Nanotechnology*, 2002, **13**, 559–564.

(368) R. Cui et al., *Electrochimica Acta*, 2011, **58**, 179–183.

(369) S. Alwarappan et al., *Analytical Letters*, 2012, **45**, 746–753.

(370) M. Shamsipur and M. Amouzadeh Tabrizi, *Materials Science and Engineering: C*, 2014, **45**, 103–108.

(371) The Emerging Risk Factors Collaboration, *The Lancet*, 2010, **375**, 2215–2222.

(372) B. Zhou et al., *The Lancet*, 2016, **387**, 1513–1530.

(373) W. D. Smith et al., *American Journal of Health-System Pharmacy*, 2005, **62**, 714–719.

(374) C. M. Wong, K. H. Wong and X. D. Chen, *Applied Microbiology and Biotechnology*, 2008, **78**, 927–938.

(375) J. M. Harris, C. Reyes and G. P. Lopez, *Journal of Diabetes Science and Technology*, 2013, **7**, 1030–1038.

(376) K. M. Rusin, T. L. Fare and J. Z. Stemple, *Biosensors and Bioelectronics*, 1992, **7**, 367–373.

(377) J. Wang et al., *PLoS ONE*, 2012, **7**, ed. M. A. Barbosa, e43478.

(378) E. M. Ekanayake, D. Preethichandra and K. Kaneto, *Biosensors and Bioelectronics*, 2007, **23**, 107–113.

(379) M. I. Pilo et al., *Nanomaterials*, 2022, **12**, 2840.

(380) B. Ç. Özkan et al., *Materials Chemistry and Physics*, 2022, **288**, 126397.